ACOUSTIC TRANSDUCTION – MATERIALS AND DEVICES

Period 1 January 1999 to 31 December 1999

Annual Report

VOLUME III

OFFICE OF NAVAL RESEARCH
Contract No: N00014-96-1-1173

APPROVED FOR PUBLIC RELEASE – DISTRIBUTION UNLIMITED

Kenji Uchino

PENNSTATE

THE MATERIALS RESEARCH LABORATORY
UNIVERSITY PARK, PA

REPORT DOCUMENTATION PAGE

Form Approved
OMB No. 0704-0188

1. AGENCY USE ONLY (Leave blank)	2. REPORT DATE	3. REPORT TYPE AND DATES COVERED
	06/12/2000	ANNUAL REPORT 01/01/2000-12/31/2000

4. TITLE AND SUBTITLE

ACOUSTIC TRANSDUCTION -- MATERIALS AND DEVICES

5. FUNDING NUMBERS

ONR CONTRACT NO.
N00014-96-1-11173

6. AUTHOR(S)

KENJI UCHINO

7. PERFORMING ORGANIZATION NAME(S) AND ADDRESS(ES)

Materials Research Laboratory
The Pennsylvania State University
University Park, PA 16802

8. PERFORMING ORGANIZATION REPORT NUMBER

9. SPONSORING / MONITORING AGENCY NAME(S) AND ADDRESS(ES)

Office of Naval Research
ONR 321SS
Ballston Centre Tower One
800 N Quincy Street
Arlington VA 22217-5660

Office of Naval Research
Regional Office Chicago
536 S Clark Str., RM 208
Chicago IL 60605-1588

10. SPONSORING / MONITORING AGENCY REPORT NUMBER

11. SUPPLEMENTARY NOTES

12a. DISTRIBUTION / AVAILABILITY STATEMENT

12b. DISTRIBUTION CODE

13. ABSTRACT *(Maximum 200 words)*

SEE FOLLOWING PAGE

14. SUBJECT TERMS

15. NUMBER OF PAGES

16. PRICE CODE

17. SECURITY CLASSIFICATION OF REPORT	18. SECURITY CLASSIFICATION OF THIS PAGE	19. SECURITY CLASSIFICATION OF ABSTRACT	20. LIMITATION OF ABSTRACT
UNCLASSIFIED	UNCLASSIFIED	UNCLASSIFIED	

GENERAL INSTRUCTIONS FOR COMPLETING SF 298

The Report Documentation Page (RDP) is used in announcing and cataloging reports. It is important that this information be consistent with the rest of the report, particularly the cover and title page. Instructions for filling in each block of the form follow. It is important to ***stay within the lines*** to meet ***optical scanning requirements***.

Block 1. Agency Use Only *(Leave blank)*.

Block 2. Report Date. Full publication date including day, month, and year, if available (e.g. 1 Jan 88). Must cite at least the year.

Block 3. Type of Report and Dates Covered. State whether report is interim, final, etc. If applicable, enter inclusive report dates (e.g. 10 Jun 87 - 30 Jun 88).

Block 4. Title and Subtitle. A title is taken from the part of the report that provides the most meaningful and complete information. When a report is prepared in more than one volume, repeat the primary title, add volume number, and include subtitle for the specific volume. On classified documents enter the title classification in parentheses.

Block 5. Funding Numbers. To include contract and grant numbers; may include program element number(s), project number(s), task number(s), and work unit number(s). Use the following labels:

C	- Contract	PR	- Project
G	- Grant	TA	- Task
PE	- Program Element	WU	- Work Unit Accession No.

Block 6. Author(s). Name(s) of person(s) responsible for writing the report, performing the research, or credited with the content of the report. If editor or compiler, this should follow the name(s).

Block 7. Performing Organization Name(s) and Address(es). Self-explanatory.

Block 8. Performing Organization Report Number. Enter the unique alphanumeric report number(s) assigned by the organization performing the report.

Block 9. Sponsoring/Monitoring Agency Name(s) and Address(es). Self-explanatory.

Block 10. Sponsoring/Monitoring Agency Report Number. *(If known)*

Block 11. Supplementary Notes. Enter information not included elsewhere such as: Prepared in cooperation with...; Trans. of...; To be published in.... When a report is revised, include a statement whether the new report supersedes or supplements the older report.

Block 12a. Distribution/Availability Statement. Denotes public availability or limitations. Cite any availability to the public. Enter additional limitations or special markings in all capitals (e.g. NOFORN, REL, ITAR).

DOD	- See DoDD 5230.24, "Distribution Statements on Technical Documents."
DOE	- See authorities.
NASA	- See Handbook NHB 2200.2.
NTIS	- Leave blank.

Block 12b. Distribution Code.

DOD	- Leave blank.
DOE	- Enter DOE distribution categories from the Standard Distribution for Unclassified Scientific and Technical Reports.
NASA	- Leave blank.
NTIS	- Leave blank.

Block 13. Abstract. Include a brief *(Maximum 200 words)* factual summary of the most significant information contained in the report.

Block 14. Subject Terms. Keywords or phrases identifying major subjects in the report.

Block 15. Number of Pages. Enter the total number of pages.

Block 16. Price Code. Enter appropriate price code *(NTIS only)*.

Blocks 17. - 19. Security Classifications. Self-explanatory. Enter U.S. Security Classification in accordance with U.S. Security Regulations (i.e., UNCLASSIFIED). If form contains classified information, stamp classification on the top and bottom of the page.

Block 20. Limitation of Abstract. This block must be completed to assign a limitation to the abstract. Enter either UL (unlimited) or SAR (same as report). An entry in this block is necessary if the abstract is to be limited. If blank, the abstract is assumed to be unlimited.

ABSTRACT

This report describes the research performed over the period of 1 January 1999 to 31 December 1999 on a MURI under Office of Naval Research contract N00014-96-1-1173 on the topic "Acoustic Transduction: Materials and Devices" brings together work from the Materials Research Laboratory (MRL), the Applied Research Laboratory (ARL), and the Center for Acoustics and Vibrations (CAV) at The Pennsylvania State University. As has become customary over many years research on the program is described in detail in the 87 technical appendices to this report and only a brief narrative description connecting this research is given in the text.

Perhaps the most outstanding accomplishment of the year is a "spin on" from our earlier single crystal studies now involving Brookhaven National Laboratory and Professor Gonzalo's group in Madrid, Spain. Using exceptionally homogeneous polycrystal lead zirconate titanate samples prepared in MRL, precise synchotron x-ray analysis has confirmed a new monoclinic phase at lower temperature in composition close to the important morphotropic phase boundary. This work demands a re-thinking of both intrinsic and extrinsic contributions to response in this most important practical transducer material family. Domain Engineering/Domain Averaging in lead zinc niobate:lead titanate (PZN:PT) in lead magnesium niobate:lead titante (PMN:PT) and inn barium titanate ($BaTiO_3$) continues to offer single crystal systems with outstanding transducer and actuator properties and new insights into the field induced strain mechanisms in all perovskite type piezoelectrics. Excellent progress with the new high strain irradiated P(VDF:TrFE) relaxor ferroelectric copolymer system has helped catalyze a new DARPA initiative in this area and a re-awakening of interest in the whole area of electrostrictive polymer systems.

A primary objective of this MURI grouping was to help shorten the time constant for new materials and device concepts to be applied in practical Navy Systems. We believe this has now been realized in joint work on the composite cymbal type flextensional arrays for large area projectors, and in the progress made towards a micro-tonpilz array system.

Original work on new step and repeat piezoelectric high strain systems continues to make good progress now using commercial motion rectifiers to produce both linear and rotary systems with high torque capability. New composite designs are pushing toward 1 mm diameter motors in the size regimen where there are real difficulties for conventional electromagnetic designs.

A new area of activity this year is in piezoelectric transformers where a circular symmetry design in conjunction with controlled inhomogeneous poling is shown to offer capabilities which are of real interest for energy recovery actuator power systems. Basic studies have evolved a new environmental SEM technique for high resolution domain wall studies without changing problems. Work is continuing on reliable measurements of electrostrictive constants in simple solids confirming by both direct and converse methods and permitting the first generalization of trends in these fundamentally important coupling constants.

ACOUSTIC TRANSDUCTION – MATERIALS AND DEVICES

Period 1 January 1999 to 31 December 1999

Annual Report

VOLUME III

OFFICE OF NAVAL RESEARCH
Contract No: N00014-96-1-1173

Kenji Uchino

APPENDICES

VOLUME I

GENERAL SUMMARY PAPERS

1. Cross, L.E., "Newnham Festschrift Introduction." Guest Editorial, Mat. Res. Innovations **2**, 251 (1999).
2. Newnham, R.E., "Ceramics into the Next Millennium," *British Ceramic Transactions* **98**(5), 251-255 (1999).
3. Uchino, K. and S. Takahashi, "New Trend in Multilayer Ceramic Actuators," Proc. Int'l Symp. Dielectric Ceramics, Amer. Ceram. Soc. '98; Ceramic Trans., Vol. 100, Dielectric Ceramic Materials, p.455 - 468 (1999).
4. Uchino, K., "Smart Composite Materials," Chap.5.19, Comprehensive Composite Materials, Elsevier Science, Oxford, UK (2000). [in press]
5. Kelly, A., R. Davidson, and K. Uchino "Smart Composite Materials Systems," Chap.5.20, Comprehensive Composite Materials, Elsevier Science, Oxford, UK (2000). [in press]
6. Fousek, J., L.E. Cross, and D.B. Litvin, "Possible Piezoelectric Composites Based on the Flexoelectric Effect." Materials Letters **39**, 287-291 (1999).

2.0 MATERIALS STUDIES

2.1 Polycrystal Perovskite Ceramics

7. Noheda, B., D.E. Cox, G. Shirane, J.A. Gonzalo, L.E. Cross, and S.-E. Park, "A Monoclinic Ferroelectric Phase in the $Pb(Zr_{1-x}Tix)O_3$ Solid Solution." Applied Physics Letters **74**(14), 2059-2061 (1999).
8. Noheda, B., J.A. Gonzalo, R. Guo, S.-E. Park, L.E. Cross, D.E. Cox, and G. Shirane, "The monoclinic phase in PZT: new light on morphotropic phase boundaries," Proceedings of the Workshop on Fundamental Physical of Ferroelectrics, Aspen, CO (February 2000).
9. Noheda, B., J.A. Gonzalo, L.E. Cross, R. Guo, S.-E. Park, D.E. Cox, and G. Shirane, "Tetragonal-to-monoclinic phase transition in a ferroelectric perovskite: The structure of $PbZr_{0.52}Ti_{0.48}O_3$," *Physical Review B* **61**(13), 8687 (April 2000).
10. Guo, R., L.E. Cross, S.-E. Park, B. Noheda, D.E. Cox, and G. Shirane, "Origin of the high piezoelectric response in $PbZr_{1-x}Ti_xO_3$," *Physical Review Letters* **84**(23) (June 2000).
11. Zhang, Q.M., "Electromechanical Properties of Lead Zirconate Titanate Piezoceramics Under the Influence of Mechanical Stresses," IEEE Transactions on Ultrasonics, Ferroelectrics, and Frequency Control **46**(6) (November 1999).
12. Wang, H., W. Jiang, and W. Cao, " Characterization of Lead Zirconate Titanate Piezoceramic Using High Frequency Ultrasonic Spectroscopy," J. Appl. Phys. **85**, 8083-8091 (1999).
13. Zhao, J., V. Mueller, and Q.M. Zhang, "The Influence of External Stress on the Electromechanical Response of Electrostrive 0.9PMN-0.1PT in the DC Field Biased State," J. Mater. Res. **14**, 948-956 (1999).

2.0 MATERIALS STUDIES

2.1 Polycrystal Perovskite Ceramics (continued)

14. Zhao, J., A.E. Glazounov, and Q.M. Zhang, "Change in Electromechanical Properties of 0.9PMN-0.1PT Relaxor Ferroelectric Induced by Uniaxial Compressive Stress Directed Perpendicular to the Electric Field," Appl. Phys. Lett. 74, 436-438 (1999).
15. Albert, E.F., A.S. Bhalla, and T. Takenaka, "Large Hydrostatic Piezoelectric Constant and Temperature Dependence of the Piezoelectric Properties $Bi(Ni_{1/2}Ti_{1/2})O_3$:$PbTiO_3$ Ceramics," Ferroelectrics Letters **25**, 45-52 (1999).
16. Alberta, E.F. and A.S. Bhalla, "Investigation of the Lead Indium Niobate–Lead Magnesium Niobate Solid Solution," Materials Letters **40**, 114-117 (1999).
17. Alberta, E.F. and A.S. Bhalla, "Electrical Properties of the Morphotropic Phase Boundary in $Pb(In_{1/2}Ta_{1/2})O_3$-$PbTiO_3$ Ceramics," Ferroelectrics Letters **26**, 117-123 (1999).
18. Kim, J.S., S.J. Kim, H.G. Kim, D.C. Lee, and K. Uchino, "Piezoelectric and Dielectric Properties of Fe_2O_3-Doped $0.57Pb(Sc_{1/2}Nb_{1/2})O_3$-$0.43PbTiO_3$ Ceramic Materials," Jpn. J. Appl. Phys. **38**(Part 1, No. 3A), 1433-1437 (1999)..

VOLUME II

19. Liu, S.F., I.R. Abothu, S. Komarneni, P. Poosanaas, D.S. Paik, Y. Ito, and K. Uchino, "PLZT Ceramics Prepared from Conventional and Microwave Hydrothermal Powders," Ferroelectrics **231**, 179-185 (1999).
20. Chen, Y. H., S. Hirose, D. Viehland, S. Takahashi, and K. Uchino, "Mn-Modified $Pb(Mg_{1/3}Nb_{2/3})O_3$-$PbTiO_3$ Ceramics: Improved Mechanical Quality Factors for High Power Transduction Applications," Jpn. J. Appl. Phys. (1999). [accepted].
21. Chen, Y.H., S. Hirose, D. Viehland, and K. Uchino, "Doping Effects in $Pb(Mg_{1/3}Nb_{2/3})O_3$-$PbTiO_3$ Ceramics for High Power Transduction Applications," Mater. Res. Soc. Fall Mtg. '99, LL.5.9, Boston (Nov. 29-Dec.3, 1999).
22. Du, X.H., Q.M. Wang, U. Belegundu, and K. Uchino, "Piezoelectric Property Enhancement in Polycrystalline Lead Zirconate Titanate by Changing Cutting Angle," J. Ceram. Soc. Jpn. **107**(2), 190-191 (1999).

2.2 Single Crystal Systems

23. Wada, S., S.E. Park, L.E. Cross, and T.R. Shrout, "Engineered Domain Configuration in Rhombohedral PZN-PT Single Crystals and their Ferroelectric Related Properties." Ferroelectrics **221**, 147-155 (1999).
24. Liu, S.-F., S.E. Park, T.R. Shrout, and L.E. Cross. "Electric Field Dependence of Piezoelectric Properties for Rhombohedral $0.955Pb(Zn_{1/3}Nb_{2/3})O_3$–$0.045PbTiO_3$ Single Crystals." Journal of Applied Physics **85** (5), 2810-2814 (1999).
25. Erhart, J. and W. Cao, "Effective Material Properties in Twinned Ferroelectric Crystals," J. Appl. Phys. **86**, 1073- 1081 (1999).

2.0 MATERIALS STUDIES

2.2 Single Crystal Systems (continued)

26. Yin, J., B. Jiang, and W. Cao, "Elastic, Piezoelectric and Dielectric Properties of $0.955Pb(Zn_{1/3}Nb_{2/3})O_3$-$0.045PbTiO_3$ Single Crystal with Designed Multidomains," IEEE Transactions UFFC **47**, 285-291 (2000).
27. Wada, S., S.E. Park, L.E. Cross, and T.R. Shrout, "Defect-induced Domain Configuratrion in Relaxor PZN Single Crystal and Its Origin." Trans. of the Mat. Res. Soc. Of Japan **24**(1), 19-22 (1999).
28. Belegundu, U., X. Du, and K. Uchino, "Switching Current In $Pb(Zn_{1/3}Nb_{2/3})O_3$-$PbTiO_3$ Single Crystals, MRS Meeting, Boston (November 1999).
29. Park, S.-E., S. Wada, L.E. Cross, and T.R. Shrout, "Crystallographically Engineered $BaTiO_3$ Single Crystals for High-Performance Piezoelectrics." Journal of Applied Physics **86**(5), 2746-2750 (1999).
30. Du, X.H., Q.M. Wang, U. Belegundu, A. Bhalla, and K. Uchino, "Crystal Orientation Dependence of Piezoelectric Properties of Single Crystal Barium Titanate," Mater. Lett. **40**, 109-113 (1999).
31. Lu, .Y., Z.-Y. Cheng, E. Park, S.F. Liu and Q.M. Zhang, "Linear Electro-optic Effect of $0.88Pb(Zn_{1/3}Nb_{2/3})$-$0.12PbTiO_3$ Single Crystal," Jpn. J. Appl. Phys. 141-145 (2000).

2.3 High Strain Polymers

32. Bharti, V., H.S. Xu, G. Shanthi, Q.M. Zhang, and K. Liang, "Polarization and Structural Properties of High Energy Electron Irradiated P(VDF-TrFE) Copolymer Films," J. Appl. Phys. **87**, 452-461 (2000).
33. Cheng, Z.-Y., T.-B. Xu, V. Bharti, S. Wang, and Q.M. Zhang, "Transverse Strain Response in the Electrostrictive P(VDF-TrFE) Copolymer," Appl. Phys. Lett. **74**, 1901-1903 (1999).
34. Cheng, Z.-Y, V. Bharti, T.B. Xu, S. Wang, Q.M. Zhang, T. Ramotowski, F. Tito, and R. Ting, "Transverse Strain Responses in Electrostrictive P(VDF-TrFE) Films and Development of a Dilatometer for the Measurement," J. Appl. Phys. **86**, 2208-2214 (1999).
35. Bharti, V., Z-Y Cheng, S. Gross, T.B. Xu, and Q.M. Zhang, "High Electrostrictive Strain under High Mechanical Stress in High Energy Electron Irradiated Poly(vinylidene fluoride-trifluoroethylene) Copolymer Films," Appl. Phys. Lett. **75**, 2653-2655 (1999).

3.0 TRANSDUCER STUDIES

3.1 Composite Structures

36. Geng, X. and Q.M. Zhang, "Resonance Modes and Losses in 1-3 Composites for Ultrasonic Transducer Applications," J. Appl. Phys. **85**, 1342-1350 (1999).
37. Tressler, J. and K. Uchino, "Piezoelectric Composite Sensors," Chap.5.25, Comprehensive Composite Materials, Elsevier Science, Oxford, UK (2000). [in press]
38. Tressler, J.F., S. Alkoy, A. Dogan, and R.E. Newnham, "Functional Composites for Sensors, Actuators and Transducers," Composites Part A: Applied Science & Manufacturing **30**, 477-482 (1999).

3.0 TRANSDUCER STUDIES

3.1 Composite Structures (continued)

39. Tressler, J.F. and R.E. Newnham, "Capped Ceramic Underwater Sound Projector: The "Cymbal" Transducer," J. of Acoustical Soc. America **105**(2), part 1, 591-600 (1999).

VOLUME III

40. Zhang, J., W.J, Hughes., P. Bouchilloux, R. Meyer Jr., K. Uchino, and R.E. Newnham, "A Class V Flextensional Transducer: The Cymbal," Ultrasonics **37**, 387-393 (1999).

41. Zhang, J., W.J. Hughes, R.J. Meyer Jr., K. Uchino, and R.E. Newnham, "Cymbal Array: A Broad Band Sound Projector," Ultrasonics **37**, 523-529 (2000).

3.0 TRANSDUCER STUDIES

3.1 Composite Structures (continued)

42. Zhang, J., W.J. Hughes, A.C. Hladky-Hennion and R.E. Newnham, "Concave Cymbal Transducers," Materials Research Innovations **2** (5), 252-255 (1999).

43. Alkoy, S., R.E. Newnham, A.C. Hladky, A. Dogan, and J.K. Cochran, Jr., "Piezoelectric Hollow Spheres for Microprobe Hydrophones," Ferroelectrics **226**, 11-25 (1999).

44. Carlson, W.B., R.E. Newnham and D.P. Williams, "Piezotensegritic Structures for Transducer Applications," Materials Research Innovations **3**, 175-178 (1999).

45. Newnham, R.E. and A. Amin, "Smart Systems: Microphones, Fish Farming, and Beyond," Chemtech **29**(12), 38-47 (1999).

3.2 3-Dimensional Acoustic Intensity Probes

46. Bastyr, K.J., G.C. Lauchle, and J.A. McConnell, "Development of a Velocity Gradient Underwater Acoustic Intensity Sensor," J. Acoust. Soc. Am. **106**, 3178-3188 (1999).

47. Lauchle, G.C. and W.A. Kargus, IV, "Scaling of Turbulent Wall Pressure Fluctuations Downstream of a Rearward Facing Step," J. Acoust. Soc. Am. **107**, L1-L6 (2000).

3.3 Piezoelectric Transformers

48. Koc, B., S. Alkoy, and K. Uchino, "A Circular Piezoelectric Transformer with Crescent Shape Input Electrodes," Proc. IEEE Ultrasonic Symp., Lake Tahoe, Nevada, Oct. 17-21 (1999).

49. Koc, B. and K. Uchino, "Disk Type Piezoelectric Transformer with Crescent Shape Input Electrodes," Proc. NATO- Advanced Research Workshop: Piezoelectric Materials, Advance in Science, Technology and Applications, Predeal, Romania (May 24-27, 1999).

4.0 ACTUATOR STUDIES

4.1 Materials and Designs

50. Uchino, K., "Recent Trend of Piezoelectric Actuator Developments," Proc. Int'l Symp. Micromechatronics and Human Science '99, p.3-9, Nagoya, Japan (Nov. 23-26, 1999).
51. Yao, K., W. Zhu, K. Uchino, Z. Zhang and L.C. Lim, "Design and Fabrication of a High Performance Multilayer Piezoelectric Actuator with Bending Deformation," **46** (4), 1020-1027 (1999).
52. Wang, Q.-M., X.-H. Du, B. Xu, and L.E. Cross, "Electromechanical Coupling and Output Efficiency of Piezoelectric Bending Actuators." IEEE Transactions on Ultrasonics, Ferroelectrics, and Frequency Control **46** (3), 638-646 (1999).
53. Wang, Q.-M. and L.E. Cross, "Analysis of High Temperature Reduction Processing of RAINBOW Actuator." Materials Chemistry and Physics **58**, 20-25 (1999).
54. Glazounov, A.E., Q.M. Zhang, and C. Kim, "Torsional Actuator Based on Mechanically Amplified Shear Piezoelectric Response," Sensors and Actuators **A79**, 22-30 (2000).
55. Yoo, J.-H., J.-I Hong, and W. Cao, "Piezoelectric Ceramic Bimorph Coupled to Thin Metal Plat as Cooling Fan for Electronic Devices," Sensors and Actuators **79**, 8-12 (1999).

4.2 Photostriction

56. Poosanaas, P., K. Tonooka and K. Uchino, "Photostrictive Actuators," J. Mechatronics (1999) [in press].
57. Poosanaas, P. and K. Uchino, "Photostrictive Effect in Lanthanum-Modified Lead Zirconate Titanate Ceramics near the Morphotropic Phase Boundary," J. Mater. Chem. and Phys. **61**, 36-41 (1999).

VOLUME IV

4.3 High Force Torsional Actuators

58. Frank, J.E., G.H. Koopmann, W. Chen, and G.A. Lesieutre, "Design and Performance of a High Force Piezoelectric Inchworm Actuator," Proceedings of SPIE 6th Annual International Symposium on Smart Structures and Materials, 1999.
59. Koopmann, G.H., G.A. Lesieutre, J. Frank, and W. Chen, "Design and Performance of a Linear Piezoelectric Wedgeworm Actuator," Piezoelectric Materials: Advances in Science, Technology and Applications, 383-390 (2000).
60. Frank, J. E.M. Mockensturm, W. Chen, G.H. Koopmann, and G.A. Lesieutre, "Roller-Wedgeworm: A Piezoelectrically-Driven Rotary Motor," 10th International Conference on Adaptive Structures and Technologies, Paris (October 1999).

4.4 Piezoelectric Mini Motors

61. Glazounov, A.E., S. Wang, Q.M. Zhang, and C. Kim, "High Efficiency Piezoelectric Motor Combining Continuous Rotation with Precise Control Over Angular Positioning," Appl. Phys. Lett. **75**, 862-864 (1999).
62. Uchino, K. and B. Koc, "Compact Piezoelectric Ultrasonic Motors," Ferroelectrics **230**, 73-86 (1999).
63. Kim, J.S., M.J. Park, and K. Uchino, "Composite Ultrasonic Motors Using a Piezoelectric Disk and an Elastic Body of "Windmill" Type," Ferroelectrics **232**, 185-190 (1999).
64. Koc. B., P. Bouchilloux, and K. Uchino, "Piezoelectric Micromotor Using A Metal-Ceramic Composite Structure," IEEE Trans. Ultrasonic, Ferroelectrics, and Frequency Control (1999).

5.0 MODELING and CHARACTERIZATION

5.1 Simulation

65. Cao, W., S. Tavener, and S. Xie, "Simulation of Boundary Condition Influence in a Second-Order Ferroelectric Phase Transition," J. Appl. Phys. **86**, 5739-5746 (1999).
66. Shen, M. and W. Cao, "Acoustic Band-Gap Engineering Using Finite Size Layered Structures of Multiple Periodicity," Appl. Phys. Lett. **75**, 3713-3715 (1999).
67. Uchino, K., and H. Aburatani, "Field Induced Acoustic Emission in Ferroelectric Ceramics," Proc. 101st Annual Mtg. of Amer. Ceram. Soc., Symp. Dielectric Materials and Devices, SE-56, Indianapolis, April 25 - 28 (1999). [accepted]
68. Uchino, K., J. Zheng, Y.H. Chen, X. Du. S. Hirose, and S. Takahashi, "Loss Mechanisms in Piezoelectrics—Extrinsic and Intrinsic Losses." Mater. Res. Soc. Fall Mtg. '99, LL.1.6, Boston, Nov. 29-Dec.3 (1999).
69. Uchino, K. and S. Hirose, "Loss Mechanisms in Piezoelectrics," submitted to *IEEE UFFC Transactions* (1999).

VOLUME V

70. Uchino, K., J. Zheng, Y.H. Chen, X. Du, and S. Hirose, "Loss Mechanisms in Piezoelectrics," Mater. Res. Soc. Fall Mtg. '99, Boston (Nov. 29-Dec.3, 1999).

5.2 Thin and Thick Films

71. Abothu, I.R., Y. Ito, P. Poosanaas, S. Kalpat, S. Komarneni, and K. Uchino, "Sol-Gel Processing of Piezoelectric Thin Films," Ferroelectrics **232**, 191-195 (1999).
72. Kalpat, S., I.R. Abothu, A. Akiba, H. Goto, S. Trolier-McKinstry, and K. Uchino, "Dielectric and Piezoelectric Property Dependence on Highly Textured (100), (111) and Random Thin Films Grown by RF Sputtering," Symp. LL Proc., Mater. Res. Soc. Fall Mtg. '99, LL.1.3, Boston, Nov. 29-Dec.3 (1999).
73. Xu, F., F. Chu, and S. Trolier-McKinstry, "Longitudinal Piezoelectric Coefficient Measurement for Bulk Ceramics and Thin Films Using Pneumatic Pressure Rig," J. Appl. Phys. 86 (1) 588 -594 (1999).

5.0 MODELING and CHARACTERIZATION

5.2 Thin and Thick Films (continued)

74. Shepard, J. F., Jr., F. Chu, I. Kanno, and S. Trolier-McKinstry, "Characterization and Aging Response of the d_{31} Piezoelectric Coefficient of Lead Zirconate Titanate Thin Films," J. Appl. Phys. **85**(9), 6711-6716 (1999).

75. Xu, B., Y. Ye, L.E. Cross, J.J. Bernstein, and R. Miller, "Dielectric Hysteresis from Transverse Electric Fields in Lead Zirconate Titanate Thin Films." Applied Physics Letters **74** (23), 3549-3551 (1999).

76. Xu, B., R.G. Polcawich, S. Trolier-McKinstry, Y. Ye, L.E. Cross, J.J. Bernstein, and R. Miller, "Sensing Characteristics of In-Plane Polarized Lead Zirconate Titante Thin Films," Applied Physics Letter **75** (26), 4180 (December 1999).

77. Xu, B, L.E. Cross, and D. Ravichandran, "Synthesis of Lead Zirconate Titanate Stannate Antiferroelectric Thick Films by Sol-Gel Processing." J. Am. Ceramic Soc. **82** (2), 306-312 (1999).

78. Xu, B., Y. Ye, Q.-M. Wang, and L.E. Cross, "Dependence of Electrical Properties on Film Thickness in Lanthanum-Doped Lead Zirconate Titanate Stannate Antiferroelectric Thin Films." Journal of Applied Physics **85** (7), 3753-3758 (1999).

5.3 Domain Studies

79. Belegundu, U., X.H. Du, A. Bhalla, and K. Uchino, "Effect of Electric Field on Domain Formation in Relaxor Based $Pb(Zn_{1/3}Nb_{2/3})O_3$-$PbTiO_3$ Single Crystals, Ferroelectrics Letters **26** (5-6), 107-116 (1999).

80. Belegundu, U., X.H. Du, L.E. Cross and K. Uchino, "In Situ Observation of Domains in $0.9Pb(Zn_{1/3}Nb_{2/3})O_3$-$0.1PbTiO_3$ Single Crystals," Ferroelectrics 221, 67-71 (1999). (First Author Supervised by Candidate).

81. Hatch, D.M. and W. Cao, "Determination of Domain and Domain Wall Formation at Ferroic Transitions," Ferroelectrics **222**, 1-10 (1999).

82. Cao, W. and S.N. Zhu, "Observation of Ferroelectric Domains in $LiTaO_3$," Ferroelectrics **226**, 27-35 (1999).

83. Zhu, S.N. and W. Cao, "Imaging of 180 Ferroelectric Domains in $LiTaO_3$ by Scanning Electron Microscopy," Phys. Stat. Sol. (a) **173**, 495-502 (1999).

84. Mueller, V., H. Beige, and Q.M. Zhang, "Nonlinear Ferroelectric Domain Wall Response," Ferroelectrics **222**, 295-302 (1999).

85. Liu, R., R. Guo, A.S. Bhalla, L.E. Cross, M. Levy, and R.M. Osgood Jr., "Optical Observation of Dynamic Ferroelectric Phase Transition and Static Domain Structures in Crystal Ion Sliced (CIS) $LiNbO_3$ Film." Materials Letters **39**, 264-267 (1999).

5.4 Electrostriction

86. Eury, S., R. Yimnirun, V. Sundar, P.J. Moses, S.J. Jang, and R.E. Newnham, "Converse Electrostriction in Polymers and Composites," Mat. Chem. and Phys. **61**, 18-23 (1999).

87. Yimnirun, R., S.M-L. Eury, V. Sundar, P.J. Moses, S. Jang, and R.E. Newnham, "Electrostriction Measurement on Low Permittivity Dielectric Materials," Journal of European Ceramics Society **19**, 1269-1273 (1999).

TRANSDUCER STUDIES

(continued)

APPENDIX 40

ELSEVIER

Ultrasonics 37 (1999) 387–393

Ultrasonics

www.elsevier.nl/locate/ultras

A class V flextensional transducer: the cymbal

Jindong Zhang [a,*], W. Jack Hughes [b], Philippe Bouchilloux [c], R.J. Meyer Jr. [a], Kenji Uchino [a], Robert E. Newnham [a]

[a] *Materials Research Laboratory, The Pennsylvania State University, University Park, Pennsylvania, PA 16802, USA*
[b] *Applied Research Laboratory, The Pennsylvania State University, University Park, Pennsylvania, PA 16802, USA*
[c] *Magsoft Corporation, Troy, NY 12180, USA*

Received 20 May 1999

Abstract

The cymbal is a miniaturized class V flextensional transducer which was developed for potential use as a shallow water sound projector. In underwater tests, the experimental fixture was found to have a pronounced effect on the performance of the transducer through modifications of the mechanical boundary conditions imposed on the device. A less restrictive setup was devised for the underwater test of a cymbal transducer and very good agreement between the calculations and the experimentally measured transmitting voltage response was then obtained.

Keywords: FEA modeling; Flextensional transducer; Sound projector; Underwater sound; Underwater transducer

PACS: 43.30.Yj; 43.30.-k

1. Introduction

Flextensional transducers were first developed in the 1920s and have been used as underwater transducers since the 1950s [1]. They consist of an active piezoelectric or magnetostrictive drive element and a mechanical shell structure. The shell is used as a mechanical transformer which transforms the high impedance, small extensional motion of the ceramic into low impedance, large flexural motion of the shell. According to the shape of the shell, flextensional transducers are divided into five classes [2].

Flextensional transducers generally range in size from several centimeters to several meters in length and can weigh up to hundreds of kilograms. They are commonly used in the frequency range 300–3000 Hz [3]. These transducers can operate at high hydrostatic pressures and have wide bandwidths with high power output.

A miniaturized version of the class V flextensional transducer called the 'moonie,' was developed at the Materials Research Laboratory at the Pennsylvania State University in the late 1980s [4]. Its basic structure is similar to a class V flextensional transducer, but its bonding and fabrication process is much simpler and this makes it very easy and inexpensive to mass-produce.

A second-generation moonie type transducer with a thinner cap and a slightly different shape, was also developed [5]. It was named the 'cymbal' because of the similarity in the shape of its cap to that of the musical instrument. The cymbal was originally designed as an actuator, which generates moderate force and displacement, filling the gap between bimorph and multilayer actuator. It was later developed by Tressler et al. as an underwater sound projector [6].

The moonie and cymbal transducers consist of a piezoelectric disk (poled in the thickness direction) sandwiched between two metal end-caps. The caps contain a shallow cavity on their inner surface. The cavities enable the caps to convert and amplify the small radial displacement of the disk into a much larger axial displacement normal to the surface of the caps. This contributes to a much larger acoustic pressure output than would occur in the uncapped ceramic.

The purpose of this work was to evaluate the effect of test fixtures on the performance of the cymbal transducer and to find a proper setup for underwater testing. Another goal was to model and predict the underwater performance of the cymbal transducer and compare it with experimental measurements.

* Corresponding author. Tel: +1-814-862-8461; fax: +1-814-865-2326.
E-mail address: jxz132@psu.edu (J. Zhang)

0041-624X/99/$ – see front matter
PII: S0041-624X(99)00021-9

2. Experimental procedure

The piezoelectric ceramic disks (PKI402, Piezokinetics Inc., Bellefonte, PA) have a thickness of 1 mm, a diameter of 12.7 mm and were poled in the thickness direction. The silver electrodes of PZT disks were first ground with sandpaper to remove the oxide layer and then cleaned with acetone. Titanium caps were punched from Ti foil of 0.25 mm thickness and shaped using a special die. The shaped caps had a diameter of 12.7 mm. The cavity diameter was 9.0 mm at the bottom and 3.2 mm at the top. The cavity depth was 0.32 mm. The flanges of the Ti caps were ground using sandpaper. The caps were then bonded to the piezoelectric ceramic disk. The bonding material is an Emerson and Cuming insulating epoxy. A ratio of three parts 45LV epoxy resin to one part 15LV hardener was used. The thickness of the epoxy-bonding layer was approximately 20–40 μm. The entire assembly was kept under uniaxial stress in a special die for 24 h at room temperature to allow the epoxy time to cure.

The in-air admittance was measured as a function of frequency on a Hewlett Packard 4194A impedance analyzer. Electrical leads were attached to the flange of the metal cap, taking care not to make any contact between the leads and the dome area of the metal caps.

Underwater calibration tests of single cymbals were performed at the Applied Research Laboratory at Penn State. The tank measures 5.5 m in depth, 5.3 m in width and 7.9 m in length. A pure tone sinusoidal pulse signal of 2 ms duration was applied to the test transducer and its acoustic output was monitored with a standard F33 hydrophone. The test transducer and the standard were positioned at a depth of 2.74 m and were separated by a distance of 3.16 m. The mechanical Q, transmitting voltage response (TVR), free-field voltage sensitivity (FFVS) and directivity pattern were evaluated.

In the underwater test, the cymbal transducer had to be insulated from the conductive water in the tank. In addition, it had to be rotated to observe the directivity pattern. Therefore, a fixture was needed to hold the cymbal transducer. Since we were making use of both the radial motion of the ceramic and the flextensional mode of the cap, it was difficult to test the performance of the cymbal transducer and avoid clamping effects from the fixture. Two types of fixtures were investigated for the underwater tests, as shown in Fig. 1. In the first design (PC boards, Fig. 1(a)) the cymbal transducer was sandwiched between two copper-clad PC boards each 1.5 mm thick, which also served as electrodes. A hole 11 mm in diameter was drilled through the boards. Plastic posts 1.5 mm thick were used to maintain a uniform distance between the upper and lower boards, which were then screwed tightly together to keep the transducers in place. The entire assembly was placed inside a tygon container and flooded with castor oil.

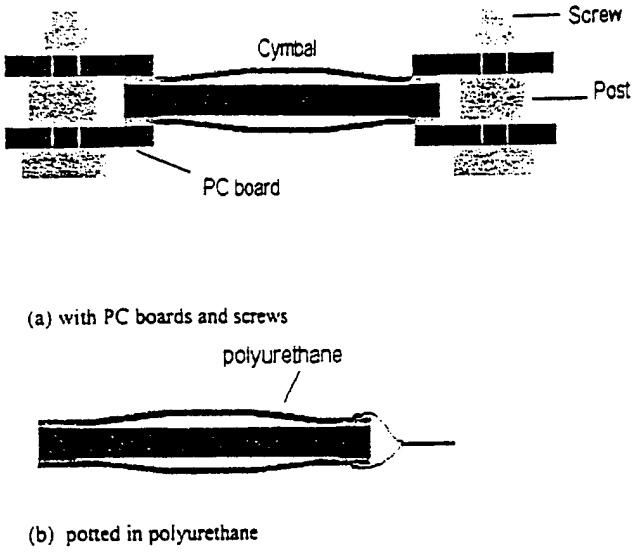

Fig. 1. Test fixtures used in the underwater tests: (a) with PC boards and screws, (b) potted in polyurethane.

This experiment was easy to set up and quite convenient to carry out.

In the second fixture (potted cymbal, Fig. 1(b)) a coaxial cable was first attached to the flange of the metal cap using silver epoxy. Care was taken to avoid any contact between the dome of the metal cap and the silver epoxy. The cymbal and part of the cable were then potted with a polyurethane coating about 0.5 mm thick. The polyurethane layer insulated the cymbal from the conductive water in the water tank.

3. Finite element analysis modeling

The finite element analysis code ATILA was used in modeling the performance of the cymbal transducer. ATILA was developed at the Acoustics Department at Institut Superieur d'Electronique du Nord (ISEN) to model underwater transducers and has been used successfully in the simulation of flextensional transducers [7]. Modal analysis was carried out to determine the vibration modes, their resonance and antiresonance frequencies and associated coupling factors. Through harmonic analysis, the in-air and in-water impedance and displacement field can be computed as a function of frequency, together with the TVR, FFVS and the directivity patterns.

A two dimensional axisymmetric model was used in which only half of the cymbal was meshed due to symmetry. The mechanical boundary conditions of the cymbal transducer were set free in both the in-air and the in-water modeling. The thickness of the epoxy layer was assumed to be 0.04 mm[8]. In the underwater simulation, a dipolar damping element was employed. The in-air and in-water meshes are shown in Fig. 2.

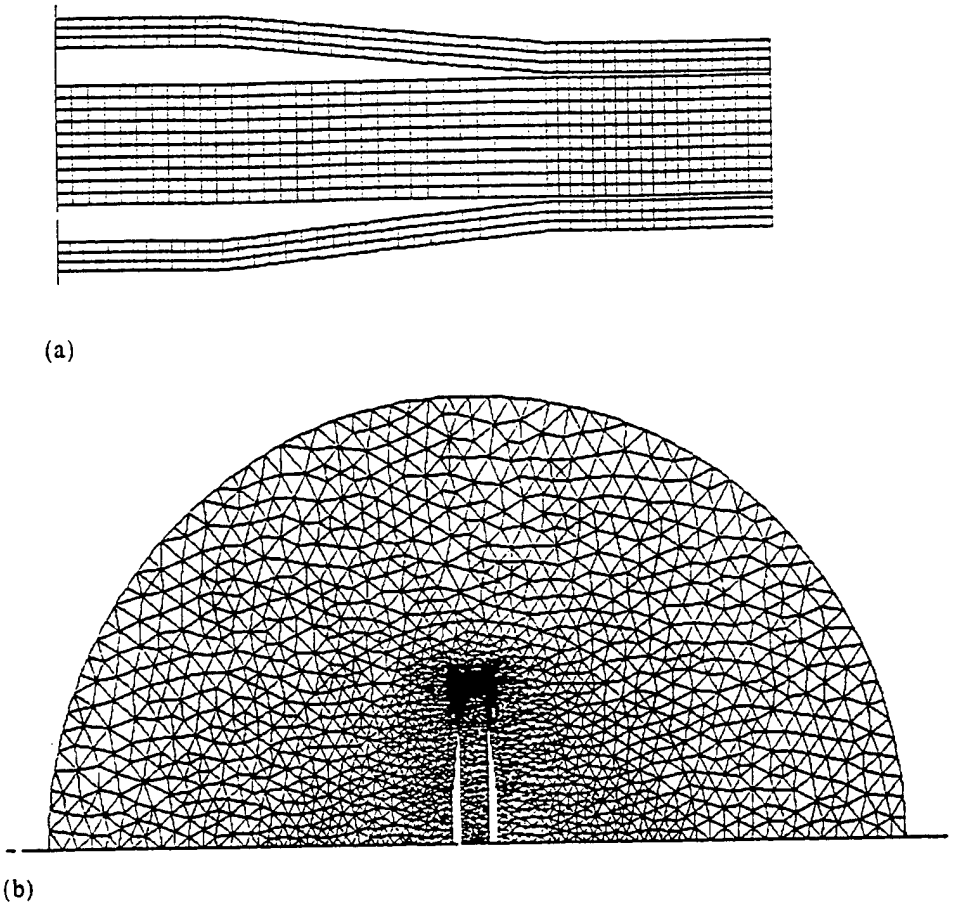

Fig. 2. Meshes of a cymbal transducer: (a) in air, (b) in water.

4. Results and discussion

Fig. 3 compares the in-air admittance spectrum of a single cymbal transducer calculated from ATILA with the experimental measurements. The calculated admittance spectrum from ATILA agreed quite well with the experimental results. The first peak corresponds to the (0, 1) or the so-called 'umbrella' flexural mode of the metal caps. In the node notation (m, n), integer m is the number of radial node lines and integer n is the number of azimuthal nodal circles. $m=0$ for a two dimensional axisymmetric body. The second peak came from the (0, 2) mode of the metal caps. The two vibration modes are illustrated in Fig. 4. There were no other modes (peaks) between the (0, 1) and (0, 2) modes. The third peak was the (0, 3) mode of the metal caps and will not be discussed here.

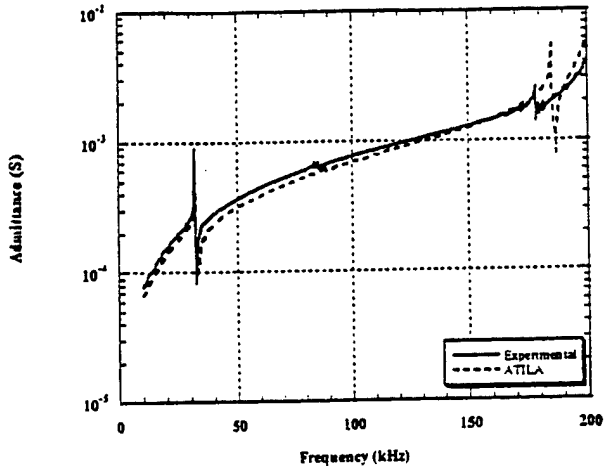

Fig. 3. Measured and calculated in-air admittance as a function of frequency for a cymbal transducer.

The calculated and measured in-water admittance spectra of the potted single cymbal transducer are also shown in Fig. 5. Fairly good agreement was achieved. The second peak in the admittance spectra was damped out by the water loading. The fundamental flextensional resonance frequency was shifted from 32 kHz in air down to 16 kHz in water due to the loading. For the cymbal transducer, its size is only one tenth of the wavelength at the first resonance frequency ($ka \ll 1$), so that the imaginary part of the radiation impedance (radiation reactance) can be approximated as [9]:

$$X_r = \rho c A^* 8ka/3\pi$$

where $k=\omega/c=2\pi/\lambda$, a is the radius of the cymbal, and $A=\pi a^2$.

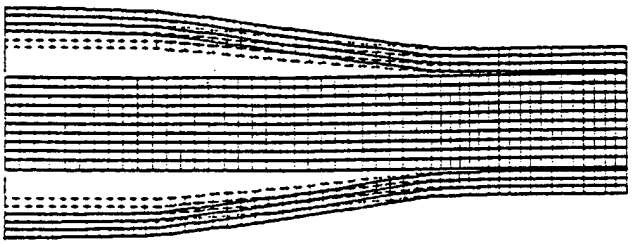

(a) (0, 1) mode

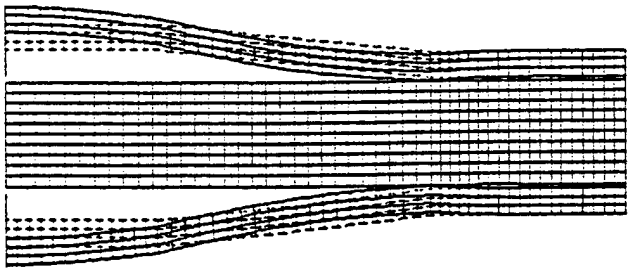

(b) (0,2) mode

Fig. 4. Vibration modes of the cymbal transducer: (a) (0, 1) mode, (b) (0, 2) mode.

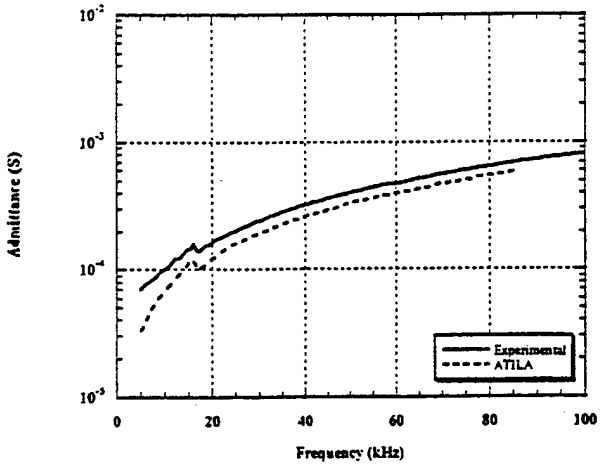

Fig. 5. Measured and calculated in-water admittance of a cymbal transducer.

The radiation reactance, X_r, can be regarded as an additional vibrating mass (M_r) given by:

$M_r = X_r/\omega = (8/3)\rho a^3$.

This mass is equivalent to that of a cylinder of water having the same cross-sectional area as the piston (cymbal) and a length of $8a/3\pi$. For a half inch cymbal transducer, the mass of the water associated with the radiation reactance is 0.7 g, which is over half the mass of the cymbal transducer itself (1.3 g). This 'associated mass' has a very significant effect on the cymbal transducer. The amplitude of the fundamental resonance

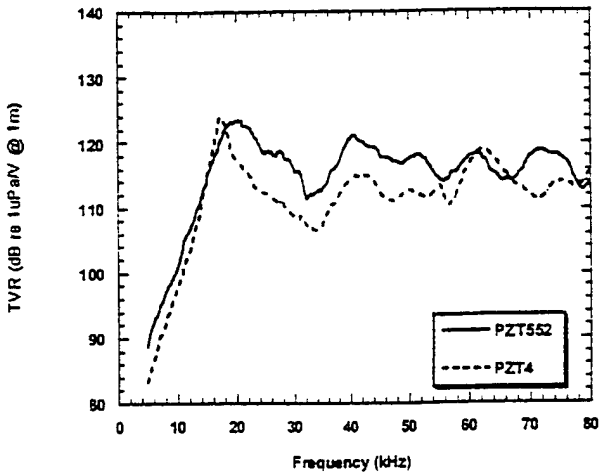

Fig. 6. Measured transmitting voltage response for a cymbal transducer of different PZT types.

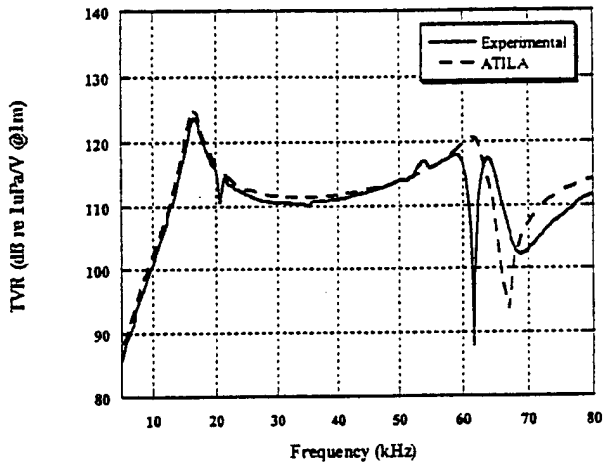

Fig. 7. Calculated and measured transmitting voltage response of a potted cymbal transducer.

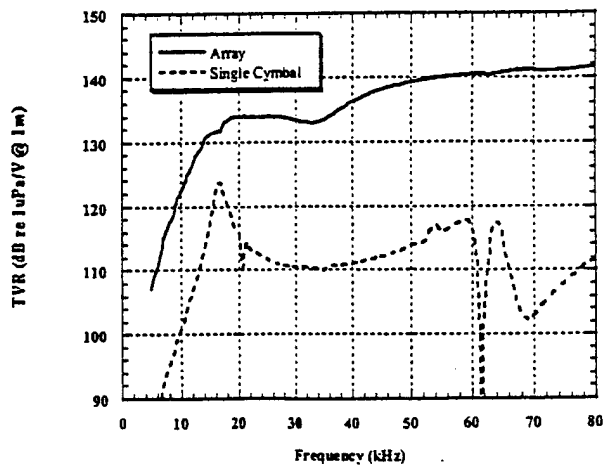

Fig. 8. Measured TVR of a potted 3 x 3 cymbal planar array.

frequency is greatly reduced, and the mechanical Q-factor was unfortunately increased.

The measured transmitting voltage response for two

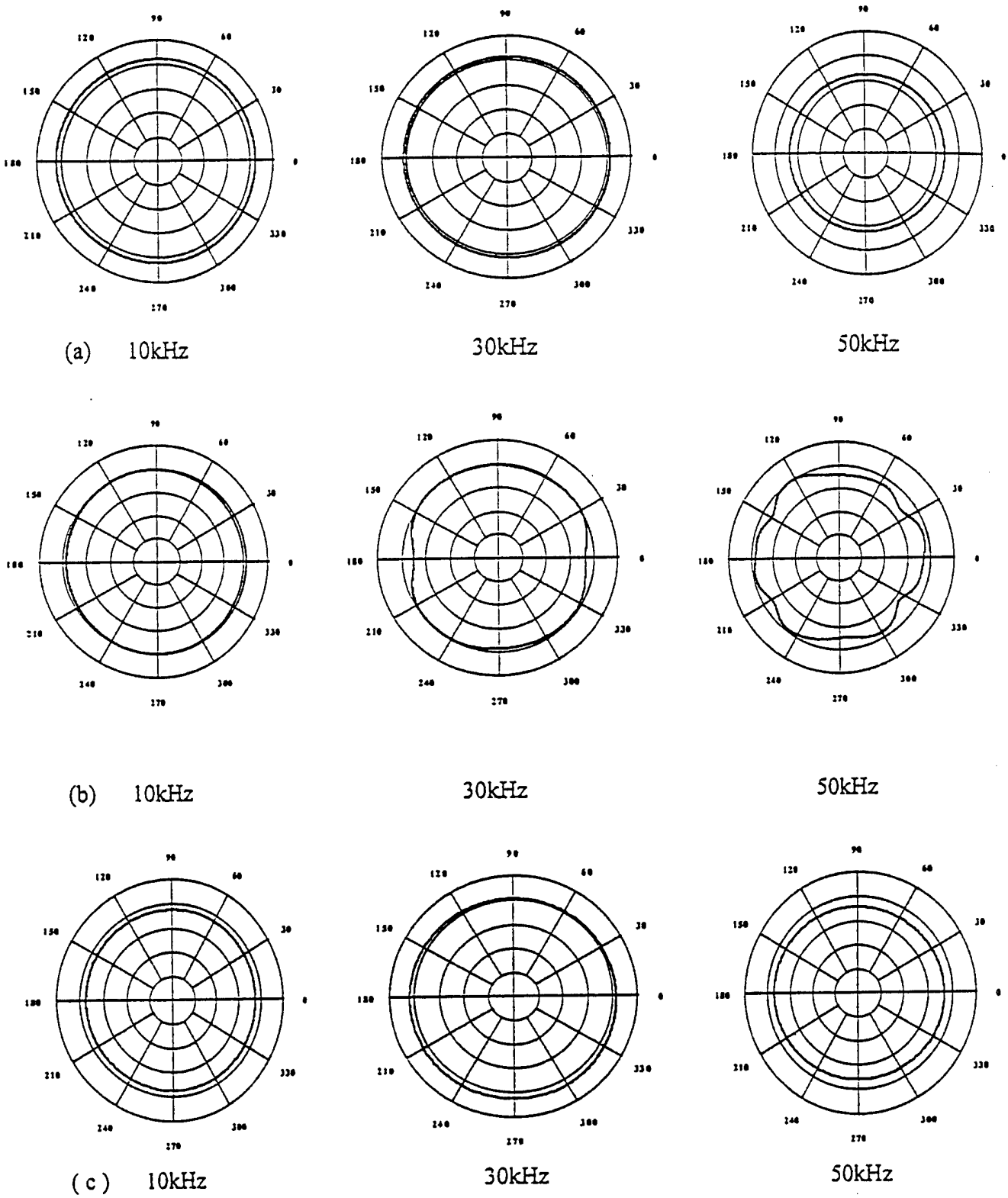

Fig. 9. Directivity patterns of a single cymbal transducer: (a) calculated from ATILA (free boundary conditions); (b)measured with PC boards (partially clamped boundary conditions); (c) measured pattern of potted sample (free boundary conditions).

single cymbals of different PZTs mounted in PC board fixtures are shown in Fig. 6. The first peak corresponds to the fundamental flextensional mode of the metal cap. After the first resonance frequency, there were several undulations in the TVR curves. The TVR patterns for different PZTs were very different, indicating that there were complex interference modes acting on the vibration of the cymbal. The calculated TVR curve from ATILA,

shown in Fig. 7, gave no peaks in this frequency range. Indeed, no peaks were expected to be in the frequency range between the (0, 1) mode and (0, 2) modes, which is apparent from the in-air admittance spectrum. We reasoned that the difference between the calculation and the measurements was related to the test fixtures which altered the mechanical boundary conditions of the cymbal transducer. In the in-air test and the FEM analysis, the boundary conditions were assumed to be 'free'. But with the PC board configuration, the small screws partially clamp the flange of the cymbal transducer. In addition, it was discovered that the PC board and the screws interfered with the vibration of the metal caps, which lead to the undulations in the TVR curves. Thus, it was difficult to predict its performance with the partially clamped boundary conditions.

A second set of test fixtures, the potted cymbal described in Section 2, was employed to minimize the clamping effect. The TVR curve of the potted cymbal transducer and the simulation are shown in Fig. 7. A nearly perfect match was obtained between them. There was a sharp dip around 65 kHz which came from the (0, 2) mode of the metal cap. As shown in the vibration mode, the two portions of the cap vibrated out of phase. The pressures from different portions of the metal caps cancelled out and lead to a sharp drop in response. There were no peaks (undulations) between the fundamental flextensional resonance frequency and the (0, 2) resonance frequency in water. The response was flat over this frequency range. This result confirms the fact that the PC board fixture plays an important role in creating the undulations observed in the previous tests.

The mechanical Q-factor is around 10 for the single cymbal transducer, which is rather high compared to other flextensional transducers. This is due to the fact that its size and weight are small, as discussed previously. Single cymbal transducers will find very limited use as sound projectors because of the high Q. But its small size and low weight and extremely low cost render possibile to incorporate it into an array to achieve the desired power and beam pattern. It has a rather flat TVR response between (0, 1) and (0, 2) modes and may be used as arrays in this frequency range. A preliminary result for a 3×3 cymbal array potted in polyurethane is shown in Fig. 8 and compared with the single cymbal transducer. The array measured 6×6 cm and had a thickness of 5 mm. A flat and much improved TVR response over the single element was observed over the frequency range of interest. Experiments are underway to design planar or conformal cymbal transducer arrays for different applications.

Directivity patterns of a single cymbal transducer tested in two types of fixtures are shown in Fig. 9 and are compared with the simulation. Near the first resonance frequency they both show omnidirectional patterns which agree with the calculation. At higher frequencies, near 30 kHz and 50 kHz, omnidirectional patterns were observed in the potted cymbal case and in the calculation. But the cymbal with the PC board fixture gave a directional pattern which deteriorates at 50 kHz. This again indicated that the test fixtures have a very pronounced effect on the performance of cymbal transducer, especially at higher frequencies, making prediction impossible. The test fixtures must be carefully chosen during the test to avoid interference with the transducer performance.

5. Conclusions

The behavior of the cymbal transducer is strongly affected by the boundary conditions imposed by the testing fixtures. Each fixture has to be properly evaluated with relation to the boundary conditions imposed on the sample and its interaction with the vibration modes of the transducer. Very good agreement between the calculated and experimentally measured transmitting voltage response and directivity patterns was obtained after the proper experimental setup was applied. ATILA can be used to predict, and therefore guide, the design of the experimental arrangements. Single cymbal transducers were characterized in underwater tests which provide valuable information that will be used in designing cymbal arrays.

Acknowledgements

The authors would like to thank Sedat Alkoy and Rattikorn Yimnirun for helpful discussions. Gregory Granville and Robert Dashem of the Applied Research Laboratory provided valuable assistance with the underwater tests. We would also like to thank MAGSOFT of New York for providing the ATILA software for this study. This work was funded by the Office of Naval Research and by Advanced Research Projects Agency, Grant #N00014-96-1-1173.

References

[1] K.D. Rolt, History of the flextensional electroacoustic transducers, J. Acoust. Soc. Am. 87 (1990) 1340.
[2] E.F. Rynne, Innovative approaches for generating high power, low frequency sound, in: M.D. McCollum, B.F. Hamonic, O.B. Wilson (Eds.), Transducers for Sonics and Ultrasonics, Technomic, Lancaster, PA, 1993, p. 38.
[3] W.J. Hughes, Encyclopedia of Applied Physics Vol. 22, Wiley–VCH, 1998.
[4] Q.C. Xu, S. Yoshikawa, J.R. Belsick, R.E. Newnham, Piezoelectric composites with high sensitivity and high capacitance for use at high pressures, IEEE Trans. UFFC 38 (1991) 634.

[5] A. Dogan, K. Uchino, R.E. Newnham, Composite piezoelectric transducers with truncated conical 'cymbals', IEEE Trans. UFFC 44 (1997) 597.
[6] J.F. Tressler, R.E. Newnham, W.J. Hughes, Capped ceramic underwater sound projector: the 'cymbal' transducer, J. Acoust. Soc. Am. 105 (1999) 591.
[7] B. Hamonic, J.C. Debus, J.-N. Decarpigy, D. Boucher, B. Tocquet, Analysis of a radiating thin-shell sonar transducer using the finite element method, J. Acoust. Soc. Am. 86 (1989) 1245.
[8] A. Dogan, PhD thesis, The Pennsylvania State University, 1994.
[9] D. Stansfield, Underwater Electroacoustic Transducer, Bath University Press and Institute of Acoustics, 1990.

APPENDIX 41

ELSEVIER

Ultrasonics 37 (2000) 523–529

Ultrasonics

www.elsevier.nl/locate/ultras

Cymbal array: a broad band sound projector

Jindong Zhang [a,*], W. Jack Hughes [b], R.J. Meyer Jr. [a], Kenji Uchino [a], Robert E. Newnham [a]

[a] *Materials Research Laboratory, The Pennsylvania State University, University Park, PA 16802, USA*
[b] *Applied Research Laboratory, The Pennsylvania State University, University Park, PA 16802, USA*

Received 20 September 1999

Abstract

A prototype 3 × 3 planar cymbal transducer array was built and tested. The array has a radiating area of 5.5 cm × 5.5 cm and a thickness of less than 8 mm. The measured transmitting voltage response was above 134 dB re 1 μPa/V @ 1 m and flat over the frequency range of 16 and 100 kHz. Array interaction was analyzed using an equivalent circuit model. The array interaction leads to variations in radiation resistance and velocity of the transducers in the array according to their surroundings in the array. The effect is enhanced overall efficiency and a flat response.

Keywords: Array modeling; Flextensional transducer; Sound projector; Transducer array; Underwater sound; Underwater transducer

1. Introduction

The cymbal transducer was developed by Newnham et al. in the early 1990s [1]. It evolved from the commercially successful moonie patent [2]. The moonie and cymbal transducers consist of a piezoelectric disk (poled in the thickness direction) sandwiched between two metal end caps. The caps contain a shallow cavity on their inner surface. The presence of the cavities allows the caps to be used as a mechanical transformer, which transforms the high impedance, small extensional motion of the ceramic into low impedance, large flexural motion of the shell. According to the shape of the metal caps, this structure is a small Class V flextensional transducer [3]. Compared to the traditional flextensional transducers, which have a complicated design, are usually assembled by hand and are therefore expensive, the fabrication process of the moonie and cymbal is very simple, easy and inexpensive to mass-produce.

The cymbal was originally designed as an actuator, which provides a sizeable displacement as well as a large generative force, bridging the gap between the two most common actuators, bimorph and the multilayer [4]. It was later proposed [5] by Newnham et al. as an underwater transducer, as both sound projector and hydrophone. As a sound projector, the cymbal transducer is attractive in its low weight, low cost and thin profile and its ability to produce medium to high output power.

Since the cymbal transducer is small compared to the wavelength in water around resonance, it has a very low radiation resistance and a relatively high radiation reactance, which means that the transfer of radiated acoustic power from the surface of the radiator to the water is very inefficient. Since the overall efficiency is the product of the radiation and mechanical transduction efficiencies, the cymbal's overall efficiency would also be low, even if the mechanical transduction rate is high [6]. The high Q and low efficiency of the cymbal transducer make it difficult for the cymbal transducer to find practical applications, and it is necessary to assemble them into arrays to achieve the desired source level and directivity. In assembling arrays, it is always desirable to have the transducer elements close packed in the array to save space.

It is well known that in closely packed arrays, acoustic interactions occur that lead to different acoustic loading on each transducer element, depending on its position in the array [7]. This then results in significant variations in the volume velocity of each array element. These interactions reduce the acoustic output power of the array, and in some extreme cases, a transducer element may have a negative radiation resistance and absorb

* Corresponding author. Tel.: +1-814-863-0180; fax: +1-814-865-2326.
E-mail address: jxz132@psu.edu (J. Zhang)

0041-624X/00/$ - see front matter
PII: S0041-624X(99)00111-0

acoustic power. The acoustic interactions are especially serious when the transducer elements are small compared to the wavelength and if they have a high efficiency. Since the single cymbal transducer has a low overall efficiency, array interactions may not pose any serious problems in cymbal arrays.

The objectives of this work were to design a planar cymbal transducer array, initially a planar array, and to model and understand the array element interaction in order to optimize the array performance. The information gathered here will be used to design larger conformal arrays for underwater vehicle applications.

2. Experimental

2.1. Single element

The piezoelectric ceramic disks (PKI402, Piezokinetics, Bellefonte, PA) have a thickness of 1 mm and a diameter of 12.7 mm. The PZT disks were poled in the thickness direction. The silver electrodes on the PZT disks were first ground with sandpaper to remove the oxide layer and then cleaned with acetone. Titanium caps were punched from Ti foil of 0.25 mm thickness and shaped using a special die. The shaped caps had a diameter of 12.7 mm. The cavity diameter was 9.0 mm at the bottom and 3.2 mm at the top. The cavity depth was 0.32 mm. The flanges of the Ti caps were ground using sandpaper. The caps were then bonded to the piezoelectric ceramic disk. The bonding material was an Emerson and Cuming insulating epoxy. A ratio of three parts 45 LV epoxy resin to one part 15LV hardener was used. The thickness of the epoxy-bonding layer was approximately 20 μm. The entire assembly was kept under uniaxial stress in a special die for 24 h at room temperature to allow the epoxy time to cure.

2.2. Array fabrication

Single element cymbal transducers were incorporated into a 3×3 square planar array. Each element has a center-to-center spacing of 13.5 mm. Two different schemes were proposed.

2.2.1. PC board technique

The nine cymbals were sandwiched between two copper-clad PC boards each 1.5 mm thick. Holes 11 mm in diameter were drilled equidistant from one another through the boards. Each element had a center-to-center spacing of 13.5 mm. Plastic posts 1.5 mm thick were used to maintain a uniform distance between the upper and lower panels, which were screwed together tightly to keep the transducers in place. The elements were electrically in parallel due to the PC board configuration.

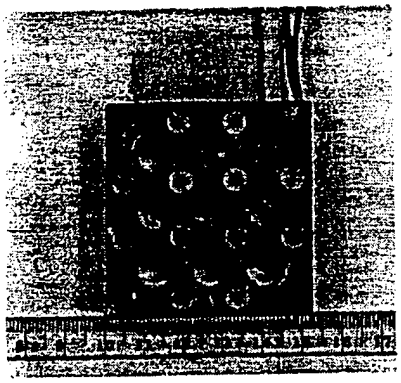

(a)

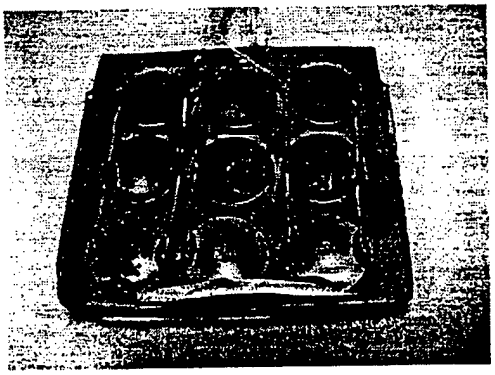

(b)

Fig. 1. Two arrays: (a) the cymbals were sandwiched between two PC boards; (b) the cymbals were potted in polyurethane.

2.2.2. Direct potting technique

The elements in the array were connected electrically in parallel using very fine electrical wire. Conductive epoxy was used to bond the wire to the flange of the cymbal transducers. The assembled cymbal transducer array was then potted in polyurethane with hardness Shore-A 90. Pictures of the two arrays are shown in Fig. 1.

Underwater calibration tests of cymbal transducers were performed at the Applied Research Laboratory at Penn State. The tank measured 5.5 m in depth, 5.3 m in width and 7.9 m in length. A pure tone sinusoidal pulse signal of 2 ms duration was applied to the test transducer, and its acoustic output was monitored with a standard F33 transducer used as a hydrophone. The test transducer and the standard were positioned at a depth of 2.74 m and separated by a distance of 3.16 m. The parameters measured were transmitting voltage response (TVR), free-field voltage sensitivity (FFVS), and directivity pattern.

3. Array modeling

A transducer can be represented by an ABCD transfer matrix, which relates input voltage and current, and the

output force and velocity in the form [8]:

$$\begin{pmatrix} e_j \\ i_j \end{pmatrix} = \begin{pmatrix} A_j & B_j \\ C_j & D_j \end{pmatrix} \begin{pmatrix} f_j \\ v_j \end{pmatrix} \quad (1)$$

where e and i are voltage and current at the electrical terminal, and f and v are the force and velocity at the mechanical (acoustical) terminals, respectively ($j=1$ to N, N is the number of transducers in the array).

By definition, the force on the jth transducer is

$$f_j = \sum_{m=1}^{N} z_{jm} v_m, \quad (2)$$

where z_{jm} is the mutual impedance matrix, which can be calculated from the Pritchard approximation [9].

Substituting Eq. (2) into Eq. (1), we obtain $2N$ linear equations. By solving this linear system, the velocities of each transducer in the array were obtained.

The ABCD parameters could be calculated from lumped equivalent circuit parameters. An equivalent circuit of the cymbal transducer is shown in Fig. 2. Here, C_0 is the clamped capacitance, and N is the electromechanical turns ratio. C represents the mechanical compliance, M the dynamic mass, and R the mechanical impedance. In calculating the ABCD parameters, an effective radiating area was required and was taken to be the surface area of the caps. The equivalent circuit parameters of the cymbal transducer are:

C_0: clamped capacitance, 2.02nF

C: compliance, 9.9×10^{-9} m/N

M: dynamic mass, 8.25 g.

The program 'ARRAY' [10], developed by J.L. Butler, was used to calculate the mutual impedance matrix and the velocities of the transducers in the array.

4. Results and discussion

The TVRs of the two 3×3 arrays with different mounting schemes, the direct potting and PC board case, are shown in Fig. 3. The direct potting array has a significantly higher TVR than its counterpart made with PC board. The transmit response was also flatter over the frequency range of interest because the PC boards impose an anisotropic stress on the flange of the cymbal transducer and partially clamp it, as it did for the single cymbal [11]. This clamping results in lowered TVR and spurious peaks in the transmit response. In addition, the PC boards lead to abnormal beam patterns over the frequency range of interest. Fig. 4 and Fig. 5 show the measured beam patterns of the two arrays along with predicted beam pattern. In the calculation, we assumed the cymbal transducer functions as a point source. This assumption was valid since a single cymbal transducer under free conditions is omnidirectional up to 60 kHz [11]. At frequencies below the resonance frequency, 15 kHz, each array shows near omnidirectional beam patterns and agrees well with the calculation. As the frequency was increased, the detrimental effect of the PC board was seen clearly as low as 30 kHz. The beam patterns of the PC board sandwiched array shows asymmetric and distorted beam patterns at 30 kHz and above. However, the beam patterns of the potted array were symmetric and agreed well with the calculation, particularly for the main lobes. As no additional boundary conditions were imposed on the transducers in assembling of the array, the beam patterns of the potted array were predictable, which is of great advantage in the design of large sonar transducer arrays.

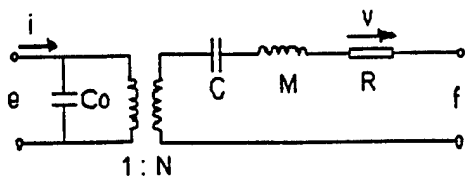

Fig. 2. Equivalent circuit of the cymbal transducer.

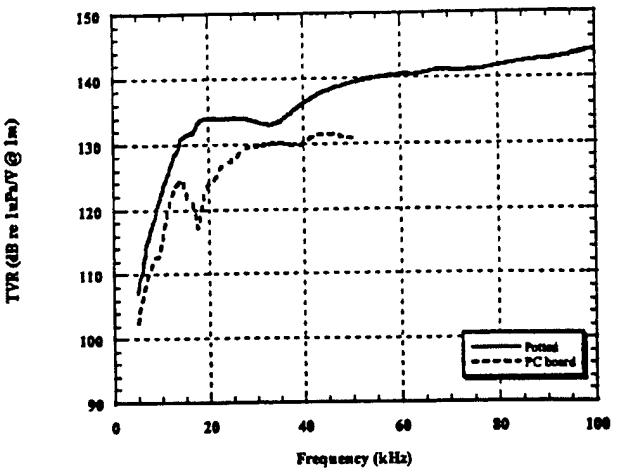

Fig. 3. Measured transmitting voltage response of 3×3 arrays assembled in two different mounting schemes.

The introduction of a polyurethane coating along with the thin profile and small size of the cymbal transducer also makes it possible to build a flexible array from the cymbal transducers. It can then be bent to make a conformal cylindrical array, which can be wrapped around the shell of underwater vehicles.

The direct potting array removes any possible interference from fixtures, making an ideal geometry for array analysis. The cymbal is much smaller than a wavelength at resonance, validating the use of the Pritchard approximation to calculate the mutual radiation impedance. In the array modeling, the cymbal transducer was modeled as a dual piston, since the cymbal has two caps. The equivalent circuit parameters used here were all measured except for the electromechanical turns ratio. The turns ratio was calculated from ATILA and is a function of frequency. In this case, a

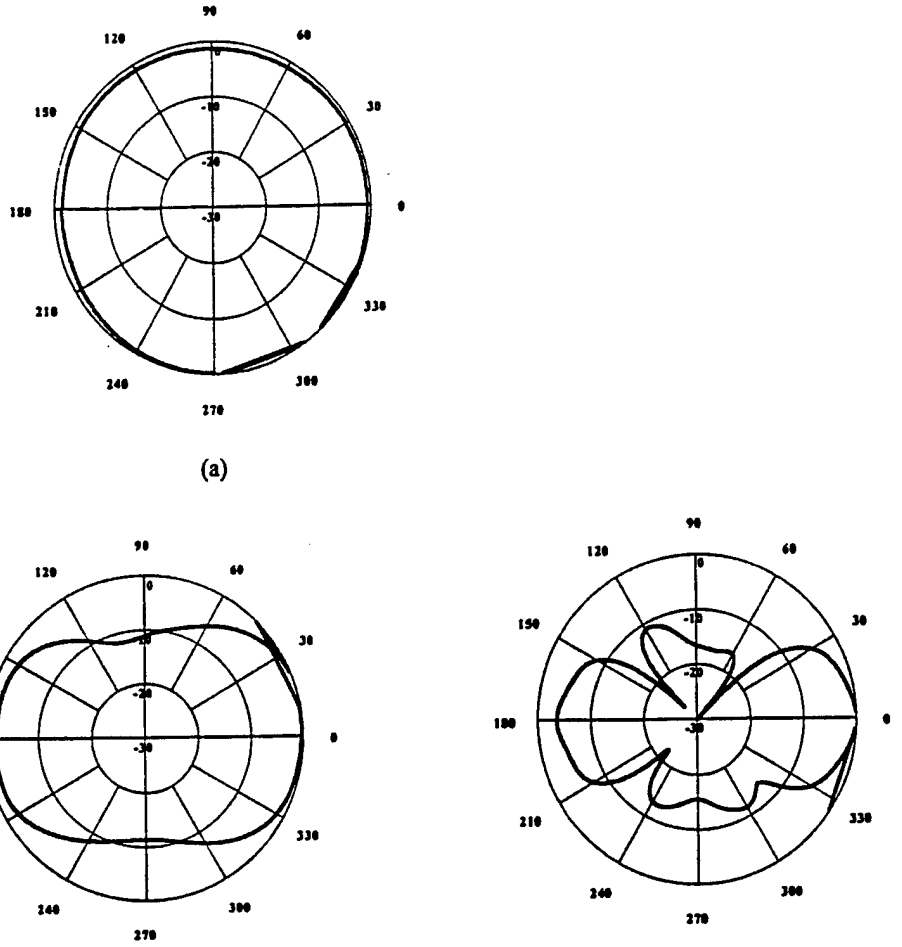

(a) 10kHz (b)30kHz (c)50kHz

Fig. 4. Beam patterns of the 3 × 3 array with PC board.

value of 0.11 N/V was adopted for the resonance frequency around 17 kHz. Fig. 6 shows the calculated TVR of a single cymbal transducer. A reasonable agreement between the measurement and calculation was obtained around resonance, validating the use of these equivalent circuit parameters. Fig. 7 shows the calculated TVR for the 3×3 planar array; a reasonable agreement was obtained between the calculation and the experiments near resonance.

When a transducer is assembled in an array, the radiation loading on each individual source is different, depending on its position in the array. The single transducer adjusts by changing its velocity. In the 3×3 array, the transducers were grouped into three categories due to the symmetry of the array, as shown in Fig. 8.

The normalized radiation resistance (relative to that of a single element) of each group of transducers in the array is shown in Fig. 9. Near resonance, the normalized radiation resistance of all three groups of transducers is greater than unity. As expected, the radiation resistance of the center transducer oscillates the most with frequency, with quite a low radiation resistance below resonance. This is where the center transducer might have a negative radiation resistance. Fortunately, the single cymbal transducer has a low overall efficiency, and does not possess a negative value in this array. As frequency increases, the radiation resistance of the transducers decreases and approaches unity, indicating less array interaction at high frequencies. Fig. 10 shows the velocities of the three types of transducers near the resonance frequency. The velocities are normalized relative to v_{11}, the velocity of a separate, single cymbal

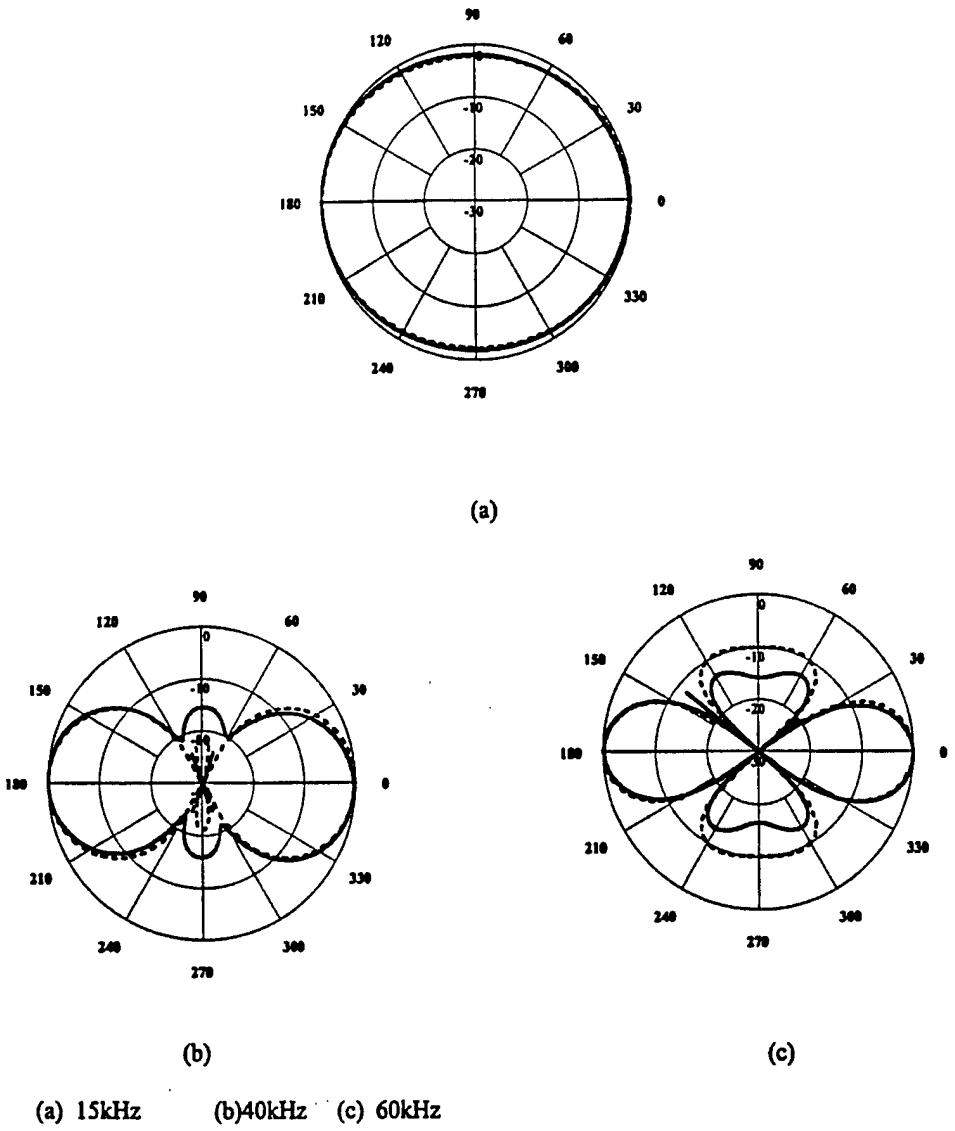

Fig. 5. Beam patterns of the potted 3 × 3 array (—: measured; - - -: calculated).

transducer. Due to the increase in radiation compared to a single transducer, the velocities of all three groups were smaller than that of a single cymbal transducer with no acoustic loading. The Group A transducer has the smallest velocity since it has more surrounding transducers than the other groups and 'feels more acoustic loading'. Another consequence of this mutual radiation resistance in the array is the much higher efficiency of an individual cymbal transducer. This is shown in Fig. 11. The array has an efficiency over 30% for this small array, compared to the very small efficiency of the single cymbal transducer.

Fig. 12 shows the normalized velocity of the Group A transducer plotted as a function of spacing between elements. At a spacing of 15 mm, the velocity of the Group A transducer in the array is only 10% of that of a single transducer, indicating a strong acoustic interaction at a small spacing. Although the strong interaction at this spacing results in small TVR values around resonance frequency, it flattens the transmit response of the array, as shown in Fig. 13. As the spacing increases, the normalized velocity variations among the three group transducers decrease and approach unity, indicating less array interaction. As a result of this, the predicted peak value of the 3 × 3 array increases at the cost of losing the flat TVR response.

5. Conclusions

In assembling arrays, care must be taken not to introduce additional mechanical boundary conditions.

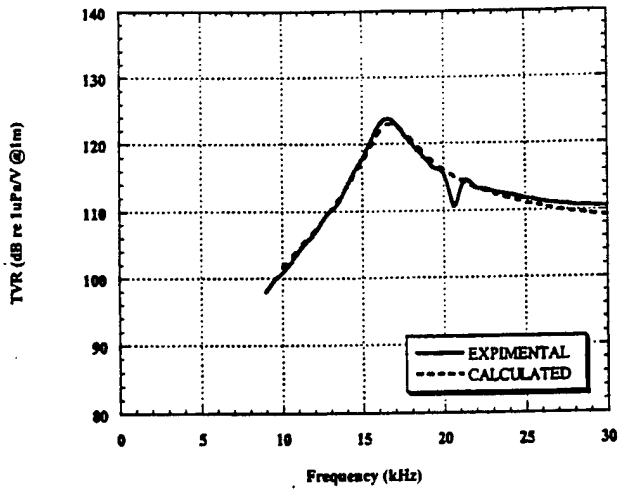

Fig. 6. Calculated and experimental transmitting voltage response of a single cymbal transducer from the equivalent circuit model.

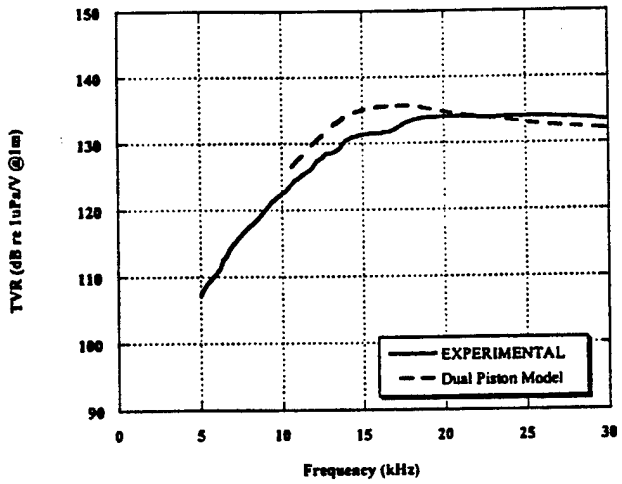

Fig. 7. Calculated transmitting voltage response of the potted 3 × 3 array using the equivalent circuit model.

The direct potting technique of mounting cymbal transducers in the array does not complicate the mechanical boundary conditions of the transducer in the array and gives more predictable beam patterns. The TVR for the direct potted array exceeds 134 dB re 1 μPa/V @1 m and is flat over the frequency range of interest. A simple equivalent circuit model was successfully used to analyze the array interaction in a small square array. The velocities of the transducer decrease significantly near

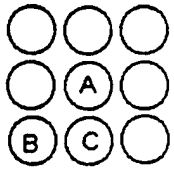

Fig. 8. Group A, B, C transducers in the array.

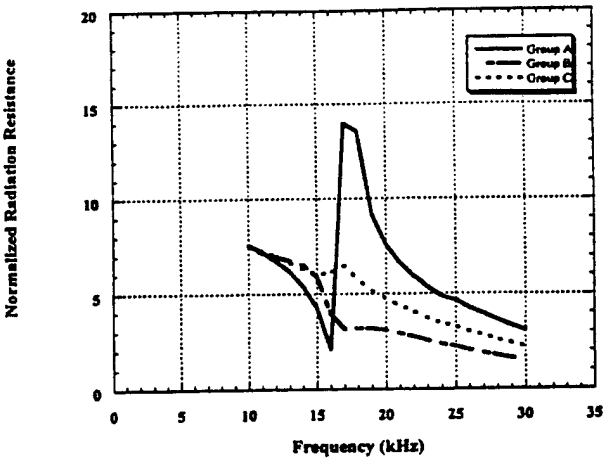

Fig. 9. Normalized radiation resistance of the transducers in the 3 × 3 array.

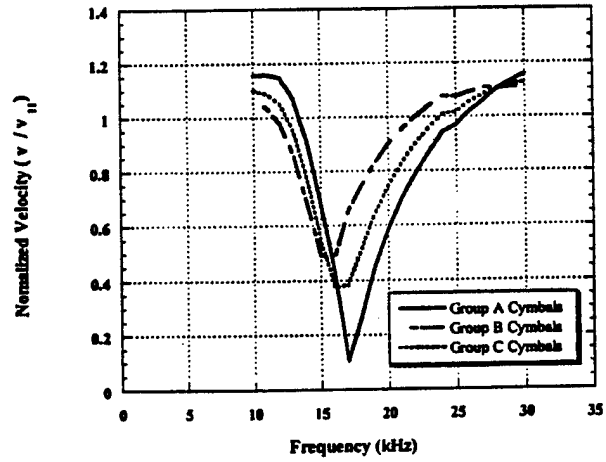

Fig. 10. Normalized velocity of transducers in the array, depending on their surroundings.

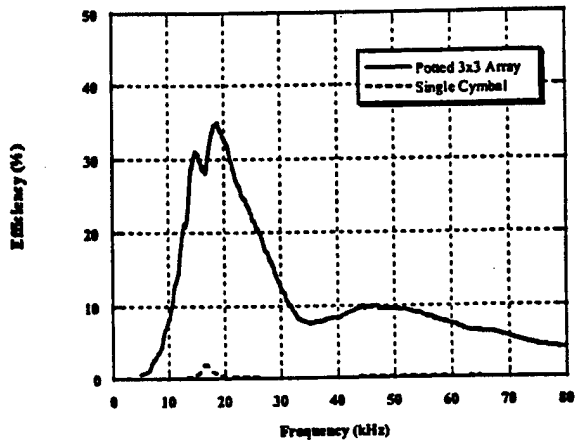

Fig. 11. Measured efficiency of a single cymbal transducer and of the potted 3 × 3 array.

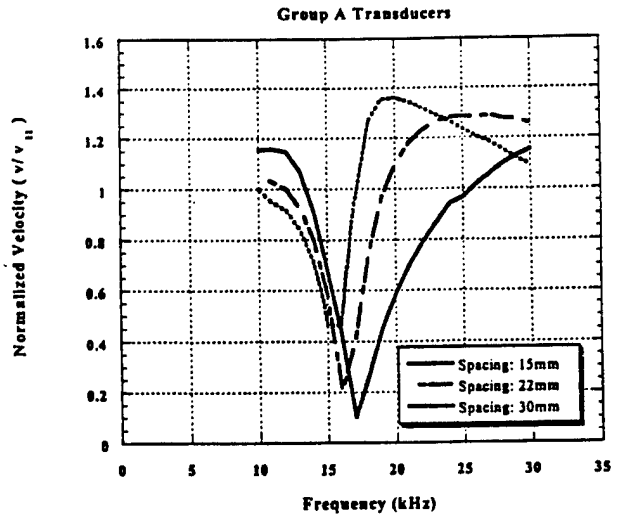

Fig. 12. Normalized velocity of group A transducers as a function of frequency and spacing.

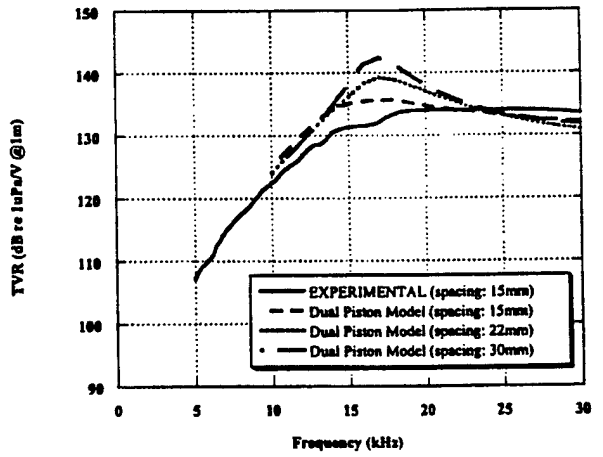

Fig. 13. Calculated transmit voltage response of a 3×3 array as a function of center to center spacing.

resonance compared to a single element, depending on the spacing between the elements and their surroundings. The array interaction works to its advantage in the sense that it flattens the transmit response around the resonance frequency, and, more importantly, it enhances the efficiency of the array.

Acknowledgements

The authors would like to thank the members of our research group and X.H. Du in ICAT for helpful discussions. Gregory Granville and Robert Dashem of the Applied Research Laboratory provided valuable assistance with the underwater test. Also we would like to thank J.L. Butler for the use of the program 'ARRAY'. This work is funded by the Office of Naval Research and by Advanced Research Projects Agency, Grant #N00014-96-1-1173.

References

[1] A. Dogan, Ph.D. thesis, The Pennsylvania State University, 1994.
[2] R.E. Newnham, Q.C. Xu, S. Yoshikawa, Metal electroactive ceramic composite actuators, US Patent, 5,276,657, 4 January 1994.
[3] K.D. Rolt, J. Acoust. Soc. Am. 87 (1990) 1340.
[4] Aydin Dogan, IEEE Trans. UFFC 44 (1997) 597.
[5] J.F. Tressler, R.E. Newnham, W.J. Hughes, J. Acoust. Soc. Am. 105 (1999) 591.
[6] B.F. Hamonic, O.B. Wilson, J.-N. Decarpigny, J.-N. Decarpigny, B. Hamonic, O.B. Wilson Jr. (Eds.), IEEE J. Oceanic Eng. 16 (1991) 107.
[7] C.H. Sherman, IEEE Trans. Sonics Ultrasonics SU 13 (1) (1966) 9.
[8] C. Audoly, J. Acoust. Soc. Am. 89 (1991) 1428.
[9] R.L. Pritchard, J. Acoust. Soc. 32 (1960) 730.
[10] J.L. Butler, User Manual for the Program ARRAY, Image Acoustics, Inc., Cohasset, MA 02025, 1990.
[11] J.D. Zhang, W.J. Hughes, P. Bouchilloux, R.J. Meyer Jr., K. Uchino, R.E. Newnham, Ultrasonics 37 (1999) 387.

APPENDIX 42

Mat Res Innovat (1999) 2:252–255

ORIGINAL ARTICLE

Jindong Zhang · W. Jack Hughes
A.C. Hladky-Hennion · Robert E. Newnham

Concave cymbal transducers

Received: 14 October 1998 / Reviewed and accepted: 15 October 1998

Abstract A new type of cymbal transducer, called the concave cymbal, has been developed to increase the pressure tolerance and reliability of the transducer under high hydrostatic pressure. The main feature of the new design is a lead zirconate titanate ceramic ring sandwiched between two concave metal endcaps. It shows much improved pressure performance and can withstand a pressure of up to 6 MPa while maintaining high effective hydrostatic piezoelectric coefficients. When incorporated into a planar array with a radiating area of 5.5 cm×5.5 cm and weight of only 30 g, a transmitting voltage response of around 125 dB re 1 μPa/V @ 1 m was obtained over a frequency range between 20 and 50 kHz.

Key words Piezoelectricity · Underwater transducer · Flextensional transducer · Ring-shell transducer · Electroacoustic transducer · Hydrophone · Sensor · Sound projector · Transducer array · Transducer modeling

Introduction

Flextensional transducers were first developed in the 1920 s and have been used as underwater transducers since the 1950s [1]. They consist of a piezoelectric or magnetostrictive drive element and a mechanical shell structure. The shell is used as a mechanical transformer which transforms the high impedance, small extensional motion of the ceramic into low impedance, large flexural motion of the shell. According to the shape of the shell, flextensional transducers are divided into five classes [2]. Flextensional transducers range in size from several centimeters to several meters in length and can weigh up to hundreds of kilograms. They are commonly used in the frequency range of 300 to 3000 Hz [3]. They can operate at high hydrostatic pressures, and have wide bandwidths with high power output. The fabrication process is labor intensive and not easy to control due to the application of pre-stress, therefore its cost is quite high.

A new type of high performance flextensional transducer, called the "moonie", was developed at the Materials Research Laboratory at the Pennsylvania State University in the late 1980's [4]. Its basic structure is similar to a Class V flextensional transducer, but its bonding and fabrication process are very simple, which makes it very easy and inexpensive to mass-produce.

A second-generation moonie type transducer, which has a thinner cap with a slightly different shape, was also developed [5]. It was named the cymbal because of the similarity in shape of its cap to that of the musical instrument of the same name.

The moonie and cymbal transducers consist of a piezoelectric disk (poled in the thickness direction) sandwiched between two metal end caps. The caps contain a shallow cavity on their inner surface. The presence of the cavities allows the caps to convert and amplify the small radial displacement of the disk into a much larger axial displacement normal to the surface of the caps, which contributes to a much larger acoustic pressure output than would occur in the uncapped ceramic.

The standard cymbal is intended for shallow water use (no deeper than 200 m water) due to its convex structure and thin caps. If the hydrostatic pressure exceeds a certain threshold, the metal caps deform permanently and the cavity collapses, thus destroying the amplification effect [6]. A new type of cymbal transducer, which is called the concave cymbal, or double-dipper cymbal, was

Presented at the *Innovations in Materials Conference*, Washington, D.C., July 19–22, 1998

J. Zhang (✉) · R.E. Newnham
254 Materials Research Laboratory,
The Pennsylvania State University, University Park,
PA 16802, USA
Fax: +1-814-865-2326, e-mail: jxz132@psu.edu

W.J. Hughes
Applied Research Laboratory, The Pennsylvania State University,
University Park, PA 16802, USA

A.C. Hladky-Hennion
IEMN-Departement I. S. E. N., 41 Boulevard Vauban,
59046 LILLE, France

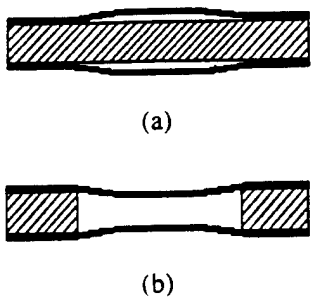

Fig. 1 Cross-sectional views of the (a) standard cymbal, and (b) double-dipper cymbal transducers

developed to improve the pressure tolerance. In this new design, a ceramic ring is used instead of a disk. The ring is sandwiched between two inverted metal caps. One advantage of this design is that it greatly improves the pressure tolerance of the cymbal transducers. Another advantage is that the ceramic and the metal caps vibrate in phase, eliminating any out-of-phase component of the radiating field. Schematic drawings of a standard and a double-dipper cymbal transducer are shown in Fig. 1.

Experimental

A Fabrication

Brass caps were punched from a metal foil of 0.25 mm thickness and shaped using a special die. The shaped caps had a diameter of 12.7 mm. The cavity diameter was 9.0 mm at the bottom and 3.2 mm at the top. The cavity depth was 0.2 mm. The caps were then bonded to a piezoelectric ceramic ring (PKI 552, Piezokinetics Inc., Bellefonte, PA) having a thickness of 1 mm, outer diameter of 12.7 mm, and inner diameter of 9.0 mm. The PZT rings were poled in the thickness direction. The bonding material is an Emerson and Cuming insulating epoxy. A ratio of three parts 45 LV epoxy resin to one part 15 LV hardener was used. The thickness of the epoxy bonding layer was approximately 20 μm. The entire assembly was kept under uniaxial stress in a special die for 24 hours at room temperature to allow the epoxy time to cure.

Single element cymbal transducers were incorporated into a 9-element square planar array. The nine cymbals were sandwiched between two copper-clad PC boards each 1.5 mm thick. Holes 11 mm in diameter were drilled equidistant from one another through the boards. Each element has a center-to-center spacing of 13.5 mm. Plastic posts 1.5 mm thick were used to maintain a uniform distance between the upper and lower panels, which were screwed together tightly to keep the transducers in place. The elements are electrically in parallel because of the PC board. After assembly, the array had a dimension of 5.5 cm×5.5 cm and a thickness of 0.4 cm. Its weight was around 30 g.

Underwater calibration tests of single cymbals and arrays were performed at the Applied Research Laboratory at Penn State. The tank measures 5.5 m in depth, 5.3 m in width and 7.9 m in length. A pure tone sinusoidal pulse signal of 2 msec duration was applied to the test transducer and its acoustic output was monitored with a standard F33 hydrophone. The test transducer and the standard were positioned at a depth of 2.74 m and separated by a distance of 3.16 m. The parameters measured for these underwater devices were resonance frequency, mechanical Q, Transmitting Voltage Response (TVR), Free-Field Voltage Sensitivity (FFVS), and beam pattern.

B Finite element analysis

The Finite Element Analysis code ATILA was used in the evaluation and further improvement of our cymbal transducer designs. ATILA was developed at the Acoustics Department at Institut Superieur d'Electronique du Nord (ISEN) to model underwater transducers [7]. A static analysis was performed to provide information concerning pre-stresses and the transducer's response under hydrostatic pressure. Modal analysis was carried out to determine the vibration modes, their resonance and antiresonance frequencies, and associated coupling factors. Through harmonic analysis, the in-air and in-water impedance and displacement field can be computed as a function of frequency, together with the Transmitting Voltage Response, Free Field Voltage Sensitivity and the directivity patterns. In this study, ATILA was used to estimate the TVR and FFVS of several cymbal transducer designs.

Results and discussions

It has previously been shown for standard cymbals that the flextensional resonance frequency can be tailored easily by changing the cap material and geometry [8]. The concave cymbal utilizes the same amplification mechanism as the standard cymbal, but its flextensional resonance frequency is slightly lower than its standard counterpart as is shown in Table I, and it is also easily tailored. Other in-air characteristics of concave cymbal transducers are also shown and compared with standard cymbal transducers in Table I. The effective d_{33} and capacitance of concave cymbal transducers are smaller than those of standard cymbal transducers due to less piezoelectric material used in the device.

Figure 2 shows a representative admittance spectrum of a concave cymbal transducer. The first peak, at 22 kHz, is associated with the flextensional mode of the composite transducer. The higher resonance peaks comes from the coupling between the radial mode of the ceramic ring and high order flextensional modes. Figure 2 also

Table 1 Typical in-air characteristics of standard and concave cymbal transducers

	Standard cymbal	Concave cymbal
Flextensional frequency	24 kHz	23 kHz
Coupling coefficient	20%	15%
Effective d_{33}	12000 pC/N	4000 pC/N
Capacitance	2.9 nF	1.2 nF

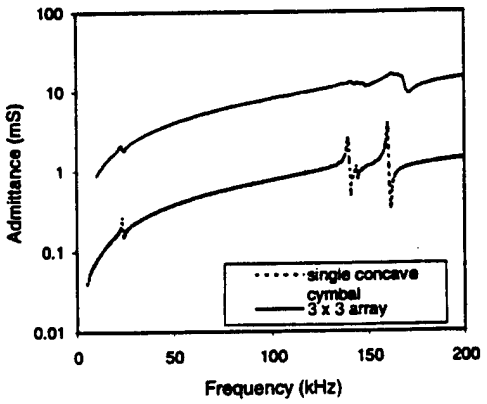

Fig. 2 Admittance spectrum of a single concave cymbal transducer and a nine-element array

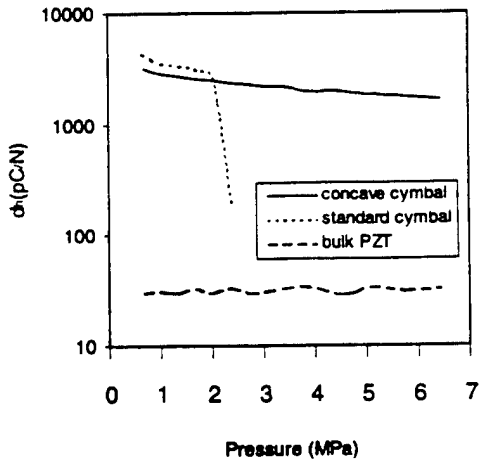

Fig. 3 Pressure dependence of the effective d_h coefficients for the standard and concave cymbal transducers

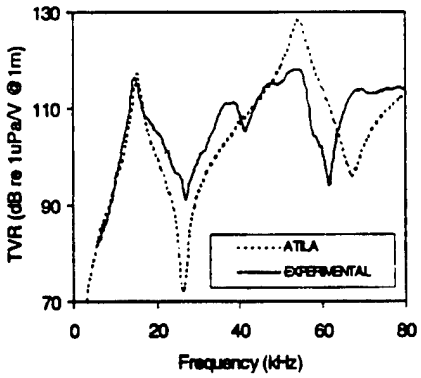

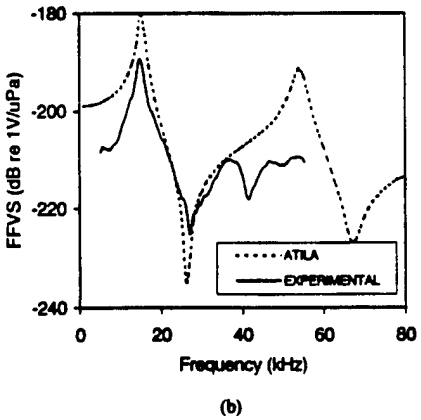

Fig. 4 Measured and calculated (ATILA) (a) TVR and (b) FFVS of a concave cymbal transducer

shows the admittance spectrum of a nine-element concave cymbal array. Its resonance is damped and broadened due to element interactions and the fact that the individual elements have slightly different frequencies.

Figure 3 shows the pressure dependence of the effective d_h of double-dipper and standard cymbals. Effective

Fig. 5 Measured (a) TVR and (b) FFVS of a nine-element array of concave cymbal transducers

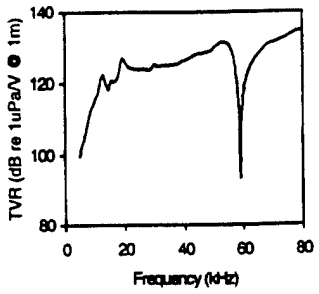

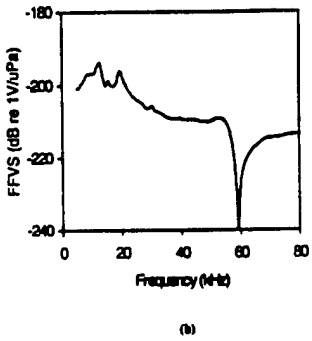

d_h for bulk PZT as a function of pressure is also shown and compared. Both standard and concave cymbals have effective d_h values over fifty times larger than that of bulk piezoelectric material. The standard cymbal can withstand 2 MPa, but when the pressure increases over 2 MPa, it fails catastrophically. In the case of the concave cymbal, it has a slightly lower d_h than the standard cymbal but it survives up to 6 MPa without significant degradation in its properties. The concave cymbal exhibits much improved pressure tolerance under hydrostatic loading. Under some certain higher pressures, the concave cymbal may fail due to the meeting of the two brass end caps which causes a short circuit. But it can be avoided by applying a thin insulating layer between the brass caps and its pressure tolerance can be further improved.

The TVR and FFVS of a single concave cymbal are shown in Fig. 4. Like the standard cymbal, the concave cymbal shows narrow band characteristics with a mechanical Q around 9. The TVR and FFVS calculated with the ATILA code are also shown for comparison with the experimental results. Fairly good agreement is obtained indicating that ATILA adequately models the cymbal behavior in water. The small discrepancies between the calculated and the experimental results may arise from imperfections in the ring, from stresses in the metal caps, or from the fact the contribution of the epoxy bonding layer and the fixtures used to hold the sample were not taken into account in modeling.

Since individual concave cymbals are not powerful enough, and are not sufficiently broad-band for practical use, the incorporation of single elements into arrays is necessary to improve underwater performance. The TVR and FFVS of a nine-element array of concave cymbal

transducers are illustrated in Fig. 5. The array shows broader band characteristics in both TVR and FFVS. It has a TVR of around 125 dB re 1 μPa/V @ 1 m and is rather flat over the frequency range from 20–50 kHz. Its FFVS is not as flat as the TVR, but a wider bandwidth can be obtained by incorporating more cymbal elements into the array and by precisely controlling and arranging the resonance frequencies and position of the array elements. Modeling studies are under way to optimize the performance of a double-dipper array.

The use of PZT rings allows the drive elements to be poled in different directions. The ring can be poled through its thickness as in this experiment, or it can also be poled radially, in which case d_{33} can be used and the electromechanical coupling coefficient is expected to be higher.

Potential applications

Concave cymbal transducers demonstrate a much improved pressure tolerance over standard cymbals and can go much deeper underwater, extending the range of operation for cymbal transducers. The simple fabrication process makes it easy to mass-produce these transducers which will greatly reduce its cost. The thin profile, light weight and low cost makes it possible to assemble a very large array of cymbals, either in a planar or conformal array. It is expected that the array can be further optimized to work as well as a standard Tonpilz array when a high source level is bit required. The cymbal transducers may be a good transducer for conformal arrays where drastically reducing the vehicle's weight and cost is important. Hard, PZT4, instead of soft, PZT5, piezoelectric drive elements can be used to achieve a high source level.

The low-cost concave cymbal array can also be used as a receiver for acoustic imaging. The most useful frequency range for underwater imaging appears to be the 5–50 kHz band [9] where the concave cymbal transducer excels. When fully optimized, an array of cymbal hydrophones may serve as a multi-element receiver capable of functioning as an acoustic camera. Phased arrays of a thousand or more hydrophones are feasible using these small low-cost, mass-produced components with high hydrostatic piezoelectric coefficients. The improved pressure performance allows the concave cymbal transducer array to work both in shallow water and in deep submergence.

Conclusion

The concave, or double-dipper cymbal, is shown to have a much higher pressure tolerance than the star dard cymbal. Its thin profile and small size make it easy to mount in a planar or curved array. When incorporated into a planar nine-element array, it shows medium output power and broad band characteristics combined with a small radiating area and light weight. The double-dipper cymbal is a promising candidate as an underwater sound projector and receiver.

Acknowledgements The authors would like to thank Dr. Kenji Uchino, Dr. J. F. Tressler, Sedat Alkoy, Rattikorn Yimnirun and Jayne Giniewicz at Materials Research Lab of Penn State for their helpful discussions, and Greg Granville and Bob Dashem at Applied Research Laboratory of Penn State for their assistance. We would also like to thank MAGSOFT Co. of New York for providing the ATILA software for this study. This work is funded by the Office of Naval Research and by Advanced Research Projects Agency, grant #N00014-96-1-1173.

References

1. Rolt KD (1990) J Acoust Soc Am 87:1340–1349
2. Rynne EF (1993) Innovative Approaches for Generating High Power, Low Frequency Sound. In: Transducers for Sonics and Ultrasonics. Technomic Pub Co, Lancaster, PA, pp 38–49
3. Hughes WJ (1998) Transducers, Underwater Acoustic. In: Encyclopedia of Applied Physics, vol 22. Wiley-vch, pp 67–84
4. Xu QC, Yoshikawa S, Belsick JR, Newnham RE (1991) IEEE Trans UFFC 38:634
5. Dogan A, Uchino K, Newnham RE (1997) IEEE Trans UFFC 44:597
6. Tressler JF, Dogan A, Fernandez JF, Fielding JT, Uchino K, Newnham RE (1995) Capped Ceramic Hydrophones. In: 1995 IEEE Ultrasonics Proceedings, pp 897–900
7. Hladky-Hennion AC, Decarpigny JN (1993) J Acoust Soc Am 94:621
8. Tressler JF (1997) PhD Thesis, Penn State University
9. Urick RJ (1967) Principles of Underwater Sound. McGraw Hill, NY

APPENDIX 43

Ferroelectrics, 1999, Vol. 226, pp. 11–25
Reprints available directly from the publisher
Photocopying permitted by license only

PIEZOELECTRIC HOLLOW SPHERES FOR MICROPROBE HYDROPHONES

S. ALKOY[a], A. C. HLADKY[b], A. DOGAN[c], J. K. COCHRAN JR.[d] and R. E. NEWNHAM[a,*]

[a] *Materials Research Laboratory, The Pennsylvania State University, University Park, PA, 16802, USA;*
[b] *I.E.M.N. Department I.S.E.N., 59046 Lille, France;*
[c] *Dept. of Ceramic Science, Eskisehir Anadolu University, Eskisehir, Turkey;*
[d] *School of Materials Science and Engineering, Georgia Institute of Technology, Atlanta GA 30332, USA*

(Received in final form 17 July 1998)

Miniature hollow spheres of lead zirconate titanate have been prepared with a coaxial nozzle process using fine grain slurry of PZT-5. Following the binder burnout and sintering, the spheres were poled radially and tangentially to be tested as piezoelectric transducers for underwater microprobe hydrophone applications. For the radially poled spheres the principal modes of vibration were found to be breathing and thickness modes with breathing mode resonance shifting to lower frequencies with increasing sphere size. For tangentially poled spheres, the main modes were determined to be an ellipsoidal, a higher order circumferential, and breathing modes near 230 kHz, 350 kHz and 700 kHz, respectively. Higher frequency coupled modes were also observed. Hydrostatic piezoelectric charge coefficients (d_h) of the transducers were measured to obtain a hydrophone figure of merit for microprobe applications, resulting in d_h values ranging from 600 to 1,800 pC/N. These values are substantially higher than that of bulk PZT transducers.

Keywords: Piezoelectric hollow spheres; hydrophones; finite element analysis

1. INTRODUCTION

Increasing use of ultrasonic techniques in biomedical and underwater applications and the sophistication of these techniques has increased the need to characterize the acoustic fields created by ultrasonic transducers. In

*Corresponding author.

the last forty years several different techniques and probe designs have been employed for this purpose, including rod-guided waves,[1] thermoacoustic sensors,[2] fiberoptic sensors utilizing acoustooptic interaction[3] and miniature ultrasonic probes made from ceramic and polymer-based piezoelectrics.[4–7] Miniature ultrasonic probes have been used both for mapping the field of a hydrophone as well as the nonacoustic field of turbulent flow. There are, however, several important requirements for microprobe sensors in these applications. In detecting underwater signals, omnidirectionality is highly advantageous. However, accurate mapping of an acoustic field requires that: (i) the physical dimensions of the probe should be smaller than the acoustical wavelength of interest, (ii) the resonance frequencies of the probe should be well above the frequency range of interest, (iii) adequate sensitivity with an acceptable signal-to-noise ratio and (iv) wide bandwidth.[7, 8]

Although volume expanders with spherical shape are thought to be the best way to achieve omnidirectionality, there are problems associated with fabricating hollow spheres with sizes in the millimeter range, as pointed out by previous researchers.[8] The literature contains a number of examples of transducers prepared from piezoelectric plates, but these transducers have a pronounced directivity even when the probe dimensions are smaller than a wavelength.[5, 8] Solutions proposed previously for the directivity problem include solid-core spherical probes [5, 8] and hollow cylindrical probes.[7]

In addition to the underwater applications, spherically shaped transducers are also desirable in medical ultrasound applications. Examples include a quasi-omnidirectional polymer-based transducer developed for ultrasonic guidance of intravascular catheters,[9] and a focused transducer for biomedical ultrasonic imaging, prepared from a spherical ceramic shell.[10]

The miniature hollow sphere transducers, sometimes called BBs, described here and first reported by Meyer *et al.* [11] are designed to satisfy the size, directionality and acoustic impedance matching requirements for underwater and biomedical applications. BBs are manufactured in large numbers by a simple inexpensive process, which makes it possible to mass-produce throw-away transducers. In this paper the results of the dielectric measurements, and the piezoelectric response of the transducers under hydrostatic pressure are presented for several types of radially and tangentially poled spheres with sizes ranging from 2–4 mm. Vibration modes and their resonance frequencies are identified using the *ATILA* finite element analysis code, and compared with the experimental results.

2. FABRICATION OF THE TRANSDUCERS

Thin-wall hollow green spheres were fabricated at room temperature using a coaxial nozzle process based on the Torobin patent.[12] This process was originally developed to mass-produce thin-wall metal, ceramic and glass hollow spheres with diameters and wall thickness, ranging from 1 to 6 mm and 12 to 150 μm, respectively. The fabrication method used in producing the lead zirconate titanate based hollow spheres involves the preparation of a fine grained slurry from soft lead zirconate titanate powders (grade PZT-501A powders from Ultrasonic Powders, Inc. and grade C5500 powders from Channel Industries, Inc.), Poly(methyl methacrylate) and acetone. This slurry is then injected through a coaxial nozzle with inert gas passing through the center. At the equilibrium of surface tension and inner gas pressure, a bubble forms and breaks free. In this study spheres with sintered diameters ranging from 2.0 to 4.0 mm were prepared from the C5500 powders (Batch I), and monosize spheres with ~2.76 mm sintered diameter from the PZT-501A powders (Batch II).

A two step process was used in the firing of the green spheres: binder burnout at 550°C for 30 minutes followed by sintering at 1285°C for 90 minutes. A physical characterization study on the sintered spheres from PZT-501A batch by Fielding *et al.* [13] indicated that the spheres contain microcracks and substantial porosity. The wall thickness variation was found to be larger than expected, ranging from 40 to 100 μm. Improvements in the fabrication process of green spheres are being undertaken to minimize these defects which degrade the dielectric and piezoelectric properties.

2.1. Poling and Electrode Configurations

The two poling configurations studied are shown in Figure 1: radially poled spheres of various sizes from Batch I with inside and outside electrodes, and top-to-bottom poling of monosize spheres from Batch II with external cap electrodes. For the top-to-bottom poling three different electrode configurations, and their effect on the capacitance, vibration modes, and piezoelectric response under hydrostatic pressure were investigated. For radial poling a fired-on silver electrode (Conductor Compositon 7095 from DuPont) was applied to the inner surface of the spheres through a 450 μm electrode hole, followed by a firing step at 600°C for 30 minutes. Silver electrical lead wires were attached and the electrode hole was sealed using a conductive silver epoxy adhesive (E-solder #3021 from Insulating Materials, Inc.). A thin layer of gold was deposited as the external electrode for all

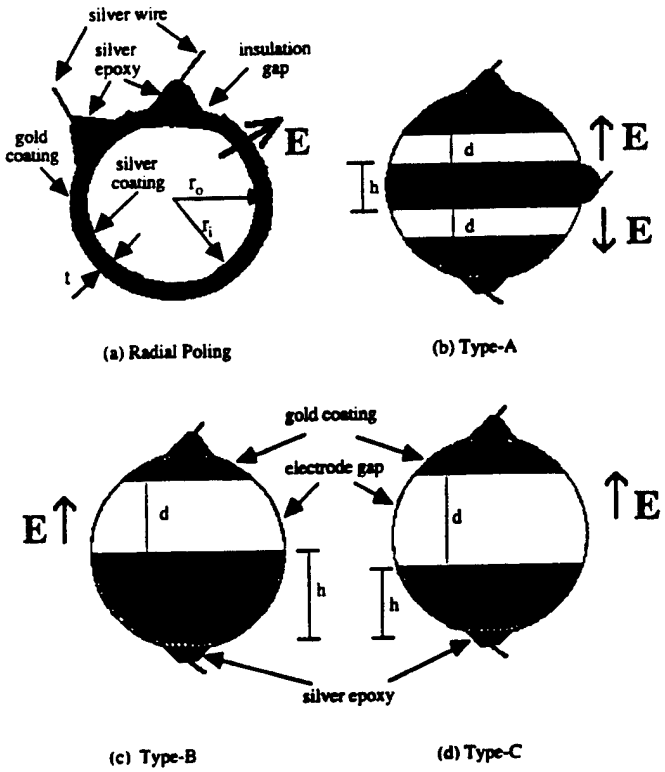

FIGURE 1 Poling and electrode configurations of piezoelectric hollow spheres. (a) Cross-section of a radially poled hollow sphere; (b) Tangential poling configuration (electrode type-A); (c) Tangential poling configuration (electrode type-B); (d) Tangential poling configuration (electrode type-C).

radial and top-to-bottom poling configurations. Poling of the spheres were carried out with an electric field of 20 kV/cm for Batch II, 60–80 kV/cm for Batch I at 120°C in a silicone oil bath. Prior to the hydrostatic pressure measurements, a soft polyurethane (Dexter Hysol us-0089) coating was applied for insulation and to provide additional strength for the hydrostatic measurements.

3. FINITE ELEMENT ANALYSIS

ATILA finite element analysis (FEA) code, developed at the Acoustics Department at ISEN specifically for modeling of sonar transducers, was

used in our modeling studies. A static analysis can be performed with *ATILA*, which provides information concerning prestresses and the behavior under hydrostatic pressure. Modal analysis can be carried out to identify the vibration modes and determine their resonance frequencies and associated coupling factors. Finally, in-air or in-water impedance and displacement field, transmit voltage response, and sonar directivity patterns can be modeled using a harmonic analysis procedure.[14–16]

In this study *ATILA* was used to identify the modes of vibration for the various electrode configurations, by predicting their resonance frequencies. The computations were performed using a 10 kHz step, except for the thickness mode of radially poled spheres. For the thickness mode a 100 kHz step was used since the frequency under investigation was in the MHz range. The calculated admittance *vs.* frequency spectra were compared with the experimental results obtained using an HP-4194-A Impedance-Gain Phase Analyzer. The polyurethane coating was not taken into consideration, since the dielectric and piezoelectric measurements were performed on spheres without protective coating.

4. RESULTS AND DISCUSSION

4.1. Dielectric Properties

As part of the characterization procedure, the capacitance and dielectric loss values of the samples were measured using a HP 4275–A Multifrequency LCR Meter at 1.0 kHz and 1.0 volt. Although capacitance values for radially poled spheres were found to follow an increasing trend from 960 pF for smaller samples up to 3,575 pF for the largest sample, there were, however, samples with same size but with different capacitance values. This is attributed to the large variations in wall thickness, defects on the sphere walls, and inner electrode problems. Therefore, the capacitance was used to evaluate the quality of the inner electrodes. The dielectric losses of radially poled spheres ranged from 0.0174 to 0.0430. For the top-to-bottom poled samples, capacitance of 2.5 to 10 pF were measured (Tab. I). The values are somewhat smaller than those calculated using a cylindrical tube approximation (6 to 10.5 pF).[11] As expected, the capacitance of top-to-bottom poled spheres is highly dependent on the electrode size and uniformity. The effect of electrode quality on the properties of the transducers is also discussed in the results of the hydrostatic piezoelectric measurements.

TABLE I Comparison of the dielectric and piezoelectric properties of tangentially poled hollow spheres

Property		*Tangentially poled spheres*		
	PZT-5A disc	*Type-A*	*Type-B*	*Type-C*
Electrode gap, d (mm)	n/a	0.77	1.06	1.81
Electrode height, h (mm)	n/a	0.75	1.38	0.84
Capacitance, C (pF)	131	9.73	4.5	2.6
Dielectric Loss, tan δ	0.017	0.017	0.022	0.014
Hydrostatic piezoelectric charge coefficients, (pC/N)	30	630	736	966
Hydrophone figure of merit, $d_h \times g_h$ (10^{-12}m^2/N)	0.06	24.23	33.07	56.97

4.2. Modes of Vibration of Radially Poled Transducers

Results of the finite element analysis suggest two main modes of vibration for the radial poling configuration: a breathing mode utilizing the d_{31} coefficient where the spheres vibrate with a volumetric expansion and contraction, and a wall thickness mode at much higher frequencies utilizing d_{33}. These modes are shown in the admittance *vs.* frequency spectrum of a sphere with 1.16 mm radius in Figure 2. The resonance frequencies of the

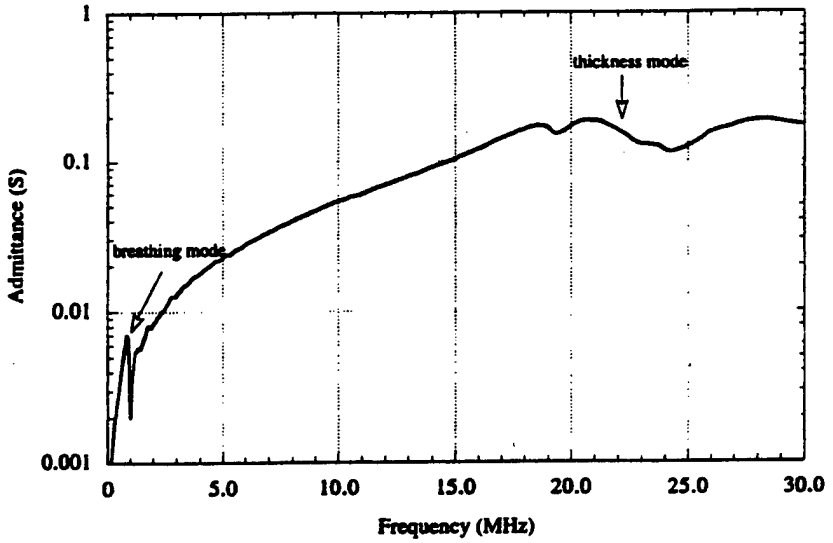

FIGURE 2 Admittance *vs.* frequency spectra for the main modes of vibration of a radially poled hollow sphere (r = 1.16 mm).

breathing mode for spheres with radii ranging from 0.5 to 3.0 mm were calculated using *ATILA*. Materials properties used in these calculations are as follows: $s_{11}^E = 16.4 \times 10^{-12}\,m^2/N$, $s_{12}^E = -5.74 \times 10^{-12}\,m^2/N$, $\rho = 7.75\,g/cm^3$. The results of these calculations along with values obtained experimentally are shown in Figure 3. From the figure, the experimental results agree well with the calculations for breathing mode for spheres with larger sizes. Experimental results on spheres with smaller sizes display higher than predicted frequencies, and this suggests that by further scaling down the size of the spheres the resonance of the probe can be pushed to even higher frequencies. As discussed in the introduction, this will increase the useful frequency range of the miniature acoustic probes. Similar agreement between the computed and measured results could not be obtained for the thickness mode. This mode was not observed in all the samples, and for the samples with a detectable thickness mode it appeared as a smooth, broad peak in the admittance *vs.* frequency spectra usually at frequencies exceeding 10 MHz. These findings suggest a large wall thickness variation for many of the spheres, as previously reported by Fielding *et al.*[13] However, spheres from other processing batches do show samples with large regions of relatively uniform thickness. These samples are being used in preparing spherically focused dish-shape transducers.[17]

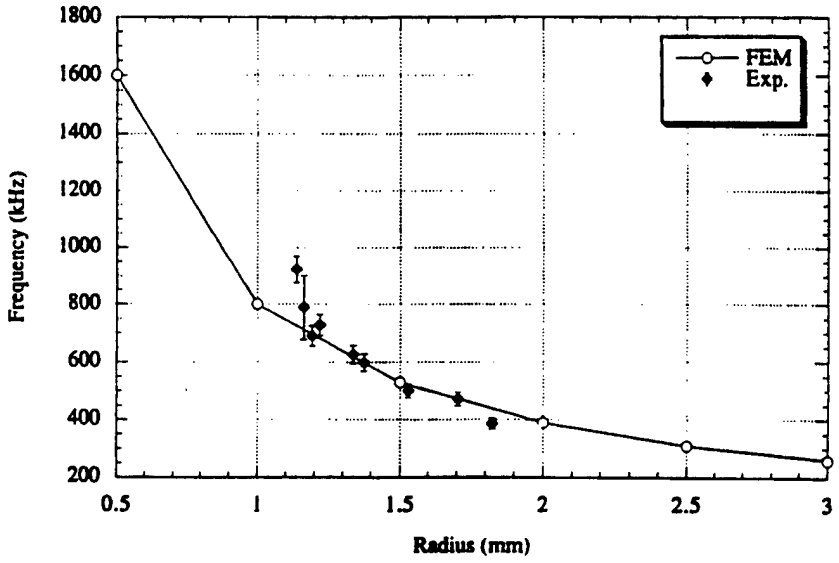

FIGURE 3 Comparison of the results of the experiments and finite element analysis on the effect of size change on the breathing mode resonance frequency.

The effect of the presence of an electrode hole on the vibrations of the spheres was also investigated using *ATILA* code and the results suggested that the hole introduce an additional peak at a frequency slightly higher than that of breathing mode. This is shown in Figure 4(a) for a sphere with a radius of 1.38 mm. A similar secondary peak was observed experimentally

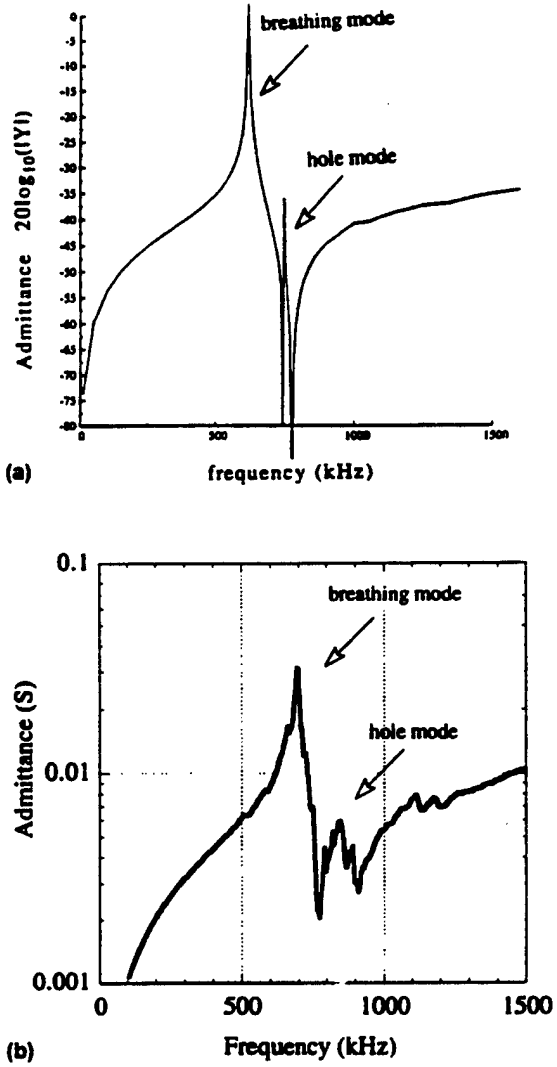

FIGURE 4 Effect of electrode hole on the breathing mode resonance frequency. (a) Fintie element analysis (r = 1.38 mm); (b) Experimental results (r = 1.19 mm).

for all the radially-poled spheres, as shown in Figure 4(b) for sphere with a radius of 1.19 mm. This secondary peak was studied using *ATILA* and the motion associated with that particular resonance is illustrated in Figure 5. In the figure the dashed lines correspond to the rest position and the solid lines show the displaced position.

4.3. Modes of Vibration of Tangentially Poled Transducers

Finite element studies of the spheres with top-to-bottom poling configuraion indicate that the material under the electrode cap is unpoled and inactive. Only the unelectroded region between the electrode caps is tangentially polarized.[18] Therefore, the size of the electrode gap is expected to control the dielectric and piezoelectric properties.

Finite element analysis of the tangentially-poled spheres identified the main modes of vibration as an ellipsoidal mode, a higher order circumferential mode, and a breathing mode near 230 kHz, 350 kHz, and 700 kHz, respectively, (Tab. II). Higher frequency modes associated with coupled motions between the ellipsoidal and thickness modes, or between the circumferential and thickness modes were also identified. The admittance *vs.* frequency spectra of a tangentialy-poled sphere obtained by finite element analysis is compared with the experimental curve in Figure 6. Comparison of the results indicates that there is close agreement between the calculated and measured values for the resonance–antiresonance frequencies of the three principal modes of vibration. However, this is not the case for the coupled modes. Since these higher frequency modes are formed as a result of a coupling between the thickness and the ellipsoidal modes, or the circumferential and the thickness modes, the lack of uniform

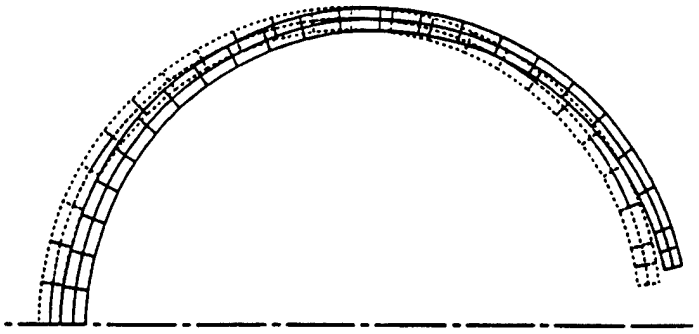

FIGURE 5 Vibration of a hollow sphere with hole at the resonance frequency of the second peak. Dashed lines correspond to the rest position, the amplitude is arbitrary.

TABLE II Comparison of the calculated and measured resonance frequencies of tangentially poled hollow spheres

Vibration mode and	*Type-A*		*Type-B*		*Type-C*	
resonance frequency (kHz)	*FEA*	*Exp.*	*FEA*	*Exp.*	*FEA*	*Exp.*
Ellipsoidal mode	240	199	240	220	240	234
Higher order circumferential	320	330	290	312	300	315
Breathing mode	590	651	590	704	590	716
Ellipsoidal coupled to thickness mode	1000	not found	980	1,264	1,030	1,300
Higher order circum. coupled to thickness	1,660	1,966	710	1,583	730	1,708
	2,520	2,870	1,300		1,380	
			1,300		1,380	
			1,660		1,840	
			1,980		2,210	

wall thickness is expected to displace and broaden these coupled modes. The displacement fields of these modes were discussed in detail elsewhere.[18]

4.4. Piezoelectric Response of the Transducers under Hydrostatic Pressure

The usefulness of a device, or a material used in the device, depends on its function. Hydrophones are designed as acoustic sensors, and noise is usually the limiting factor. Therefore, increasing the signal-to-noise ratio is the aim in most hydrophone designs.[19] In their study comparing ultrasonic microprobe designs, Moffett and co-workers [8] cited the product of the hydrostatic piezoelectric charge coefficient and the hydrostatic piezoelectric voltage coefficient ($d_h \times g_h$) as an acceptable figure of merit for a volume expander hydrophone. The d_h coefficient determines the charge delivered by the hydrophone to the preamplifier, and the g_h coefficient determines the open-circuit voltage of the transducer. The ($d_h \times g_h$) product can be taken as a measure of the signal-to-noise ratio (SNR) obtainable from a unit volume of piezoelectric material under conditions where the dominant noise source is the preamplifier.[8] Other properties such as the high electromechanical coupling coefficient and low acoustic impedance are also advantageous parameters of hydrophones[20]. Hydrophone designs utilizing hollow cylinder and spherical shapes lead to low acoustic impedance.

Based on the preceding discussion, the piezoelectric response under hydrostatic pressures up to 1,000 psi of the hollow sphere transducers was evaluated. The hydrostatic piezoelectric charge coefficient (d_h) of the samples was measured in an oil bath at hydrostatic pressures from 100 to 1,000 psi with a 30 Hz stimulus. A PZT-5A disc with a radius of 3.34 mm

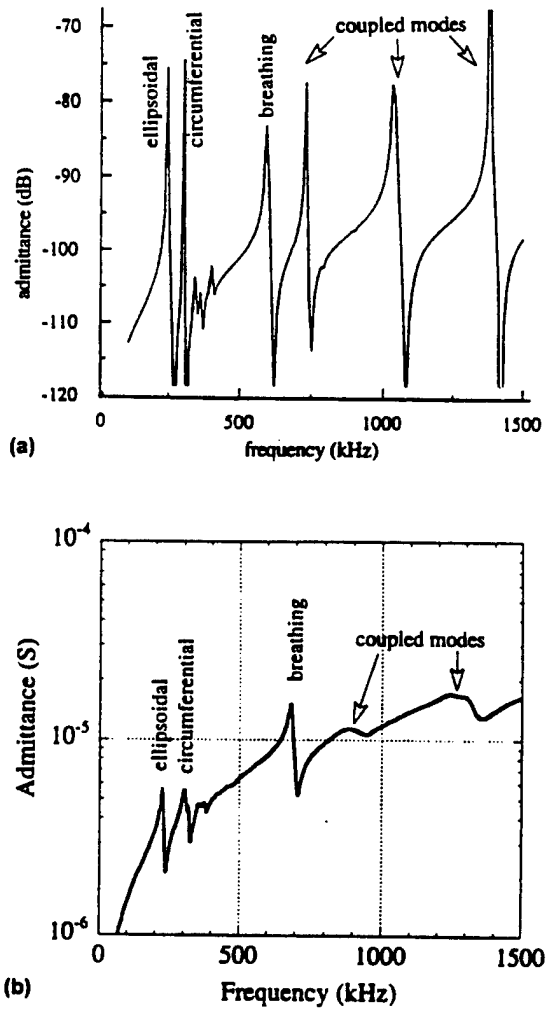

FIGURE 6 Admittance *vs.* frequency spectra for the main modes of vibration of a tangentially poled hollow sphere (r = 1.38 mm). (a) Results of the finite element analysis; (b) Results of the experimental studies.

and a thickness of 0.96 mm was used to calibrate the results obtained with the hollow spheres. From the measured d_h coefficients the hydrostatic piezoelectric voltage coefficients (g_h) and the figure of merit (FOM) of the samples were calculated using the following relations:

$$g_h = \frac{d_h}{\varepsilon_{33}} \tag{1}$$

$$\text{FOM} = d_h \times g_h \tag{2}$$

The results are plotted in Figure 7 for d_h *vs.* hydrostatic pressure for spheres with a radius of 1.38 mm. Measured values of d_h and the FOM are presented in Table I. Evaluation of these results indicate that both tangentially and radially poled BBs possess d_h values and figures of merit far larger than bulk PZT of the same composition. The amplification of d_h results from the spherical geometry and unique electrode designs, which transforms the hydrostatic pressure into radial and tangential stresses components. In this geometry, the radius to thickness ratio (r/t) can be taken as the stress amplification factor. The r/t ratio for the smallest commercially available transducer is ~3.5, whereas BBs have r/t ratios as large as 30. A detailed discussion along with a simplified model for this amplification was presented by Alkoy *et al.* [18]

The change in d_h with diameter was also investigated, and the results are plotted in Figure 8 for the radial poling configuration. As can be seen, a slight increase in d_h with increasing sphere size is evident especially at low pressures. This increase in sensitivity is thought to be a result of the decreasing wall thickness of the spheres with increasing sphere size, thereby

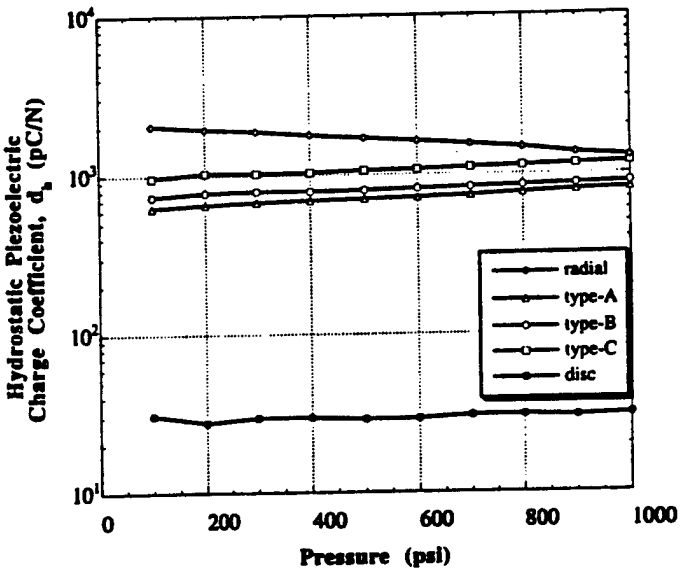

FIGURE 7 Hydrostatic piezoelectric charge coefficients (d_h) of the spheres with for different transducer designs.

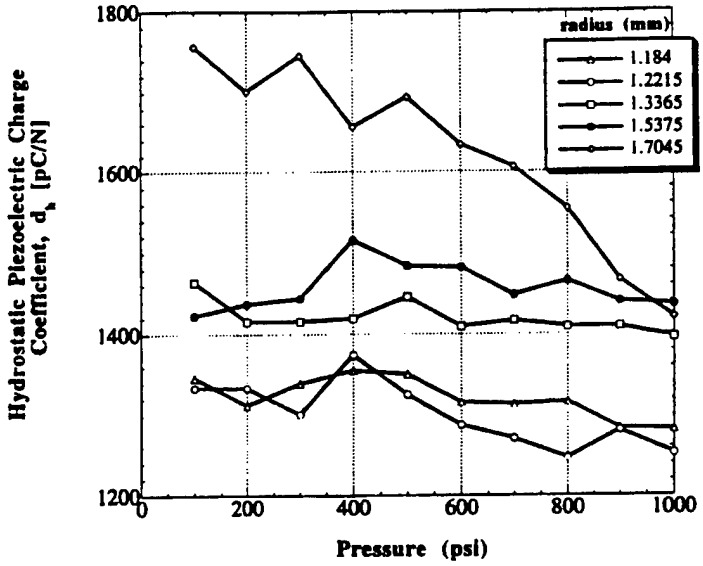

FIGURE 8 Effect of sphere size on the hydrostatic piezoelectric charge coefficients of the radially poled transducers.

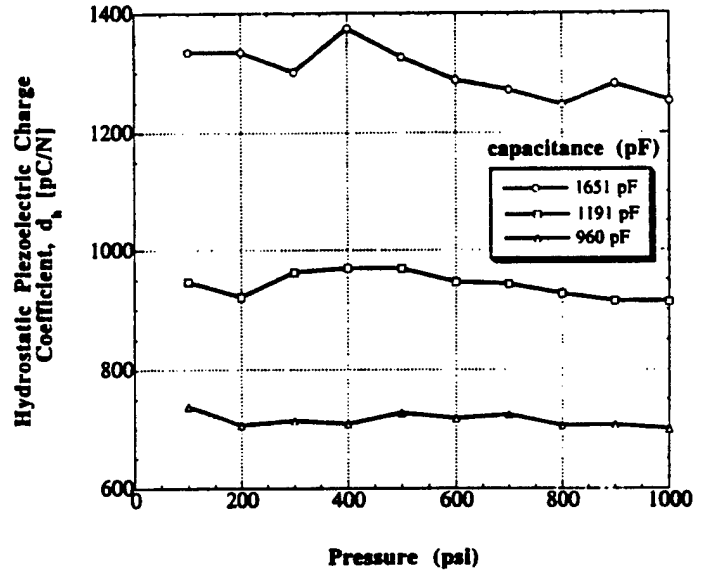

FIGURE 9 Effect of inner electrode quality on the hydrostatic piezoelectric charge coefficients of the radially poled transducers.

increasing the r/t ratio. As discussed in Section 4.1, the capacitance of the samples was taken as a qualitative indicator of the inner electrode quality. In order to assess the importance of inner electrode, the results of the d_h measurements on three spherical transducers of same size, and fabricated under the same conditions were compared in Figure 9. The plot clearly indicates a lower d_h for the sample with lower capacitance. The results given in Figure 8 for the size effect are taken from samples with the highest capacitance values.

5. CONCLUSIONS

Miniature piezoelectric hollow spheres were prepared using an inexpensive, coaxial-nozzle slurry process. Transducers were fabricated with spheres poled in several radial and tangential poling configurations for underwater hydrophone applications. Dielectric and piezoelectric measurements, along with finite element modeling, were carried out on the transducers. The principal modes of vibration were found to be breathing and thickness modes for the radial poling configuration, with the breathing mode resonance shifted to lower frequencies with increasing sphere size. Three different electrode configurations for tangential poling were examined, and regardless of the configuration the main modes of vibration were found to be an ellipsoidal, a higher order circumferential and breathing modes. High frequency coupled modes were also observed. Excellent d_h values and hydrophone figures of merit were obtained from the PZT hollow spheres.

Acknowledgements

This study is partly funded by ONR through contact # N0001492J1510, and by Gebze Institue of Technology, Turkey. We thank Georgia Institute of Technology, USA, and IEMN, Department ISEN, France for letting us use their facilities.

References

[1] Saneyoshi, J., Okujima, M. and Ide, M. (1966). *Ultrasonics*, 4, 64–6.
[2] Fay, B., Rinker, M. and Lewin, P. A. (1994). *Ultrasound in Med. & Biol.*, 20(4), 367–73.
[3] Wu, Y. Q., Shankar, P. M. and Lewin, P. A. (1994). *Ultrasound in Med. & Biol.*, 20(7), 645–53.
[4] Filmore, P. R. and Chivers, R. C. (1986). *Ultrasonics*, 24, 216–29.
[5] Romanenko, E. V. (1957). *Sov. Phys. Acoust.*, 3, 364–70.

[6] Lewin, P. A. (1981). *Ultrasonics*, **19**, 213–6.
[7] Lewin, P. A. and Chivers, R. C. (1981). *J. Phys. E: Instrum.*, **14**, 1420–24.
[8] Moffett, M. B., Powers, J. M. and Clay, W. L. Jr. (1988). *J. Acous. Soc. Am.*, **84**(4), 1186–94.
[9] Vilkomersan, D. and Lyons, D. (1997). *IEEE Trans. Ultrason., Ferroelect., Freq. Contr.*, **44**(1), 27–35.
[10] Lockwood, G. R., Turnbull, D. H. and Foster, F. S. (1994). *IEEE Trans. Ultrason., Ferroelect., Freq. Contr.*, **41**(2), 231–35.
[11] Meyer, R. Jr., Weitzing, H., Xu, Q., Zhang, Q. and Newnham, R. E. (1994). *J. Amer. Ceram. Soc.*, **77**(6), 1669–72.
[12] Torobin, L. B. (1987). *U. S. Patent*, **4**, 671, 909.
[13] Fielding, J. T. Jr., Smith, D., Meyer, R. Jr., Trolier-McKinstry, S. and Newnham, R. E. (1994). *Proc. IEEE Int. Symp. Appl. Ferroelec.*, pp. 202–5.
[14] Hladky-Hennion, A. C. and Decarpigny, J. N. (1993). *J. Acous. Soc. Am.*, **94**, 621–35.
[15] Hamonic, B., Debus, J. C., Decarpigny, J. N., Boucher, D. and Tocquet, B. (1989). *J. Acous. Soc. Am.*, **86**, 1245–53.
[16] Hladky-Hennion, A. C. and Decarpigny, J. N. (1991). *Ultrason. Int. Conf. Proc.*, pp. 415–8.
[17] Alkoy, S., Lopath, P. D., Hladky-Hennion, A. C., Cochran, J. K. Jr. and Newnham, R. E. (1997). *Proc. IEEE Int. Untrason. Symp.*, pp. 991–4.
[18] Alkoy, S., Dogan, A., Hladky-Hennion, A. C., Langlet, P., Cochran, J. K. Jr. and Newnham, R. E. (1997). *IEEE Trans. Ultrason., Ferroelect., Freq. Contr.*, **44**(5).
[19] Wilson, O. B. (1988). *Introduction to Theory and Design of Sonar Transducers* (Peninsula Publishing, Los Altos CA), pp. 135–57.
[20] Wollett, R. S. (1962). *J. Acous. Soc. Am.*, **34**(4), 522–3.

APPENDIX 44

Mat Res Innovat (1999) 3:175–178

ORIGINAL ARTICLE

William B. Carlson · Dave Williams
Robert E. Newnham

Piezotensegritic structures for transducer applications

Received: 28 April 1999 / Reviewed and accepted: 6 August 1999

Abstract Piezoelectricity and tensegrity have been coupled into an electrically active device. This concept, hereby known as piezotensegrity, can be used to sense or actuate. A composite sensor has been tested using compression elements stabilized with tensioning bands. The piezoelectric elements are arranged on the face diagonals with perimeter tension bands. Experimental piezoelectric response from this design was 1200 pC/N in air testing with peak hydrostatic response of 700 pC/N. The good device sensitivity as compared to properties of the base piezoelectric material is attributed to the internal arrangement of the piezoelectric elements and the tensioning system.

Key words Piezotensegrity · Tensegrity · Hydrophones · Piezoelectricity · Composites

Introduction

The geodesic domes of Buckminster Fuller and the sculptures of Kenneth Snelson are examples of tensegrity structures balanced by counteracting forces of compression and tension. Architects have developed a set of building rules based on tensegrity that also appear to operate in a number of biological systems [1]. Other structures which perform sensing or actuating functions are feasible as well. Electromechanical structures are capable of transforming mechanical forces into electrical signals in a variety of ways. Such devices sometimes rely on dilatational sensor motion [2] or distortional motion [3]. Here, we describe a simple planar device based on tensegrity which senses pressure and produces an electrical response. This device is a piezoelectric sensor consisting of sensing elements mechanically coupled with tensioning bands.

W.B. Carlson (✉) · D. Williams
New York State College of Ceramics, Alfred University, Alfred, NY 14802, USA
e-mail: fcarlson@bigvax.alfred.edu
Fax: +1-607-871-3469

R.E. Newnham
The Pennsylvania State University,
251A Materials Research Laboratory, University Park, PA 16802, USA

Relation to previous work

Prior work in the field of composite hydroacoustic sensors has been undertaken at the Materials Research Laboratory of The Pennsylvania State University. A number of methods have been developed to 'enhance' and to amplify the response of electroceramic materials for use in sea based hydroacoustic environments. These methods rely on the development of materials and the juxtaposition or arrangement of the shapes of these materials in composite devices. Many other researchers also have proposed designs which employ alternative materials and arrangements of sensor elements to maximize sensitivity and minimize the weight of the sensors. Compression and flexural techniques have dominated these designs in composites and hydrophone technology. Here we describe some recent work which may help to develop the use of alternative materials and alter the mechanics of the design of sensors. These piezotensegritic sensors rely on tension and compression (and possibly shear forces) to affect an improved response to acoustic pressure in contrast to flexural and compressional methods. In the past, tensioning systems have been largely ignored in favor of the more robust flexural systems. However, with recent work on high strength fibers, piezopolymers, magnetostrictive alloys, and shape memory materials other designs are now possible. Tensegrity, therefore, is introduced as a new method for configuring and designing sensitive hydrophone arrays. The primary advantages are a lightened design and the consequent minimization of driven mass.

Description of piezotensegrity

Piezotensegrity, as defined here, is an electromechanically activated structure, or sensor device, composed of pre-

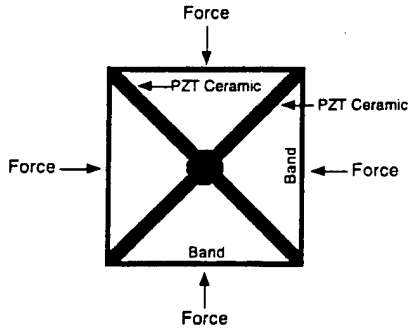

Fig. 1 Schematic of piezotensegrity transducer

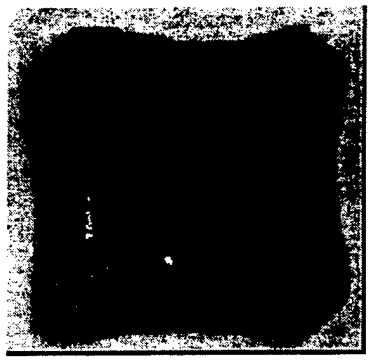

Fig. 2 Prototype of encapsulated device

tensioned elements with separated compressive elements. The active elements transduce mechanical strain to electric potential as a result of the tensile or compressive forces they carry. These devices may employ piezoresistive, electrostrictive, or magnetostrictive properties, alternatively to the aforementioned piezoelectric properties. In some cases, the device may act as a sensor, or, as an actuator, or both. These dynamic structures may also be controllable in various directions or quasi-stable configurations by changing shape.

Tensegritic topologies can be defined as a set of tensile elements linking separated compression elements in a stable or quasi-stable system. The compression elements are linked to one another by flexible tension elements which maintain a loose geometrical relationship. Solid elements may consist of bars, plates or arbitrary shapes (e.g. T-sections, X-sections, L-sections, etc.). Individual elements, either tensile or compressive, may be made active, that is strictive in nature and electrically (or magnetically) linked as mentioned above. The structural connectivity may be in various arrangements relative to the electroactive elements. Figure 1 depicts a simple two-dimensional tensegrity model consisting of two crossing compression rods and an encircling tension band.

Prototype design

A prototype similar to Fig. 1 was built and tested. In this design, piezoelectric bars were placed perpendicular to each other. The bars were laterally poled and electroded. When mechanical stress is applied axially along each bar the piezoelectric $\mathbf{d}_{31}$ property relates this stress to the charge polarization. The applied stress is transmitted to the bars via the bands. The banding material used was a shape memory alloy because it was more easily prestressed over the ends of the PZT rods. After further pretensioning with wires wound at right angles to the bands the structure was encapsulated in rigid epoxy, Fig. 2. Prior to encapsulation lead wires were attached. This device then was tested in both air and water. Small glass microballoons were added to the epoxy for the water tests.

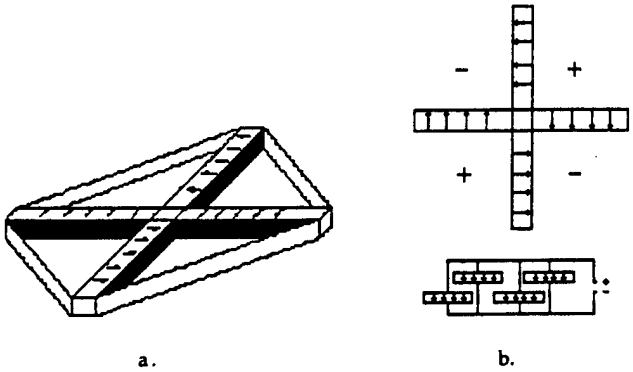

Fig. 3 (**a**) Pictorial of banded ceramic sensor, (**b**) Electrical schematic and circuit

The PZT ceramic was formed from a PZT-5H powder containing a small amount of polyvinyl alcohol as a binder. Approximately 12 grams of powder was loaded into a square pressing die (25 mmx25 mm) which was then subjected to a pressure of 56 MPa. After pressing, the blocks were fired at 1300°C for 1 hour. To minimize lead volatilization, 50 grams of lead zirconate powder was used to line the crucible. After firing, the blocks were ground to a thickness of 2.5 mm, and then bars were cut using a low speed diamond saw. Final dimensions of these bars were 2.5 mmx2.5 mmx15 mm. A center cube of PZT was formed in the same manner as the bars, but with dimensions 2.5 mmx2.5 mmx2.5 mm. After machining, the bars were electroded on opposite faces (2.5 mm x 15 mm) using a silver-filled epoxy. The bars were then poled for ten minutes at 70°C using a field of 26 kV/cm. Wire leads were then attached to two of the bars. Silver-filled epoxy was used to make these connections.

The sample devices fabricated in this work utilized piezoelectric bars arranged in a parallel electrical connectivity. To accomplish this, the bars were positioned in a cross pattern, Fig. 3, so that electroded faces with the same polarity were facing each other. A small amount of silver filled epoxy was placed at the point where two electroded faces joined to ensure a complete circuit. For

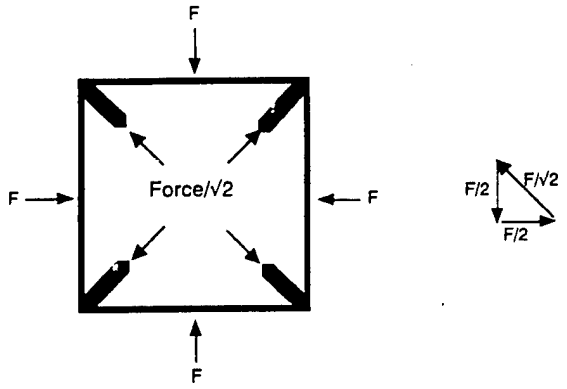

Fig. 4 Non-tensegrity force polygon and sensor mechanics

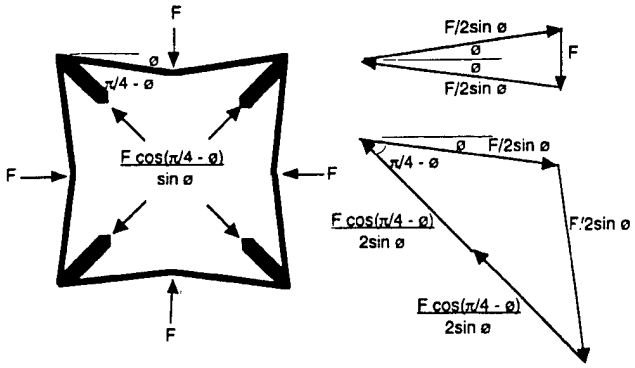

Fig. 5 Piezotensegrity mechanics: sensor forces and force polygons

a series connection, the same procedure could be followed except that the bars would be arranged with electroded areas of opposite polarity facing each other.

Once the bars were arranged in a cross pattern with the cube at the center, the assembly was temporarily clamped down to prevent movement. A tension band (32 AWG steel wire) was then wrapped around the perimeter of the assembly as tightly as possible, and the ends of the band were tied together. The device was then removed from the clamp, and a second set of tension bands were wrapped across the device to remove any slack from the first set of bands. After wrapping the tensional bands the entire device was encapsulated in Spurrs epoxy. This was performed in several stages by placing each face of the device in a layer of epoxy 1 mm thick, and allowing it to cure before beginning the next face. Once all of the epoxy faces were formed, Spurrs epoxy containing 50 volume percent plastic microballoons was injected into the cavity in the middle of the device. This was done to ensure that no small pinholes were present in the encapsulate. After the epoxy had cured, the device was ready to be tested.

Analysis and performance

We provide two examples to show how a piezotensegrity device compares to a similarly configured non-tensegrity device. These examples may help to explain how external loads are redistributed to the internal sensing elements.

In Example 1, we assume a set of uniaxial forces, F, are applied at 45 degrees to the piezoelectric rod directions in a non-tensegrity structure. If the forces are applied to rigid sides, this results in a force of $F/\sqrt{2}$ in each rod, Fig. 4. The applied force is distributed among the rods and can be sensed from each direction. The individual rod sensitivity for this applied force is reduced to the ratio of $1/\sqrt{2}$ times the piezoelectric constant **d**. This sensor may be considered omnidirectional if forces are applied to all the sides. The voltage coefficient, **g**, is similarly reduced.

In Example 2, we assume a set of forces are applied perpendicular to flexible bands (a tensegrity structure) instead of to rigid sides. These forces are then transmitted to the piezoelectric ceramic. In this example the force in the flexible band is $F/(2 \sin ø)$, where ø is the band angle measured from horizontal. The force in the ceramic is $F \cos(\pi/4)/\sin ø$, Fig. 5. If the band angle is small($ø \approx 0$) then there is significant force amplification and the rod sensitivity is $\cos(\pi/4)/\sin ø$ times the piezoelectric constant **d**.

Results

Air tests and water tests were performed on the square piezotensegritic sensor. The air tests employed a Berlincourt meter modified for testing $\mathbf{d}_{31}$ response with an applied force from one direction. In this air test the piezoelectric device response (effective $\mathbf{d}_{31}$) was 1200 pC/N. This value held constant across a low frequency range(<200 hz). Certain samples had lower performance due to inadequate pretensioning on the bands. The results from poorly tensioned bands were as low as 120 pC/N. In this case the epoxy carried most of the force and very little force was applied to the piezoelectric rods.

The water tests were performed in a small hydrostatic testing chamber. The chamber was used to uniformly pressurize the device and collect data across a limited pressure range. The performance of the device was recorded as the hydrostatic piezoelectric coefficient $\mathbf{d}_H$. This piezoelectric coefficient is a device coefficient and includes all the effects of the materials and the design topology under triaxial pressure. Figure 6 shows the results for the hydrostatic piezoelectric coefficient as recorded between 100 kPa (20 psi) and 1100 kPa (180 psi) pressures. The pressurization experiments gave a maximum $\mathbf{d}_H$ coefficient of 700 pC/N at ≈800 kPa (110 psi). This result decreases rapidly to 300 pC/N at 1100 kPa (160 psi). An average $\mathbf{d}_H$ of 500 pC/N was observed over the lower pressure range (100 to 600 kPa). The piezoelectric voltage coefficient ($\mathbf{g}_H$) and the piezoelectric

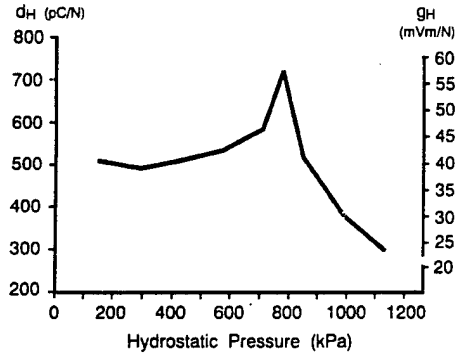

Fig. 6 Device piezoelectric performance vs. hydrostatic pressure

charge coefficient $\mathbf{d}_H$ are shown in Fig. 6. Maximum $\mathbf{g}_H$ was 57 mV-m/N and maximum $\mathbf{d}_H\mathbf{g}_H$ was 42000 fm²/N. Only an atmospheric permittivity constant was used in the calculation of $\mathbf{g}_H$ and therefore the $\mathbf{g}_H$ voltage coefficient is a calculated value. Reversible tests were not performed on the sample.

Discussion

The success of the air and water tests for this prototype were due mainly to the greater sensor area of the piezoelectric bar, the device pressure area (compared to the area of calibrating ceramic), and the force amplification from the flexible bands. In the air tests the 1200 pC/N response is a direct result of these effects. This implies that there is a significant amount of stress enhancement since PZT-5H has a $\mathbf{d}_{31}$ coefficient of only 270 pC/N. The very low values of 120 pC/N, however, show that when the bands have inadequate pretensioning there is no force amplification from the bands. The higher 700 pC/N response may be due to anomalous behavior from the crushing of microballoons within the device.

The maximum theoretical value for force amplification for tightly stretched bands(ϕ=0 radians) is infinity. However, this would imply infinite force to the ceramic. For the present design, the lowest force that can be applied to the ceramic is $1/\sqrt{2}$ of the applied force (dictated by the largest angle between the band and the bar ($\pi/4$ radians)). It may be concluded that the bands supply some amplification assuming the band angle ϕ is small.

During the hydrostatic tests the response increased with prestress on the bands until a maximum was reached at 110 psi pressure. Above this pressure the response rapidly degenerated. The planar nature of the device, with the bands transmitting the pressure, limits the stressing capability. In comparison with other underwater sensors the planar design suffers from its modest pressure tolerance <700 kPa (<100 psi). Other designs are being tested which have a three-dimensional capability. Table 1 lists composite designs employing amplified piezoelectric response.

Table 1 Comparison of piezoelectric properties for composite hydrophones

Device Type	$\mathbf{d}_H$ (pC/N)	$\mathbf{g}_H$ (mVm/N)	$\mathbf{d}_H\mathbf{g}_H$ (fm²/N)	Ref.
Moonie	9000	–	50,000	[4, 5]
Cymbal	15000	–	100,000	[6, 7]
Piezotensegrity(2-D)	500	40	20,000	paper

Conclusions

A planar piezotensegritic device was designed and tested for air and water environments. This simple device distributes applied loads to independent compression elements via pretensioning. Drawing on the ideas of biological functions which utilize tensegrity, the piezotensegritic structures demonstrate the use of electromechanically active elements. We have tested a simple device for use in hydroacoustic applications where the advantages may be their low weight and good piezoelectric response. Geodesic domes and other more complex structures might also be configured for different pressures and forces. Future work is needed to optimize topologies for a variety of actuator and sensing functions.

Acknowledgments This research was, in part, supported by the University Research Initiative Support Program (URISP), funded by the Department of Defense (DARPA/ONR) contract N00014-96-1-0961.

References

1. Ingber DE (1997) Ann Rev Physiology 59:575
2. Tressler JF, Alkoy S, Newnham RE (1998) J of Electroceramics 2:4, 257
3. Carlson WB, Schulze WA, Newnham RE, Cross LE (1996) Ferroelectrics 188:11
4. Onitsuka K, Dogan A, Tressler JF, Xu QC, Yoshikawa S, Newnham RE (1995) J Intelligent Mat Sys Struct 6:447
5. Xu QC, Yoshikawa S, Belsick JR, Newnham RE (1991) IEEE Trans UFFC 38:634
6. Dogan A, Uchino K, Newnham RE (1997) IEEE Trans UFFC 44:597
7. Tressler JF, Dogan A, Fernandez JF, Fielding JT, Uchino K, Newnham RE (1995) IEEE Ultrasonics Symp Proc, 897

APPENDIX 45

Smart systems: Microphones, fish farming, and beyond

Smart materials, acting as both sensors and actuators, can mimic biological behavior.

Robert E. Newnham
Ahmed Amin

The term "smart systems" appears with increasing frequency in scientific and engineering publications as well as in the popular press. Several smart systems have been commercialized and are widely used. Many more systems are in various stages of development. Aerospace engineers are interested in smart air foils to control drag and turbulence. Diabetics need medical systems to sense sugar levels and deliver insulin. Architects are designing smart buildings with self-adjusting windows that control how much sunlight and heat flows in and out. Tennis players will want smart racquets to make overhead smashes and delicate drop shots. Smart motion detectors will monitor authorized and unauthorized entries into buildings. Smart toilets are capable of analyzing urine to identify health problems. Smart irrigation systems will be needed to optimize the world's food supply. Smart transducers can "talk" to fish, a leading source of protein in many parts of the world, to herd them like cattle.

How do smart systems accomplish all this? They are made from "smart" materials, which have the ability to perform sensing and actuating functions and therefore are capable of imitating living systems. Four of the most widely used classes of smart materials are piezoelectrics, electrostrictors, magnetostrictors, and shape-memory alloys—all of which are ferroic. Ferroic materials have active domain walls, that is, crystallographic boundaries that can be moved by applying an external force or field. The resulting changes in the shapes of these materials are large enough to make them useful as actuators. Smart materials undergo two or more phase transformations, which can be used to tune their performance. Smart materials also can be manufactured by using multifunctional composites. These composites are made by combining two materials in a connectivity pattern that optimizes the functionality of the composite.

A sensor receives a stimulus and responds with a signal; an actuator produces a useful motion or action. By definition, smart materials are both sensors and actuators, because they perform both functions. They may or may not have control systems. "Passively smart" materials function like a vertebrate's spinal cord, producing involuntary reflex responses, without thought or signal processing. "Actively smart" systems analyze the sensed signal—perhaps for its frequency components—and then decide what kind of response to make.

The integration of sensors, actuators, and control systems is an ongoing process in the automotive, medical, military, and consumer electronic markets as systems become more miniaturized and more complex. By incorporating sensors, actuators, and evolvable chips into these systems, we can begin to emulate biological behavior. Small electronic and optical subsystems are capable of evolving into more complex systems that have the ability to sense and respond to changes in their surroundings.

Meanwhile, biochemists are making major advances in understanding how the human brain functions and what it means to be alive. In the coming century, there will be a confluence of organic and inorganic life into some kind of

The authors are at Pennsylvania State University.

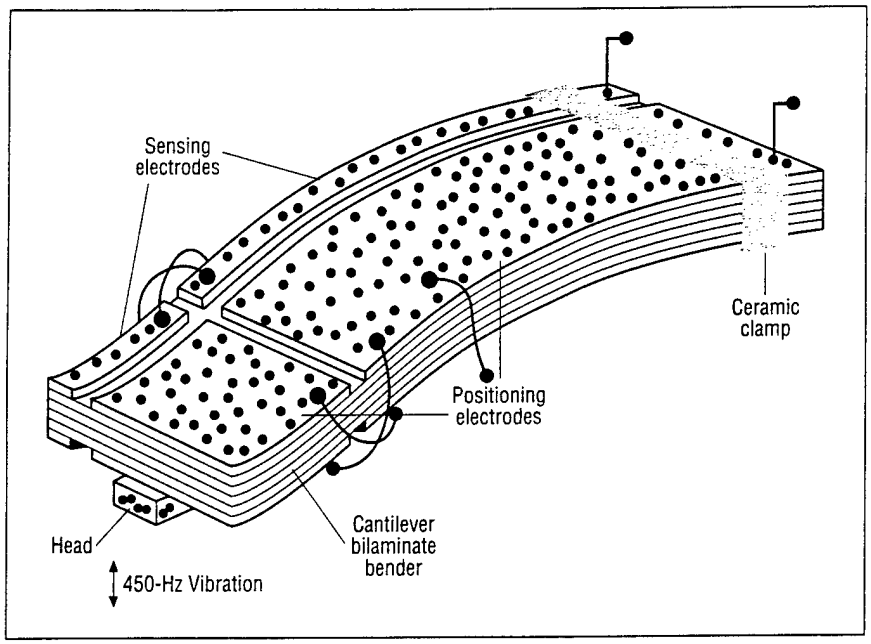

***Figure 1.* A videocassette tape head positioner senses and follows the tape track path.** Using direct and converse piezoelectric effects, the lead zirconate titanate (PZT) bender acts as a smart material with separate electrodes for sensing and actuating. Adapted from Ref 5. Used by permission.

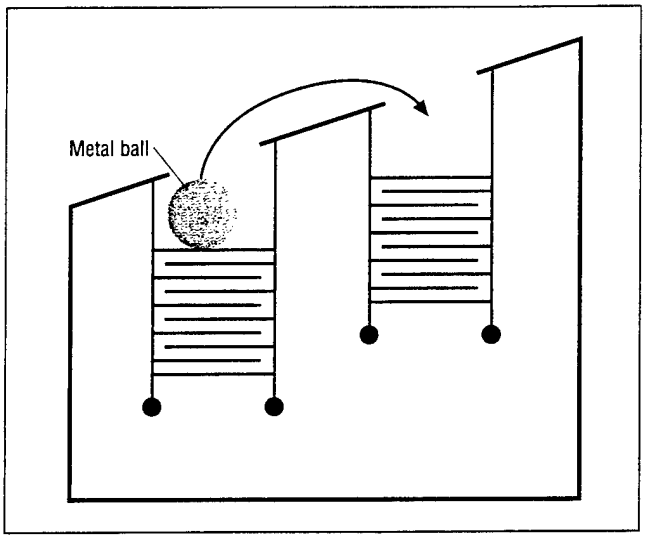

***Figure 2.* The piezoelectric Pachinko machine is a smart system that has a PZT sensor–actuator stack with a feedback network.** Adapted from Ref 5. Used by permission.

a composite life form—perhaps an immortal life form—with a common consciousness that transcends individual beings. The Internet and the World Wide Web seem to be leading us in that direction. The evolution of machine technology into global intelligence is the theme of a major book that was published in 1997 (*1*).

Sensors + actuators = smart materials

A piezoelectric ceramic videocassette tape head positioner illustrates the basic idea of a smart material (Figure 1). Piezoelectric materials have the unusual ability to generate a voltage when a mechanical force is applied or to generate mechanical force when a voltage is applied. Bimorph piezoelectric ceramics are usually made from lead zirconate titanate (PZT). Bimorph cells are constructed from pairs of piezoelectric plates. When a voltage is applied, one plate expands, the other plate contracts, and the cell bends in proportion to the voltage. The videocassette tape head positioner has large actuator electrodes that move the material and smaller electrodes that sense the position and orientation of the tape head. This combination of sensing and actuating mimics two of the functions of a living system: awareness of the surroundings and a useful response, which usually is in the form of motion.

The piezoelectric Pachinko game illustrates the principle of a smart material. Pachinko parlors with hundreds of vertical pinball machines are popular in Japan. The machine, constructed by engineers at Nippon Denso (Kiriya, Japan), is made from multilayer PZT stacks that act as both sensors and actuators (Figure 2). When a ball falls on the stack, the force of impact generates a piezoelectric voltage. Acting through a feedback system, the voltage pulse triggers a response from the actuator stack. The stack expands rapidly, throwing the ball out of the hole. The ball moves up a spiral ramp during a sequence of such events. Eventually, it falls into a hole and begins the spiral climb again.

Very smart materials can learn

During the past 20 years, in addition to smart materials, we have been developing a family of "very smart materials"—we are not yet willing to call them intelligent—that have a learning or tuning function that makes it possible for them to become smarter. These materials take advantage of nonlinear properties such as electrostriction or higher order elastic constants. By applying a bias field, we can tune the level of sensitivity, that is, the degree of "smartness".

Looking ahead to the use of thin-film microelectromechanical systems (MEMSs) (*2*), more intelligent materials are coming on the scene that integrate the control system with the sensors and actuators, all in one common piece of material. MEMS-based devices that have found applications in everyday use include inkjet cartridges in printer

heads, accelerometers as airbag sensors in automobiles, and tire-pressure sensors. Chemical sensor arrays and high-resolution displays are two emerging MEMS products. Figure 3 shows a digital mirror display (DMD) array developed by Texas Instruments that was fabricated by micromachining. It consists of 800 × 600 tiltable mirrors that function as pixels; the associated circuitry is batch processed on a silicon chip. The mirrors are electrostatically actuated. The DMD array is a promising technology for lightweight displays that offer high definition, high contrast, and high brightness.

We believe that when sensors, actuators, and control systems can be combined like the eyes, arms, and brain of the human body, the system will deserve the name "intelligent". Finally—although we have no idea how to do this yet—we will make "wise" materials that make moral decisions. Perhaps they will evolve in some way like living systems (see box, ***Forecasts for the future***).

Forecasts for the future

The World Future Society (http://www.wfs.org) has listed the top 10 predictions for the coming decade. Several involve using "smart" materials (i.e., materials with sensing and actuating capabilities).

- Cashless economy (smart cards)
- Electronic immigration (telecommuters, independent contractors, and other "lone eagles")
- Robots smarter than humans (inorganic evolution)
- Automated parole (implants replace prisons)
- Voice-driven furniture (smart chairs)
- Population shift to north (smart houses)
- Defective gene replacement (nanosensors and nanoactuators)
- Collision avoidance systems (smart automobiles)
- Older generation families (smart drug delivery devices)
- Automatic gardens (just-in-time farming)

One application: smart shock absorbers

Current research is focused on vibration suppression in automobiles using smart shock absorbers. Inside the smart shock absorber developed by Toyota (Figure 4) is a multilayer piezoelectric ceramic that has about five layers for sensing road vibrations. The multilayer stacks positioned near each wheel of the automobile have about 100 layers, all part of the same PZT ceramic, which act as the actuator. After analyzing the vibration signals, a voltage is fed back to the actuator stack, which responds by pushing on the hydraulic system of the automobile to enlarge the motion. In this way, signal processors in the automobile can analyze acceleration signals from road bumps and respond with a motion that cancels the vibration. Such active systems are used to alleviate excessive vibrations in helicopter blades and in the twin tails of F-18 fighter jets.

Traditionally, vibration problems in engineering structures were solved by using mechanical dampers or by isolating vibration with foam rubber pads, but the piezo-dampers developed by Active Control eXperts (ACX; Cambridge, MA) are readily tuned to the frequencies that most require attenuation. Passive piezo-dampers that use either a resistance–capacitance shunt circuit or a resistance–inductance shunt circuit are used as electronic shock absorbers in skis and baseball bats. A piezoelectric ceramic converts the unwanted mechanical vibrations in the skis or bats to voltage, which is dissipated as heat in the shunt circuit.

Underlying structure–property relationships

Four major families of ceramic and metallic actuators are under development: piezoelectrics, electrostrictors, magnetostrictors, and shape-memory alloys. All of these

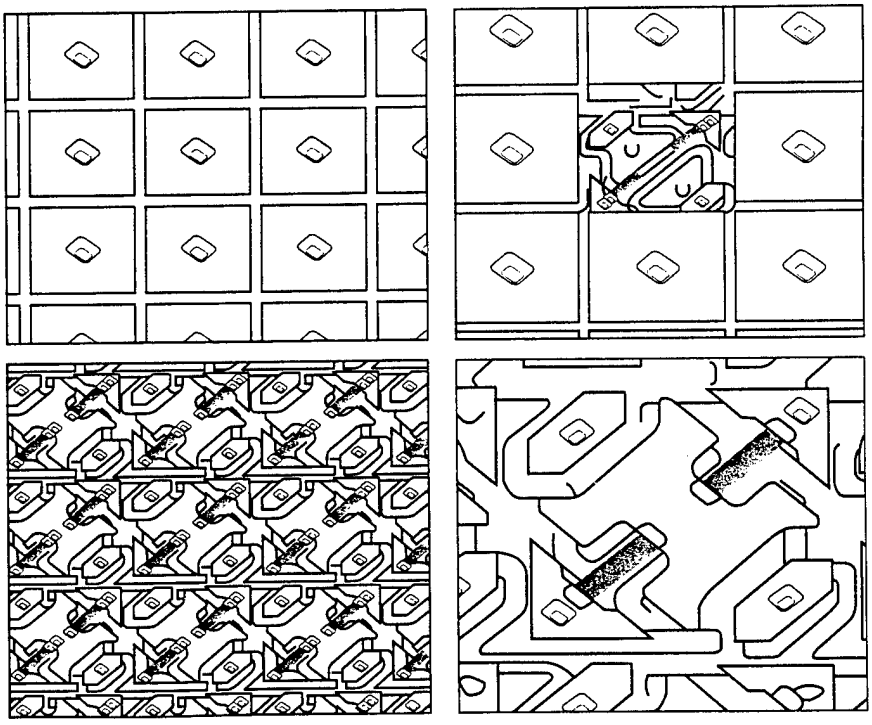

Figure 3. **Schematic representations of the Texas Instruments digital mirror display (DMD).** Top left, completed DMD chip; top right, completed DMD chip with mirror layer and yoke-and-hinge layer removed; bottom left, completed DMD chip with mirror layer removed; bottom right, close-up image of 1 pixel with mirror layer removed. Source: Ref 2. Used by permission.

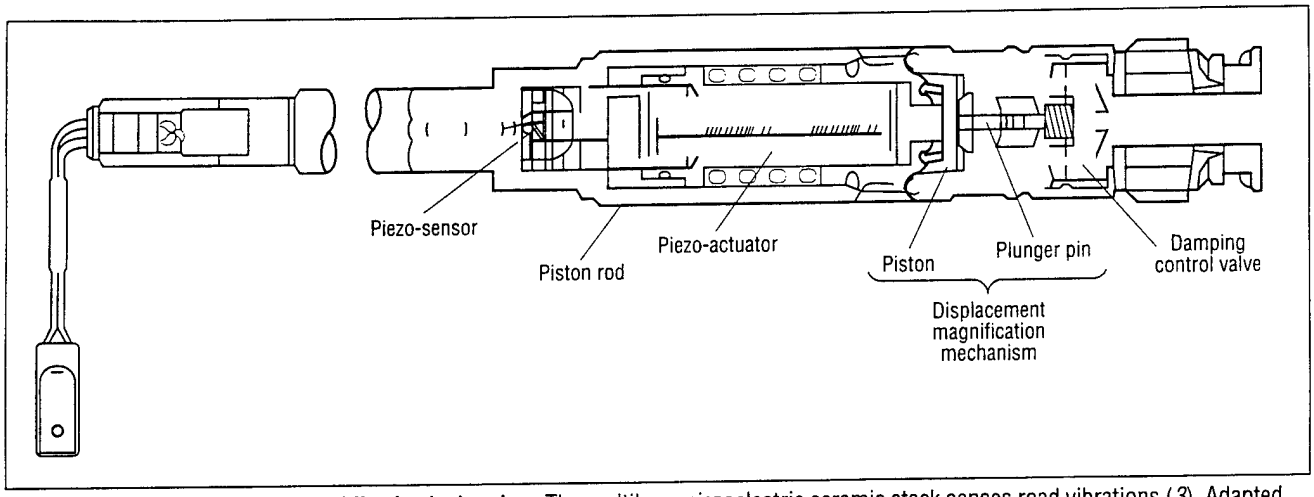

***Figure 4.* Smart electronic automobile shock absorber.** The multilayer piezoelectric ceramic stack senses road vibrations (*3*). Adapted from Ref 5. Used by permission.

materials undergo at least two phase transformations with coupled thermodynamic order parameters. These transformations lead to complex domain wall behaviors, which strongly contribute to the sensing and actuating capabilities. Domain wall motion is initiated by electric fields (ferroelectrics), magnetic fields (ferromagnetics), mechanical stress (ferroelastics), or temperature changes as they transform from ferroic to nonferroic states.

In the following sections, we review the atomistic origins of piezoelectricity, electrostrictive, magnetostrictive, and thermostrictive properties.

Piezoelectrics: Smart ceramics. Most piezoelectric transducer formulations are based on PZT, $Pb(Zr,Ti)O_3$, one of several ferroelectric substances that crystallize with the perovskite structure, described as follows: Lead atoms are located at the corners of a cubic unit cell and oxygen atoms at the centers of the cube faces. Lead and oxygen ions have radii of ~1.4 Å, and together make up a face-centered cubic array (unit cell) ~4 Å on one side. Octahedrally coordinated titanium or zirconium ions are located at the center of the unit cell. Ferroelectric materials exhibit spontaneous electric polarization; that is, the electric dipole moments within a domain align in a common direction, even in the absence of an external electrical field.

On cooling from a high temperature, the crystal structure of PZT undergoes a displacive phase transformation with atomic displacements of ~0.1 Å. For titanium-rich compositions, the point symmetry changes from cubic $m3m$ to tetragonal $4mm$ on cooling through the Curie temperature near 350 °C. (Note: The Curie temperature marks the transition from the high-temperature paraelectric phase, in which the electrical dipoles only align when a field is applied, to the polar low-temperature phase, in which the dipoles align spontaneously.) The tetragonal state with its spontaneous polarization along the [001] crystallographic direction (i.e., perpendicular to the square face) persists down to temperatures approaching 0 K. Structural changes are illustrated in Figure 5 (page 42).

To use these piezoelectric ceramics with their large polarizations, compositions near a second phase transition are chosen. At the Curie point, PZT converts from a paraelectric state with the ideal cubic perovskite structure to a ferroelectric phase located near a morphotropic phase boundary between the tetragonal and rhombohedral states. The morphotropic phase boundary delineates two solid phases that remain in a near-equilibrium state over a very wide temperature range. Very large piezoelectric coupling between electric and mechanical variables is obtained near this phase boundary. Much of the current research in this field involves looking for other morphotropic phase boundaries to further enhance the electromechanical coupling factors.

Two piezoelectric effects are used in PZT transducers: direct and converse. The direct effect relates polarization to stress and is used in sensors. The converse effect relates strain to electric field and is used in actuators.

Piezoelectric ceramics are prepared by "poling" them; that is, subjecting them to a large dc electrical field to align their domains. For a poled ceramic with symmetry ∞m (an infinite number of mirror planes parallel to the poling direction), the appropriate tensor coefficients are d_{31}, d_{33}, and d_{15}. These piezoelectric coefficients make intrinsic and extrinsic contributions. Under mechanical stress parallel to the dipole moment, the spontaneous polarization (P_s) is enhanced along the poling direction (X_3); and when stress is applied perpendicular to that dipole moment, electric charges develop along X_3. These are the d_{33} and d_{31} effects, respectively. When the dipole is tilted by shear stress, charges appear on the side faces (the d_{15} coefficient).

There are extrinsic contributions to the piezoelectric coefficient as well, and these can be extremely large, often involving the domain wall motions.

Ferroelectric ceramics such as PZT do not become piezoelectric until electrically poled. Poling is carried out under intense electric fields at elevated temperatures below the ferroelectric Curie point at which the domains are easily aligned. Titanium-rich compositions in the PZT system favor a tetragonal modification, with sizable elongation along [001] and a large spontaneous polarization in the same direction. Six equivalent polar axes in the tetragonal phase correspond to the [100] direction (the unit cell edge that forms one side of a square) and directions of the cubic paraelectric state. A rhombohedral ferroelectric state is favored for zirconium-rich compositions. The distortion and polarization are along <111> (body diagonal) directions, giving rise to eight possible domain states.

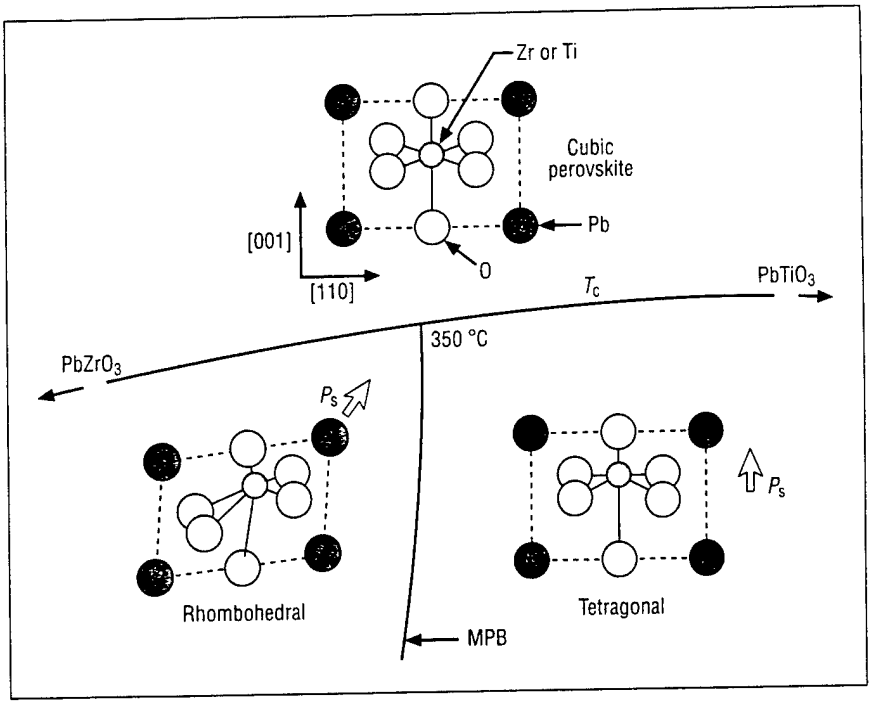

***Figure 5.* Portion of the $PbZrO_3$–$PbTiO_3$ phase diagram.** Structure changes at the Curie temperature (T_c) and the morphotropic phase boundary (MPB) are shown. Adapted from Ref 4. Used by permission.

The compositions that pole best lie near the morphotropic boundary between the rhombohedral and tetragonal ferroelectric phases. For these compositions, 14 possible poling directions exist over a wide temperature range, explaining in part why the ceramic piezoelectric coefficients are largest near the morphotropic boundary. Phase changes between the rhombohedral and tetragonal phases also occur during the poling process.

Electrostrictors: Very smart ceramics. Piezoelectricity is a third-rank tensor that relates strain and electric field. Electrostriction is a fourth-rank tensor that relates strain to the square of the electric field. Above the Curie temperature, the perovskite structure is cubic (centrosymmetric, or nonpolar), and the electrostriction effect is more important than the piezoelectric effect because third-rank tensors disappear in centrosymmetric media. It leads to what we call very smart ceramics.

In a smart ceramic, the direct piezoelectric effect is used for sensing, followed by feedback through the converse piezoelectric effect. In a very smart material, we monitor the change in capacitance of the material, then feed back with both dc and ac fields: first to tune the magnitude of the electromechanical coupling coefficient, then to drive it. For higher order coupling coefficients such as those that describe electrostriction, three coupled effects arise (rather than two): change in the dielectric constant with stress, field dependence of the piezoelectric voltage coefficient, and electrically driven mechanical strain. The electrostrictive ceramic becomes a tunable transducer.

We began work on several of these electrostrictive materials almost 20 years ago for active optic systems. Much of this work was done with the Itek Corp. in Lexington, MA. During the Cold War, many satellites flying over the Soviet Union used active optic systems to eliminate the effects of atmospheric turbulence. Electrostrictive materials have an advantage over piezoelectrics in adjusting the position of optical components, because much less hysteresis is associated with the motion.

Work on active optic systems has continued over the years. Similar multilayer actuators were used to correct the positioning of the optical elements in the Hubble telescope. Supermarket scanners use actuators and flexible mirrors to interrogate bar codes optically.

Relaxor ferroelectrics. Disordered perovskites contain regions where "active" ions (those that promote ferroelectricity) are in close proximity. Ordered perovskites usually have low dielectric constants because active and inactive ions are evenly dispersed and the linkage between "active" ions is severed. In partially disordered structures such as the relaxor ferroelectrics, the dielectric constant can be extremely large, making disordered materials useful as capacitor dielectrics and as electrostrictive actuators. The most widely used compositions are modifications of lead magnesium niobate (PMN), $Pb_3MgNb_2O_9$.

Relaxor ferroelectrics, often perovskite materials, are characterized by temperature-sensitive microdomains that result from the many different "active" ion linkages in the disordered octahedral framework. Each NbO_6 octahedron may be bonded to zero to six other NbO_6 octahedra (with the remaining connections involving MgO_6 octahedra). Connections between these octahedra are assumed to be essential to ferroelectricity and high anisotropy coefficients (K values). As the temperature decreases from the high-temperature paraelectric state, ferroelectric microdomains gradually coalesce to macrodomains, giving rise to a diffuse phase transformation. These polarization fluctuations are also dependent on bias field and the frequency used to measure the dielectric or piezoelectric constant. The dielectric constant drops off rapidly with increasing frequency (hence the name "relaxor") because it takes time for the polarization fluctuations to respond. The dc bias fields favor coalescence, giving the same effect as lowering the temperature.

Relaxor behavior is very common among lead-based perovskites, suggesting that the "lone pair" electrons of Pb^{2+} play a role in the microdomain process, possibly by

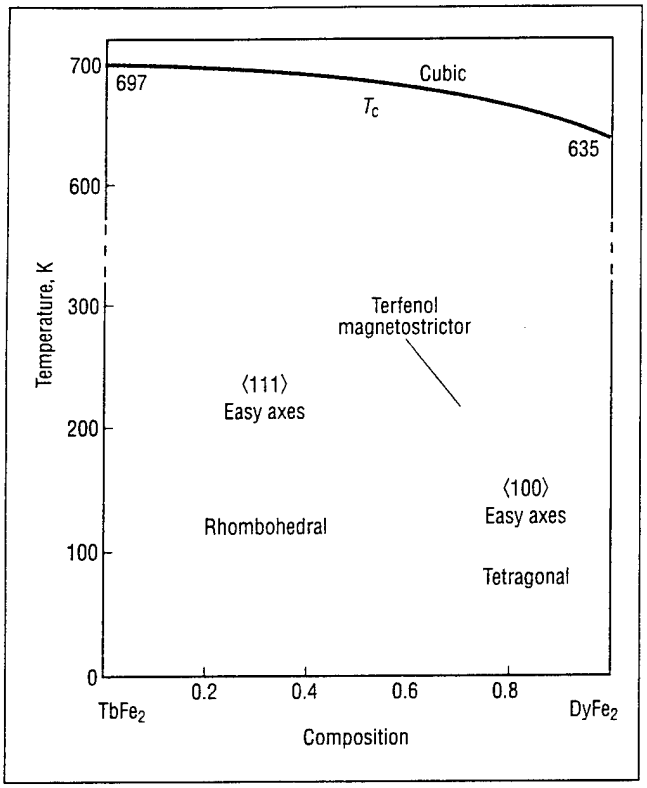

***Figure 6.* Binary phase diagram for the $Tb_{1-x}Dy_xFe_2$ (Terfenol-D) system.** Compositions near the magnetic spin boundary at $x = 0.7$ are used in magnetostrictive applications. T_c, Curie temperature.

adjusting their orientations. Electrostriction is described by a 6 × 6 matrix that relates strain to the square of the electric polarization. This kind of matrix is familiar to most materials scientists because electrostriction is a fourth-rank tensor almost identical to elasticity in form. For a cubic crystal, we deal with the same coefficients, *11*, *12*, and *44* that would normally be used to describe the elastic properties of a cubic crystal. In this case, strain is induced electrically rather than mechanically.

Whereas piezoelectricity is observed in polar materials, electrostrictive transducers use cubic (nonpolar) materials, whose compositions are near a phase instability with microscopic regions that fluctuate in polarization. On average, atoms are located in the ideal cubic sites but continually shift off these positions. The underlying origin of these effects is a partial ordering of the PMN perovskite structure in which the niobium and the magnesium atoms of PMN alternate in position but over only a few unit cells (usually 30–50 Å). Within these ordered islands, an external field acts upon fluctuating dipoles to make large electrostrictive motions.

Magnetostrictive actuators. PZT and PMN ceramics are outstanding ferroelectric actuators. However, equally interesting developments are taking place in the field of ferroelastic and ferromagnetic materials. All these ferroic materials have a domain structure in which the walls can be moved with electric fields, magnetic fields, or mechanical stresses.

Magnetostrictive alloys (e.g., Terfenol-D, $Tb_{1-x}Dy_xFe_2$) function well as sensors and actuators. (The name Terfenol refers to terbium and iron, and the Naval Ordnance Lab, NOL, where it was developed. The "D" refers to the dysprosium-containing variety.) Magnetostrictive materials exhibit strain (i.e., a change in dimension) in proportion to the direction and extent of magnetization. High-power actuators can deliver forces >50 MPa with strains up to 0.6%, whereas magnetostrictive sensor materials can provide hundreds of times the sensitivity of semiconductor strain gages. Magnetoelastic materials (in which elastic strain alters the magnetization) also have tunable elastic moduli that can be controlled by external magnetic fields.

Many magnetomechanical transducers and actuators have been designed and manufactured with Terfenol-D. The high energy density, ruggedness, and reliability of these actuators make them attractive for vibration suppression and high-power sonar. Thin films of magnetostrictive rare earth–iron alloys can be sputtered onto silicon and patterned by etching or sputtering through masks. Micropump and microvalve membranes and cantilevers appear to be promising MEMS components.

The rare earth atoms in Terfenol have large orbital moments that interact with fields to give large magnetostrictive strains. The rotation of magnetization is largely responsible for the shape change. The field-induced strain in Terfenol-D is ~100 times larger than strains in iron and nickel.

The iron in Terfenol produces the high Curie temperature. The rare earth terbium and dysprosium atoms produce the large magnetostriction. In combination, these three elements produce the useful alloys. The phase diagram of Terfenol is the magnetic equivalent to the morphotropic boundary of PZT. A portion of the magnetic phase diagram of Terfenol is plotted in Figure 6. Terfenol is cubic and paramagnetic at high temperature, and it undergoes a magnetic phase transformation to a rhombohedral structure with magnetic spins parallel to the <111> family of crystallographic directions. Near room temperature, it is poised on an instability with the spins ready to reorient into the tetragonal directions, the former <100> directions of the cube. There is a complex domain structure both above and below the transition, and like PZT, Terfenol is poised on a rhombohedral–tetragonal phase boundary.

The figure of merit for magnetostrictive actuators is proportional to the saturation strain coefficient. But in addition to a large shape change, the strain must be easy to move. The figure of merit for magnetostrictive actuators is the ratio of the saturation strain (λ) to the anisotropy coefficient (*K;* an indicator of the ease of rotation of the magnetization). In addition to producing a large shape change, the strain must be easy to move. $TbFe_2$ has a very large λ and a large positive *K,* which reduces its figure of merit. $DyFe_2$ has a *K* of opposite sign. *K* greater than zero indicates the spins preferentially align along <111>, and *K* less than zero means <100> is preferred. By tuning the composition of the ternary alloy to near the point at which *K* goes to zero, one can make an easily movable strain in this magnetostrictive alloy, maximizing the figure of merit.

Thus, it is important to alloy $TbFe_2$ with $DyFe_2$. A large shape change is very useful in actuators and transducers, but controlling the shape change with small applied fields is also important. In contrast, a large shape change frozen in position is of no practical value. To lower the driving field, a second phase change is positioned near room temperature by adjusting the alloy composition. It can be done

by lowering the Curie temperature, but this method demagnetizes the actuator and greatly reduces the magnetostriction coefficient. It is preferable to choose a composition near the rhombohedral–tetragonal phase boundary where the easy axis, the preferred direction of the magnetic dipoles, switches from <111> to <100>. Compositions near $Dy_{0.7}Tb_{0.3}Fe_2$ have large magnetostrictive coefficients with easily controlled shape changes. Below room temperature, the magnetic symmetry changes from rhombohedral to tetragonal with a significant decrease in the magnetostrictive shape change.

Shape-memory metals. The final example of an actuator material is the shape-memory alloys, which are thermally driven in contrast to the magnetic drive of magnetostrictors or the electrical drive of piezoelectric and electrostrictive materials. Shape-memory alloys also have phase transitions associated with the large thermomechanical coupling coefficients. One commonly used material is Nitinol, a nickel–titanium alloy that was initially investigated at U.S. Navy laboratories (*4*). Near 1:1 compositions, the nickel–titanium intermetallic compound melts congruently at ~1300 °C and has a martensitic phase transformation near room temperature.

The shape-memory alloys undergo martensite-type phase transformations similar to those observed in steel processing. Two characteristics of martensitic phase changes are the absence of long-range diffusion and the appearance of a shape change. Ferroelastic phase transformations are distortive and diffusionless and have much in common with martensitic transformations. Ferroelastic crystals exhibit mechanical hysteresis between the stress and strain caused by stress-induced movement of domain walls. Martensites also are internally twinned, but mechanical stress causes phase changes and domain wall movements.

Typically, these materials are partially ordered as they undergo transition from a body-centered cubic structure to a partially ordered CsCl structure (Figure 7). The shape-memory effect takes place at a martensitic transformation from the CsCl-like structure into a distorted multidomain martensite phase. Under stress, the martensite deforms easily; when reheated, it returns to the original morphology of the high-temperature structure.

Single-phase smart materials

Most of the best actuators are primary ferroics. These ferroelastic, ferromagnetic, or ferroelectric solids are poised on an instability, often with two or more phase changes involved. PZT is cubic at high temperatures and is poised on a tetragonal–rhombohedral phase boundary. Partially ordered PMN is poised on a cubic–rhombohedral transition. The shape-memory alloys also are partially ordered and are poised on a martensitic phase transformation. Magnetostrictive Tb–Dy–Fe alloys are cubic at high temperatures and are operated at a rhombohedral–tetragonal spin reorientation.

In addition to the four materials that we discuss here, other kinds of actuators are under development. Field-induced phase transitions in modified lead zirconate ceramics involve transitions among paraelectric, antiferroelectric, and ferroelectric phases. Two phase transitions also are involved in photostrictive materials (in which electrical and mechanical characteristics change under illumination) and in chemostrictive materials such as human muscle (which consists of partially hydrated polymeric systems in which phase transitions take place in the polymer and in the surrounding sheath of water molecules during actuation).

Functional composites

Composite materials, another approach to actuation and sensing, are closer to our own interests. So far, we have described materials that are single-phased—at least at high temperatures. Another approach to making smart materials is to bring together two or more materials, each of which has an associated phase transition. For example, in our transducer program, we combine polymeric materials (which have phase transitions in which the elastic properties undergo large changes) and ferroelectric materials (in which the dielectric properties have an associated instability). Because the two materials have different kinds of instability, we can build up structures that are especially good for sensing and actuating (*4*).

In working with this family of functional composites, we do not have to optimize all of the tensor coefficients—only those that appear in the figure of merit. Thus, we

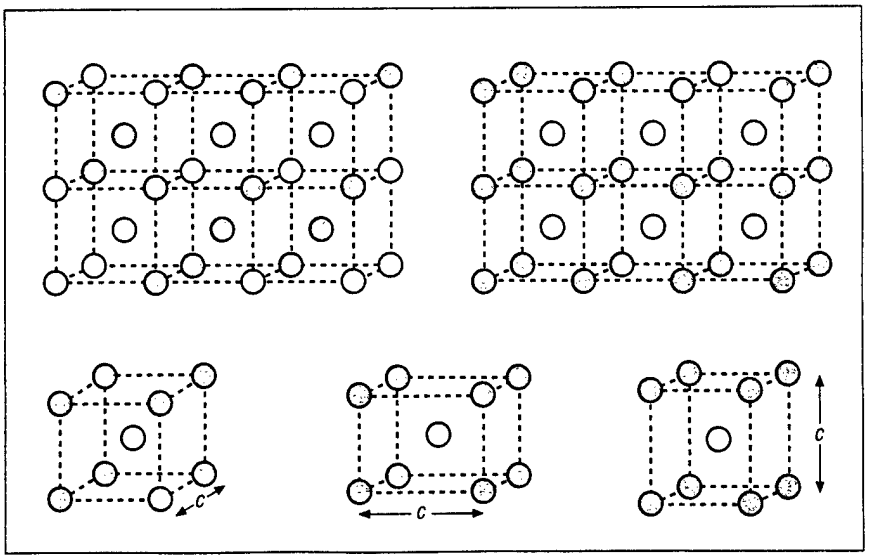

***Figure 7.* Body-centered binary intermetallics often show a structural transformation from a high-temperature, disordered body-centered cubic phase** (top left, space group *Im*3*m*) to an ordered austenite phase with the CsCl structure (top right, space group *Pm*3*m*). At lower temperatures, a second phase transition takes place from an austenite structure to a twinned martensite phase, pictured here (bottom) as three variants of a body-centered tetragonal phase (space group *P*4/*mmm*, unique axis *c* indicated with arrows). Different domains in the material adopt these structure variants. When the domain walls move under applied stress, reversible strain is produced. Adapted from Ref 4. Used by permission.

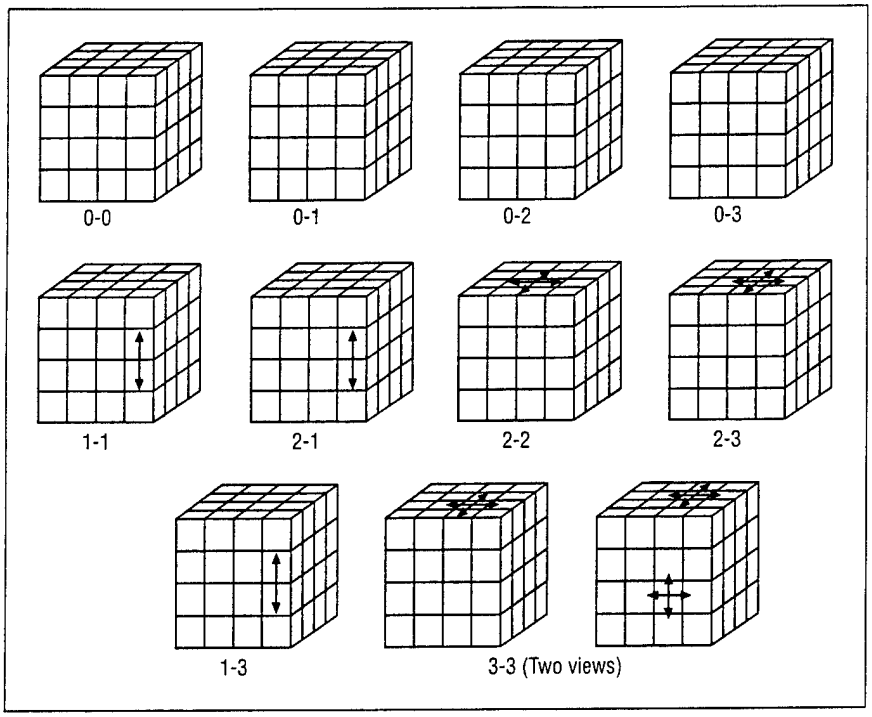

***Figure 8.* Connectivity patterns used in composite smart materials.** By arranging two materials in series and parallel patterns, internal stress and field distributions can be optimized to improve device performance. The directions of connectivity are indicated by arrows. Adapted from Ref 4. Used by permission.

have built different connectivity patterns (Figure 8) into these materials by using electrically soft materials (ferroelectrics) that have high dielectric constants and electrically hard materials (polymers) that have very low dielectric constants. Although the polymers are electrically hard, they are mechanically soft; compliance coefficients are several orders of magnitude larger than those of ceramics. Using the connectivity patterns in Figure 8, we build up parallel and series connections that optimize particular combinations of tensor coefficients.

Composite materials are used in many structural applications, but their use in the electronics industry has been limited. As the advantages and disadvantages of composite sensors and actuators become better understood, we expect this picture to change. Composite electromechanical transducers offer many advantages over single-phase transducers (see box, ***Composite electromechanical vs single-phase transducers***).

Better microphones can be made by reducing acoustic impedance. Acoustic impedance can be reduced by partially replacing ceramics with a soft polymer that better couples the transducer vibrations to water and to human tissue (i.e., eardrums). Inserting electrodes inside the transducers lowers the drive voltage, improves sensitivity to hydrostatic waves, and enlarges displacements. Composite transducers illustrate a very general approach that applies to not only piezoelectric materials but also many other functional composites.

Composite piezoelectric transducers (Figure 9, page 46) have been manufactured and tested in our laboratory during the past two decades. These functional composites incorporate several underlying ideas, including

- connectivity patterns that lead to field and force concentration;
- use of periodicity and scale in resonant structures;
- symmetry of a composite structure and its influence on physical properties;
- polychromatic percolation and coupled conduction paths;
- varistor action and other interfacial effects;
- sum, combination, and product properties;
- coupled phase transformation phenomena; and
- the important role that porosity and inner spaces composites play in many functional composite materials.

Up to now, we have discussed primarily piezoelectric transducers with electromechanical sensing and actuating functions. However, the idea of smart materials is much more general (Figure 10, page 46). There are many types

Composite electromechanical vs single-phase transducers

Composites offer

- Reduced acoustic impedance; better coupling to water and human tissue
- Lower drive voltage with internal electrodes
- Improved sensitivity to hydrostatic waves
- Larger displacements for a given electrical stimulus
- Acoustic isolation of adjacent sound sources
- Passive and active vibration absorption
- Improved high-frequency performance with smaller active regions
- Mechanical strength and flexibility
- Backing layers to absorb unwanted vibrations
- Reduced hysteresis
- Internal stresses and field rearrangements optimized to the direction that produces the most motion
- Improved breakdown strength
- Tuned coupling coefficients, permittivity, and elasticity
- Beam-forming capability
- Rapid ring-down, that is, rapid vibration damping (important in pulsed-sound applications, including biomedical ultrasound)

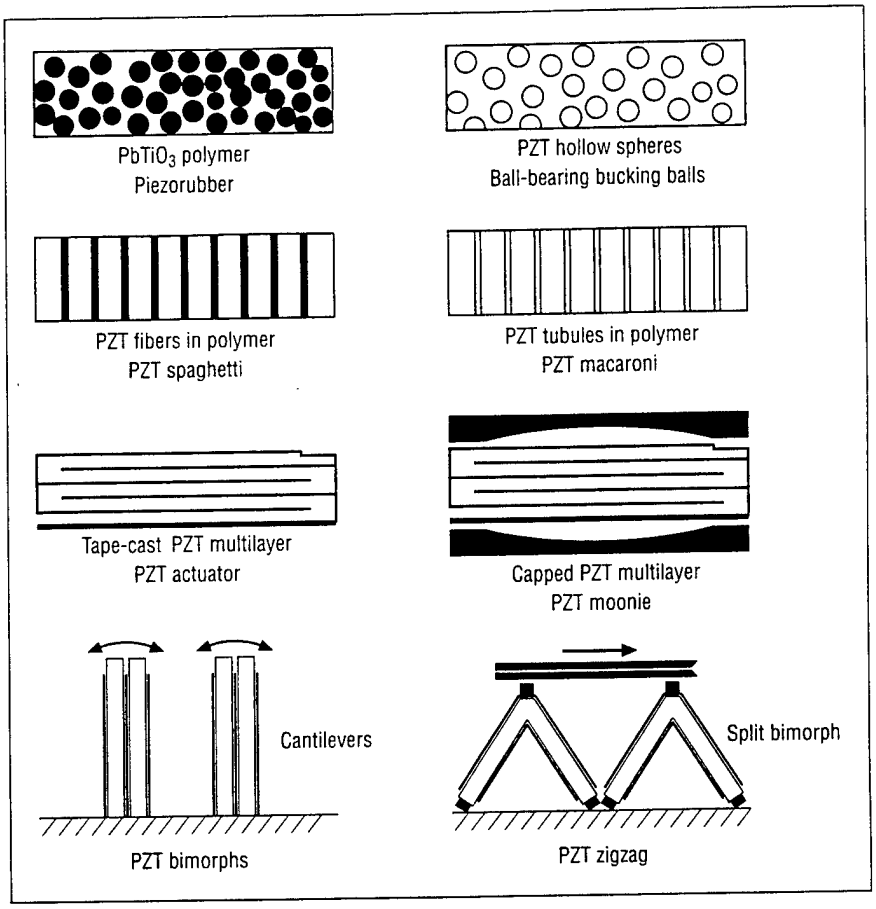

***Figure 9.* Piezoelectric composites for use as sensors, actuators, and transducers.** Bucking balls exhibit sudden changes in shape when an electric field is applied. A moonie is a disc-shaped transducer, and this is an edge-on view. Adapted from Ref 4. Used by permission.

of sensors, actuators, and feedback circuits.

Many such sensors and actuators can be fabricated in the form of a multilayer ceramic package. Multilayer packages originally consisted of low-permittivity dielectric layers, interconnected through metallized structures called "via holes", with metal circuitry printed on each layer. Buried capacitors and resistors have been added to the three-dimensional packages. Smart sensors, adaptive actuators, and display panels—with thermistors and varistors to guard against current and voltage overloads—continue to be developed.

Putting instability to work

Two transformations are involved in most of these smart materials. Because these materials often are primary ferroics (ferroelastic, ferroelectric, or ferromagnetic), they have domain wall motions that assist in the sensing and actuating processes. The ferroics are operated near an instability to make these domain walls—and their associated dipoles and strains—movable. We identify three kinds of commonly used actuator materials (and others appear to be possible):

- In the first kind, as in PZT or Terfenol, Curie temperature is high, and the actuator is operated near an orientational change of the electric or the magnetic dipole moment.
- The second kind involves a partially ordered phase, as in electrostrictive PMN or the shape-memory alloys. These materials are operated near a diffuse phase transition with two coexisting phases: the high-temperature or austenite-like phase and the low-temperature or martensitic-type phase.
- The third kind involves composite materials with coupled phase transformations. For example, piezoelectric ceramic fibers embedded in elastomers can be used to make biomedical transducers. The fibers produce sound waves, and the elastomer adjusts the acoustic impedance. This reduces sound reflection at the interface between the trans-

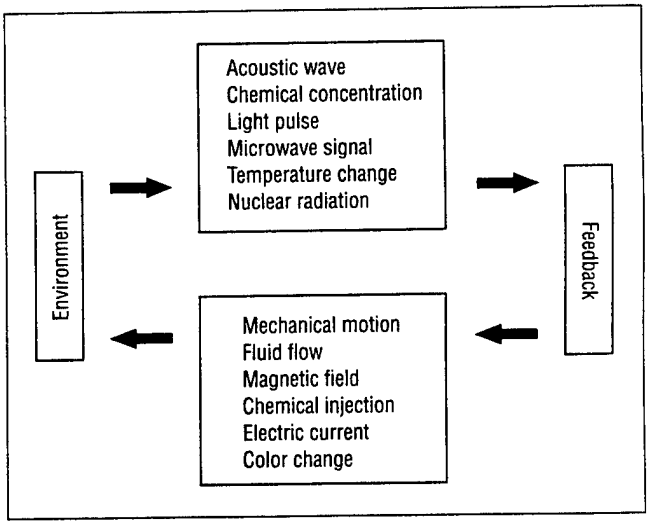

***Figure 10.* Possibilities for smart electroceramic packages.** Smart devices may bring together many different sensor–actuator combinations. Adapted from Ref 5. Used by permission.

More to come

Marie-Paule Pileni discusses magnetic nanosized alloys and composites in the February 2000 issue of *Chemical Innovation*. For those of us who are a little rusty on our p-chem, she gives a tutorial on the basic concepts of magnetism, including the domain wall motion and anisotropy effects discussed in this article.

ducer and the biological tissue, allowing more efficient penetration of the acoustic waves into the tissue.

The underlying reasons for the material choices are fairly obvious. Why use primary ferroics? Because small external fields or forces, whether they are strains, electric dipoles, or magnetic dipoles, can be used to produce large responses. Why use a cubic prototype phase? Because the symmetry of cubic phases produces many equivalent orientation states, making it unnecessary to grow single crystals and allowing us to use polycrystalline materials instead. Why is partial ordering advantageous? Because it provides many nucleation sites for generating a diffuse phase transformation. Why operate materials near a morphotropic transition? Because the instability ensures persistent disequilibrium over a wide range of temperatures.

By imitating sensor, actuator, and analyzer mechanisms already used by living organisms, it may be possible to build systems and devices that mimic the functions of life itself. If motion sensors, audio receivers, and microphones are artificial eyes, ears, and voices, can artificial minds be far behind?

References

(1) Dyson, G. *Darwin Among the Machines;* Perseus Books: Reading, MA, 1997.
(2) National Research Council. *Microelectromechanical Systems;* National Academy Press: Washington, DC, 1997.
(3) Uchino, K. *Piezoelectric Actuators and Ultrasonic Motors;* Kluwer Academic Publishers: Boston, MA, 1997.
(4) Newnham, R. E. *Mater. Res. Soc. Bull.* **1997,** *22,* 20–34.
(5) Newnham, R. E. *Bull. Am. Ceram. Soc.* **1996,** *75* (10), 51–59.

Robert E. Newnham is a professor of solid-state science at Pennsylvania State University (814-865-1612; bobnewnham@psu.edu). He pioneered the development of composite piezoelectric transducers, and his work in ferroelectric materials is known worldwide. A member of the National Academy of Engineering and the International Academy of Ceramics and an honorary lifetime member of the American Ceramic Society, he has written or co-written more than 500 research papers, 4 books, and 15 patents. Newnham received a Ph.D. in physics from the Pennsylvania State University and a Ph.D. in crystallography from Cambridge University.

Ahmed Amin worked with Dr. Newnham while he was a senior visiting scientist at the Materials Research Laboratory at Pennsylvania State University. Previously, he was a senior member of the technical staff at Texas Instruments Inc. (1980–1998), where he worked in the development of thermistors, pyroelectric imaging for night vision applications, and automotive and commercial sensor technologies. He has published 43 research papers, 3 book chapters, and 2 patents.

BOOK ALERT

Short treatments of longer works

Marc C. Fitzgerald

How the experts would improve innovation

Scientists and managers who are interested in R&D policy will find *Investing in Innovation: Creating a Research and Innovation Policy That Works* worth reading. This compendium of viewpoints, based on the government report, *Investing in Innovation: Toward a Consensus Strategy for Federal Technology Policy*, comes at a time when investments in science, basic engineering, and education have never been more important. The editors, Lewis M. Branscomb and James H. Keller, have assembled a hard-hitting contribution to the debate over the proper role of government in the nation's science and technology policy.

Investing in Innovation is presented in three parts. It begins with an examination of the technology policy that the Clinton administration issued in 1993. The statement was the logical culmination of more than 20 years of debate on how the United States should respond to the challenge of foreign competition in high-technology industries and the investments of foreign governments in support of national innovation initiatives. The second part of the book assesses seven specific technology programs promoted by the Clinton–Gore administration as a result of the aforementioned report, which was presented at the annual colloquium of the Americans Association for the Advancement of Science in April 1997. The third part focuses on moving the debate beyond partisanship and determining how new policy tools can be used as a basis for federal activity. In the last chapter, the editors have compiled six principles for policy makers in support of research and innovation: encourage private innovation, emphasize basic technology, facilitate access to new and old technologies, use all policy tools (not just R&D), leverage globalization of innovation, and improve government effectiveness in policy development.

Most of the authors are academicians in public policy and economics, but there is also representation from private nonprofit organizations and independent consultancies.

MIT Press: Cambridge, MA, 1998 (hard), 1999 (paper); 516 pages; ISBN 0-262-02446-2; $38.50 and $20.00, respectively. To order, call 800-356-0343.

TRANSDUCER STUDIES

3-D Acoustic Probes

APPENDIX 46

Development of a velocity gradient underwater acoustic intensity sensor

Kevin J. Bastyr[a] and Gerald C. Lauchle
The Pennsylvania State University, Graduate Program in Acoustics, State College, Pennsylvania 16802

James A. McConnell
The Pennsylvania State University, Graduate Program in Acoustics, State College, Pennsylvania 16802 and Acoustech Corporation, P.O. Box 139, State College, Pennsylvania 16804

(Received 29 March 1999; revised 29 July 1999; accepted 3 September 1999)

A neutrally buoyant, underwater acoustic intensity probe is constructed and tested. This sensor measures the acoustic particle velocity at two closely spaced locations, hence it is denoted a "***u-u***" intensity probe. A new theoretical derivation infers the acoustic pressure from this one-dimensional velocity gradient, permitting the computation of one component of acoustic intensity. A calibration device, which produces a planar standing-wave field, is constructed and tested. In this calibrator, the performance of the ***u-u*** intensity probe compares favorably to that of an acoustic intensity probe which measures both pressure and velocity directly. © *1999 Acoustical Society of America.* [S0001-4966(99)05312-6]

PACS numbers: 43.30.Xm, 43.30.Yj, 43.58.Fm [DLB]

INTRODUCTION

Acoustic intensity is a measure of the magnitude and direction of acoustic energy transport. Quantitatively, intensity is the period averaged product of acoustic pressure and acoustic particle velocity at a single point.[1] Fahy[2] shows that intensity is the product of the complex acoustic pressure, p, and the complex conjugate of the acoustic particle velocity, $\mathbf{u}^*$:

$$\mathbf{I}=\frac{1}{t}\int_0^t \mathrm{p}(t)\mathbf{u}(t)dt=\frac{1}{2}\mathrm{p}\mathbf{u}^*. \tag{1}$$

Intensity is a vector quantity: there is a direction associated with it. As a vector quantity, it provides physical information that scalar acoustic pressure simply cannot. In a complex sound field, i.e., one having multiple sound sources, an acoustician measuring intensity will be able to quantify the sound power radiated from each source. The vector nature of intensity also enables the location of individual acoustic sources to be determined by simple triangulation.

In the late 1970's Chung[3] developed the cross-spectral formulation of the two microphone, or *p-p*, technique. Basing his formulation on the linearized Euler's equation, Chung showed that intensity is proportional to the cross spectrum between two pressure microphones. Chung's technique, along with FFT analyzers and microphones with approximately matched phases, marked the beginning of reliable intensity measurements. In 1991, Ng[4] extended the *p-p* intensity measurement technique to underwater environments. In 1995, McConnell *et al.*[5] invented an underwater acoustic intensity sensor that uses a pair of velocity sensors. This ***u-u*** intensity probe is quite similar in principle to the *p-p* probe.

The first section of this paper deals with the issues fundamental to the operation of the ***u-u*** intensity probe. In the second, the theory and procedures used to calibrate the ***u-u*** intensity probe are presented. Verification of the calibration's accuracy is then accomplished by comparing intensity measurements made by the ***u-u*** probe to those made by a *p-u* probe,[6,7] a device that directly measures both particle velocity and pressure.

I. VELOCITY GRADIENT INTENSITY

Measurements of intensity in a single dimension are commonly obtained from a pressure gradient. This technique uses the linearized Euler's equation and a finite difference approximation to infer velocity from the pressure gradient measured by two pressure sensors.[2] In this paper, a new technique invented by McConnell *et al.*[5] will be used to infer pressure from the velocity gradient measured by two acoustic velocity sensors.

The linearized equation of continuity,[1] a statement of conservation of mass in a fluid, indicates

$$\frac{\partial \rho}{\partial t}+\rho_0(\nabla\cdot\mathbf{u})=0, \tag{2}$$

where $\mathbf{u}$ is the particle velocity, and ρ_0 is the ambient fluid density. The instantaneous density, ρ, is related to the acoustic pressure, p, through the equation of state. Hence, Eq. (2) takes the form

$$\frac{\partial p}{\partial t}+c^2\rho_0(\nabla\cdot\mathbf{u})=0. \tag{3}$$

Assuming time harmonic quantities and solving for acoustic pressure yields

$$p=\frac{j\rho_0c^2}{\omega}(\nabla\cdot\mathbf{u}), \tag{4}$$

where ω is the radian frequency of the acoustic wave and c is the speed of sound in the fluid. A finite difference approximation to the velocity gradient yields

[a]Electronic mail: zabour@sabine.acs.psu.edu

 0001-4966/99/106(6)/3178/11/$15.00

$$p \approx \frac{j\rho_0 c^2}{\omega}\left[\frac{\Delta u_x}{\Delta x}+\frac{\Delta u_y}{\Delta y}+\frac{\Delta u_z}{\Delta z}\right], \tag{5}$$

where Δu_x is the difference of the x-component of acoustic particle velocity between two locations separated by a distance Δx (similar definitions apply in the y and z directions). It is apparent that pressure depends upon the components of velocity in all three directions. Thus in a three-dimensional acoustic field, all three components of velocity at each of two locations are required to measure the acoustic pressure. However, if the acoustic field is one-dimensional, as in this experimental investigation, a measurement of pressure can be obtained from two single-dimensional velocity sensors. The velocity at the mid-point between these sensors is approximated by the average of the two known velocities. Therefore, the z-component of Eq. (1) takes the form

$$I_z = \frac{j\rho_0 c^2}{2\omega\Delta z}[u_2 - u_1][u_2^* + u_1^*]. \tag{6}$$

Multiplying out the bracketed terms, and noting that $u_1 u_2^* = G_{12}$, the cross-spectrum of u_1 and u_2, Eq. (6) becomes

$$I_z = \frac{j\rho_0 c^2}{2\omega\Delta z}[G_{22} + G_{21} - G_{12} - G_{11}]. \tag{7}$$

Next, the total intensity is separated into its two constituent parts—active intensity and reactive intensity. The active and reactive components of intensity are the real and imaginary parts of Eq. (7), respectively. Pressure and velocity are entirely in-phase for active intensity, implying both a *net* transport of acoustic energy, and a nonzero time average. The presence of a local active intensity does not infer that energy is being transported throughout an extended region of the field. For reactive intensity, the pressure and velocity are out-of-phase. Therefore, reactive intensity has a zero time average and corresponds to local *oscillatory* transport of energy.[2] Note that in practice, an acoustic field that is either purely active, or purely reactive cannot exist.

The derivation of an expression for active intensity begins with the real part of Eq. (7). Since auto-spectra are purely real quantities, that expression becomes

$$I_z^a = \frac{\rho_0 c^2}{2\omega\Delta z}\mathrm{Re}[jG_{21} - jG_{12}]. \tag{8}$$

Substituting G_{12}^* for G_{21} and separating the cross-spectra into their real and imaginary components produces the final form:

$$I_z^a = -\frac{\rho_0 c^2}{\omega\Delta z}\mathrm{Im}[G_{12}]. \tag{9}$$

In a similar manner, a simplified form for the reactive component of intensity can be derived; starting with the imaginary part of Eq. (7),

$$I_z^r = \mathrm{Im}\left[\frac{j\rho_0 c^2}{2\omega\Delta z}[G_{22} + G_{21} - G_{12} - G_{11}]\right]. \tag{10}$$

Separating the cross-spectra into their real and imaginary parts and canceling like terms produces the final form:

$$I_z^r = \frac{\rho_0 c^2}{2\omega\Delta z}[G_{22} - G_{11}]. \tag{11}$$

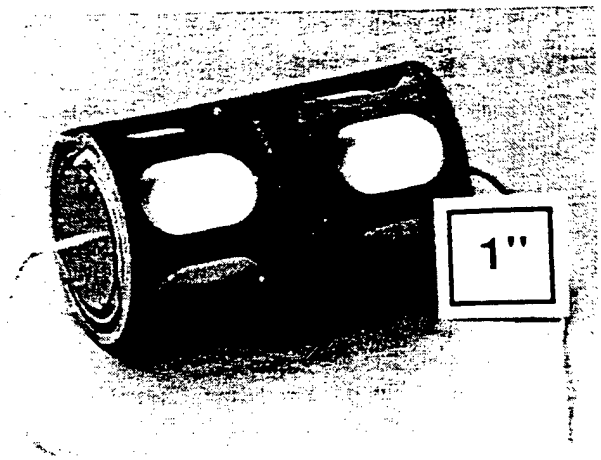

FIG. 1. The velocity gradient, or *u-u*, intensity probe.

As a final note, this development is based on the linearized equation of continuity; thus, the validity of the equations presented is limited to the regime of linear acoustics. In addition, Eqs. (6)–(11) are valid only in one-dimensional acoustic fields.

II. INTENSITY PROBE DESIGN

The *u-u* probe, as described by McConnell *et al.*,[5] is a single axis intensity sensor consisting of two moving coil velocity sensors in two separate, coaxially oriented cylindrical bodies. The velocity sensors in this design, GeoSpace GS-14-L3 geophones,[8] are located in the geometric center of each cylinder. The velocity sensor bodies are neutrally buoyant, meaning that their density is substantially equal to the ambient density of the surrounding fluid medium. The coaxial orientation of the sensor bodies is maintained by suspension springs which connect the ends of each body to a free flooding, acoustically transparent support structure, as illustrated in Figs. 1 and 2. The suspension springs have a high radial stiffness and an extremely low axial stiffness to facilitate the positioning of the sensor without adversely influencing its dynamics.

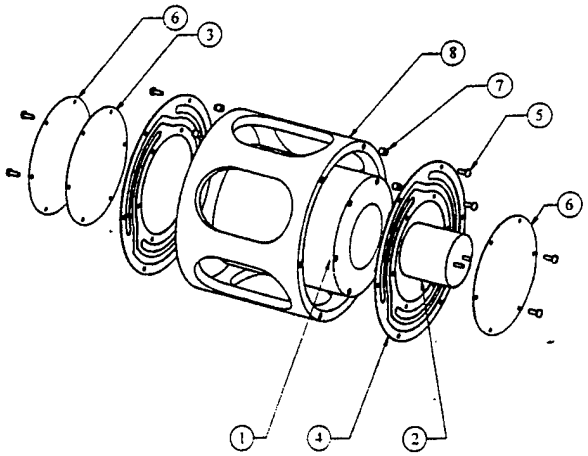

FIG. 2. An exploded view of a single velocity sensor body and its suspension system. 1 is the syntactic foam body, 2 is the geophone, 3 is μ-metal which minimizes magnetic cross-talk, 4 is a suspension spring, 5 are screws, 6 are ballast disks, 7 are inserts, and 8 is the support tube.

A. Fundamentals

Moving coil sensors such as the geophone are primarily used by geophysicists to measure the low frequency movement of the Earth's surface. However, there are distinct advantages to employing geophones as underwater sensors. Geophones have one of the highest signal-to-noise ratios of currently existing transducers, and in comparison to piezoelectric devices, they have a very high receiving sensitivity. In addition, due to their low output impedances, geophones can drive impressive lengths of signal cable without preamplification.

The transducing elements in a geophone consist of a permanent magnet running through the center of the geophone case, and a coil of wire around a spindle. The spindle is constrained by springs to move along the length of the bar magnet. The physics governing the transduction of a geophone is that $e=Blv$. The voltage, e, induced across the ends of the geophone's moving coil equals the product of the transduction coefficient, Bl, and the relative velocity, v, between the coil and the bar magnet running through it.[9]

The mechanical elements of a geophone impose limits on its direct measurement of velocity. The resonance frequency of the geophone is set by its mass-spring system, consisting of the moving coil-spindle and the springs that position it along the bar magnet. For mechanical excitation at frequencies above this resonance frequency, the coil remains virtually motionless while the geophone oscillates around it.[7] Under these conditions, the output voltage of the geophone is proportional to the case velocity. Below the resonance frequency, the output of the geophone is proportional to jerk, acceleration's time rate of change.

For the geophone's output voltage to be proportional to the acoustic particle velocity, the geophone's velocity must equal the acoustic particle velocity. This can only be achieved if the density of the sensor body matches that of the ambient fluid medium.[10,11] This condition, known as neutral buoyancy, exists when an object submerged in a fluid neither floats nor sinks. For moving coil sensors, the desired condition is dynamic neutral buoyancy (DNB); i.e., when the dynamic (moving) density of a body matches that of the fluid medium. As previously discussed, for excitation at frequencies above the geophone's resonance frequency, the proof mass remains essentially motionless; therefore, a geophone's dynamic density is less than its static density.

For the GS-14-L3 geophone to become neutrally buoyant, it must be imbedded in a substantially larger volume of positively buoyant material. Syntactic foam, a composite of epoxy binder[12] and tiny hollow glass spheres called microballoons,[13] is such a material. To obtain foam of very low density, a mixture of 4 parts microballoons to 1 part epoxy binder is used. When the foam has cured, it is machined to allow insertion of a geophone into the geometric center of the body. Due to the foam's low density of $\approx$0.5 g/cc, the length of a 3.80 cm diameter neutrally buoyant right circular cylinder is less than 5 cm. For the calculation of the cylinder's exact length, the masses of all the sensor's components must be known. Table I outlines the mass and volume of each component in a single velocity sensor body, which is illustrated in Fig. 2.

TABLE I. The masses and volumes of the *u-u* probe's constituent parts. Note that SNB denotes static neutral buoyancy, and DNB denotes dynamic neutral buoyancy.

Component	Mass (g)	Volume (cc)
Foam cylinder	22.7	45.5
Geophone	18.3	3.82
μ-metal	1.43	0.232
Springs (2)	1.82	0.177
Fasteners	0.053	0.006
Ballast for SNB	6.10	0.695
Subtotal	50.4	50.4
Ballast for DNB	2.43	0.276
Total	52.9	50.7

To achieve neutral buoyancy, even the effective mass of the suspension springs must be accounted for. To first order, the moving mass of a cantilever-type spring in a simple harmonic oscillator is equivalent to one quarter the moving mass of the spring.[14]

To test for neutral buoyancy, the sensor body is submerged in water. If the sensor neither sinks nor floats, it is statically neutrally buoyant. Testing indicated that a 1% deviation from neutral buoyancy was observable. That is, if the total sensor mass was 1% lower (or higher) than that of a neutrally buoyant body, the sensor would float (or sink). To achieve dynamic neutral buoyancy, the sensor body is ballasted with a mass equal to the geophone's proof mass, without displacing any additional volume. In practice it is easier to add mass in the form of ballast disks, as in Fig. 2. As these disks displace volume, a mass equal to the proof mass plus the mass of water displaced by the ballast disk is added, as listed in Table I.

B. Suspension system

The suspension system consists of two elements: a support tube and two beryllium copper springs. The support tube was machined from nylon-6, a material that exhibits an acoustic impedance substantially equal to that of bulk water. The suspension springs, which are illustrated in Figs. 1 and 2, serve two primary functions: maintaining the coaxial orientation of the sensor bodies and isolating the sensors from any vibration in the structure to which the *u-u* probe is mounted. Due to the springs' high radial stiffness and extremely low axial stiffness, the sensor body is "free" to move in the axial (sensing) direction, but has no excursion in the radial direction.

The suspension springs were photo-etched from 0.20 mm (8 mil) beryllium copper shim stock. These springs are similar in design to those used to support the proof mass in typical geophones. However, they have two subtle differences: the suspension springs are larger and have two bolting rings. The bolting rings allow the springs to be connected to both the support tube and the sensor body. The springs are fastened using 00-90 screws and threaded press-fit inserts as shown in Fig. 2.

The suspension springs' design gives the sensor mass-spring system a sufficiently low resonance frequency that the suspension dynamics do not adversely affect the probe's performance. Modeling the spring as a cantilever beam allows

the theoretical prediction of its resonance frequency. This model rests on several assumptions. First, the mass of the sensor body is approximated as a point mass at the end of the cantilever beam. Further, the slightly curved cantilevers are modeled as straight beams. This approximation is valid because the amplitude of the beams' deflection is small compared to their overall length. Note that each of the six spring members (i.e., three per spring) support one-sixth the sensor's total mass. The theoretical resonance frequency of the probe-suspension system is 6.28 Hz, as calculated using equations from Thomson.[15]

The resonance frequency of the probe-suspension system was experimentally measured underwater. An underwater source acoustically excited a single probe body's geophone, while a hydrophone was used as a reference transducer. The probe-suspension system resonance frequency was determined from the frequency response measured between the two transducers to be (6.13 ± 0.05) Hz. The Q of the probe-mass/suspension-spring resonance is approximately 15, and the system's resonance frequency is substantially lower than that of the geophone (28 Hz). Accordingly, the phase and amplitude errors introduced at frequencies above the geophone's resonance are negligible.[7]

C. Performance issues

The distance separating the acoustic centers of the velocity sensors determines the upper frequency of operation. This distance also affects the amount of undesirable interaction between the sensor bodies. This cross-talk between the sensors manifests itself in three forms: structural, magnetic, and hydrodynamic.

The upper frequency limit of the ***u-u*** intensity probe is defined as the frequency at which a 10% (1 dB) bias error occurs in the estimation of acoustic intensity. A bias error is the difference between the measurement of a quantity, and the quantity's true value. In this case, the bias error results from using a finite difference approximation of the velocity gradient in Eq. (5). Following Fahy's[2] bias error derivation for *p-p* intensity probes exposed to a plane wave field, the normalized bias error in the ***u-u*** probe's estimation of pressure and velocity are

$$\epsilon_b[p] = \frac{\sin(k\Delta z)}{k\Delta z} - 1, \text{ and } \epsilon_b[u_z] = \cos(k\Delta z) - 1, \tag{12}$$

where $k = \omega/c$. Forming the normalized bias error of the intensity estimate, and making a Taylor series expansion[16] yields:

$$\epsilon_b[I_z] \approx -\tfrac{2}{3}(k\Delta z)^2 + \tfrac{1}{20}(k\Delta z)^4. \tag{13}$$

The lower frequency limit of the probe is effectively set by the phase mismatch between the two sensors. Of course, the majority of the phase mismatch can be removed through proper calibration, as will be shown later.

In addition to the finite difference error, the sensor spacing also affects the amount of cross-talk between the sensors. Magnetic coupling can occur between two geophones in close proximity, as in the ***u-u*** probe. Relative motion between the magnet of one geophone and the coil of the second will induce an undesirable current in that second coil.

Hydrodynamic coupling between the sensor bodies occurs when slight deviations from neutral buoyancy alter the bodies' velocity from that of the acoustic particle velocity. This nonideal movement of one sensor body disturbs the acoustic field sensed by the second body. Due to their design, the suspension springs may also entrain mass, and contribute to hydrodynamic coupling. The suspension springs employed in the ***u-u*** intensity probe are attached to both the moving probe bodies, and the stationary structural support tube. The spring members are neither stationary nor moving with the acoustic particle velocity; therefore, there is mass entrained with the springs' motion.

The mechanical connection between the sensor bodies (via the support tube) gives rise to the possibility of undesirable vibrational coupling between them. However, the vibration isolation provided by the suspension springs renders this negligible.[17]

To ensure the proper operation of the ***u-u*** probe, the contributions of all these coupling mechanisms occurring in typical operating conditions must be measured. Accordingly, a scenario to simulate these conditions was devised. The coil of one geophone is electrically driven to simulate the motion (effective acoustic velocity) that would occur if the ***u-u*** probe were subjected to an acoustic plane wave field of amplitude 150 dB *re*: 1 μPa. The voltage induced (in the second geophone) by the combined magnetic and hydrodynamic coupling can be adjusted by the geophone's receiving sensitivity, providing an "effective velocity due to coupling." This velocity can then be compared to the effective acoustic velocity in order to quantify the extent of the coupling.

In water, a plane wave with an amplitude of 150 dB *re*: 1 μPa corresponds to an effective plane wave particle velocity of 2.1×10^{-3} cm/s. A GS-14-L3 geophone with known sensitivity was driven with a broadband signal equivalent to 150 dB *re*: 1 μPa in each frequency analysis bin.

In this measurement, one body was driven electrically at the aforementioned level, and the motion induced in the other body was measured. This test was performed in water so that the combined hydrodynamic and magnetic effects could be compared to in-air test results, which essentially measured only the magnetic effects. Figure 3 illustrates these velocities normalized by the effective acoustic velocity. The velocity induced by these coupling mechanisms is at most 25 dB below the acoustic disturbance of interest (the effective 150 dB *re*: 1 μPa plane wave). Therefore, the effects of the coupling mechanisms are considered to be insignificant.

III. CALIBRATION FACILITY

Calibrating an acoustic intensity sensor underwater is a formidable challenge. Standard underwater intensity and velocity transducers do not exist at this time, so a relative calibration is impossible. Simply attaching an accelerometer to each sensor body is initially an attractive option; however, this adds mass to the body, causing deviations from neutral buoyancy. Further, it can provide no indication of whether or not the probe body's velocity matches the acoustic particle velocity. Calibration in air, where velocity sensors are avail-

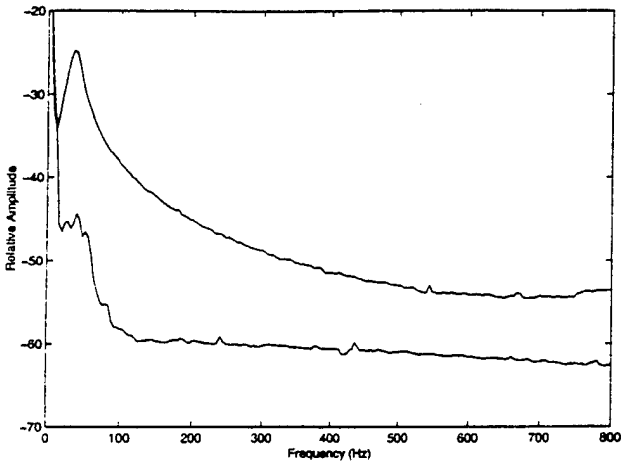

FIG. 3. The ratio of the hydrodynamicly and magneticly induced velocity relative to the effective acoustic velocity, the 150 dB *re*: 1 μPa plane wave. The upper and lower curves are in water and in air, respectively.

able in the form of hot wire anemometers, is not an option, because the sensor bodies are not neutrally buoyant in air.

A reasonable option for a transducer to employ in an underwater comparison calibration is a hydrophone. The use of a hydrophone in a relative calibration relies on knowledge of the phase relationship between pressure and velocity in the acoustic field. The ideal calibration would take place in a progressive plane wave field, where the phase between pressure and velocity is 0°. Such fields are difficult to achieve, even in a laboratory setting. A standing plane wave field, where the pressure and velocity are 90° out-of-phase, offers an alternative option for calibration. This is perhaps the harshest field in which to perform a calibration, due to the presence of pressure and velocity nodes. However, this type of field can be created in the laboratory, which is a benefit outweighing its numerous detriments.

A. Description of the slow wave calibrator

The slow wave calibrator (SWC) developed in this research is a vertically oriented, water filled, elastic walled, one-dimensional waveguide. The SWC is illustrated in Fig. 4. A piston sound source is located at the lower end, while the opposite end is an air–water interface. The 20.3 cm diameter cylindrical acrylic wall of the SWC is 1.22 m tall, and has a thickness of 0.64 cm. A USRD J9 source,[18] with a piston diameter of 7.5 cm, acts as the sound source for the SWC. The acoustic standing waves in the SWC depend on the acoustic reflection from the water–air interface, which is a pressure-release boundary. Accordingly, the phase between pressure and velocity at any axial location in the SWC is 90°.

One advantage a SWC has over a rigid walled calibrator is that the phase speed of the fluid inside the elastic walled SWC is substantially reduced from that in the bulk medium.[19,20] This decreased phase speed dramatically shortens the wavelengths, and the accuracy of low frequency measurements made by the ***u-u*** probe is improved by lessening the influence of transducer phase mismatch. This advantage may be offset by an increase in the finite difference error given by Eq. (13).

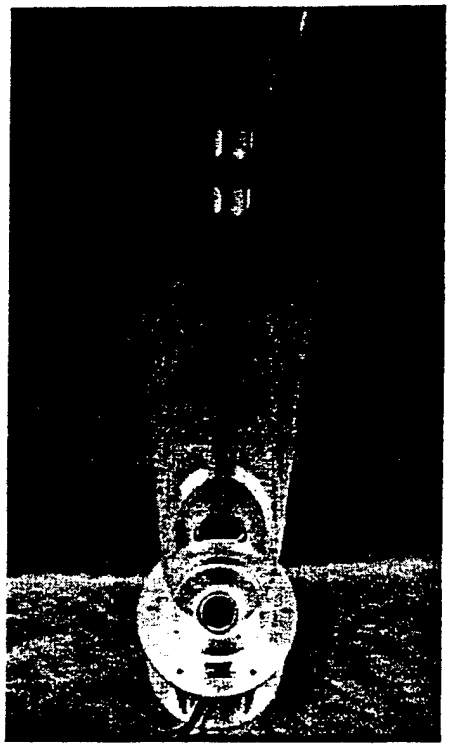

FIG. 4. The slow wave calibrator with the *u-u* intensity probe and reference transducers suspended from above. Note that the two cables attached to the USRD J9 source are for the electrical driving signal and the driver's hydrostatic pressure compensation.

B. SWC acoustic performance

The acoustic waveguide nature of the SWC largely contributes to the planarity of the wavefronts. Detailed mapping of the cross section of the SWC with a hydrophone found the wavefronts were to be planar within 1 dB from 28 Hz to 850 Hz in the section used for sensor calibration.

The longitudinal sound speed in the SWC dictates two important parameters of the facility: the modal resonance frequencies, and the plane-wave cutoff frequency. The phase speed of acoustic waves in a fluid medium is proportional to the square root of an elastic modulus. In a large body of fluid, the relevant quantity is the bulk modulus. However, the elastic vessel constraining the fluid in the SWC contributes the majority of the system's compliance. Consequently, the effective sound speed, c_{eff}, in an elastic-walled waveguide[20] is given by

$$c_{\text{eff}} = \sqrt{B \Big/ \rho_0 \left(1 + \frac{2r\rho_0 c^2}{tE}(1-\nu^2) \right)}. \tag{14}$$

where B is the bulk modulus of the fluid, ρ_0 is the density of the fluid, r is the inner radius of the duct, c is the bulk phase speed of sound, t is the thickness of the duct wall, E is Young's modulus of the wall material and ν is the Poisson's ratio of the wall material. Using Eq. (14), the theoretical phase speed, c_{eff}, in the SWC is (290 ± 10) m/s. The uncertainty is due to the variance in the acrylic wall's Young's modulus, as specified by the manufacturer.[21]

This theoretically determined sound speed was verified experimentally by two independent measurements. The first was to ensonify the SWC at its resonance frequencies and measure the distance between adjacent nodes. The steep pressure gradient around each node improves the accuracy with which an axially scanned hydrophone can locate each pressure minimum. The distance between two adjacent pressure minima corresponds to a half wavelength of the driving frequency. The nodes of three resonance frequencies of the SWC were measured, and basic acoustics[22] (i.e., $c=f\lambda$) indicated that the sound speed was (355 ± 8) m/s, which is less than one-quarter the bulk speed in water. Note that within the uncertainty of the data, the SWC is a nondispersive system.

Recall that the resonance frequencies of a system are the frequencies at which the imaginary part of the total impedance vanishes. The SWC is not a purely acoustic system because the mechanical impedance of the sound source is coupled to the acoustic domain, resulting in a nonnegligible shift of the resonance frequencies. The second method to measure the sound speed effectively uncouples the acoustic and mechanical domains, thus removing the influence of the driver's impedance from measurements of the SWC's resonance frequencies.

The details of this method were presented by McConnell;[23] therefore, only a brief overview will be presented here. The resonances of the acoustic portion of the SWC can be obtained from a measurement of the transfer function between a hydrophone at an arbitrary depth below the surface of the SWC and an accelerometer[24] mounted on the piston of the J9. From these frequencies, the speed of sound can easily be determined with the following relationship:

$$c_{\text{eff}}=\frac{2f_n l}{n+\frac{1}{2}}, \tag{15}$$

where $n=0.1.2,....$, and l is the length (height) of the SWC. Employing Eq. (15), and averaging together the five lowest measured resonance frequencies, results in a sound speed of (360 ± 3) m/s. All five resonance frequencies fell within 3 Hz of the theoretical values calculated with the assumption of this sound speed.

According to the experimentally determined sound speed, the plane-wave cutoff frequency of the SWC is ≈ 1 kHz. Measurements of the wavefront planarity show abrupt deviations from planar behavior at 900 Hz, supporting this estimate. The wavefronts are planar within 1 dB from 28 Hz to 850 Hz in the section of the SWC used during the sensor's calibration.

The theoretically calculated sound speed is within 20% of the experimentally measured value. The discrepancy is likely due to the uncertainty in many of the published material properties of the acrylic tube. The agreement between the two experimental methods is quite good, however. The sound speed as determined by the transfer function method is (360 ± 3) m/s. This value lies within the experimental uncertainty of the (355 ± 8) m/s value obtained from the pressure null measurements.

C. System transfer functions for calibration

The *u-u* intensity probe must be calibrated to produce a measurement of intensity. The SWC is used as the calibration facility. Excluding the extreme outer radial area of the SWC, sensors at coincident depths are subjected to the same acoustic field. Because the phase between the pressure and velocity is a known 90°, a calibration relative to pressure hydrophones can be performed. Note that this procedure is a proof of principle; it is neither an absolute calibration, nor the best method of calibration conceivable.

The measurement of active intensity produced by the *u-u* intensity probe is proportional to the imaginary part of G_{12}, whereas that of reactive intensity is proportional to the difference of G_{22} and G_{11} as illustrated in Eqs. (9) and (11). Spectral quantities such as these are not directly measurable, because they involve particle velocities, whereas the sensors' output is voltage. A transfer function, H, relates an input quantity, x, to a measured output quantity, $\hat{x}$:

$$x=\frac{\hat{x}}{H}. \tag{16}$$

It follows that

$$G_{11}=\frac{\hat{G}_{11}}{H_{11}}, \tag{17}$$

where $\hat{G}_{11}$ is a voltage spectrum, and H_{11} is the transfer function that relates geophone velocity to output voltage. In order that no assumptions be made about the magnitude and phase of the geophone output voltage, an expression for H_{11} that depends on the reference hydrophone output voltage will be derived. For this reason, the velocity field in the SWC must be expressed in terms of the acoustic pressure. Figures 5 and 6 illustrate the layout of the sensors in the SWC. The expression describing the pressure at a depth z below the free surface of the SWC is:

$$p(z,t)=p_0 \sin(kz)e^{j\omega t}. \tag{18}$$

The particle velocity is:

$$u_z(z,t)=j\frac{p_0}{\rho_0 c}\cos(kz)e^{j\omega t}. \tag{19}$$

Combining these produces:

$$u_{z_1}(d_1)=j\frac{p_1(d_1)}{\rho_0 c\tan(kd_1)} \text{ and } u_{z_2}(d_2)=j\frac{p_2(d_2)}{\rho_0 c\tan(kd_2)}. \tag{20}$$

The transfer functions for the pressure and velocity sensors are:

$$u_{z_1}=\frac{\hat{e}_{u_1}}{H_{u_1}},\quad u_{z_2}=\frac{\hat{e}_{u_2}}{H_{u_2}},\quad p_1=\frac{\hat{e}_{p_1}}{H_{p_1}},\quad p_2=\frac{\hat{e}_{p_2}}{H_{p_2}}, \tag{21}$$

where subscripts 1 and 2 refer to locations d_1 and d_2, respectively. Note that the subscript z is suppressed in the voltage and transfer function terms.

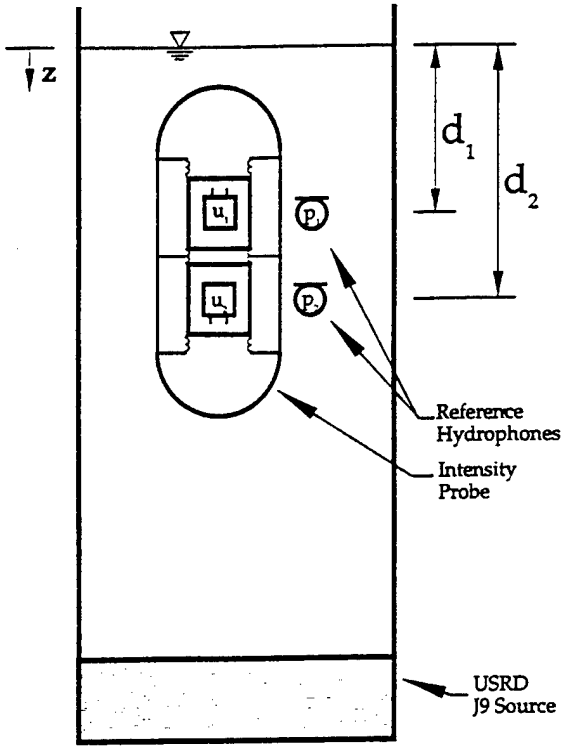

FIG. 5. The orientation of the reference hydrophones and *u-u* intensity probe in the SWC.

Substituting the acoustic quantities from Eq. (21) into Eq. (20) produces a transfer function for each velocity sensor that involves the voltages measured by the pressure and velocity sensors:

$$H_{u_1} = -j\rho_0 c \tan(kd_1) H_{p_1} \frac{\hat{e}_{u_1}}{\hat{e}_{p_1}}$$

and (22)

$$H_{u_2} = -j\rho_0 c \tan(kd_2) H_{p_2} \frac{\hat{e}_{u_2}}{\hat{e}_{p_2}}.$$

Recall that the quantities H_{11}, H_{12}, and H_{22}, which are used for adjusting the three measured velocity spectra involved in intensity measurements, are defined as:

$$H_{11} = H_{u_1} H_{u_1}^*, \quad H_{12} = H_{u_1} H_{u_2}^*, \quad H_{22} = H_{u_2} H_{u_2}^*. \tag{23}$$

Combining Eqs. (22) and (23) produces:

$$H_{12} = (\rho_0 c)^2 \tan(kd_1)\tan(kd_2) H_{p_1} H_{p_2}^* \frac{\hat{e}_{u_1}}{\hat{e}_{p_1}} \frac{\hat{e}_{u_2}^*}{\hat{e}_{p_2}^*}, \tag{24}$$

$$H_{11} = (\rho_0 c)^2 \tan(kd_1)\tan(kd_1) H_{p_1} H_{p_1}^* \frac{\hat{e}_{u_1}}{\hat{e}_{p_1}} \frac{\hat{e}_{u_1}^*}{\hat{e}_{p_1}^*}, \tag{25}$$

and

$$H_{22} = (\rho_0 c)^2 \tan(kd_2)\tan(kd_2) H_{p_2} H_{p_2}^* \frac{\hat{e}_{u_2}}{\hat{e}_{p_2}} \frac{\hat{e}_{u_2}^*}{\hat{e}_{p_2}^*}. \tag{26}$$

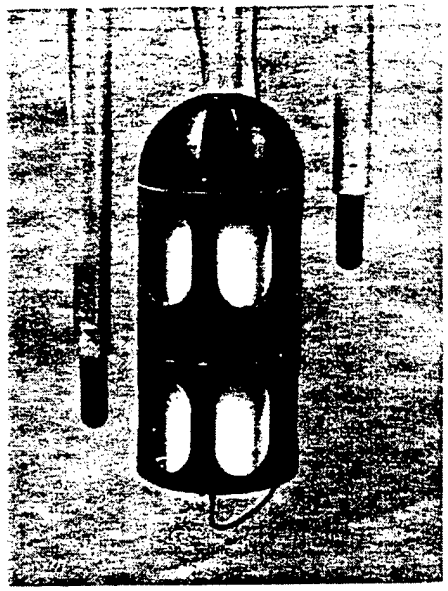

FIG. 6. The arrangement of the sensors in the *u-u* probe calibration procedure. Note that the aluminum positioning rods are attached to a three axis positioning system from above.

The hydrophone transfer functions can be separated into magnitude and phase components such that.

$$H_{p_{12}} = H_{p_1} H_{p_2}^* = |H_{p_1}||H_{p_2}| e^{j(\phi_1 - \phi_2)}, \tag{27}$$

where $|H_{p_1}|$ and $|H_{p_2}|$ are the open circuit receiving sensitivities of hydrophones 1 and 2, M_{p_1} and M_{p_2}, respectively. The phase difference between the two hydrophones can be measured using a standard switching technique.[3,25]

Substituting a simplified version of the transfer function into Eq. (9) produces the final form of the equation for active intensity measurements:

$$I_z^a = -\frac{1}{\omega\rho_0 \Delta z \tan(kd_1)\tan(kd_2) M_{p_1} M_{p_2}} \times \mathrm{Im}\left[\frac{\hat{G}_{12}\hat{G}_{p_1p_2}^c}{\hat{G}_{u_1u_2}^c} e^{j(\phi_1 - \phi_2)}\right]. \tag{28}$$

Here the transfer function given in Eq. (24) has been simplified by a change in notation: $\hat{G}_{u_1u_2}^c$ is the cross-spectrum between the geophone output voltages, and $\hat{G}_{p_1p_2}^c$ is the cross-spectrum between the hydrophone output voltages. The superscript c denotes that both of these quantities are measured in the probe's calibration procedure. The term $\hat{G}_{12}$ is the voltage cross-spectrum between the geophone outputs in an intensity measurement situation.

The analogous substitutions into Eq. (11) produce the working expression for reactive intensity:

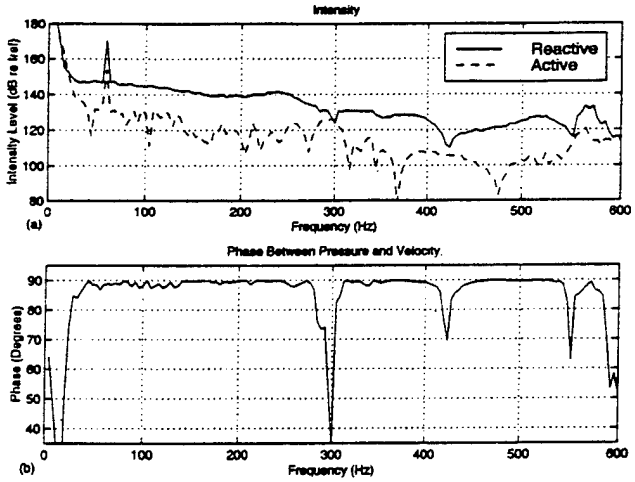

FIG. 7. Intensity and pressure-velocity phase at a depth of 20 cm in the SWC, as measured by the reference hydrophones using the *p-p* technique. The peak at 60 Hz is due to EMI. Note that Iref is $10^{-12}/\rho c$ W/m^2.

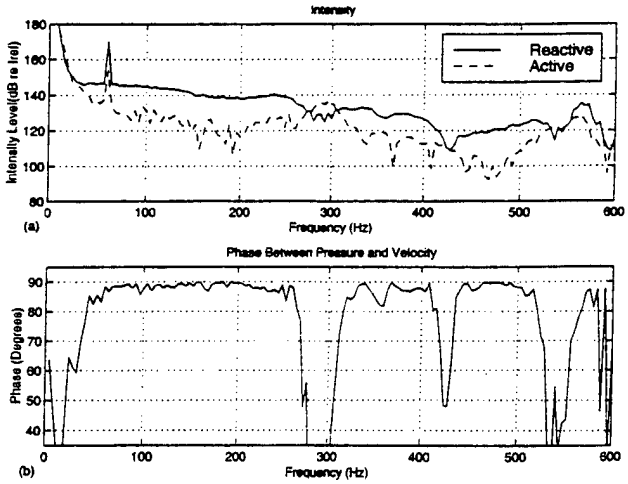

FIG. 8. Intensity and pressure-velocity phase at a depth of 20 cm in the SWC, as measured by the *u-u* intensity probe. The peak at 60 Hz is due to EMI, and Iref is $10^{-12}/\rho c$ W/m^2.

$$I_z^r = \frac{1}{2\omega\rho_0\Delta z} \times \left[\frac{\hat{G}_{22}\hat{G}^c_{p_2p_2}}{\tan^2(kd_2)M^2_{p_2}\hat{G}^c_{u_2u_2}} - \frac{\hat{G}_{11}\hat{G}^c_{p_1p_1}}{\tan^2(kd_1)M^2_{p_1}\hat{G}^c_{u_1u_1}} \right]. \quad (29)$$

IV. MEASUREMENT OF INTENSITY

The calibration setup depicted schematically in Fig. 5 and photographically in Fig. 6 can also be used to measure the acoustic intensity of the standing-wave field set up within the SWC. The two pressure hydrophones can be used for a *p-p* intensity measurement that can be compared to the ***u-u*** probe's measurement. A second verification of the ***u-u*** probe's accuracy is based on a comparison of a ***u-u*** intensity measurement with a measurement made by a ***p-u*** intensity probe.[26]

An eight channel Hewlett Packard 3567A dynamic signal analyzer (DSA) was used to process the transducer outputs. Any phase difference between the eight DSA channels will have a significant impact on the measurement accuracy. The greatest amount of amplitude and phase mismatch between any of the DSA channels was measured to be 0.1% and 0.02°, respectively.

The hydrophones[27] used for the calibration have a sensitivity of −210 dB *re*: 1 V per μPa. These piezoceramic hydrophones have a nominal capacitance of 3.4 nF. A preamp was used with these hydrophones to avoid amplitude and phase errors. The former would be created by the voltage divider consisting of the hydrophone capacitance and the input capacitance of the DSA (100 pF), while latter would be introduced at low frequencies by the low pass filter consisting of the hydrophone's capacitance and the input impedance of the DSA. Ithaco 1201 preamplifiers.[28] with a nominal input impedance of 100 MΩ, were used with all the hydrophone measurements presented in this paper.

The signal driving the J9 source, which ensonified the SWC, was generated by the DSA. Due to the limitation of the DSA's source voltage and the low sensitivity of the J9, a power amplifier[29] was required to boost the driving signal's amplitude. The frequency response of the power amplifier is flat within 0.1 dB over the range of 28 Hz to 2800 Hz.

A. Pressure gradient technique

In effort to remove any phase mismatch between the reference hydrophones in subsequent measurements, their phase difference was measured with a standard switching technique[3,25] conducted in the SWC with the acoustic centers of the hydrophones located at coincident depths. Recall that the wavefronts in the SWC are planar within 1 dB; therefore, the implementation of the switching technique might seem unnecessary. However, the switching technique lessens the effects of the SWC's standing-wave resonances on the measurement. In this measurement, the coherence function between the hydrophones fell below 0.999 only at 60 Hz, and at frequencies above the plane-wave cutoff frequency (≈1 kHz).

A velocity maximum exists for all frequencies at the air–water interface, making it the ideal location for achieving a high signal-to-noise ratio for velocity sensor measurements. However, the pressure at that location is effectively zero for all frequencies, making it the worst possible location for hydrophone measurements. Similarly, for a given frequency, the locations of pressure maxima are velocity minima. Therefore, the location of the sensors in the SWC is essentially an arbitrary choice, because at every location in the SWC except the surface, a velocity minima exists for some frequency. For the following measurements, the ***u-u*** intensity probe and reference hydrophones were mounted 20 cm below the free surface of the SWC, which was filled with water until a meniscus formed above the top of the acrylic wall. Completely filling the SWC alleviates any concern of standing-wave formation in the air column above the air–water interface.

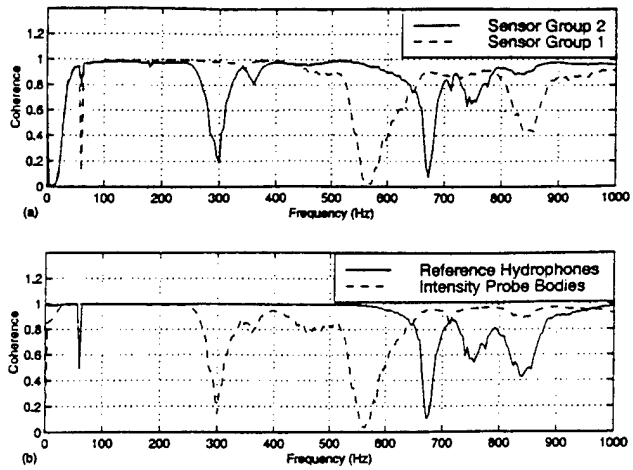

FIG. 9. (a) The coherence functions between each probe body and the corresponding reference hydrophone. (b) The coherence functions between the probe bodies, and between the reference hydrophones.

Intensity is measured with the *p-p* technique during the calibration of the ***u-u*** intensity probe. Equations (28) and (29) predict that if the calibration procedure and intensity measurement are coincident, all the velocity spectra from the ***u-u*** probe bodies will cancel, producing a *p-p* intensity measurement. The phase information determined by the switching technique and the various cross-spectra and physical quantities illustrated in Eqs. (28) and (29) generated the intensity curve in Fig. 7(a). This measurement was repeated without the intensity probe located between the hydrophones, and no significant changes resulted. This indicates that the presence of the ***u-u*** probe did not adversely affect the *p-p* probe intensity measurement.

The reactive component of intensity illustrated in Fig. 7(a) is nominally 20 dB higher than the active component. This is expected, because the energy in the SWC is predominantly reverberant, or reactive. To quantify the extent to which the field is reactive, the phase between pressure and velocity is calculated. An equivalent and simpler method is to calculate the phase between the real and imaginary parts of intensity. This is equivalent to the phase of G_{pu}, which is given in Fig. 7(b). The phase between pressure and velocity should be 90°; however, the data of Fig. 7(b) indicate that there are deviations from this ideal. Recall that active intensity corresponds to local transport of energy. This occurs to a small extent in the form of sound emitted from the SWC. In addition, viscous and thermal relaxation losses in the acoustic boundary layer, near the tube wall, contribute to the presence of active intensity. Energy transport may also occur through flexure-induced dissipation in the acrylic walls of the SWC. Limitations in the extent to which the phase difference between the hydrophones can be removed from their measurements is another source of error.

Because the random error in a spectrum level is inversely proportional to the square root of the number of spectral averages,[30] the random error in the intensity measurements given here (with 256 averages) is ±0.3 dB.

B. Velocity gradient technique

The procedure for measuring intensity with the ***u-u*** probe is analogous to that of the *p-p* measurement. This measurement employs the same sensors, instrumentation, and SWC. Equations (28) and (29) are again used to compute intensity; however, the calibration procedure must be separate from the measurement of intensity. The results of the ***u-u*** intensity measurement are presented in Fig. 8. Note that both the calibration procedure and intensity measurement occurred at the same location in the SWC.

As in the *p-p* measurements in Fig. 7(b), the phase between pressure and velocity exhibits some deviations from 90°. The extent to which the phase difference between the hydrophones cannot be removed significantly contributes to these deviations. The lack of coherence between the individual velocity sensors and their reference hydrophones at certain frequencies is the most significant source of these phase deviations. This lack of coherence results from presence of standing-waves: at any location in the SWC, there exist frequencies at which either the pressure or velocity is approximately zero. The accuracy of the calibration and subsequent measurements is diminished at these frequencies.

Figure 9 illustrates the various coherence functions between pairs of sensors during the calibration. Cross referencing these plots yields a great deal of information about the standing-wave nature of the SWC. The frequencies of 300 Hz and 560 Hz are antiresonance frequencies of the SWC. These are the frequencies at which the most energy must be input to produce a constant level of acoustic pressure (at a given location) in the system. The coherence functions of several sensor pairs have an extremely low value at these antiresonance frequencies. Further, the frequency range for which the calibration has validity is limited by the overlapping drop-outs in coherence at 560 Hz and 670 Hz.

A comparison of the intensity levels of Figs. 7(a) and 8(a) shows excellent agreement between the *p-p* and ***u-u*** techniques. This agreement is not conclusive proof that the ***u-u*** probe functions properly, because the transducers used in the former measurement served as the reference transducers in the latter; however, it certainly is supporting evidence.

C. Pressure-velocity technique

An independent method to verify that the **u-*u*** probe properly measures acoustic intensity is now discussed. A measurement was performed using a well calibrated underwater acoustic intensity probe on loan from Acoustech Corporation.[26] This sensor is called a ***p-u*** probe,[6,7] because it measures both pressure and velocity directly. Accordingly, the ***p-u*** probe does not suffer from the finite difference errors that affect the accuracy of the other intensity transducers used in this investigation.

The signal processing required to measure intensity with the ***p-u*** probe is surprisingly simple. By definition, intensity is the cross-spectrum of pressure and velocity. Consequently, the sensor output voltages are adjusted by their measured sensitivities to obtain direct measures of the acoustic quantities. The cross-spectrum of pressure and velocity is computed and then separated into real and imaginary parts. The

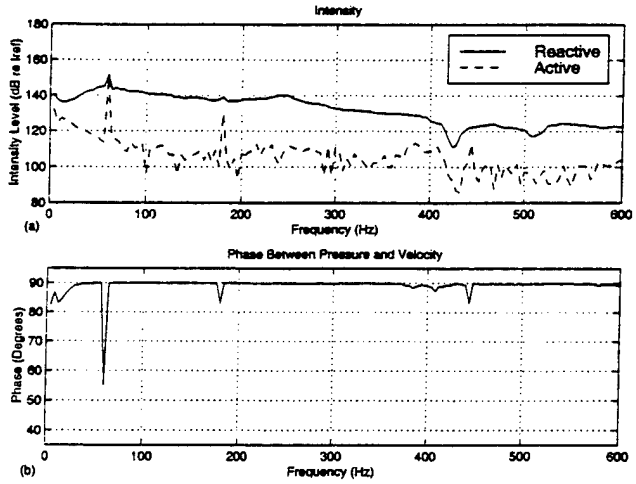

FIG. 10. Intensity and pressure-velocity phase in the SWC, as measured by the p-u intensity probe at a depth of 20 cm. The peak at 60 Hz is due to EMI, and Iref is $10^{-12}/\rho c$ W/m^2.

resulting data appear in Fig. 10. Note that the phase between pressure and velocity, as computed by the p-u probe, is almost a perfect 90° over the entire frequency range of interest. The reactive intensity levels are very similar to those of Figs. 7(a) and 8(a), except at the antiresonance frequencies. The active intensity levels do not compare well for reasons discussed in the next section.

V. SUMMARY AND CONCLUSIONS

A new technique for measuring underwater acoustic intensity has been presented. The theory to infer acoustic pressure from a velocity gradient was derived. It was shown that in a typical acoustic field, six velocity sensors (to measure three velocity gradients) are required for the measurement of the three components of acoustic intensity. In a single dimensional acoustic field, measurement of the acoustic velocity gradient was accomplished using two neutrally buoyant bodies with imbedded velocity sensors (geophones). Active intensity was shown to be proportional to the imaginary part of the cross-spectrum between the velocity sensors, while reactive intensity was proportional to the difference of their auto-spectra.

The suspension system of the neutrally buoyant body maintains their proper coaxial orientation and simplifies the mounting of the probe. This suspension does not adversely affect measurement quality in the frequency range of interest, from 28 Hz to 800 Hz. The lower limit is imposed by the resonance frequency of the geophones.

The geometry of the u-u intensity probe gave rise to potential undesirable interaction between the two sensor bodies. However, when the probe was subjected to an effective 150 dB SPL field, the total coupling between the bodies was shown to be negligible.

A facility to calibrate the u-u intensity probe has been designed and constructed. Termed the slow wave calibrator (SWC), this device is essentially an acoustic standing-wave guide. The elastic walls of the SWC lower the longitudinal phase speed of sound from the bulk speed of 1480 m/s to (358 ± 5) m/s. The acoustic wavefronts in the SWC have a cross-section that is planar within 1 dB. Thus sensors located at coincident depths are subjected to the same acoustic field.

The u-u probe calibration procedure is based on only one assumption: that the free surface of the calibrator is an ideal pressure-release surface. This assumption implies that the phase between pressure and velocity in the SWC is exactly 90°. A relative calibration of the u-u probe's velocity sensor bodies with pressure hydrophones was therefore possible.

To verify that the two reference hydrophones are phase matched accurately enough to provide a reliable u-u probe calibration, a p-p intensity measurement was made using the hydrophones. The intensity levels measured by the u-u probe differ only slightly from those measured by the p-p probe.

Differences in level are attributed both to the numerous pressure and velocity nulls present in the SWC, and to the antiresonances of the SWC itself. With the exception of these frequencies, the level of the reactive intensity measured by the u-u probe matches that of a p-u probe within 6 dB. This is consistent with the findings of Gabrielson *et al.*[7] in which a 10 dB difference existed between measurements made by p-u and finite differencing p-p probes in a reactive field.

The u-u probe's acoustic intensity measurement methodology is viable. Measurements of reactive intensity require subtracting two nearly equal signals, which the u-u intensity probe does fairly accurately in the reactive field of the SWC. On the other hand, measurements of active intensity in a highly reactive field using a finite differencing technique, such as a p-p or u-u probe, are difficult to perform accurately. Figures 8(a) and 10(a) show a 20 dB difference in the active intensity levels measured by the u-u and p-u probes. Figure 7(a) indicates that this difference is associated either with the reference transducer phase matching, or the finite difference approximation employed by both the p-p and u-u probes. In future applications, the p-u probe is recommended.

ACKNOWLEDGMENTS

This work has been supported by the Office of Naval Research, Code 321 (Grant No. N00014-96-1-1173) and Code 333 (Grant Nos. N00014-94-1-0708 and N00014-99-1-0259). Particular appreciation is extended to Scott Littlefield and Dr. Kam Ng.

[1] A. D. Pierce, *Acoustics: An Introduction to Its Physical Principles and Applications* (Acoustical Society of America, Woodbury, NY, 1989).
[2] F. J. Fahy, *Sound Intensity*, 2nd ed. (E & F Spon, London, 1995).
[3] J. Y. Chung, "Cross-spectral method of measuring acoustic intensity without error caused by instrument phase mismatch," J. Acoust. Soc. Am. **64**, 1613–1616 (1978).
[4] K. W. Ng, "Acoustic intensity probe," U.S. Patent No. 4,982,375 (1 January 1991).
[5] J. A. McConnell, G. C. Lauchle, and T. B. Gabrielson, "Two geophone underwater acoustic intensity probe," U.S. Patent Disclosure (30 August 1995).
[6] T. B. Gabrielson, J. F. McEachern, and G. C. Lauchle, "Underwater acoustic intensity probe," U.S. Patent No. 5,392,258 (21 February 1991).
[7] T. B. Gabrielson, D. L. Gardner, and S. L. Garrett, "A simple neutrally

buoyant sensor for direct measurement of particle velocity and intensity in water," J. Acoust. Soc. Am. **97**, 2227–2237 (1995).
[8] GS-14-L3 Geophone, Geospace Corp., 7334 Gessner, Houston, TX 77040.
[9] R. A. Serway, *Physics for Scientists and Engineers*, 3rd ed. updated (Saunders College, Philadelphia, PA, 1990).
[10] L. D. Landau and E. M. Lifshitz, *Fluid Mechanics*, 2nd ed. (Butterworth-Heinemann, New York, 1987).
[11] C. B. Leslie, J. M. Kendall, and J. L. Jones, "Hydrophone for measuring particle velocity," J. Acoust. Soc. Am. **23**, 711–715 (1956).
[12] E-Cast F-8 Low Viscosity Epoxy Resin and Hardener 118, United Resin Corp., 4359 Normandy Ct., Royal Oak, MI 48073.
[13] K & B Glass Microballoon Filler, K & B Manufacturing, Inc., 2100 College Dr., Lake Havasu, AZ 86403.
[14] C. M. Harris, *Shock and Vibration Handbook*, 4th ed. (McGraw-Hill, New York, 1996).
[15] W. T. Thomson, *Theory of Vibration with Applications*, 3rd ed. (Prentice-Hall, Englewood Cliffs, NJ, 1988).
[16] M. R. Spiegel, Ed., *Mathematical Handbook: Schaum's Outline Series*, 30th ed. (McGraw-Hill, New York, 1992).
[17] K. J. Bastyr, "A velocity gradient underwater accoustic intensity sensor," MS Thesis, The Pennsylvania State University, December 1998.
[18] L. E. Ivey, "Underwater electroacoustic transducers," Naval Research Labratory Specifications Sheet, August 1994. The USRD is now affiliated with the Naval Undersea Warfare Center in Newport, RI.
[19] M. B. Johnson, "Reciprocity calibration in a compliant cylindrical tube," MS Thesis, Naval Postgraudate School, June 1985. DTIC Report Number ADA 158998.
[20] M. C. Junger and D. Feit, *Sound, Structures, and Their Interaction* (Acoustical Society of America, Woodbury, NY, 1993).
[21] Townsend Plastic, "Physical properties of townsend cast acrylic," Manufacturers Specification Sheet, dated 1998.
[22] E. Skudrzyk, *The Foundations of Acoustics: Basic Mathematics and Basic Acoustics* (Springer-Verlag, New York, 1971).
[23] J. A. McConnell, K. J. Bastyr, and G. C. Lauchle, "Sound-speed determination in a fluid-filled elastic waveguide," J. Acoust. Soc. Am. **105**, 1143 (1999).
[24] PCB Model W353B66 Accelerometer, PCB Piezotronics, Inc., 3425 Walden Ave., Depew, NY 14043.
[25] G. S. K. Wong and T. F. W. Embleton, Eds., *AIP Handbook of Condenser Microphones: Theory, Calibration, and Measurements* (AIP Press, New York, 1995).
[26] Acoustech Corporation, P.O. Box 139, State College, PA 16804.
[27] Reson Model TC4013 Hydrophone, Reson, Inc., 300 Lopez Rd., Goleta, CA 93117.
[28] 1201 Low Noise Preamplifier, Ithaco Corp., 735 West Clinton St., Ithaca, NY 14850.
[29] Servo 150 Studio Amplifier, Samson Technologies Corp., Syosset, NY 11791.
[30] J. S. Bendat and A. G. Pierson, *Random Data: Analysis and Measurement Procedures*, 2nd ed. (Wiley, New York, 1986).

APPENDIX 47

Scaling of turbulent wall pressure fluctuations downstream of a rearward facing step

Gerald C. Lauchle
Penn State University
Graduate Program in Acoustics and Applied Research Laboratory
State College, Pennsylvania 16804
gcl1@psu.edu

Walter A. Kargus IV
Johnson Electric Automotive
47660 Halyard Drive, Plymouth, Michigan 48170
wkargus@lear.com

Abstract: The turbulent boundary layer that forms downstream of a surface discontinuity is locally inhomogeneous. Here, we consider the boundary layer that occurs downstream of a rearward facing step discontinuity on a flat plate that is exposed to a zero incidence, uniform subsonic flow. The wall pressure "point" spectra are measured by small, flush-mounted pressure transducers located at various locations downstream of the step. A new form of the non-dimensional point wall pressure auto-frequency spectrum is proposed that includes the statistical variations of the reattachment location. This form is shown to collapse quite well all of the spectra measured slightly upstream, within, and downstream of the flow reattachment location.

PACS numbers: 43.50.Nm, 43.28.Ra, 43.50 Yw

1. Introduction

Flow over a rearward facing step is characterized as a discontinuous boundary-layer flow over a surface in which the elevation of the downstream surface is lower than that of the upstream surface. Lap-joints and cutouts on surfaces exposed to flow are examples. The assumed upstream turbulent boundary layer will separate at the step discontinuity forming a free shear layer and a local recirculation zone immediately downstream of the step. The shear layer eventually reattaches to the downstream surface, and a new highly energized turbulent boundary layer begins to form. This process produces wall pressure fluctuations that are significantly higher than those created by nonseparated, equilibrium turbulent boundary layers. In turn, this increases the direct flow-induced noise radiation and nonrigid surface vibrations that radiate as structural vibration-induced noise.

The scaling of the wall pressure point power spectrum under an equilibrium turbulent boundary layer (TBL) has been subdivided into major regions.[1] Each region conforms to different layers of the flow and has a particular pressure and time scale. The rms pressure fluctuations within the viscous sublayer, for example, scale on the wall shear stress and the viscous time scale. The convecting turbulence in the log-law region causes these pressures to scale on the wall shear stress and a larger time scale that is related to the TBL thickness and shear velocity. The region beyond the log-law region is termed the outer boundary layer. Here, the low-frequency pressure fluctuations scale on the dynamic pressure of the flow, $q = 1/2\rho_o U_o^2$, and on the time scale δ^*/U_o, where δ^* is the TBL displacement thickness, ρ_o is the fluid mean density, and U_o is the free stream velocity. The higher frequencies scale on viscous variables.

Each region of the TBL influences a different range of frequencies of the point wall

pressure spectrum. The regions beyond the log-law region influence the lower and mid frequencies, whereas the log-law region influences the "overlapping" frequencies between the mid and high frequency range. The region of the viscous sublayer influences the high frequencies. These different scalings are still open to discussion[2] because of the complexity in modeling a TBL.

In this study, we consider the scaling of the point wall pressure spectrum downstream of a surface step discontinuity, which is more complex than that of a typical nonseparating TBL on a flat plate under zero pressure gradient conditions because of additional length scales, nonhomogeneous flow statistics, and reversed flow patterns. An experiment to characterize the statistics of the wall pressure fluctuations that occur downstream of a rearward facing, 2-D step on a flat plate has been conducted. Presented are scaling relationships that can be used to predict the auto-spectral characteristics of the wall pressure fluctuations for similar situations in which experimental data are unavailable. It is found that the spectra scale on the height of the step, the mean velocity upstream of the separation point, and on the *variance* of the estimated distance from the reattachment point-to-the point of measurement. By incorporating the variance between a fixed measurement location (or point of interest) and the reattachment point, which is known to be chaotic, a useful scaling law is established that has no singularity[3] when the measurement location happens to correspond to the reattachment location. This scaling relationship is different from earlier proposals[4,5] for a similar flow, and provides a better collapse of the experimentally measured spectra.

2. Experimental setup

A special facility was designed and used in a large anechoic chamber to measure the local wall pressure fluctuations and radiated sound from the flow over a rearward-facing step located on an otherwise flat, 2-D plate that supports a TBL on one side only. Figure 1 shows a schematic of the experiment, and the facility is described in complete detail elsewhere.[6]

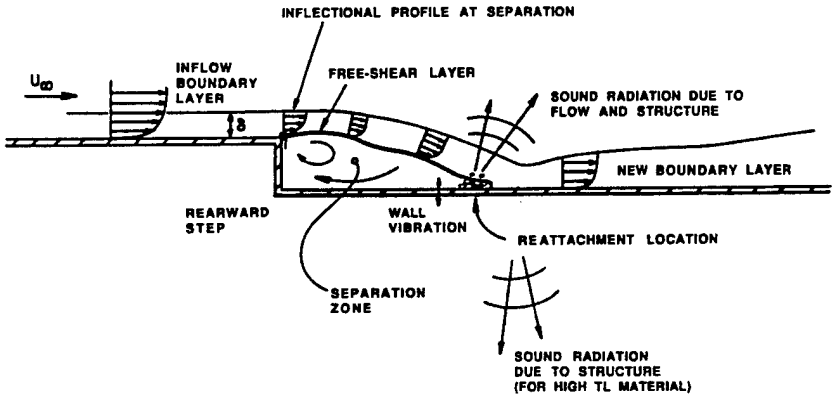

Fig. 1. Schematic of boundary-layer separation over a rearward-facing step. The inflow is from a convergent jet impinging on a 2-D flat plate that supports a TBL.

The flush-mounted pressure transducers are composed of B&K model 4165 (1.27 cm dia) microphones and supporting model 2639 preamplifiers powered by model 2087 power supplies. They are interfaced with the flow surface by a reduced area tube of 1.09 mm inside diameter and 5.7 mm in length. A cavity exists between the diaphragm of the microphone and

the inlet to the tube. It causes a microphone resonant response centered at 1 kHz. The peak response is 12 dB above the nominal free-field response of the microphone, and the half-power bandwidth of the resonance is ~200 Hz.

3. Flow reattachment

It is crucial to understand the fluid mechanics of the flow reattachment region to interpret the measured fluctuating wall pressure statistics. This can be accomplished conveniently by flow visualization. Figure 2 shows the flow pattern in the reattachment zone on the lower plate. This has been determined by photographing flourescent mini-tufts under black light conditions. The tufts are secured to the plate surface using cyanoacrylate adhesive. The flow direction and "steadiness" is indicated by the orientation and "blurriness," respectively of the individual tufts. One can see tufts aligned with the flow direction downstream of reattachment and regions of reversed flow upstream of the reattachment zone. Of particular interest is the overall width of this zone, identified by the band of tufts that have random orientations. Upon studying many different flow visualizations like this, under various velocity conditions, the reattachment location is clearly identified as a random variable with a mean value, $\bar{x}_r$, that is weakly dependent on flow speed being proportional to $U_o^{0.1}$. The variation of the reattachment location, $\sigma_{x_r}^2$, is also determined from these data and is found to be proportional to $U_o^{0.5}$.

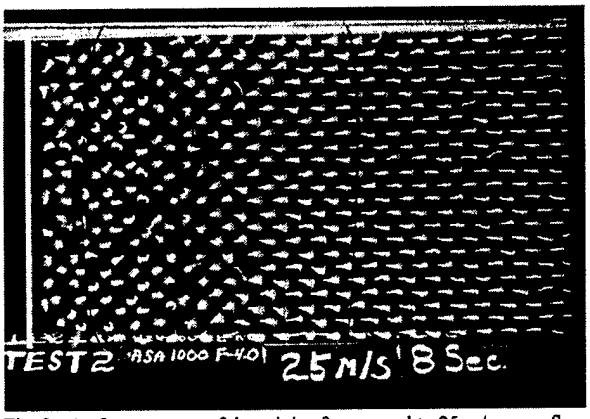

Fig. 2. An 8-s exposure of the mini-tufts exposed to 25 m/s mean flow velocity. The step is the vertical light line seen at the left.

4. Wall pressure fluctuations in reattachment region

The tube microphone was mounted at many streamwise locations along the centerline of the test plate. The signals were collected and analyzed using a Zonic System 7000 digital signal processor that was controlled by a Digital Equipment Corporation VAX Station 3100 m38. The spectral bandwidth is typically 3.125 Hz. Sufficient spectral averages were used to reduce random error to within ±1 dB. Figure 3 shows the variation of root-mean-square wall pressure through the reattachment region. The peak rms level is high; it is only 24 dB below the dynamic head of the flow. It is seen to occur from 7 to 8 step heights downstream of the step.

The mean position of the flow reattachment region occurs at approximately 6 step heights downstream. Figure 4 shows the details of these variations with flow speed. The location of peak rms wall pressure is a short distance downstream of the mean position of flow reattachment. This difference is possibly due to the short lag time required for the new TBL to form and generate pressure producing velocity fluctuations.

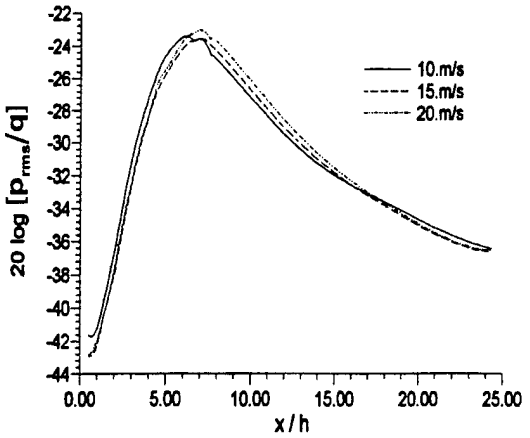

Fig. 3. Variation of rms wall pressure fluctuations with streamwise distance at different speeds.

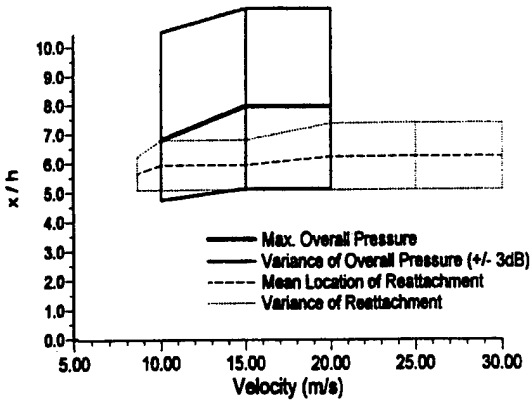

Fig. 4. Position of reattachment compared to the peak value of the rms wall pressure fluctuation.

The wall pressure spectral measurements were performed over extensive ranges of flow velocity ($7.82 \le U_o \le 25.1$ m/s) and streamwise location ($3.0 \le x/h \le 24.38$). The various types of TBL wall pressure spectrum scaling[1,4,5] were considered in an unsuccessful attempt to collapse the current spectral data into a single, reasonably well-bounded, universal function. Thus, traditional spectral normalization methods appear to be inappropriate for the pressure fluctuations occurring downstream of a step discontinuity. As noted previously,[3] and also from the data of Fig. 3, we recognize that on both sides of the mean reattachment location, the mean-square wall pressure decreases approximately as $|x-\bar{x}_r|^{-1}$. This means that the spectral amplitude should be weighted by such a factor to compare spectra measured at various locations. The dependence of the spectral magnitude on velocity is found to be satisfied by the outer (inertial) flow scaling typical of TBLs, i.e., spectrum level is proportional to q^2. The time scale h/U_o appears to be a more appropriate scale than δ^*/U_o. Physically, this means that the time scale of the wall pressure fluctuations is similar to that of the separation-induced vortex.

Now, Figs. 2 and 4 indicate that the reattachment location is chaotic; therefore, it must

be treated as a random variable. To use $|x-\bar{x}_r|^{-1}$ directly in a scaling formula without taking this fact into account will result in a singularity when the measurement point equals $\bar{x}_r$. To overcome this problem we define:

$$\Psi^2 = E[(x-x_r)^2] = (x-\bar{x}_r)^2 + \sigma_{x_r}^2 , \qquad (1)$$

where E[ ] represents the expected value operation performed over N >> 1 individual records. The mean and variance terms of this expression are shown in Fig. 4. The new scaling formulation for the spectra, $G_{pp}(f)$, of the turbulent wall pressure fluctuations that occur at most locations downstream of a rearward facing step on a flat plate that supports a TBL and at any subsonic velocity is given by:

$$\frac{G_{pp}(f)\ \Psi\ U_o}{q^2\ h^2} \quad vs. \quad \frac{fh}{U_o} . \qquad (2)$$

Using Eq. (2), point power spectral densities measured at locations slightly upstream, near, and downstream of $\bar{x}_r$ are nondimensionalized and presented for the considered range of velocities in Fig. 5. The collapse of these measured spectra into a single, well defined function is seen to be quite good. The variations for $1.5 < fh/U_o < 3$ are due to the microphone tube resonance. We note that the definition of Ψ assumes that the data shown in Fig. 3 are symmetric about the peak. This is strictly not the case, so the scaling is less valid for locations upstream of reattachment that are in the recirculation region. The spectra of Fig. 5 for x/h = 3.05 are measured as far upstream from $\bar{x}_r$ as the scaling appears to apply.[6] Equation (2) is actually most valid for locations that are within and farther downstream of the reattachment zone where the pressure fluctuations are created by energized boundary layer turbulence. In the recirculation zone, there is essentially no near-wall region of the boundary layer; thus, there would be less high-frequency pressure fluctuations created there. This statement is supported when comparing the spectra of Fig. 5 for x/h = 3.05 with those for x/h = 6.10 and 12.19. The spectral levels measured just upstream of $\bar{x}_r$ are some 11 to 15 dB lower than those measured within and downstream of $\bar{x}_r$ for $fh/U_o \geq 1$.

5. Conclusions

The rms wall pressure fluctuations measured downstream of a rearward facing step discontinuity on a flat plate that supports a turbulent boundary layer are found to scale on the dynamic head of the flow, and to peak slightly downstream of the mean position of flow reattachment. The spectra of these fluctuations are found to be proportional to the inertial scales of the separated flow in addition to the statistical parameters describing the location of flow reattachment, which is a random variable. The scaling is most accurate within and downstream of the separation reattachment mean location. Upstream in the recirculation zone, the absence of any substantial near-wall turbulence results in pressure fluctuations that are quite low at high frequencies.

Acknowledgments

The work reported here was supported by Ford Motor Co., and ONR, Code 333.

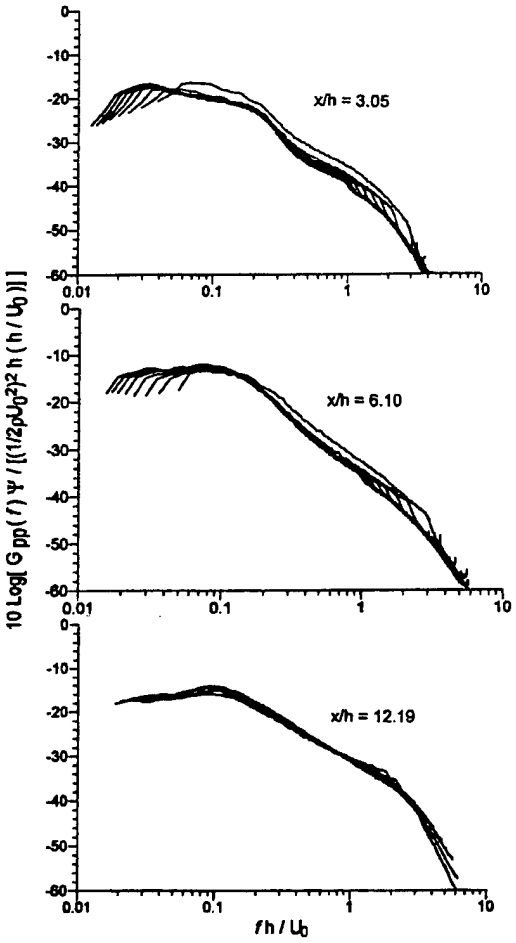

Fig.5. Dimensionless point power spectra of the local wall pressure fluctuations measured upstream (x/h = 3.05), near (x/h = 6.10), and downstream (x/h = 12.19) of the mean position of flow reattachment. The range of velocities for these measurements is from 7.82 to 25.1 m/s, and the step height, h = 2.5 cm.

References and links

[1] T. M. Farabee and M. J. Cassarella, "Spectral Features of Wall Pressure Fluctuations Beneath Turbulent Boundary Layers," Phys. Fluids A **3**, 2410-2420 (1991).
[2] W. L. Keith, D. A. Hurdis, and B. M. Abraham, "A Comparison of Turbulent Boundary Layer Wall-Pressure Spectra," Trans. ASME J. Fluids Eng. **114**, 338-347 (1992).
[3] T. A. Brungart, "Boundary Condition Effects on Turbulent Boundary Layer Wall Pressure Fluctuations," Ph.D. thesis, The Pennsylvania State University (1997).
[4] T. M. Farabee, "An experimental Investigation of Wall Pressure Fluctuations Beneath Non-Equilibrium Turbulent Flow," Ph.D. thesis, Catholic University of America (1986).
[5] T. M. Farabee and M. J. Casarella, "Effects of Surface Irregularity on Turbulent Boundary Layer Wall Pressure Fluctuations," Trans. ASME J. Vib., Acoust., Stress, and Relia. Des. **106**, 343-350 (1984).
[6] W. A. Kargus IV, "Flow-Induced Sound from Turbulent Boundary Layer Separation Over a Rearward Facing Step," Ph.D. thesis, The Pennsylvania State University (1997).

TRANSDUCER STUDIES

Piezoelectric Transformers

APPENDIX 48

IEEE Ultrasonic symposium, Lake Tahoe, Nevada, October 17-21, 1999.

A Circular Piezoelectric Transformer with Crescent Shape Input Electrodes

Burhanettin KOC, Sedat ALKOY and Kenji UCHINO

Materials Research Laboratory

The Pennsylvania State University,

University Park PA 16802

Abstract - For most PZT based piezoelectric materials, the shear mode electromechanical coupling constant is twice as large as the transverse mode coupling. In this study, a new disk type piezoelectric transformer was designed. Crescent shape electrodes at the input side and focused poling direction at the output side on a commercially available PZT disk were designed so that the planar and shear mode electromechanical coupling factors becomes effective rather than the transverse mode coupling. ATILA finite element code was used to analyze transformer behavior and to optimize electrode and poling configurations. The voltage step-up ratio of the proposed transformer has been dramatically improved in comparison with an equivalent rectangular type. A single layer prototype transformer 25.4mm in diameter and 1.0mm in thickness, operated at 93 kHz, was fabricated and its characteristics, such as step-up ratio, power transformation efficiency and temperature rise were measured.

Introduction

One of the bulkiest components in information processing equipment (such as note-book-type personal computers) is the power supply, specifically the electromagnetic transformer used in power supply. Losses such as skin effect, thin wire loss and core loss of the electromagnetic transformer increase rapidly as the size of the transformer is reduced. Therefore, it is difficult to realize miniature low profile electromagnetic transformers with high efficiency.

The original design to transform an input ac voltage to step up or step down, using converse and direct piezoelectric properties of ceramic materials, was proposed by Rosen [1]. The principle of this type of transformer is to excite a piezoelectric element at its mechanical resonance frequency (Fig. 1). Applying an electrical input to one part of the piezoelectric element generates a mechanical vibration and then the mechanical vibration is converted into electrical voltage from the other part of the piezoelectric plate.

The initial Rosen type transformer had a major reliability problem, which is the easy mechanical breakdown at the center position due to the coincidence of the residual stress concentration and the vibration nodal point. In addition to improved mechanically tough ceramic materials, by redesigning the electrode configuration and exciting a third longitudinal resonance mode of the rectangular plate, the piezoelectric transformers for miniaturized back-light inverter was commercialized in 1994 [2].

In addition to no electromagnetic noise generation, small size and high efficiency are some of the advantages of the piezoelectric transformers over the electromagnetic types particularly for computer applications.

All the rectangular type transformers use the transverse mode coupling constant (k_{31}) of the piezoelectric materials [1-3]. For most piezoelectric materials, however, the shear mode coupling constant (k_{15}) is twice as large as the transverse mode coupling constant (k_{31}). From this motivation, a new circular piezoelectric transformer is designed that uses the shear (k_{15}) and the planar (k_p) mode coupling constants of the piezoelectric effects (Fig 2). The transformer is operating at the first radial resonance frequency of the piezoelectric disk. In this paper, the operating principles, FEA models and preliminary experimental results are introduced.

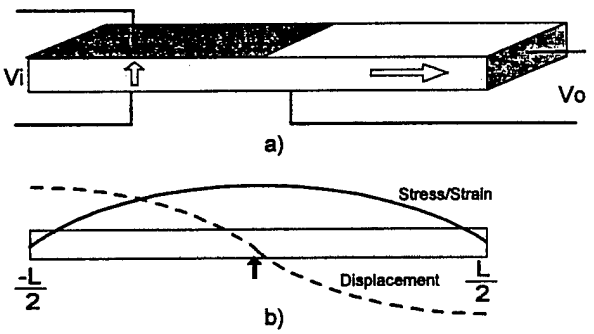

Fig. 1 a) Transverse type piezoelectric transformer (arrows indicate polarization direction), b) Stress/strain and displacement distribution at first longitudinal resonance mode.

Circular Piezoelectric Transformer Design

In a piezoelectric ceramic transformer for high voltage inverter application, the excitation voltage is powered by a battery source of 12 volts. Therefore, the

step-up ratio of the transformer needs to be high for the inverter application. Using a laminated structure in the input part is one way to increase the step-up ratio. However, this increases the cost and decreases the efficiency of a transformer due to lamination.

The proposed transformer, which was made of a single layered piezoelectric ceramic disk, has a crescent shaped asymmetric primary electrode on one side of a piezoelectric disk and a secondary electrode on the other side of the unelectroded section. The arrows in the figure denote the polarization direction of the piezoelectric ceramic disk. This piezoelectric transformer uses the planar mode electromechanical coupling constant (k_p) effectively in the input side and shear mode coupling constant (k_{15}) in the output side. For inverter applications the transformer operates at the radial mode resonance frequency of the piezoelectric disk.

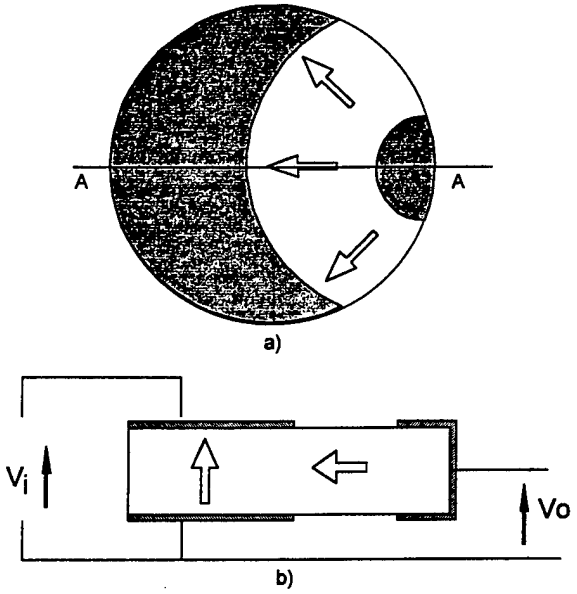

Fig. 2 Structure of the transformer and its poling direction a) Top view, b) cross-sectional view (A-A)

The behavior of the transformer was modeled using ATILA finite element analysis code. The potential field and mode shapes at the radial mode resonance are shown in Fig 3. Since the input electrode configuration is asymmetric, the mode shape is not purely radial but slightly distorted.

The optimized transformer structure is made of a single layered piezoelectric ceramic disk. The operating frequency is under 100 kHz, which is required for the back-lights of a color liquid crystal display (LCD), and the step-up ratio of the transformer is less sensitive to the load resistance as compared to our previous design [4].

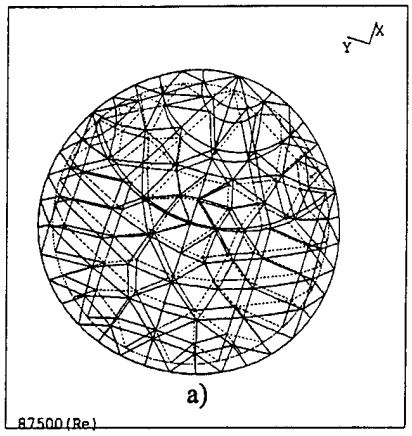

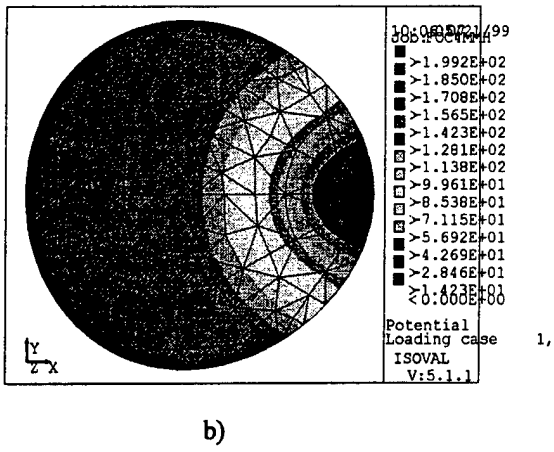

Fig. 3 a) Displacement shape of the transformer at 87.5 kHz, b) Potential field in the transformer at 87.5 kHz (FEM calculation using ATILA).

Experimental Results

The transformer structure shown in Fig. 2 was fabricated using a commercially available piezoelectric ceramic material (APC International, USA). Hard piezoelectric ceramic disks (APC841) of 25.4 mm in diameter and 1.0 mm in thickness were sputtered with platinum electrodes according to the proposed electrode configuration. The transformer input and output sections were poled by applying a DC voltage of 3.0 kV/mm at 150 °C across the input and output electrical terminals.

In order to identify the operating frequency of the transformer, the input (output terminal open-circuited) and output admittance spectra were measured and the results are shown in Fig. 4a and b. The best performance was

obtained when the transformer was driven at its radial mode resonance frequency (92.8 kHz).

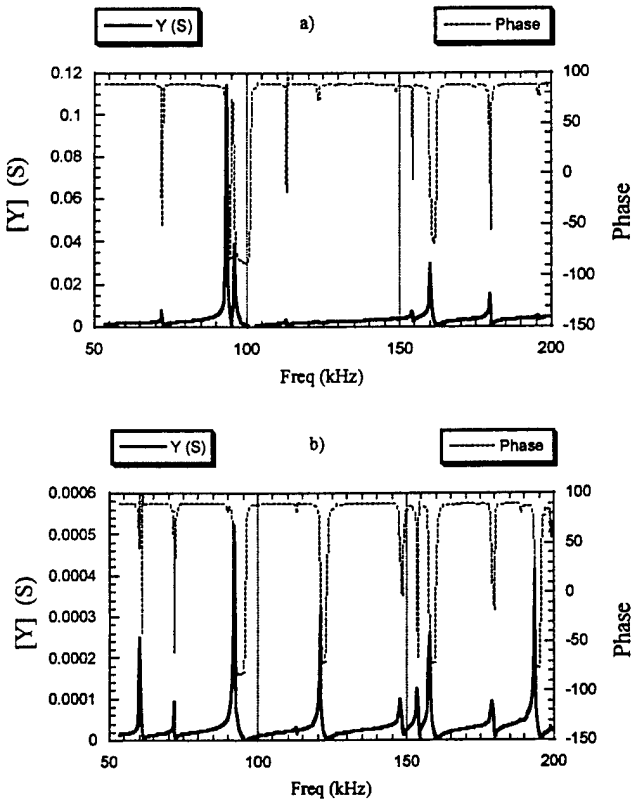

Fig. 4 a) Measured input admittance spectrum. Magnitude and Phase when output electrode is open-circuited to the ground, b) Measured output admittance spectrum. Magnitude and Phase when input electrodes are short-circuited to the ground.

The transformer voltage step-up ratio and efficiency were measured for different resistive loads and the results are shown in Fig. 5. The output power on the resistive loads was 0.5 Watt and the transformer was driven around 92.8 kHz. The operating frequency and driving voltage of the transformer were tuned during the efficiency measurement so that the maximum efficiency could be obtained for different resistive load conditions. The efficiency for a resistive load ranging from 50 to 200 kΩ is more than 90 %. For the same range of load resistance the voltage step-up ratio was increased from 43 to 60.

Fig. 6 shows the vibration velocity and displacement in the radial direction as a function of input voltage. This measurement was performed using a Finer Optic Interferometer system (OFV-511 and OVF 3001, Polytec PI). A resistive load of 103 kΩ was connected to the output terminal of the piezoelectric transformer.

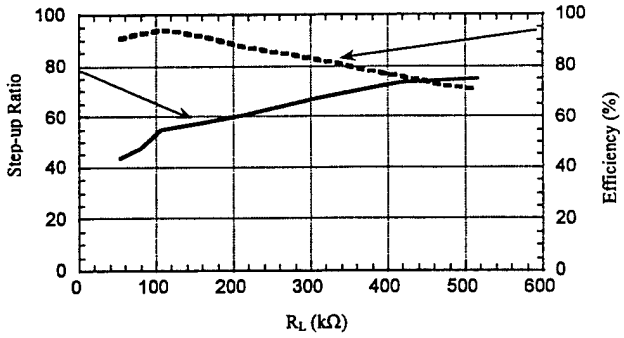

Fig. 5 Step-up ratio and efficiency as a function of load resistance.

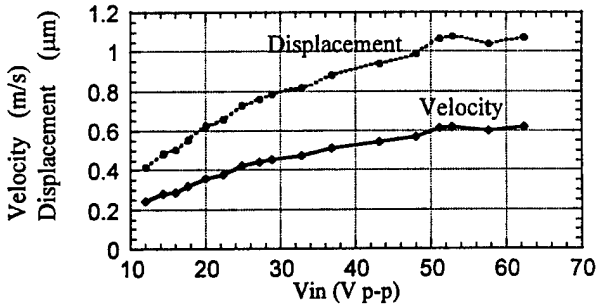

Fig. 6 Magnitude of vibration velocity and displacement in the radial direction as a function of input voltage.

Fig. 7 shows the output voltage and power of the piezoelectric transformer as a function of input voltage for a resistive load of 103 kΩ. The output voltage and power increases fairly linearly for a 103 kΩ resistive load for the input voltage range from 4 to 60V.

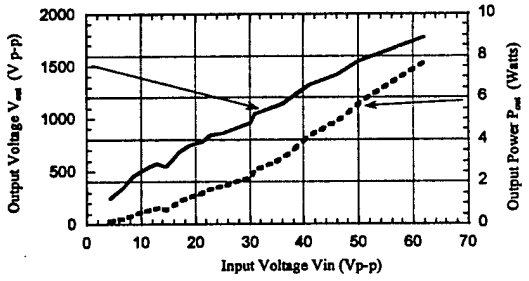

Fig. 7 Output Voltage and Output Power as a function of input voltage.

The input and output voltage waveform of the transformer when driving a Cold Cathode Fluorescent Lamp (CCFL) is shown in Fig. 8. These preliminary

results state that the designed transformer can generate enough step-up ratio and power to light up the cold cathode fluorescent lamps (CCFL) for back-lights of a color liquid crystal displays (LCD) when it is operated at the radial resonance frequency.

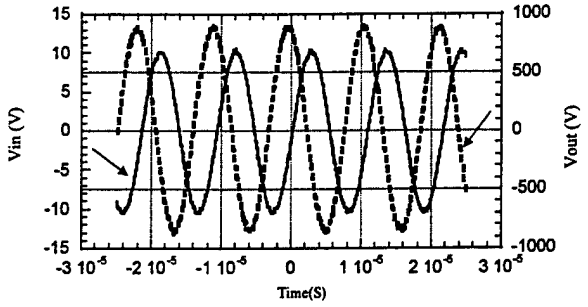

Fig. 8 Input and output voltage waveforms of the transformer when it drives a Cold Cathode Fluorescent Lamp (CCFL).

Conclusion

A circular type piezoelectric transformer design was proposed using commercially available hard piezoelectric disks (APC841). Non-concentric input electrodes and non-uniform output poling led to the use of the shear mode piezoelectric effect at the radial mode resonance frequencies. A prototype single-layered transformer of 25.4 mm diameter and a 1.0 mm thickness, operating around 93 kHz, was fabricated and its characteristics were measured.

The designed transformer was investigated for high voltage inverter applications. It can generate a large enough step-up ratio and power to light up the CCFL for back-lights of color liquid crystal displays (LCD). An intriguing application of this design, in addition to the conventional, will be for a buffer element to drive ultrasonic motors by tailoring the transformer size to match the driving frequency to the motor, which may eliminate a bulky and expensive high voltage power amplifier.

Acknowledgment

The authors would like to thank the Office of Naval Research for supporting this work through contract: N00014-96-1-1173

References

[1] C.A. Rosen "Electromechanical Application", in H.W. Katz (eds), Solid State Magnetic and Dielectric Devices, New York: Wiley, pp. 171-229, (1959).

[2] S. Kawashima, O. Ohnishi, H. Hakamata, S. Tagami, A. Fukuoka, T. Inoue, and S. Hirose, "Third Order Longitudinal Mode Piezoelectric Ceramic Transformer and its Application to High-Voltage Inverter" IEEE Int. Ultrasonic Symp, Cannes, 525-530 (1994).

[3] K. Kanayama, N. Maruko and H. Saigoh, "Development of the Multilayer Alternately Poled Piezoelectric Transformers, Jpn. J. Appl. Phys. Vol. 37, pp.2891-2895, 1998 (1998).

[4] B. Koc and K. Uchino, "Disk Type Piezoelectric Transformer with Crescent Shape Input Electrodes", NATO-Advanced Research Workshop: Piezoelectric Materials, Advance in Science, Technology and Applications, Predeal, Romania, May 24-27, (1999).

APPENDIX 49

A DISK TYPE PIEZOELECTRIC TRANSFORMER WITH CRESCENT SHAPE INPUT ELECTRODES

BURHANETTIN KOC AND KENJI UCHINO
International Center for Actuators and Transducers
Materials Research Laboratory
The Pennsylvania State University, University Park PA 16802

Abstract

For most PZT based piezoelectric materials the shear mode coupling constant is twice as large as the transverse mode coupling. From this motivation, a new circular piezoelectric transformer was designed. Non-concentric input electrodes and non-uniform output poling lead to the usage of shear mode piezoelectric effect at (3,0) radial mode resonance frequency. A prototype three layered transformer with 25.4-mm in diameter and 1.5 mm in thickness, operating at 153 kHz, was fabricated and its characteristics were measured. Characteristics, such as efficiency, step-up ratio and temperature rise of the proposed transformer are presented.

1. Introduction

One of the bulkiest components in information processing equipment (such as note-book-type personal computers) is the power supply, specifically the electromagnetic transformer used in power supply. Losses such as skin effect, thin wire loss and core loss of the electromagnetic transformer increase rapidly as the size of the transformer is reduced. Therefore, it is difficult to realize miniature low profile electromagnetic transformers with high efficiency.

High efficiency, small size, no electromagnetic noise are some of the attractive features of piezoelectric transformers making them more suitable for miniaturized power inverter elements such as lighting up the cold cathode fluorescent lamp (CCFL) behind a color liquid crystal displays (LCD) or generating high voltage for air-cleaners.

The original design to transform an input ac voltage to step up or step down using converse and direct piezoelectric properties of ceramic materials was proposed by Rosen [1]. The principle of this type of transformer is to excite a piezoelectric element (Figure 1) at its mechanical resonance frequency. Applying an electrical input to one part of the piezoelectric element generates a mechanical vibration and then this mechanical vibration is converted into electrical voltage from the other part of the piezoelectric plate.

C. Galassi et al. (eds.), Piezoelectric Materials: Advances in Science, Technology and Applications, 375–382.

The initial Rosen type transformer had major reliability problem, which is the easy mechanical breakdown at the center position due to the coincidence of the residual stress concentration and the vibration nodal point. In addition to improved mechanically tough ceramic materials, by redesigning the electrode configuration and exciting a third longitudinal resonance mode of the rectangular plate, the piezoelectric transformer shown in Figure 2a was commercialized by NEC in 1994 for miniaturized back-light inverter to light up the cold cathode fluorescent lamp (CCFL) behind a color liquid crystal displays (LCD) [2].

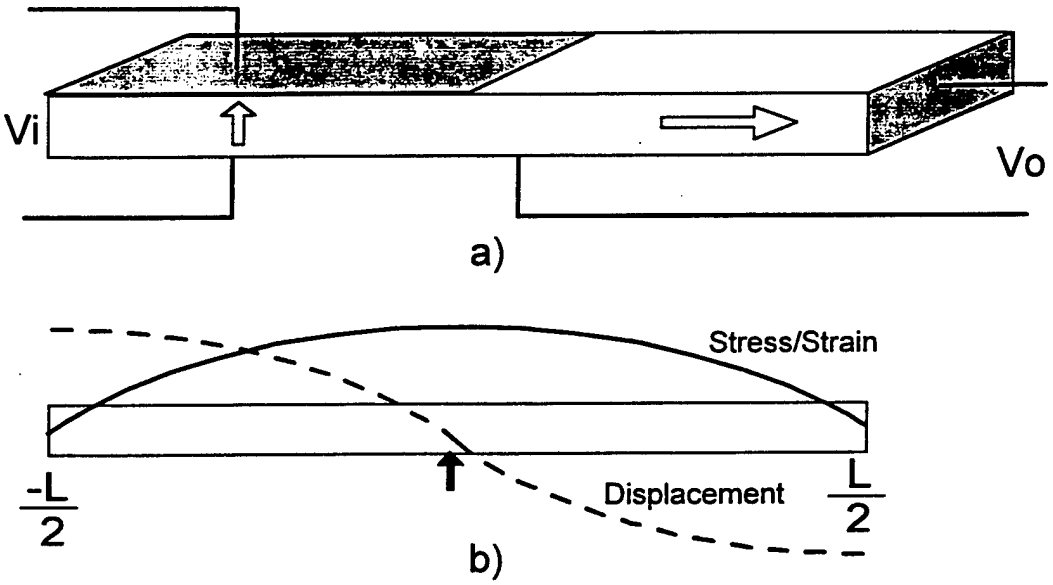

Figure 1. a) Rosen type piezoelectric transformer, b) Stress/strain and displacement distribution at first longitudinal resonance mode.

Another third mode transformer shown in Figure 2b was commercialized, recently, by Mitsui-Sekka to use it also for miniaturized power inverter element [3]. In addition to no electromagnetic noise generation, small size and high efficiency are some of the advantages of the piezoelectric transformers over the electromagnetic types particularly for computer applications.

The third mode transformers have some advantages over original Rosen type first mode transformer, such as follows:
i) for the third mode transformer, stress concentration on the bar is separated into three different points which makes the transformer mechanically stronger. The electric field and stress concentration are not at the same point on the piezoelectric bar, while for the first mode transformer, the maximum stress and nodal point are at the center of the piezoelectric bar that makes the transformer mechanically weaker. This is the major problem of the first mode transformer. Moreover, in order to get higher efficiency the transformer has to be clamped only at a nodal point. Because the third mode transformers have three nodal points on the bar, they can be clamped at two points

easily without affecting the vibration modes. Therefore, third mode transformers can be packaged more safely.

ii) the third mode transformers are more efficient (96%) than the first mode transformers (90 %).

iii) impedance matching of the third mode transformer with CCFL is better than the first mode transformer.

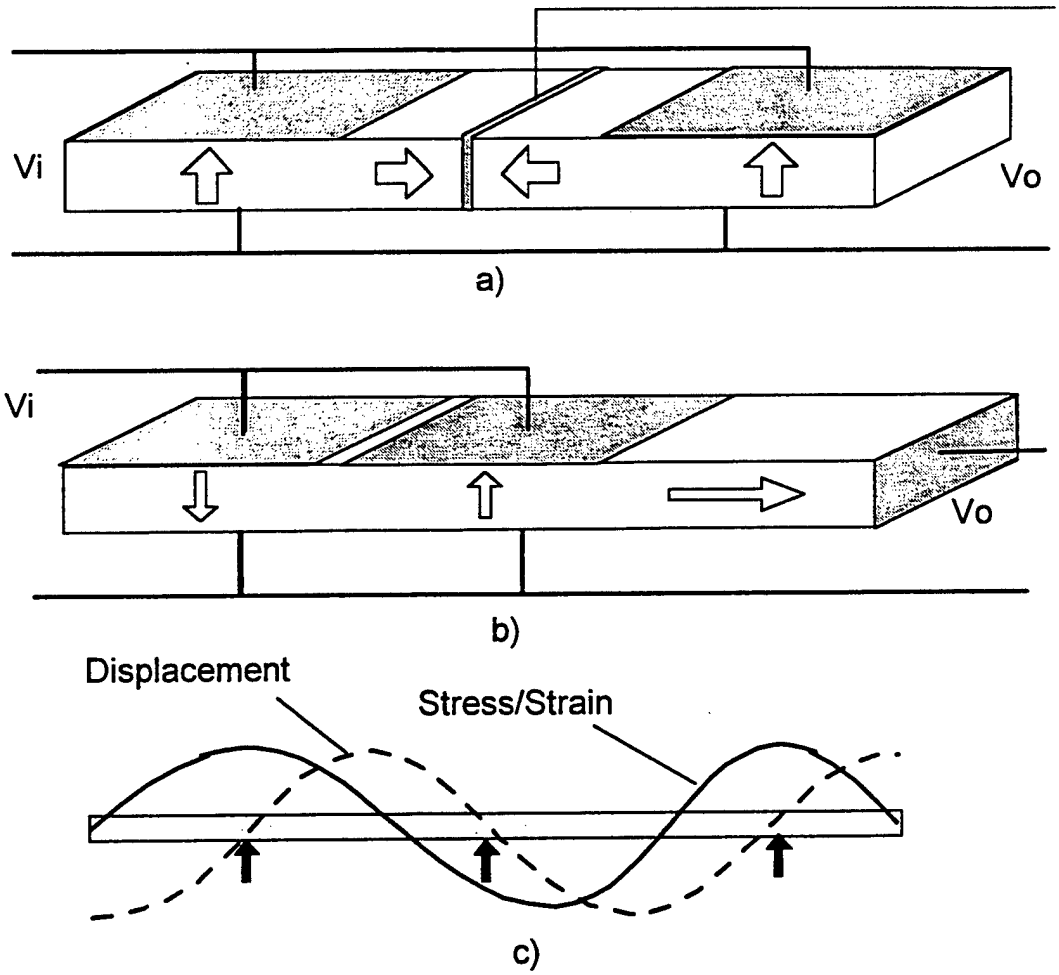

Figure 2. Structures of the third mode piezoelectric transformers, proposed by (a) NEC, (b) Mitsui-Sekka, (c) stress/strain and displacement distribution.

For most PZT based piezoelectric materials, the shear mode coupling constant is twice as large as the transverse mode coupling. From this motivation, a new disk type piezoelectric transformer was designed and it will be introduced in the following section.

2. Disk Type Piezoelectric Transformer

All the rectangular type transformers explained in the previous section are using the transverse mode coupling constant (k_{31}) of the piezoelectric materials. For most piezoelectric materials, however, the shear mode coupling constant (k_{15}) is twice as large as the transverse mode coupling constant (k_{31}). From this motivation, we designed a new circular piezoelectric transformer, which uses shear (k_{15}) or planar (k_p) mode coupling constants of the piezoelectric effect (Fig 3). The transformer is operating at the third radial resonance frequency of the piezoelectric disk.

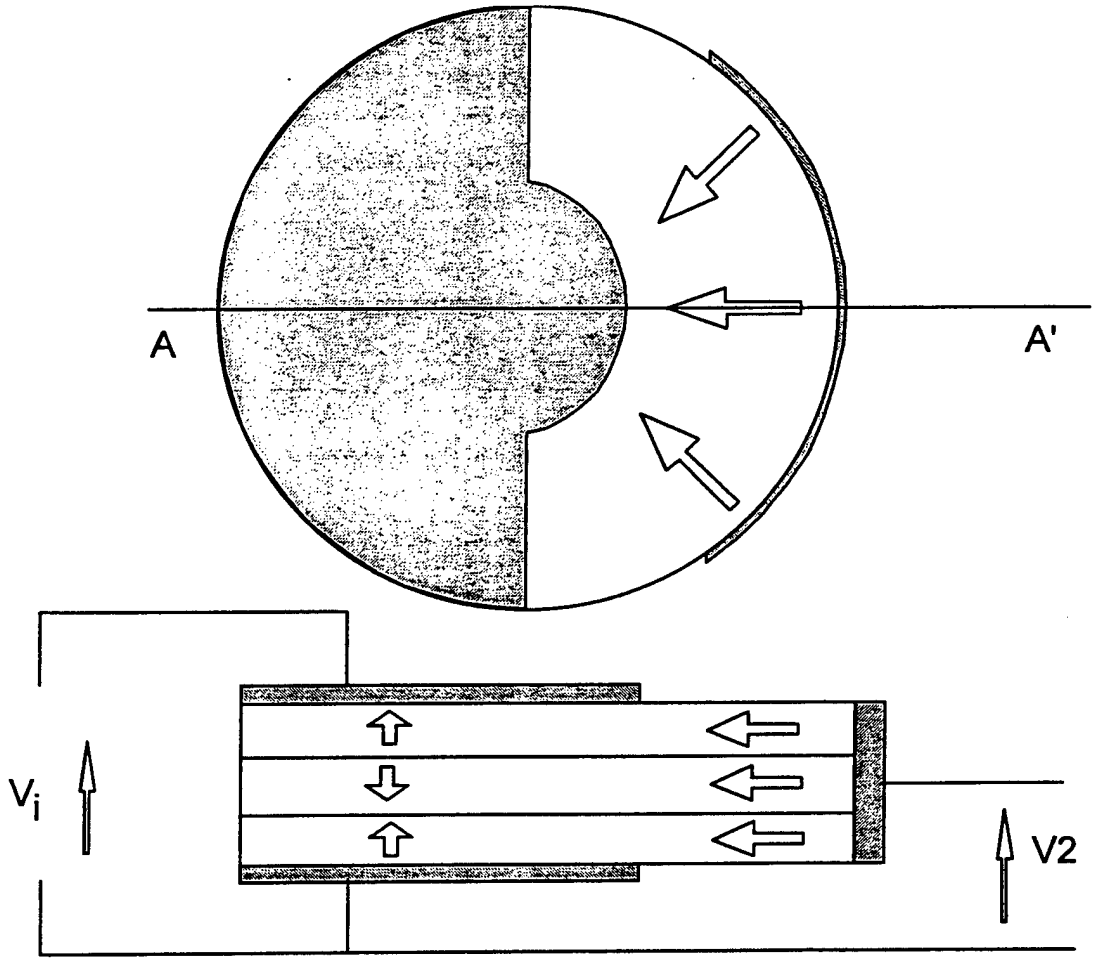

Figure 3. Newly designed circular type piezoelectric transformer structure.

The behavior of the transformer was modeled using ATILA finite element software. The fundamental and third harmonic mode shapes and potential fields are shown in Figures 4 and 5. When the transformer is driven at the first radial resonance frequency it uses planar mode coupling constant effectively. If the transformer is driven at the third

harmonic radial frequency, it uses shear mode coupling coefficient. This can be seen from the mode shape and potential field shown in Figure 5.

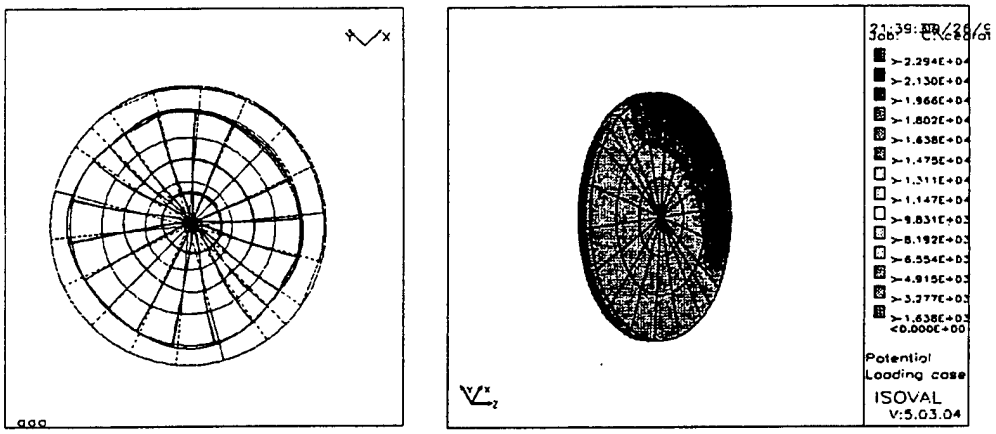

Figure 4. First mode potential field and displacement shape of the circular transformer (67 kHz FEM calculations using ATILA©).

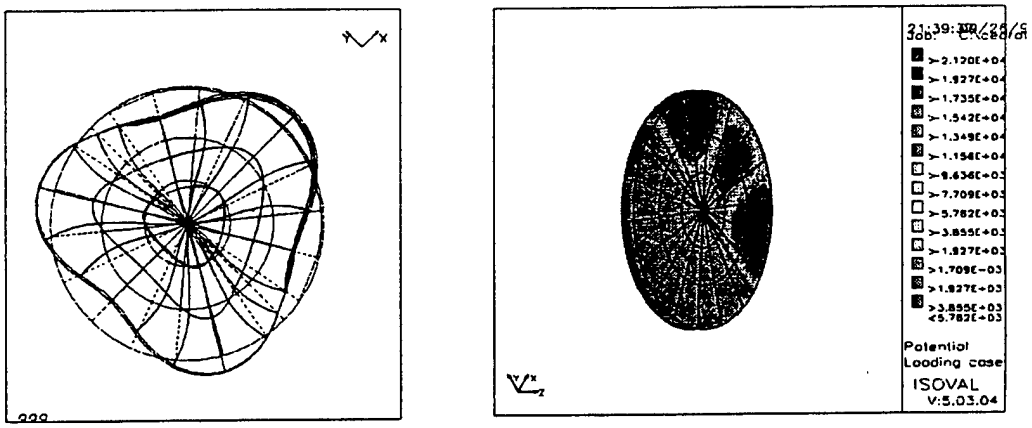

Figure 5. Third mode potential field and displacement shape of the circular transformer (152 kHz FEM calculations using ATILA©).

3. Experimental

The transformer structure shown in Figure 4 was fabricated using commercially available piezoelectric ceramic material (APC International, USA). Hard piezoelectric ceramic disks 25.4 mm in diameter and 0.5 mm in thickness were sputtered with

platinum electrodes according to the proposed electrode configuration. The transformer was subjected to a polarization treatment by applying a DC voltage of 3.0 kV/mm at 150 °C across the input and output electrical terminals. Three identical single layer transformers were then stacked using adhesive epoxy as the last step of the fabrication process.

In order to clarify the operating frequency of the transformer, the input (output terminal open-circuited) and output admittance spectra were measured and the results are shown in Figure 6. The possible operating frequencies of the transformer are first three radial mode resonance frequencies of which both input and output terminals can excite. The best performance was obtained when the transformer was driven at the third mode resonance frequency.

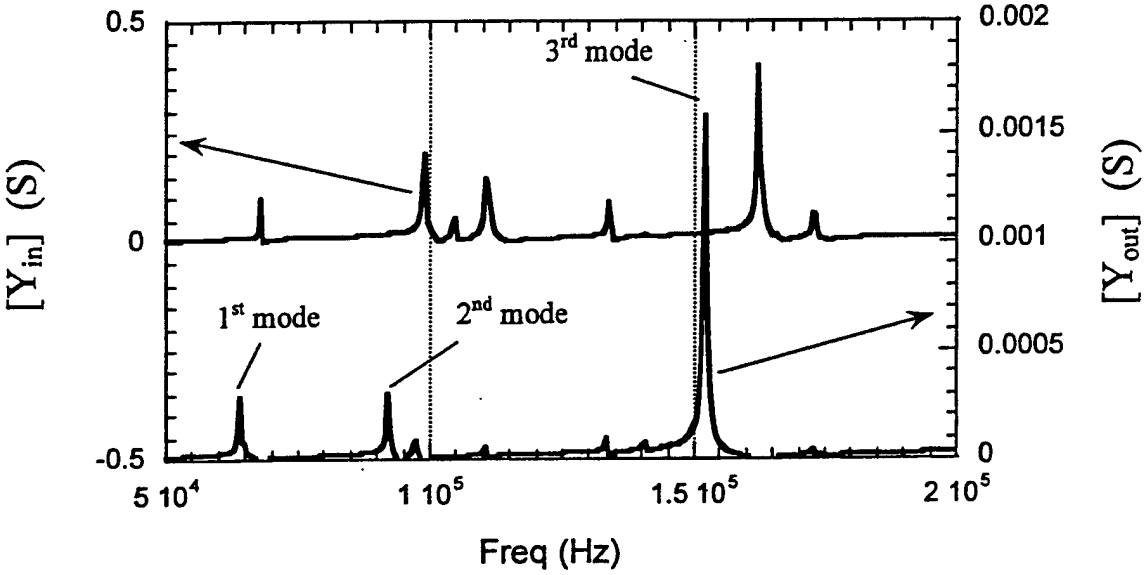

Figure 6. Input and output admittance spectrum.

The transformer low field voltage step-up ratio and efficiency were measured for different resistive loads and the results are shown in Figure 7. The output power on the resistive loads was 1.5 Watts and the transformer was driven around 153 kHz. When measuring the efficiency, the operating frequency of the transformer was tuned so that the maximum efficiency could be obtained for different resistive loads. The efficiency for a resistive load ranging from 100 to 1200 kΩ is found to be around 90 %. For the same range of load resistance, the voltage step up ratio was increased from 70 to 320. These primary results clearly indicate that the proposed transformer can realize a step up ratio and power high enough to light up the cold cathode fluorescent lamp (CCFL) for back-lights in color liquid crystal displays (LCD) when it is operated at the third mode resonance frequency.

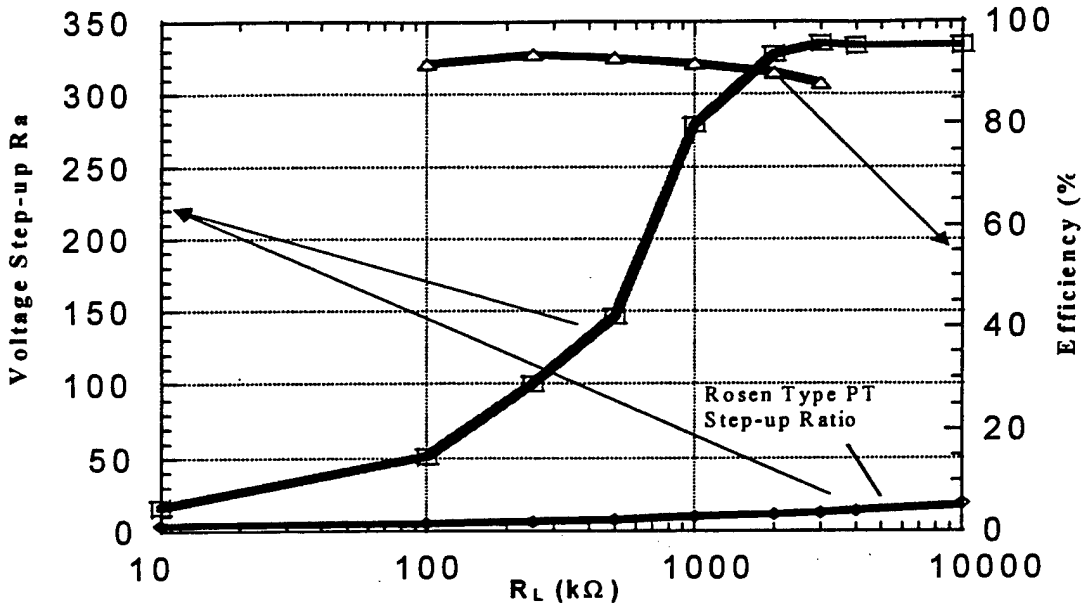

Figure 7. Step-up ratio and efficiency as a function of load resistance.

Figure 8 shows the output/input voltage step-up ratio and temperature rise of the piezoelectric transformer with variable output power for a constant resistive load of 110 kΩ. Temperature rise for a 110 kΩ resistive load is not significant up to 10 Watts of output power. When the output power is further increased, the temperature of the transformer was observed to increase by more than 80 °C from room temperature. The transformer step-up ratio, however, decreased gradually from 100 to 70 for the same load condition.

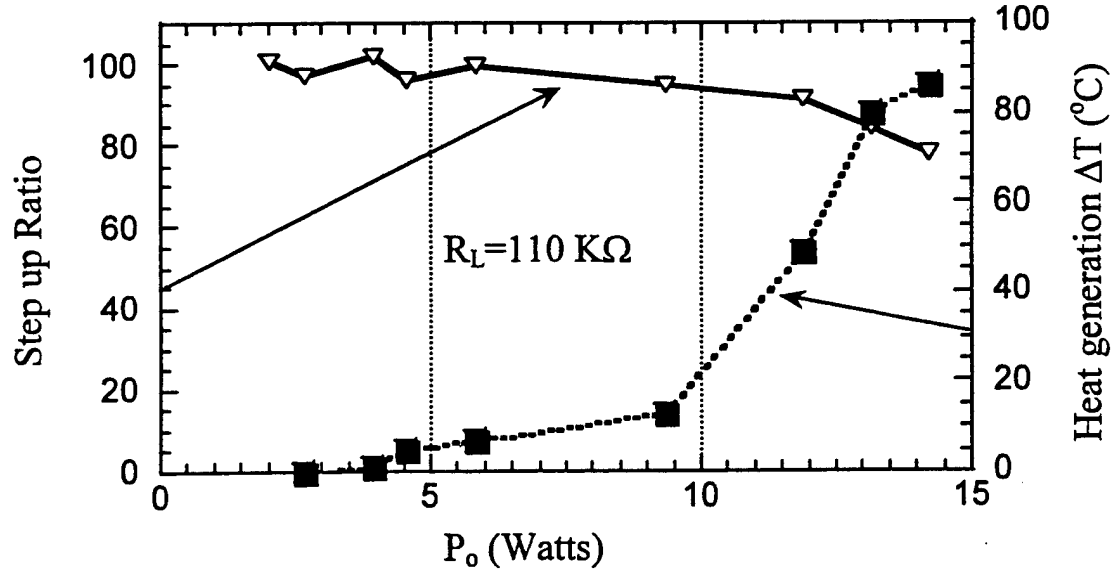

Figure 8. Step-up Ratio and Temperature rise as a function of output power on a resistive load.

4. Conclusions

A new disk type piezoelectric transformer design was proposed using three layered commercially available hard piezoelectric disks. Non-concentric input electrodes and non-uniform output poling lead to the usage of shear mode piezoelectric effect at (3,0) radial mode resonance frequency. A prototype three layered transformer of 25.4-mm in diameter and 1.5 mm in thickness, operating at 153 kHz, was fabricated and its characteristics were measured. The transformer can generate enough step-up ratio and power to light up CCFL for back-light of color liquid crystal displays (LCD) when it is operated at the third mode resonance frequency.

Heat generation and step up ratio as a function of output power was also investigated. Temperature rise for a 110 kΩ resistive load is not significant up to 10 Watts range of output power. When the output power was further increased the temperature of the transformer increased more than 80 °C from room temperature. The transformer step-up ratio however decreased gradually from 100 to 70 for the same load condition.

Acknowledgements

This work was partially supported by the Turkish Higher Educational Council and the Office of Naval Research, USA.

5. References

1. Rosen, C.A. (1959), Electromechanical Application, in H.W. Katz (eds), *Solid State Magnetic and Dielectric Devices*, New York: Wiley, pp. 171-229.
2. Kawashima, S., Ohnishi, O., Hakamata, H., Tagami, S., Fukuoka, A., Inoue, T. and Hirose, S. (1994) Third Order Longitudional Mode Piezoelectric Ceramic Transformer and its Application to High-Voltage Inverter, *IEEE Int. Ultrasonic Symp,* Cannes, 525-530.
3. Kanayama, K., Maruko, N. and Saigoh, H. (1998) Development of the Multilayer Alternately Poled Piezoelectric Transformers, *Jpn. J. Appl. Phys.* Vol. 37, pp.2891-2895, 1998.
4. Tsuchiya, H. and Fukami, T. (1986) Design and Principles for Multilayer Piezoelectric Transformers, *Ferroelectrics*, **68**, 225-234.

ACTUATOR STUDIES

Materials and Designs

APPENDIX 50

Recent Trend of Piezoelectric Actuator Developments

Kenji Uchino
International Center for Actuators and Transducers
Materials Research Laboratory, The Pennsylvania State University
University Park, PA 16802, USA

Abstract:

In these several years, piezoelectric materials have bocome key components in smart actuator/sensor systems such as precision positioners, miniature ultrasonic motors and adaptive mechanical dampers. This paper reviews recent developments of piezoelectric and related ceramic actuators with particular focus on the improvement of actuator materials, device designs and applications.

1. INTRODUCTION

Piezoelectric actuators are forming a new field between electronic and structural ceramics [1-4]. Application fields are classified into three categories: positioners, motors and vibration suppressors. The manufacturing precision of optical instruments such as lasers and cameras, and the positioning accuracy for fabricating semiconductor chips, which must be adjusted using solid-state actuators, is of the order of 0.1 μm. Regarding conventional electromagnetic motors, tiny motors smaller than 1 cm are often required in office or factory automation equipment and are rather difficult to produce with sufficient energy efficiency. Ultrasonic motors whose efficiency is insensitive to size are superior in the mini-motor area. Vibration suppression in space structures and military vehicles using piezoelectric actuators is also a promising technology.

This article reviews recent developments of piezoelectric and related ceramics to smart actuator/sensor systems, including the improvement of actuator materials, design of the devices, and applications.

2 CERAMIC ACTUATOR MATERIALS

Recent four topics are reviewed here.

2.1 Relaxor Single Crystal Transducers

In 1981, we firstly reported an enormously large electromechanical coupling factor k_{33} = 92 - 95% and piezoelectric constant d_{33} = 1500 pC/N in solid solution single crystals between relaxor and normal ferroelectrics, $Pb(Zn_{1/3}Nb_{2/3})O_3$-$PbTiO_3$ [5,6]. This discovery has not been marked for more than 10 years until high k materials have been paid attention in medical acoustics recently. These date have been reconfirmed, and much more improved data were obtained recently, aiming at medical acoustic applications [7,8]. The strains as large as 1.7% can be induced practically for a morphotropic phase boundary composition of the PZN-PT solid solution single crystals. It is notable that the highest values are observed for a rhombohedral composition only when the single crystal is poled along the perovskite [001] axis, not along the [111] spontaneous polarization axis.

2.2 Epitaxial PZT Films

A series of theoretical calculations made on perovskite type ferroelectric crystals suggests that large d and k values in similar magnitudes to PZN-PT can also be expected in PZT. Crystal orientation dependence of piezoelectric properties was phenomenologically calculated for compositions around the morphotropic phase boundary of PZT [9]. The maximum longitudinal piezoelectric constant d_{33} (4 - 5 times enhancement) and electromechanical coupling factor k_{33} (more than 90 %) in the rhombohedral composition were found to be at 57° and 51° angles, respectively, canted from the spontaneous polarization direction [111], which correspond roughly to the perovskite [100] axis.

Figure 1 shows the principle of the enhancement in electromechanical couplings. Because the shear coupling d_{15} is the highest in perovskite piezoelectric crystals, the applied filed should be canted from the spontaneous polarization direction to obtain the maximum strain.

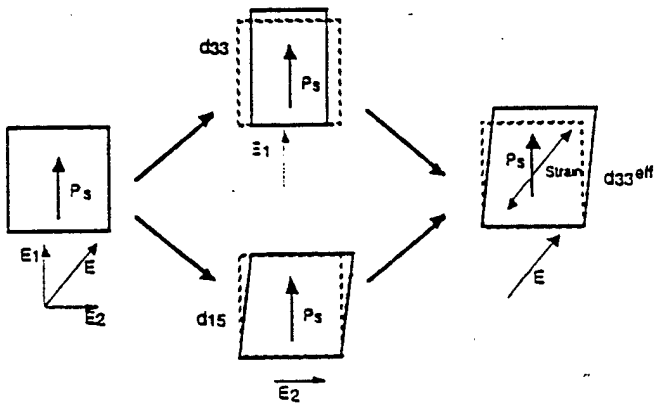

Fig.1 Principle of the enhancement in electromechanical couplings.

1999 INTERNATIONAL SYMPOSIUM ON
MICROMECHATRONICS AND HUMAN SCIENCE
0-7803-5790-6/99/ $10.00

We are demonstrating [001] oriented epitaxially grown thin/thick films using a rhomboherial PZT compostion, which are expected to enhance the effective piezoelectric constant by 4-5 times.

2.3 Phase-Change Materials

Concerning the phase-change-related strains, polarization induction by switching from an antiferroelectric to a ferroelectric state, has been proposed [10]. Figure 2 shows the field-induced strain curves taken for the lead zirconate stannate based $Pb_{0.99}Nb_{0.02}((Zr_xSn_{1-x})_{1-y}Ti_y)_{0.98}O_3$ system. The longitudinally induced strain reaches up to 0.4%, which is larger than that expected in normal piezostrictors or electrostrictors. A rectangular-shape hysteresis in Fig.2 top, referred to as a "digital displacement transducer" because of the two on/off strain states, is interesting. Moreover, this field-induced transition exhibits a shape memory effect in appropriate compositions (Fig.2 bottom). Once the ferroelectric phase has been induced, the material will "memorize" its ferroelectric state even under zero-field conditions, although it can be erased with the application of a small reverse bias field [11]. This shape memory ceramic is used in energy saving actuators. A latching relay is composed of a shape memory ceramic unimorph and a mechanical snap action switch, which is driven by a pulse voltage of 4ms. Compared with the conventional electromagnetic relays, the new relay is much simple and compact in structure with almost the same response time.

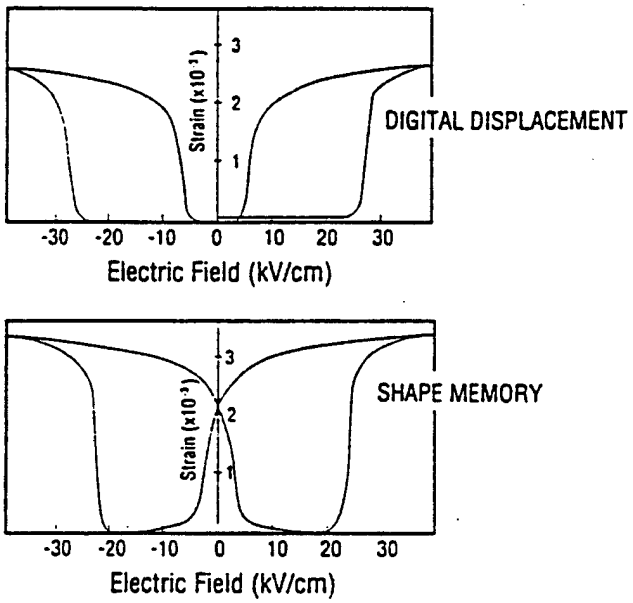

Fig.2 Field-induced strain curves for the lead zirconate stannate system $Pb_{0.99}Nb_{0.02}((Zr_xSn_{1-x})_{1-y}Ti_y)_{0.98}O_3$. Top: x = 0.060, and bottom: x = 0.065.

2.4 Photostrictive Actuators

A photostrictive actuator is a fine example of an intelligent material, incorporating "illumination sensing" and self production of "drive/control voltage" together with final "actuation." In certain ferroelectrics, a constant electromotive force is generated with exposure of light, and a photostrictive strain results from the coupling of this bulk photovoltaic effect to inverse piezoelectricity. A bimorph unit has been made from PLZT 3/52/48 ceramic doped with slight addition of tungsten [12]. The remnant polarization of one PLZT layer is parallel to the plate and in the direction opposite to that of the other plate. When a violet light is irradiated to one side of the PLZT bimorph, a photovoltage of 1 kV/mm is generated, causing a bending motion. The tip displacement of a 20mm bimorph 0.4mm in thickness was 150μm, with a response time of 1 sec.

A photo-driven micro walking device, designed to begin moving by light illumination, has been developed [13]. It is simple in structure, having neither lead wires nor electric circuitry, with two bimorph legs fixed to a plastic board. When the legs are irradiated alternately with light, the device moves like an inchworm with a speed of 100μm/min.

In pursuit of thick film type photostrictive actuators for space structure applications, in collaboration with researchers at Jet Propulsion Laboratory we investigated the optimal range of sample thickness and surface roughness dependence of photostriction. We have found that 30 μm thick PLZT films exhibit the maximum photovoltaic phenomenon [14].

3 ACTUATOR DESIGNS

Two of the most popular actuator designs are multilayers and bimorphs. The multilayer, in which roughly 100 thin piezoelectric/electrostrictive ceramic sheets are stacked together, has advantages in low driving voltage (100V), quick response (10μsec), high generative force (100kgf) and high electromechanical coupling. But the displacement in the range of 10μm is not sufficient for some applications. This contrasts with the bimorph, consisting of multiple piezoelectric and elastic plates bonded together to generate a large bending displacement of several hundred μm, but the response (1msec) and the generative force (100gf) are low.

A multilayer actuator with interdigital internal electrodes has been developed by Tokin [15]. In contrast to the conventional electrode configuration, line electrodes are printed on piezoelectric green sheets, and are stacked so that alternationg electrode lines are displaced by one-half pitch (see Fig.3). This actuator generates motions at right angles to the stacking direction using the longitudinal piezoelectric effect. Long ceramic actuators up to 74 mm in length are manufactured.

A three-dimensional positioning actuators with a stacked structure has been proposed by PI Ceramic (Fig.4), in which shear strain is utilized to generate x and y displacements [16].

A monomorph device has been developed to replace the conventional bimorphs, with simpler structure and manufacturing process. The principle is a superposed effect of piezoelectricity and semiconductivity [17]. The contact between a semiconductor and a metal (Schottky barrier) causes non-uniform distribution of the electric field, even in a compositionally uniform ceramic. Suppose that the ceramic

possesses also piezoelectricity, only one side of a ceramic plate tends to contract, leading to a bending deformation in total. A monomorph plate with 30mm in length and 0.5 mm in thickness can generate 200μm tip displacement, in equal magnitude of that of the conventional bimorphs. The "rainbow" actuator by Aura Ceramics [18] is a modification of the above-mentioned semiconductive piezoelectric monomorphs, where half of the piezoelectric plate is reduced so as to make a thick semiconductive electrode to cause a bend.

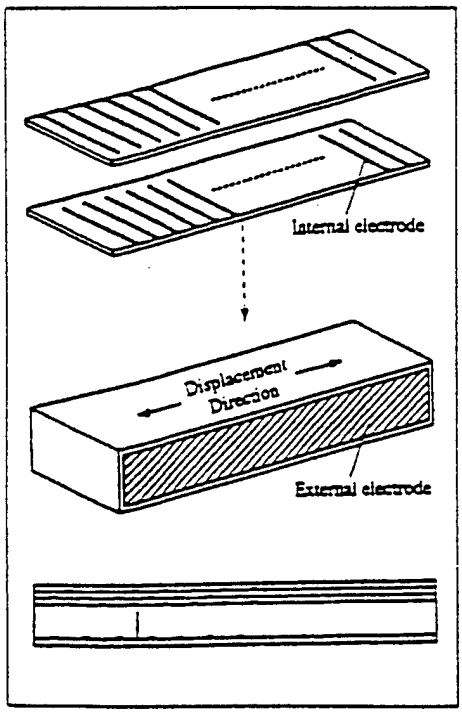

Fig.3 Structure of an internal interdigital electrode actuator.

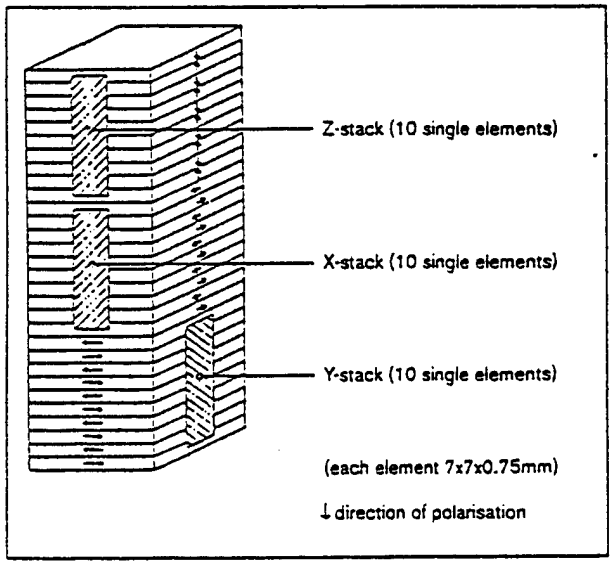

Fig.4 3D controllable multilayer piezoelectric actuator.

A composite actuator structure called the "moonie" has been developed at Penn State to provide characteristics intermediate between the multilayer and bimorph actuators; this transducer exhibits an order of magnitude larger displacement than the multilayer, and much larger generative force with quicker response than the bimorph [19,20]. Figure 5 shows the displacement characteristics for a Moonie, a modified version, and a Cymbal. A Cymbal with a thickness 1-2 mm and a diameter 12 mm can generate a displacement up to 100 μm. This new compact actuator has been applied to make a miniaturized laser beam scanner.

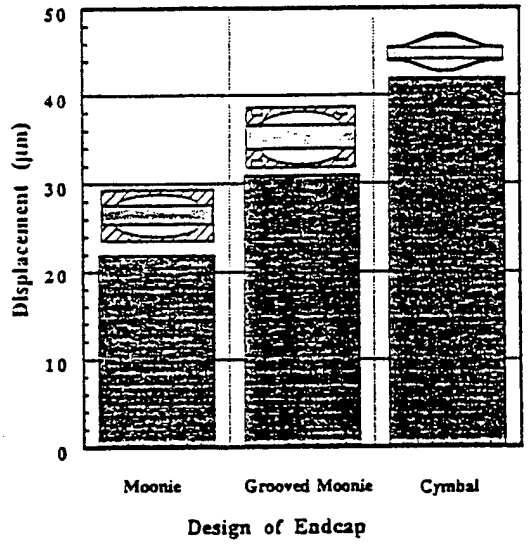

Fig.5 Comparison of the displacement levels for different designs of the endcap in Moonies/Cymbals.

Table I Difference in the ceramic actuator developments among USA, Japan and Europe.

	U.S.	Japan	Europe
TARGET	Military-oriented product	Mass-consumer product	Lab-equipment product
CATEGORY	Vibration suppressor	Micro-motor Positioner	Micro-motor Positioner Vibration suppressor
APPLICATION FIELD	Space structure Military vehicle	Office equipment Camera Precision machine Automobile	Lab stage/stepper Airplane Automobile Hydraulic system
ACTUATOR SIZE	Up-sizing (30 cm)	Down-sizing (1 cm)	Intermediate size (10 cm)
MAJOR MANUFACTURERS	AVX/Kyocera Morgan Matroc Itek Opt. Systems Burleigh AlliedSignal	Tokin Corporation NEC Hitachi Metal Mitsui Chemical Canon Seiko Instruments	Philips Siemens Hoechst CeramTec Ferroperm Physik Instrumente

4 DEVICE APPLICATIONS

Table I compares the difference in the ceramic actuator developments among USA, Japan and Europe. The details will be described in this section.

4.1 USA

The target of the development is mainly for military-oriented applications such as vibration suppression in space structures and military vehicles. Notice the up-sizing trend of the actuators for these purposes.

A typical example is found in a space truss structure proposed by Jet Propulsion Laboratory [21]. A stacked PMN actuator was installed at each truss nodal point and functioned actively so that unnecessary mechanical vibration was suppressed immediately. A "hubble" telescope has also been proposed using multilayer PMN electrostrictive actuators to control the phase of the incident light wave in the field of optical information processing (Fig.6)[22]. The PMN electrostrictor provided superior adjustment of the telescope image because of negligible strain hysteresis.

Passive dampler application is another smart usage of piezoelectrics. Mechanical noise vibration is radically suppressed by the converted electric energy dissipation through Joule heat when a suitable resistance, equal to an impedance of the piezoelectric element $1/\omega C$, is connected to the piezo-element [23]. Piezoceramic:carbon black:polymer composites are promising useful designs for practical application. The damping time constant change with volume percentage of the carbon black, which determines the resistance. The minimum time constant (i.e. quickest damping) was obtained at 6 % of carbon black, where a drastic electric conductivity change was observed (percolation threshold) [24].

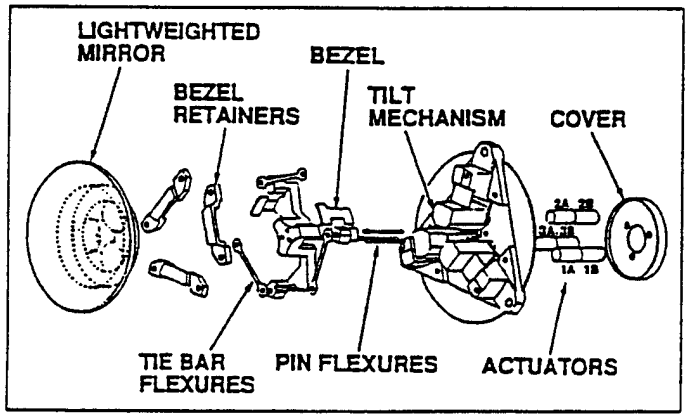

Fig.6 Hubble telescope using PMN electrostrictive actuators.

4.2 Japan

Japanese industries seek to develop mass-consumer products, and the categories are only limited to mini-motor and positioner areas, aiming at the applications to office equipment and cameras/video cameras. In that sense, tiny actuators smaller than 1cm are the main focus.

A dot matrix printer is the first widely-commercialized product using ceramic actuators. Each character formed by such a printer is composed of a 24 x 24 dot matrix. A printing ribbon is subsequently impacted by a multiwire array. A sketch of the printer head appears in Fig.7(a) [25]. The printing element is composed of a multilayer piezoelectric device, in which 100 thin ceramic sheets 100μm in thickness are stacked, together with a sophisticated magnification mechanism (Fig.7(b)). The magnification unit is based on a monolithic hinged lever with a magnification of 30, resulting in an amplified displacement of 0.5 mm and an energy transfer efficiency greater than 50%. A piezoelectric camera shutter is currently the largest production quantity item. A piece of piezoelectric bimorph can open and close the shutter in a milli-second through a mechanical wing mechanism [26]. Piezoelectric gyro-sensors are now widely used to detect the noise motion of a handy video camera. Figure 8 shows a Tokin's cylinder type gyroscope [27]. Among the 6 electrode strips, two of them are used to excite total vibration and the other two pairs of electrode are used to detect the Corioli's force or the rotational acceleration cause by the hand motion. By using the gyro signal, the image vibration can be compensated electrically on a monitor display.

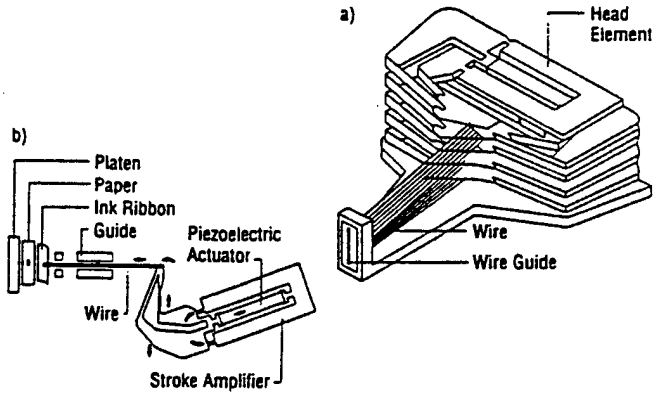

Fig.7 Structure of a printer head (a), and a differential-type piezoelectric printer-head element (b).

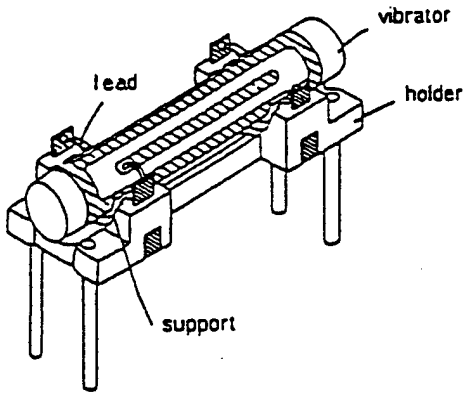

Fig.8 Piezo-ceramic cylinder vibratory gyroscope.

Efforts have been made to develop high-power ultrasonic vibrators as replacements for conventional electromagnetic motors. The ultrasonic motor is characterized by "low speed and high torque," which is contrasted with "high speed and low torque" of the electromagnetic motors. Two categories are being investigated in Japan for ultrasonic motors: a standing-wave type and a propagating-wave type.

The standing-wave type is sometimes referred to as a vibratory-coupler type or a "woodpecker" type, where a vibratory piece is connected to a piezoelectric driver and the tip portion generates flat-elliptical movement. Attached to a rotor or a slider, the vibratory piece provides intermittent rotational torque or thrust. The standing-wave type has , in general, high efficiency, but lack of control in both clockwise and counterclockwise directions is a problem. An ultrasonic linear motor equipped with a multilayer piezoelectric actuator and fork-shaped metallic legs has been developed as shown in Fig.9 [28]. Since there is a slight difference in the mechanical resonance frequency between the two legs, the phase difference between the bending vibrations of both legs can be controlled by changing the drive frequency. The walking slider moves in a way similar to a horse using its fore and hind legs when trotting. A trial motor 20 x 20 x 5 mm^3 in dimension exhibited a maximum speed of 20 cm/s and a maximum thrust of 0.2 kgf with a maximum efficiency of 20%, when driven at 98kHz of 6V (actual power = 0.7 W). This motor has been employed in a precision X-Y stage.

By comparison, the propagating-wave type (a surface-wave or "surfing" type) combines two standing waves with a 90 degree phase difference both in time and in space, and is controllable in both rotational directions (Fig.10) [29]. By means of the traveling elastic wave induced by the thin piezoelectric ring, a ring-type slider in contact with the "rippled" surface of the elastic body bonded onto the piezoelectric is driven in both directions by exchanging the sine and cosine voltage inputs. Another advantage is its thin design, which makes it suitable for installation in cameras as an automatic focusing device. 80 % of the exchange lenses in Canon's "EOS" camera series have already been replaced by the ultrasonic motor mechanism.

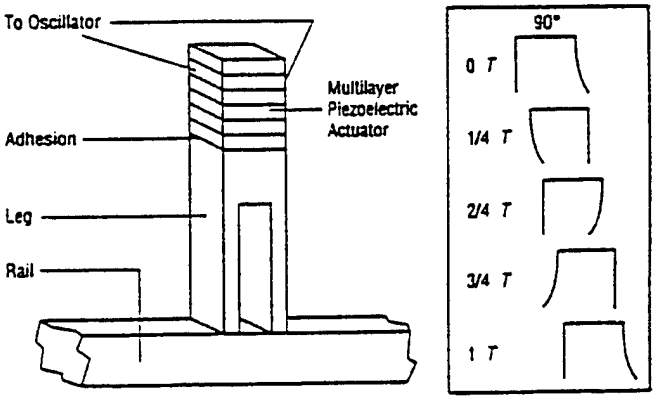

Fig.9 Ultrasonic linear motor of a vibratory coupler type.

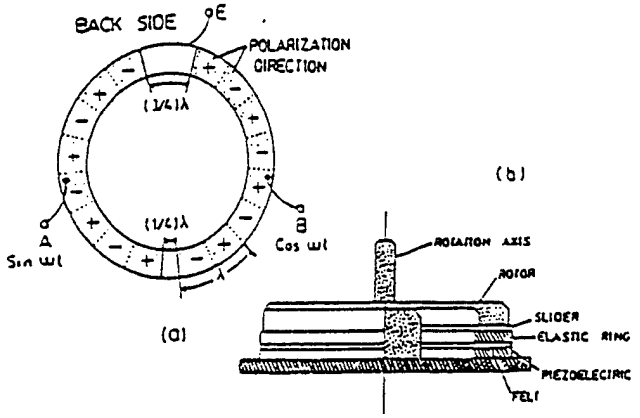

Fig.10 Design of the surface wave type motor (a), and its electrode configuration (b).

4.3 Europe

Ceramic actuator development has started relatively recently in Europe, and the research topics diverges very widely. However, the current focus by major manufacturers is probably put on lab-equipment products such as lab-stages and steppers with sophisticatedly complicated structures.

Figure 11 shows a walking piezo motor with 4 multilayer actuators [30]. Shorter two are used to function as clamplers and longer two provide the proceeding distance in an inchworm mechanism.

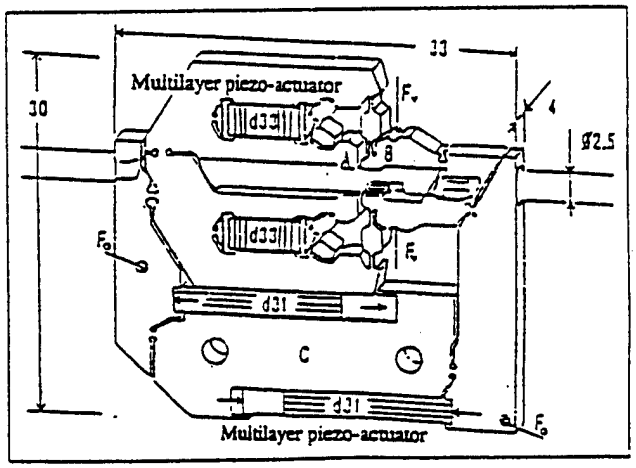

Fig.11 Walking piezo motor.

5 FUTURE OF CERAMIC ACTUATORS

5.1 Market of Piezoelectric Actuators

20 years have passed since the intensive development of piezoelectric actuators began in Japan, then spreaded worldwidely. Presently, the focus has been shifted to practical device applications.

The market in USA is limited to military and defense applications, and it is difficult to estimate the sales amount. The current needs from Navy are smart submarine skins,

hydrophone actuators, prop noise cancellation etc., and smart aircraft skins from Air Force, while Army requires hilicopter rotor twisting, aeroservoelastic control and cabin noise/seat vibration cancellation.

The European situation is still too early to calculate the market size, because most of the manufacturing is a prototyping stage sometimes under the government support.

On the contrary in Japan, ink-jet printers (Epson), piezoelectric shutters (Minolta Camera) and automatic focusing mechanisms (Canon) in cemeras, dot-matrix printers (NEC) and part-feeders (Sanki) are now commercialized and mass-produced by tens of thousands of pieces per month. During the commercialization, new designs and drive-control techniques of the ceramic actuators have been mainly developed in the past few years. A number of patent disclosures have been found particularly in NEC, TOTO Corporation, Matsushita Electric, Brother Industry, Toyota Motors, Tokin, Hitachi Metal, Toshiba etc.

5.2 Future Research Trend

Future research trends will be divided into two ways: up-sizing in space structures and down-sizing in office equipment. Further down-sizing will also be required in medical diagnostic applications such as blood test kits and surgical catheters. Piezoelectric thin films campatible with silicon technology will be much focused in micro-electromechanical systems. An ultrasonic rotary motor as tiny as 2 mm in diameter fabricated on a silicon membrane is a good example [31].

One ceramic multilayer component actuator proposed by Mitsui Chemical is very suggestive for predicting the future trend. Figure 12 shows the electrode pattern [32]. Only by the external connection, a combined vibration of the longitudinal L_1 and bending B_2 modes can be excited.

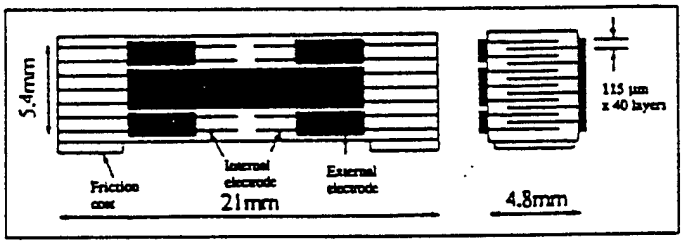

Fig.12 Multilayer ceramic simple linear motor (Mitsui Chemical).

The Penn State University has developed a compact ultrasonic rotory motor as tiny as 3 mm in diameter. As shown in Fig. 13, the stator consists basically of two piezoelectric rings and a metal ring with "windmill" shaped fingers bonded together, so as to generate a coupled vibration of radial and bending types on a finger [33]. Since the component number and the fabrication process were minimized, the fabrication price would be decreased remarkably, and it would be adaptive to the disposable usage. When driven at 160 kHz, the maximum revolution 2000rpm and the maximum torque 0.8mN·m were obtained for a 5 mm motor. Notice that even the drive of the motor is intermittent, the output rotation becomes very smooth because of the inertia of the rotor. Figure 14 shows motor characteristics plotted as a function of motor size for "windmill" motors.

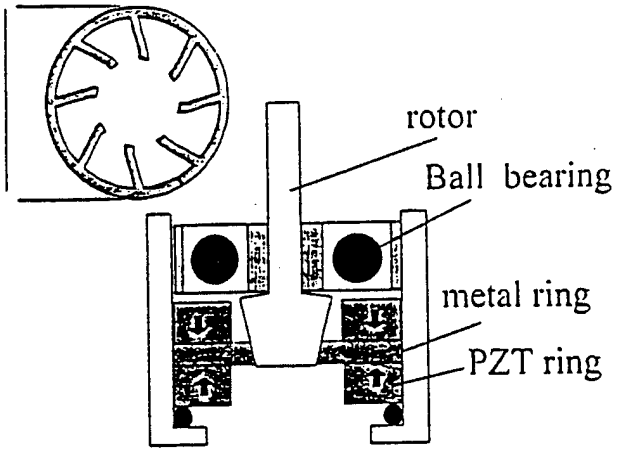

Fig.13 Compact ultrasonic motor with a "windmill"-shaped torsional coupler.

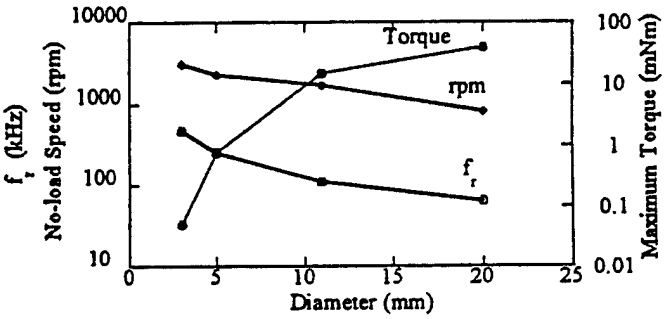

Fig.14 Radial mode resonance frequency, no-load speed and starting torque vs. diameter of the stator. Speed and torque were measured at 15.7 V.

With expanding the application field of ceramic actuators, the durability/reliability issue becomes more important. The final goal is, of course, to develop much tougher actuator ceramics mechanically and electrically. However, the reliability can be improved significantly if the destruction symptom of the actuator is monitored.

Safety systems or health monitoring systems have been proposed with two feedback mechanisms: position feedback which can compensate the position drift and the hysteresis, and breakdown detection feedback which can stop the actuator system safely without causing any serious damages onto the work, e.g. in a lathe machine [34]. Acoustic emission and

internal potential measurements, and resistance monitoring of a strain-gauge type internal electrode embedded in a piezo-actuator under a cyclic electric field drive are good predictors for the life time [35].

Future research and development should focus on superior systems ecologically (i.e. fit for human!) as well as technologically. Safety systems, which can monitor the fatigue or the destruction symptom of materials/devices, and stop the equipment safely without causing serious problems, will be desired.

REFERENCES

[1] K.Uchino, Piezoelectric/Electrostrictive Actuators, Morikita Publishing, Tokyo 1986
[2] K.Uchino, Bull.Am.Ceram.Soc., 65(4), 647 (1986)
[3] K.Uchino, MRS Bull., 18(4), 42 (1993)
[4] K.Uchino, Proc. 4th Int'l Conf. Electronic Ceramics & Appl., p.179(1994)
[5] J.Kuwata, K.Uchino and S.Nomura, Ferroelectrics, 37, 579 (1981)
[6] J.Kuwata, K.Uchino and S.Nomura, Jpn.J.Appl.Phys., 21, 1298 (1982)
[7] K.Yanagiwawa, H.Kanai and Y.Yamashita, Jpn.J.Appl. Phys., 34, 536 (1995)
[8] S.E.Park and T.R.Shrout, Mat.Res.Innovt., 1, 20 (1997)
[9] X.H.Du, J.Zheng, U.Belegundu and K.Uchino, J.Appl. Phys.Lett., 72, 2421 (1998)
[10] K.Uchino and S.Nomura, Ferroelectrics, 50(1), 191 (1983)
[11] A.Furuta, K.Y.Oh and K.Uchino, Sensors and Mater., 3(4), 205 (1992)
[12] K.Uchino, Mat.Res.Innovat., 1, 163 (1997)
[13] K.Uchino, J.Rob.Mech., 1(2), 124 (1989)
[14] P.Poosanaas, K.Tonooka and K.Uchino, J.Mechatronics [in press]
[15] J.Ohashi, Y.Fuda and T.Ohno, Jpn.J.Appl.Phys., 32, 2412 (1993)
[16] A.Banner and F.Moller, Proc. 4th. Int'l Conf. New Actuators, AXON Tech.Consult.GmbH, p.128 (1995)
[17] K.Uchino, M.Yoshizaki, K.Kasai, H.Yamamura, N. Sakai and H.Asakura, Jpn.J.Appl.Phys., 26(7), 1046 (1987)
[18] Aura Ceramics, Inc., Catalogue "Rainbow"
[19] Y.Sugawara, K.Onitsuka, S.Yoshikawa, Q.C.Xu, R.E.Newnham and K.Uchino, J.Am.Ceram.Soc., 75(4), 996 (1992)
[20] A.Dogan, K.Uchino and R.E.Newnham, IEEE Trans. .UFFC, 44,597 (1997)
[21] J.T.Dorsey, T.R.Sutter and K.C.Wu, Proc. 3rd Int'l Conf. Adaptive Structures, p.352 (1992)
[22] B.Wada, JPL Document D-10659, p.23 (1993)
[23] K.Uchino and T.Ishii, J.Jpn.Ceram.Soc., 96(8), 863 (1988)
[24] Y.Suzuki, K.Uchino,H.Gouda,M.Sumita,R.E.Newnham and A.R.Ramachandran, J.Jpn.Ceram.Soc., 99 (11), 1135 (1991)
[25] T.Yano, I.Fukui, E.Sato, O.Inui and Y.Miyazaki, Proc. Electr. & Commun.Soc., p.1-156 (Spring,1984)
[26] Y.Tanaka, Handbook on New Actuators for Precision Control, Fuji Technosystem, p.764 (1994)
[27] Tokin Corporation, Catalogue "Ceramic Gyro"
[28] M.Tohda, S.Ichikawa, K.Uchino and K.Kato, Ferroelectrics, 93, 287 (1989)
[29] Y.Akiyama (Editor), Ultrasonic Motors/Actuators, Triceps, Tokyo 1986
[30] M.P.Koster, Proc. 4th Int'l Conf. New Actuators, Germany, p.144 (1994)
[31] A.M.Flyn, L.S.Tavrow, S.F.Bart, R.A.Brooks, D.J. Ehrlich, K.R.Udayakumar and L.E.Cross, J. Microelectro-mechanical Systems, 1, 44 (1992)
[32] H.Saigo, 15th.Symp.Ultrasonic Electronics, No.PB-46, p.253 (Nov.1994)
[33] B.Koc and K.Uchino, IEEE int'l. Ultrasonic Symp., YY-6, Sendai, Japan (Oct.1998)
[34] K.Uchino, J.Industrial Education Soc. Jpn., 40, 28 (1992)
[35] K.Uchino and H.Aburatani, Proc. 2nd Int'l Conf. Intelligent Materials, p.1248 (1994)

APPENDIX 51

Design and Fabrication of a High Performance Multilayer Piezoelectric Actuator with Bending Deformation

Kui Yao, *Member, IEEE*, Weiguang Zhu, *Member, IEEE*, Kenji Uchino, *Member, IEEE*, Zhe Zhang, and Leong Chew Lim, *Life Member, IEEE*

Abstract—A new bending mode multimorph actuator was designed and fabricated successfully by a multiple screen printing process. Unlike the conventional bimorph actuator in which the bend occurs in the thickness direction, the bend in the multimorph actuator occurs in the widthwise direction because of synchronistical deformation of each single monolithic layer in the multilayer structure. The theoretical analysis and experimental measurements were conducted to study the performance of this type of actuator, and a comparison was made with the conventional bimorph actuator. Larger displacement, higher resonance frequency, and much larger blocking force could be achieved with the multimorph actuator than with a bimorph actuator of similar dimensions. The multimorph actuator presented in this paper provides a valuable alternative for actuator applications beyond those available with the popular bimorph and longitudinal multilayer actuators.

I. Introduction

MULTILAYER and bimorph actuators are two popular piezoelectric ceramic designs currently in wide use [1]. The multilayer piezoelectric actuator has several advantages: quick response, large generative force, and high electromechanical coupling. Many applications such as a printer head [2] and an X-Y stage [3] have been attempted using the multilayer actuators. However, higher displacement/voltage sensitivity can only be achieved for this type of actuator by greatly increasing the number of piezoelectric layers and decreasing the thickness of each layer, resulting in higher cost, lower reliability, and larger dimensions. Compared with the multilayer stack structure, the bimorph actuator consists of a simple, low cost structure that has been applied in tracking control systems [4] and swing CCD mechanisms [5]. Unfortunately, this kind of actuator can only provide a small generative force and has a low resonance frequency, thus limiting its responsivity.

In some specific cases, such as the magnetic head tracking mechanism in the hard disk drive of a computer, high displacement/voltage sensitivity as well as high resonance frequency are essential for the successful application of an actuator in the servo control system. The applicability of the aforementioned two types of actuators for this case is restrained because of the low resonance frequency of the bimorph structure and the low displacement/voltage sensitivity of the multilayer structure. It was disclosed that a multilayer piezoelectric actuator could be built in the distal end portion of the head-supporting arm of the hard disk drive to position the head precisely [6]. However, to achieve sufficient displacement, this required large numbers of piezoelectric layers coupled with increasing cost and/or a voltage that is too high for hard disk drive applications. Moreover, the large mass and moment of inertia to be driven by the d_{33}-based longitudinal actuator and the corresponding additional mechanical structure limit the feasibility of the entire dynamic mechanism.

A new design for a piezoelectric actuator compromising the merits of high displacement/voltage sensitivity, high resonance frequency, and low cost is presented in this paper. Such a multilayer piezoelectric actuator essentially consists of a multilayer bending mode actuator with displacement occurring in the transverse widthwise direction. The blocking force, resonance frequency, and even the displacement/voltage sensitivity can be greatly improved over the conventional bimorph actuator. This new design is substantially different from the previously reported multimorph bending actuator [7] in which displacement occurs in the thickness direction as is the case for the bimorph structure.

In the conventional fabrication process for bimorph actuators, two ceramic plates are bonded using a cohesive coating, such as resin. However, this method is not efficient to realize a multilayer structure capable of low-driving voltage, miniaturization, and hybridization. Therefore, a thick-film, multiple screen printing process followed by cofiring of metal electrodes and ceramic layers has been applied to produce the newly designed bending mode actuators. Some studies about fabricating d_{33}-based longitudinal piezoelectric multilayer actuators by the screen print-

Manuscript received September 9, 1998; accepted December 16, 1998. The authors gratefully acknowledge the support of Data Storage Institute of Singapore.

K. Yao is with the Institute of Materials Research and Engineering, Singapore 119260 and the Microelectronics Center, School of Electrical and Electronic Engineering, Nanyang Technological University, Singapore 639798. His current address is A5 Materials Research Laboratory, The Pennsylvania State University, University Park, PA 16802 (e-mail:k-yao@imre.org.sg).

W. Zhu and Z. Zhang are with the Microelectronics Center, School of Electrical and Electronic Engineering, Nanyang Technological University, Singapore 639798.

K. Uchino is with the International Center for Actuators and Transducers, Materials Research Laboratory, The Pennsylvania State University, University Park, PA 16802.

L. C. Lim is with the Institute of Materials Research and Engineering, Singapore 119260.

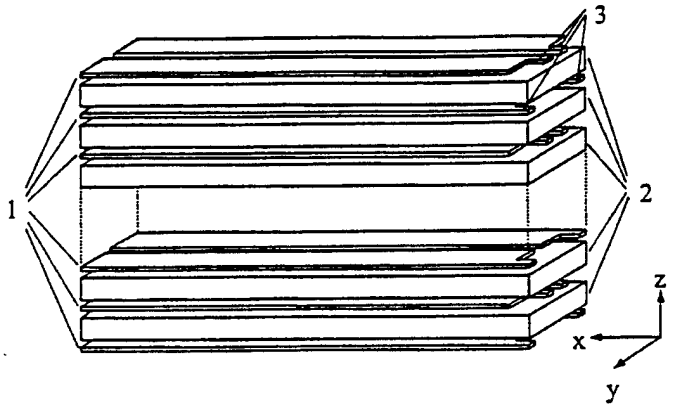

Fig. 1. An exploded view for the assembly of the multiple electrode and piezoelectric layers in the multilayer bending mode actuator, 1–electrode layers, 2–piezoelectric layers, and 3–the electrode fingers.

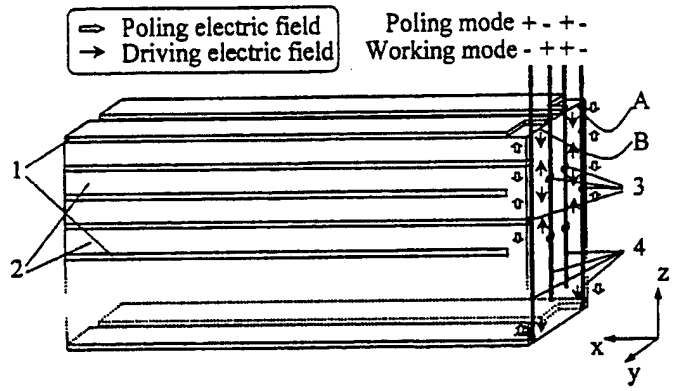

Fig. 2. The structure and working principle for the multilayer bending mode actuator: 1–electrode layers, 2–piezoelectric layers, 3–the terminals of the electrode fingers, and 4–the four external electrical leads. A and B stand for the two symmetric portions of the actuator.

ing methods have been reported in previous literature [8], [9]. The preparation process is compatible with the industrial manufacturing process to keep high yield and productivity at low cost.

II. Design of the Actuator

Fig. 1 shows an exploded view of the new multilayer piezoelectric device design comprising a plurality of piezoelectric layers alternately laminated with a plurality of electrode layers. Each of electrode layers includes a separate pair of electrodes with each separate electrode portion consisting of a finger at its terminal point. The two fingers of each odd-numbered electrode layer are spaced by much smaller distance in the widthwise direction (i.e., the y direction in Fig. 1) than that between the fingers of even-numbered electrode layers. Therefore, the four groups of exposed terminals of the fingers can be connected to their separate external electrical collectors as shown in Fig. 2.

Thus, each piezoelectric layer is sandwiched between two pairs of electrodes, and the two electrodes of each pair are opposed in the thickness direction (i.e., the z direction). From the view along the length direction (i.e., the x direction) the multilayer actuator seems to be divided into two symmetric portions, which are designated as A and B, respectively, in Fig. 2. The poling electric field can be applied to each half of each piezoelectric ceramic layer separately through the external electrodes as depicted in Fig. 2. The resulting polarization vectors of all of the piezoelectric ceramic layers in each portion of the actuator are parallel with each other in the z direction in the same portion. However, the polarization vector of the piezoelectric ceramic layers in portion A is anti-parallel to those in portion B.

The driving field is applied such that on each half of the piezoelectric layer, the electric field is parallel to the polarization vector in each layer of one portion of the actuator but antiparallel to the polarization vector in each layer of the other portion. Consequently, each piezoelectric ceramic layer in one portion of the multilayer body extends synchronistically in the x direction, and each layer in another portion of the multilayer body contracts in the x direction. Thus, a transverse bending deformation is realized in the y direction. Clamping the end of the actuator to form a cantilever beam, a displacement of the free end is produced in the widthwise direction.

The poling mode shown in Fig. 2 is not only for the designed structure. Another working mode is that in which the poling vector of all layers is kept parallel but the applied drive electric fields in the two portions are antiparallel to each other.

III. Preparation and Morphology of the Actuator

The samples were prepared from lead zirconate titanate (PZT) by a multiple screen printing process. PZT ceramic powders (Shanghai Ceramic Institute, Shanghai, China) with 4 wt% lead oxide powders added were dispersed in a commercial organic vehicle, and then the mixture was ball-milled to prepare the thick film paste. Excess PbO was added to the PZT powders to promote the sintering process and to compensate Pb loss caused by vaporization at a high firing temperature.

The prepared PZT paste and commercial Pd-Ag paste were printed on Al_2O_3 substrate alternatively to construct the multilayer structure. Each PZT layer is rectangular shaped, and each electrode layer includes a separate pair of electrodes such that the odd-numbered electrode layers and even-numbered electrode layers have the terminal fingers spaced by a different distance in the widthwise direction, as depicted in Fig. 2. Fig. 3 shows the photo of the PZT multilayer green bodies printed on 2×2 inch Al_2O_3 substrates. Multiple printings are required for each PZT layer to achieve the expected thickness. After being released from the substrate, the multilayer green bodies were cofired at 1130°C in a furnace.

Each fired PZT layer is about 60 to 70 μm, and each

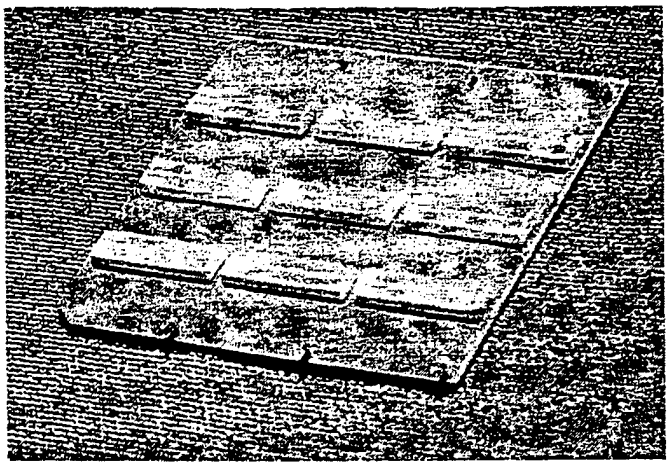

Fig. 3. The photo of the PZT multilayer green bodies printed on the 2×2 inch Al_2O_3 substrate.

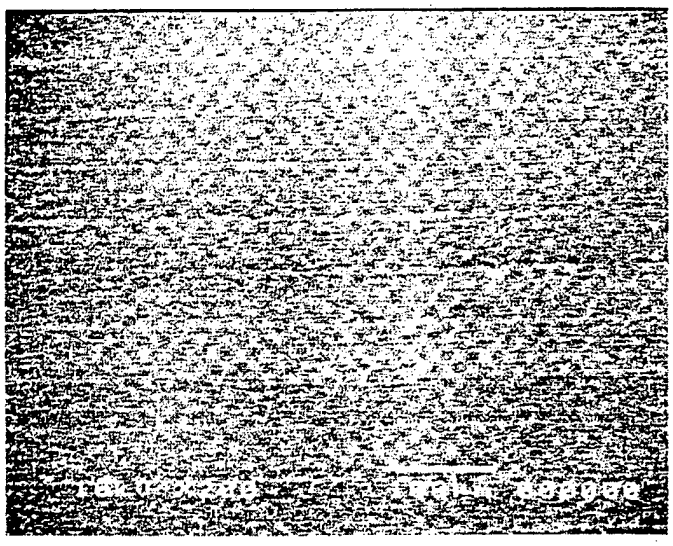

Fig. 4. The cross-sectional morphologies of the PZT multilayer cofired with Pd-Ag electrode.

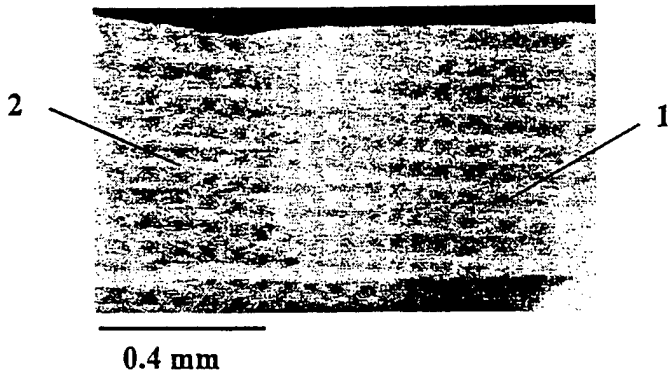

Fig. 5. Two adjacent groups of the terminals of the electrode fingers that are exposed in the side surface of the laminate body for electrical connection. 1–Exposed terminals of the electrode fingers, and 2–PZT.

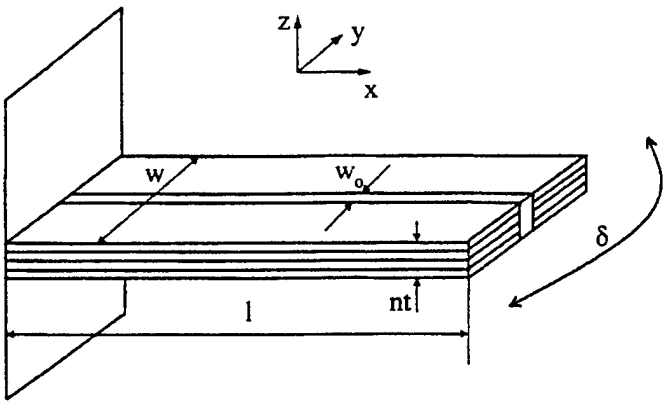

Fig. 6. The schematically illustrated structure of the cantilevered PZT multimorph actuator.

electrode layer is approximately 3 to 5 μm in thickness. Multilayer samples with 7 to 15 layers were fabricated. The scanning electron microscopic (SEM; JEOL-JSM-5410LV) photo of the cross-section of the multilayer sample, as presented in Fig. 4, shows a dense cofired multilayer structure. Two adjacent groups of the edges of the electrode fingers, exposed in the side surface of the laminate body for electrode connection, are shown in Fig. 5. The electrode terminal groups are clearly spaced from each other so that they can be connected to separate electrical leads.

Four fine leads were bonded to the four groups of exposed edges of the electrode finger, respectively, as illustrated in Fig. 2. The final multimorph sample consisted of an overall width of 3.5 mm and a length of 11 mm. The total thickness of the sample depends on the number of the layers. For 7-layer to 15-layer samples, the thickness is about 0.44 to 0.95 mm, respectively.

Finally, the multilayer samples were poled as illustrated in Fig. 2 with a voltage of 250 V for 30 min to obtain the multimorph actuators.

IV. Experimental Measurements

The multimorph actuator was clamped in one end to form a cantilever structure as shown in Fig. 6, and the bend displacement δ in widthwise direction was measured by an HP 5529A due-frequency dynamic laser interferometer controlled by a host computer. The laser interferometer was set on an optical table and was well shielded to minimize environmental disturbance. In terms of the Doppler-shift effect, the displacement of the actuator response was determined from variations in frequency of the reflected laser beam from a highly reflective mirror, which was adhered to the lateral surface of the free end of the actuator. The specified resolution of the system was 1 nm for static displacement measurement and 10 nm for the time-based dynamic measurement.

Fig. 7 shows the static displacement of a cantilevered multimorph actuator in response to a step voltage. The efficient length of the cantilevered sample, excluding the length of the clamped stub, was about 9.2 mm. The stepped voltage was increased from 0 to 12 V (correspond-

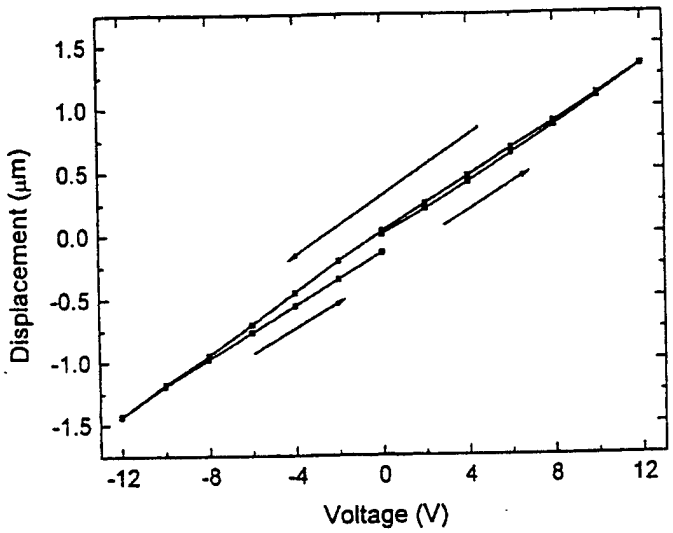

Fig. 7. The static displacement of a multimorph actuator sample in widthwise direction in response to step voltage (l = 9.2 mm, w = 3.5 mm, w_0 = 0.3 mm, n = 15, and nt = 0.945 mm). The designations as specified in Fig. 6.

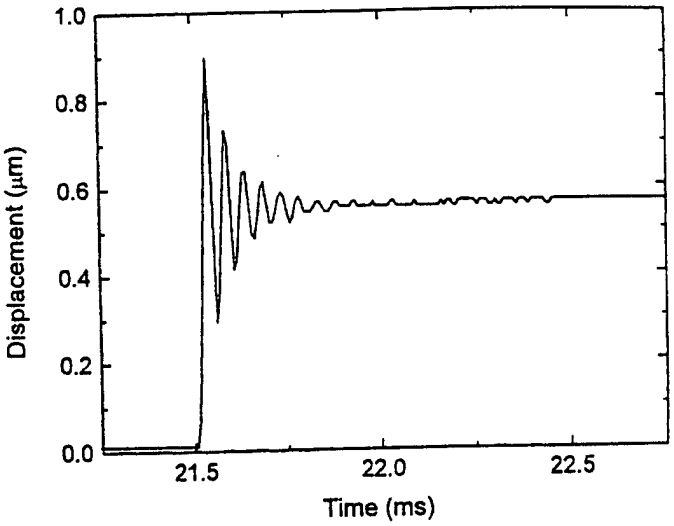

Fig. 9. The real time transient vibration of a multimorph actuator sample in response to a step voltage (l = 9.2 mm, w = 3.5 mm, w_0 = 0.3 mm, n = 15, nt = 0.945 mm, and V = 6 V). The designations as specified in Fig. 6.

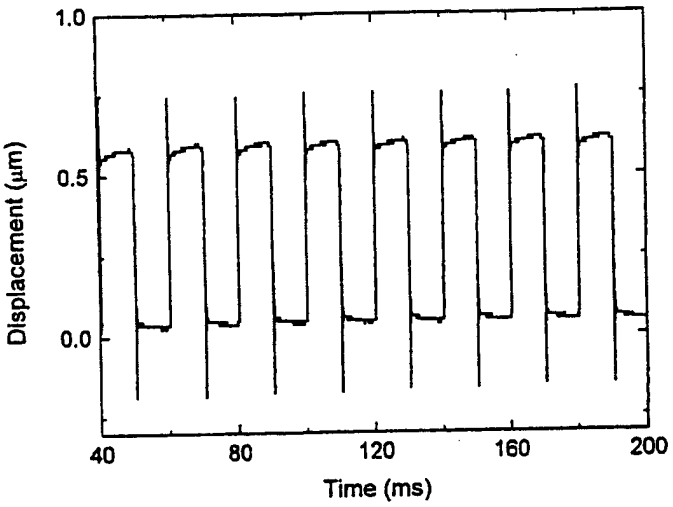

Fig. 8. The dynamic displacement behavior of a multimorph actuator sample under a square-wave driving signal (f = 50 Hz, V = 6 V, l = 9.2 mm, w = 3.5 mm, w_0 = 0.3 mm, n = 15, and nt = 0.945 mm). The designations as specified in Fig. 6.

ing to 0.19 kV/mm), then decreased from 12 to −12 V, and finally increased from −12 to 0 V to form one cycle with an increment of 1 V for each step. The bending displacement was increased from 0 to 1.3 μm with the drive voltage increased from 0 to 12 V then changed from 1.3 μm to about −1.3 μm when the drive voltage decreased from 12 to −12 V step by step. Finally, with the voltage coming back to 0 from −12 V, the displacement returned to near 0 from −1.3 μm. Fig. 7 also indicates that the displacement was approximately linear with the applied voltage.

Fig. 8 presents the dynamic displacement behavior of the multimorph actuator sample under a square-wave driving signal. The input was 6 V at a frequency of 50 Hz. The measured displacement response is reasonably rapid, stable, and repeatable. The displacement response to a step voltage in a short period is magnified in Fig. 9. The roughness of the dynamic displacement response curve is attributed to the limited number of data points because of the measurement system. The frequency of the transient vibration of the actuator accompanying the displacement overshoot should be mathematically equivalent to the resonance frequency of the actuator. From the measurement result in Fig. 9, the resonance frequency of the actuator is determined to be about 20.5 kHz.

V. Theoretical Analysis

The theoretical analysis in this section is aimed to clarify the performance of the cantilever structure comprising the piezoelectric multimorph actuator as is illustrated in Fig. 6. The resonance frequency, displacement, and the blocking force of the actuator are analyzed subsequently.

A. Resonance Frequency

If the effect of the electrode layers can be ignored, the stiffness of the cantilevered structure in the widthwise direction can be expressed as:

$$E_p I = \frac{ntw^3}{12} E_p \tag{1}$$

where E_p is Young's modulus of the PZT ceramic; I is the moment of inertial of the cantilevered structure; n and t are the numbers representing PZT layers and thickness of each layer, respectively; and w is the width of the actuator.

By only considering the internal shear forces and moment in the y direction and neglecting the other forces in the y direction and all the forces in other directions in

Fig. 6, the followed Euler's beam equation [10] can be used to describe the elastic vibration in the width direction:

$$\frac{E_p I}{m}\frac{\partial^4 y}{\partial x^4} + \frac{\partial^2 y}{\partial \tau^2} = 0 \tag{2}$$

where m is the mass of the beam per unit length along the x axis and τ stands for time.

Equation (2) can be solved under the boundary conditions of the one-end clamped cantilever beam, and the fundamental natural bending resonance frequency f_r in the widthwise direction can be obtained as

$$f_r = \frac{\lambda_1^2}{2\pi l^2}\sqrt{\frac{E_p I}{m}} = \frac{\lambda_1^2 w}{4\pi l^2}\sqrt{\frac{E_p}{3\rho}} \tag{3}$$

where ρ is the density of the PZT ceramic, and $\lambda_1 = 1.875$. The resonance frequency is proportional to the width of the multilayer body but not related to the thickness.

B. Displacement

The multimorph actuator can be divided into three portions along the width direction (i.e., two symmetric active portions with electrode layers sandwiched) and the central inactive portion without electrodes. The stain and stress of the two active portions in the length direction, S_1 and T_1, can be expressed according to their piezoelectric and elastic equations:

$$S_1 = s_{11}^E T_1 \pm d_{31} E_3 \tag{4}$$

$$T_1 = E_p S_1 \pm E_p d_{31} E_3 = E_p \kappa y \pm E_p d_{31} E_3 \tag{5}$$

where s_{11}^E is the compliance constant under constant electric field, d_{31} is the piezoelectric constant, E_3 is the electric field in the z direction, and κ is the curvature of the bending cantilever [11]. The positive and negative signs in the equations are used when electrical fields are parallel and antiparallel to the polarization vector.

The stress along the x direction in the inactive portion of the ceramic between the two active portions is:

$$T_1 = E_p \kappa y. \tag{6}$$

Thus, the torque M caused by the elastic force can be expressed as:

$$M = \int_{-\frac{w}{2}}^{-\frac{w_0}{2}} (E_p \kappa y + E_p d_{31} E_3) n t y dy + \int_{-\frac{w_0}{2}}^{\frac{w_0}{2}} E_p \kappa y n t y dy + \int_{\frac{w_0}{2}}^{\frac{w}{2}} (E_p \kappa y - E_p d_{31} E_3) n t y dy. \tag{7}$$

The curvature of the cantilever beam at zero loading can be determined by setting $M = 0$ in (7), and the displacement δ of the free end of the cantilever beam can be hence determined by (8):

$$\delta = \frac{\kappa l^2}{2} = \frac{3l^2(w^2 - w_0^2)}{2w^3 t} d_{31} V \tag{8}$$

where V is the voltage applied to each PZT layer. Taking account of $w_0 \ll w$, (8) can be simplified as:

$$\delta = \frac{3l^2}{2wt} d_{31} V. \tag{9}$$

When $w_0 < 0.1w$, the error from ignoring the effects of w_0 is less than 1%.

According to (9), for an actuator with specific length and d_{31}, the displacement is inversely proportional to the total width and thickness of each PZT layer under constant voltage but not related to the number of the layers. Under the condition of constant electric field, the displacement becomes independent on the thickness of a single PZT layer.

C. Blocking Force

Another important parameter for the bending mode actuator is the blocking force at the tip of the beam to characterize the strength of the actuator. The blocking force is an external equivalent force, F_b, which can be applied at the tip to counteract the electric field-induced tip deflection and hence to maintain the tip of the cantilever at a fixed original position. It is also termed the maximum generative force. For the cantilever beam, the force required to make the beam produce a displacement δ is [11]:

$$F_b = \frac{3E_p I \delta}{l^3}. \tag{10}$$

Substituting (10) with (1) and (8), F_b can be expressed as:

$$F_b = \frac{3nt(w^2 - w_0^2)}{8l} E_p d_{31} E_3. \tag{11}$$

By ignoring the minor effect of w_0, (11) can be further simplified to:

$$F_b = \frac{3nw^2}{8l} E_p d_{31} V. \tag{12}$$

When the length and the material are fixed, the blocking force of the actuator is proportional to the number of the layers and the square of the width under the condition of constant voltage.

D. Calculated Results for the Measured Sample

The performance of the PZT multimorph actuator can be calculated based on the previously obtained equations and the material's parameters. The density ρ, Young's modulus E_p, and piezoelectric constant d_{31} for the PZT material used in this work are about 7.5×10^3 kg/m^3, 6.5×10^{10} N/m^2, and 175×10^{-12} C/N, respectively. The resonance frequency calculated from (3) is 19.7 kHz for the multimorph actuator sample. When 12 V is applied, the displacement and the blocking force, calculated from (9) and (12), are 1.2 μm and 1.02 N, respectively. Therefore,

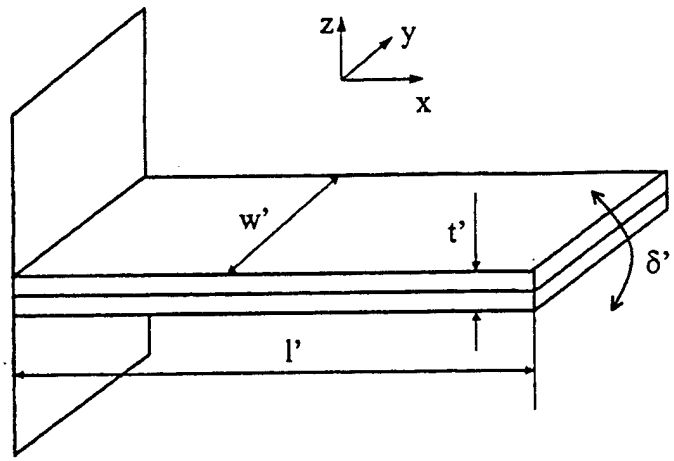

Fig. 10. The schematically illustrated structure of the cantilevered bimorph actuator.

TABLE I
COMPARISON BETWEEN THE CALCULATED PERFORMANCE PARAMETERS OF THE CANTILEVERED BIMORPH ACTUATOR AND THE NEW MULTIMORPH ACTUATOR WITH SIMILAR DIMENSIONS.*

Actuators	Conventional bimorph	New multimorph
Resonance frequency f_r	5.3 kHz	19.7 kHz
Displacement δ ($V = 12$ V)	0.6 μm	1.2 μm
Blocking force ($V = 12$ V)	0.037 N	1.02 N

*For the multimorph actuator, $l = 9.2$ mm, $w = 3.5$ mm, $w_0 = 0.3$ mm, $n = 15$, and $nt = 0.945$ mm; for the bimorph actuator, $l' = 9.2$ mm, $w' = 3.5$ mm, and $t' = 0.945$ mm. The designations of the dimensions for the two actuators are specified in Figs. 6 and 10, respectively. The voltage given in this table is applied to each layer of the multimorph actuator and each layer of the bimorph actuator.

the calculated displacement and resonance frequency are very close to the measured values.

It is useful to make a comparison with the well-known bimorph actuator for clarifying the outstanding features of the new multimorph design. Fig. 10 shows the cantilever beam comprising a PZT bimorph. The fundamental resonance frequency f_r', displacement δ', and the blocking force F_b' are expressed as follows:

$$f_r' = \frac{3.52t'}{4\pi l'^2}\sqrt{\frac{E_p}{3\rho_p}}, \tag{13}$$

$$\delta = \frac{3l'^2}{t'^2}d_{31}V, \text{ and} \tag{14}$$

$$F_b' = \frac{3w't'}{4l'}E_p d_{31}V \tag{15}$$

where V is the voltage applied to each PZT layer of the bimorph [12]. The theoretically calculated performance parameters of the conventional bimorph actuator and our multimorph actuator are listed in Table I. The dimensional data of the bimorph structure are supposed to be similar to those of the multimorph counterpart. The displacement of the multimorph actuator is two times that of the bimorph actuator, and the blocking force is more than 27 times that of the bimorph actuator. Moreover, the resonance frequency is about 3.7 times that of the bimorph actuator. It is obvious that the multimorph structure is superior to the bimorph structure with the similar dimension as a piezoelectric actuator.

VI. DISCUSSION

Comparing the structures shown in Figs. 6 and 10, it can be found that the multimorph actuator is distinct from the bimorph actuator in the direction in which the transverse bend occurs. This distinction is one of the essential reasons for the subsequent difference in performance. Another feature is that the multilayer structure has been adopted into a multimorph actuator.

For the bimorph actuator, the bend of the cantilever structure occurs in the thickness direction in which the two plates are bonded (i.e., the z direction in Fig. 10). This direction is the same direction in which the drive electric field is applied. Increasing the dimension of the actuator in which bend occurs is advantageous to improve the resonance frequency, and the blocking force, however, is disadvantageous to increase the bend displacement. According to (13) through (15), the resonance frequency and the blocking force of the bimorph actuator are proportional to the thickness t', but the displacement/voltage sensitivity is inversely proportional to t'^2. The quadrically inverse proportion relation is attributed to the consistence of the electric field direction and the bending direction, which results in the decrease of the efficient electric field with increasing thickness under constant voltage. Hence, this further aggravates the thickness-dependent decrease of the displacement accordingly. Therefore, the improvement of the resonance frequency and blocking force by improving the thickness can only be achieved at a great sacrifice of the displacement/voltage sensitivity. The common improvement of the resonance frequency and the displacement/voltage sensibility at the same time is restrained to a great extent by the bimorph characteristics.

Unlike the bimorph structure, the transverse bend of the multimorph actuator occurs in the widthwise direction rather than in the thickness and the lamination direction in which the drive voltage is applied. According to (3) and (12), the resonance frequency increases linearly with the width w, and the blocking force increases quadrically. Although the displacement decreases linearly with w according to (9), this unfavorable effect is substantially smaller than that for the bimorph structure. The displacement/voltage sensitivity of the bimorph degrades quadrically with thickness, but its blocking force only linearly increases with thickness.

Because the width of the multimorph structure is actually much larger than the thickness of the bimorph without the unfavorable effect of decreasing the efficient electric field, the multimorph structure can possess a higher res-

onance frequency and a much larger blocking force. Anyway, the unfavorable side effect of the decreased displacement/voltage sensitivity because of the large dimension in width still exists for the multimorph actuator, even if this side effect is not so strong as in the case of the bimorph actuator according to the previous analyses. Thus, the multilayer structure is adopted into our actuator to improve the efficient driving electric field under constant voltage, and the displacement/voltage sensitivity, which is inversely proportional to the thickness of each PZT single layer.

It should be noted that the resonance frequency and the displacement of the multimorph actuator are independent of the number of the PZT layers as expressed in (3) and (9). The number of the laminated layers can be reduced to fewer and even a single layer for various applications without affecting the resonance frequency and displacement. This differs from longitudinal piezoelectric multilayer actuators [13] in which the great number of the laminated layers is a prerequisite to produce sufficient displacement under a very low drive voltage. Thus, the cost of the multimorph actuator can be reduced over that of the longitudinal multilayer actuator because of its small number of laminated piezoelectric layers. The displacement of a longitudinal multilayer with such a small number of active layers is much smaller than the displacement of the multimorph actuator. For example, a seven-layer multimorph actuator can produce a displacement of more than 30 times that of the longitudinal multilayer actuator under a specific drive voltage.

According to (12), the blocking force is proportional to the number of the laminated layers. The strength and generative force of the multimorph actuator can be improved by increasing the number of the laminated piezoelectric layers. In comparison with the bimorph structure of a similar size, the blocking force of the multimorph actuator is tens of times that of the bimorph structure and on the order of Newtons. This is a very appreciable force for bend mode piezoelectric actuator with such a small size.

Because the displacement of the multimorph actuator is derived from the bending mode, the generative force and the resonance frequency are still lower than the longitudinal multilayer piezoelectric actuator. However, the new multimorph actuator presents a useful compromise to the displacement, resonance frequency, blocking force, and cost. From a comprehensive evaluation on the performance and cost, the multimorph actuator overcomes or ameliorates one or more of the disadvantages of the conventional bimorph and longitudinal multilayer actuators and provides a valuable alternative to actuator applications. For example, such a multimorph actuator with a very low drive voltage, large servo bandwidth, and high displacement/voltage sensitivity is particularly suitable for application for the servo control system in the magnetic head-tracking mechanism in the hard disk drive of computers [14], [15].

VII. Conclusions

A bending mode multimorph actuator has been designed and successfully fabricated by a multiple screen printing process. The bend displacement occurs in the widthwise direction not in the thickness direction as in the conventional bimorph actuator. By both theoretical analysis and actual measurements, it was found that larger displacement, higher resonance frequency, and much larger blocking force could be achieved with the multimorph actuator than with the bimorph actuator of a similar size. It is believed that the presented multimorph actuator provides a valuable alternative for piezoelectric actuator applications in addition to existing conventional bimorph and longitudinal multilayer actuators.

Acknowledgments

The authors gratefully acknowledge discussions with Dr. Qing-Ming Wang.

References

[1] K. Uchino, *Piezoelectric Actuators/Ultrasonic Motors*. Boston, MA: Kluwer Academic Publishers, 1996.

[2] T. Kitahara, "Ink jet head with multilayer piezoelectric actuator," in *Proc. IS&T's 11th Int. Congr. on Advances in Non-Impact Printing Technol.*, 1995, pp. 346–349.

[3] K. Mori, T. Kumagae, and H. Hirai, "Ultrasonic linear motor for a high precision X-Y stage," *Proc. IEEE Ultrason. Symp.*, 1989, pp. 657–660.

[4] Z. W. Jiang, S. Chonan, and J. Tani, "Tracking control of a miniature flexible arm using piezoelectric bimorph cell," *Int. J. Robotics Res.*, vol. 11, no. 3, pp. 260–267, 1992.

[5] P. Li and Y. Wen, "Image resolution improvement by swing CCD array imager in two dimensions and its signal processing," in *Proc. SPIE*, 1994, vol. 2308, part 2, pp. 915–920.

[6] K. Mori, H. Hirai, H. Otsuki, T. Takahashi, J. Naruse, Y. Nishimura, and M. Kawamoto, "Disk system with sub-actuators for fine head displacement," U.S. Patent 5189578, 1993.

[7] Y. Zhao and B. Jones, "Pulse width modulated reinforced piezo air jet actuators," *Mechatronics*, vol. 7, no. 1, pp. 11–25, 1997.

[8] H. Moilanen, J. Lappalainen, and S. Leppavuori, "Development of piezoelectric micromovement actuator fabrication using a thick-film double-paste printing method," *Sens. Actuators A*, vol. 43, pp. 357–365, 1994.

[9] K. Yao and W. Zhu, "Improved preparation procedure and properties for multilayer piezoelectric thick-film actuator," *Sens. Actuators A*, vol. 71, pp. 139–143, 1998.

[10] M. L. James, G. M. Smith, J. C. Wolford, and P. W. Whaley, *Vibration of Mechanical and Structural Systems: With Microcomputer Applications*. New York: Harper & Row, 1989, pp. 600–609.

[11] S. P. Timoshenko and J. M. Gere, *Mechanics of Materials*. New York: Van Nostrand, 1972, pp. 167–179.

[12] J. G. Smits, S. I. Dalke, and T. K. Cooney, "The constituent equations of piezoelectric bimorphs," *Sens. Actuators A*, vol. 28, pp. 41–61, 1991.

[13] S. Takahashi, "Longitudinal mode multilayer piezoelectric actuators," *Ceram. Bull.*, vol. 65, no. 8, pp. 1156–1157, 1986.

[14] L. S. Fan, H. H. Ottesen, T. C. Reiley, and R. W. Wood, "Magnetic recording head positioning at very high track densities using a microactuator-based, two-stage servo system," *IEEE Trans. Ind. Electron.*, vol. 42, no. 3, pp. 222–233, 1995.

[15] K. Takaishi, T. Imamura, Y. Mizoshita, S. Hasegawa, T. Ueno, and T. Yamada, "Micromotor control for disk drive," *IEEE Trans. Magn.*, vol. 32, no. 3, pp. 1863–1866, 1996.

Kui Yao (M'99) was born in China on October 14, 1967. He received the B.S. degree in E.E. and the Ph.D in electronics materials and devices, both from Xi'an Jiaotong University, China in 1989 and 1995, respectively, and the M.S. degree in technical physics from Xidian University, China in 1992.

He is a Research Fellow of the Institute of Materials Research and Engineering (IMRE), Singapore and currently is working in the Materials Research Laboratory, the Pennsylvania State University as an Adjunct Research Associate. His research interests are in functional materials and devices, sensors, and actuators.

Weiguang Zhu (M'94) received his BSc. in 1982 and MSc. in 1984 from Shanghai Jiaotong University, China and the Ph.D in 1989 from Purdue University. Currently, he is a Senior Lecturer in Nanyang Technological University, Singapore. He is also the coordinator of Sensors and Actuators research group and the supervisor of Hybrid Microcircuits Laboratory in the School of Electrical and Electronic Engineering in the same university. He is a member of American Physical Society, American Ceramic Society, IEEE, MRS, and ISHM and has published widely in international journals. His research interests include electronic materials, thin films, ferroelectrics, diamond films, gas sensors, high-Tc superconductors, superionic conductors, shape memory alloys, atomic diffusion with Path Probability Method and Cluster Variation Method, optical and electron holography, crystallography, and ferroelectric composite.

Kenji Uchino (M'89) was born on April 3, 1950 in Tokyo, Japan. He received the B.S. degree in physics in 1973 and the M.S. and Ph.D. degrees in physical electronics in 1975 and 1981, respectively, from Tokyo Institute of Technology, Tokyo, Japan.

He is presently Director of the International Center for Actuators and Transducers and Professor of Electrical Engineering at The Pennsylvania State University, University Park, PA and is vice-president of NF Electronic Instruments, Inc., State College, PA. Previously, he was a faculty member at Tokyo Institute of Technology and Sophia University, Tokyo, Japan. His research interests are in dielectrics; ferroelectrics and piezoelectrics, including basic research on materials, device design and fabrication processes; as well as applicational development of solid state actuators to precision positioners, ultrasonic motors, etc.

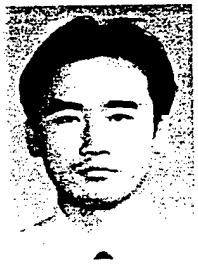

Zhe Zhang was born in Beijing on March 19, 1972. He received his B. Eng. degree in electronic engineering from Tsinghua University, Beijing in 1995. Currently, he is a postgraduate student in the school of electrical and electronic engineering, Nanyang Technological University, Singapore.

Leong Chew Lim (M'60–LM'93) obtained his B.Sc., M.Sc. (with distinction), and Ph.D. from the Nanyang University (Singapore), the University of Leeds (UK), and Cornell University (USA) in 1976, 1978, and 1985, respectively.

He joined the Department of Mechanical and Production Engineering, National University of Singapore (NUS) in 1985 and is currently the Programme Director of the Advanced Engineering Materials Programme of the Institute of Materials Research and Engineering (IMRE). His areas of research cover novel processing of functional ceramics, optical crystal growth, grain boundary phenomena in materials, and weld and braze repair of aeroengine materials and components.

APPENDIX 52

Electromechanical Coupling and Output Efficiency of Piezoelectric Bending Actuators

Qing-Ming Wang, Xiao-Hong Du, *Member, IEEE*, Baomin Xu, and L. Eric Cross

Abstract—Electromechanical coupling mechanisms in piezoelectric bending actuators are discussed in this paper based on the constitutive equations of cantilever bimorph and unimorph actuators. Three actuator characteristic parameters, (e.g., electromechanical coupling coefficient, maximum energy transmission coefficient, and maximum mechanical output energy) are discussed for cantilever bimorph and unimorph actuators. In the case of the bimorph actuator, if the effect of the bonding layer is negligible, these parameters are directly related to the transverse coupling factor k_{31}. In the case of the unimorph actuator, these parameters also depend on the Young's modulus and the thickness of the elastic layer. Maximum values for these parameters can be obtained by choosing proper thickness ratio and Young's modulus ratio of elastic and piezoelectric layers. Calculation results on four unimorph actuators indicate that the use of stiffer elastic material is preferred to increase electromechanical coupling and output mechanical energy in unimorph actuators.

I. Introduction

PIEZOELECTRIC bending actuators, such as bimorphs and unimorphs, have been used widely in areas related to precision position controlling, loud-speakers, vibration damping, noise control, relays, phonograph pick-up, acoustics, and pressure sensing [1]–[3]. A significant amount of scientific literature has been published to detail the operation mechanisms and applications of these devices. A quite comprehensive literature review has been given in [4] and [5]. Interested readers are referred to those articles. Most of the investigations explore the uses of bimorphs, unimorphs, or multilayer morphs in acoustic areas as pressure sensors, resonators, etc. A wide range of piezoelectric materials, such as PVF2, ZnO, CdS, and PZT, have been used for fabricating these devices. Most recently, piezoelectric actuators have been studied for low frequency vibration damping and noise control [6]–[12]. In our previous work [13], [14], cantilever bimorph and unimorph actuators were used as driving elements in a new type of low frequency air transducer for low frequency noise control. Actuators with large tip displacement and generative force are required in this application.

Manuscript received March 19, 1998; accepted September 24, 1998.

Q.-M. Wang is with Lexmark International, Inc., Lexington, KY 40550 (e-mail: qmwang@lexmark.com).

X.-H. Du, B. Xu, and L. E. Cross are with the 187 Materials Research Laboratory, The Pennsylvania State University, University Park, PA 16801.

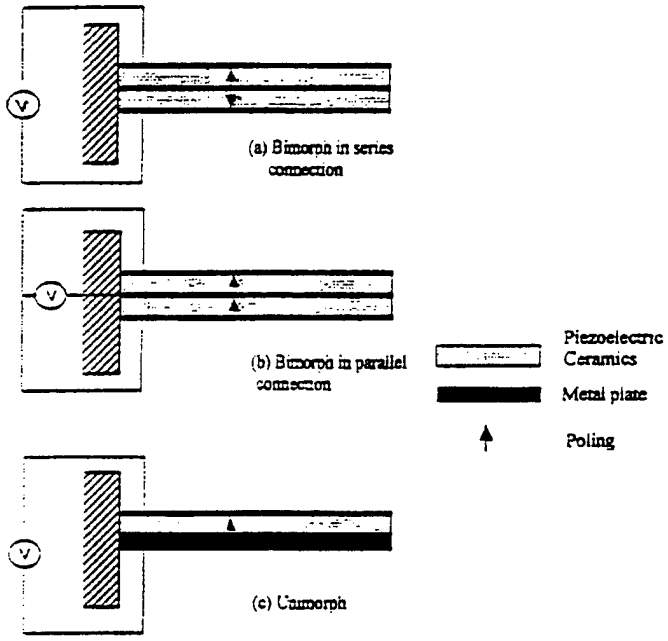

Fig. 1. Structure of bimorph and unimorph actuators.

The structure of bimorph and unimorph actuators is quite simple. As schematically shown in Fig. 1, bimorph actuator consists of two thin ceramics plates bonded together and driven with opposite electrical field. Two type of connections are often used in bimorph fabrication. One is a series or antiparallel connection, in which two piezoelectric sheets with opposite polarization direction are bonded together by epoxy resin. The electrical voltage is applied across the total thickness. The electrical field E_3 is the voltage divided by actuator total thickness t. The other is the parallel connection, in which the two piezoelectric layers have the same polarization directions. The electric voltage is applied between the intermediate electrode and the top/bottom electrodes. Within the two piezoelectric layers, the polarity of driving voltage is opposite. The electric field E_3 now is the voltage V divided by the thickness of a piezoelectric layer. In both cases, one plate expands while the other contracts. The net result is a bending deflection. In parallel connection, driving voltage can be reduced to half the value in the series case while keeping the same field strength. In some cases, a triple-layer structure is used in which a neutral elastic layer is sandwiched between two piezoelectric layers. In a unimorph actuator, one piezoelectric layer and one elastic layer are bonded to-

gether. When the piezoelectric layer is driven to expand or contract, the elastic layer resists this dimension change, leading to bending deformation. The use of an elastic layer can greatly increase the mechanical reliability of the actuator, which is an important issue in practical applications. One significant characteristic of bimorph and unimorph actuators is that they can generate the largest displacement among all piezoelectric actuators: in the range of tens of microns to several millimeters, depending on the geometrical dimensions of actuators. However, bending actuators have low electromechanical coupling and small generative force, because flexural strength is lower than tensile or compressive strength in general. Also, internal stresses are built up in bending actuators when transverse motion is converted into bending motion, which lessens the output mechanical energy.

For a single end clamped actuator two parameters, tip deflection and generative force, usually are used to characterize actuator performance. In a previous paper [15], performance analysis of both bimorph and unimorph actuators were made based on their tip deflection, generative force, and bending resonant frequency. These properties have been shown to strongly depend on actuator dimensions and piezoelectric and elastic properties of each component. The electromechanical coupling and output mechanical energy also are important concerns in actuator applications. Although a significant amount of literature exists dealing with the operation mechanism and applications of bimorph and unimorph, very few papers are available on these issues. Smits and Cooney [16] discuss the effectiveness of bimorph actuators to perform mechanical work under various constant loading conditions, based on the constitutive equation they derived earlier [4]. In the present paper, the electromechanical coupling, energy transmission coefficient, and output mechanical energy of both cantilever bimorph and unimorph benders will be discussed, using tip displacement and tip generative force as the actuator outputs. This analysis is believed to be useful for materials selection and actuator structure design in actuator fabrication.

II. Analysis of Bimorph Actuator

The constitutive relations for cantilever-mounted bimorph have been derived by Smits and Choi [5], which describes the behavior of the bimorph under static conditions. If an electric voltage V is applied across the thickness of bimorph and an external force F is vertically acting at the bimorph tip, then the generated tip deflection and electrical charge can be expressed by the following equation:

$$\begin{pmatrix} \delta \\ Q \end{pmatrix} = \begin{pmatrix} \frac{4s_{11}^E L^3}{wt^3} & \frac{3d_{31}L^2}{2t^2} \\ \frac{3d_{31}L^2}{2t^2} & \frac{\varepsilon_{33}^X Lw(1-k_{31}^2/4)}{t} \end{pmatrix} \begin{pmatrix} F \\ V \end{pmatrix} \tag{1}$$

where s_{11}^E is the elastic compliance, d_{31} is the transverse piezoelectric coefficient, ε_{33}^X is the dielectric permittivity, k_{31}^2 is the transverse electromechanical coupling coefficient, and L, w, t are the length, width, and thickness of bimorph, respectively. Equation (1) can be reduced to:

$$\begin{aligned} \delta &= aF - bV \\ Q &= bF - cV \end{aligned} \tag{2}$$

where

$$a = \frac{4s_{11}^E L^3}{wt^3}, \quad b = \frac{3d_{31}L^2}{2t^2}, \quad c = \frac{\varepsilon_{33}^X Lw(1-k_{31}^2/4)}{t}. \tag{3}$$

The electromechanical coupling coefficient for bimorph actuator can be derived based on the constitutive equations.

A. Electromechanical Coupling of Bimorph Actuator

Because mechanical load is applied to the vibrating end of cantilever bimorph in many cases, the most important quasi-static characteristics are free-tip deflection δ_0, and blocking force F_{bl}. Blocking force is defined as a force perpendicularly applied at the actuator tip to counteract the effect of the applied electric field so that actuator tip remains at the fixed position. Blocking force is the maximum force generated by the electric field induced bending or deformation. The free-tip deflection and blocking force of bimorph actuator can be obtained by (2):

$$\delta_0 = \frac{3d_{31}L^2}{2t^2}V_0. \tag{4}$$

$$F_{bl} = -\frac{b}{a}V_0 = -\frac{3d_{31}wt}{8s_{11}^E L}V_0. \tag{5}$$

For a cantilever bimorph actuator, if no external mechanical load is present at the vibrating end, with an applied voltage V_0, electrical energy is input into the bimorph, it will be bent to a maximum tip deflection δ_0, but no work will be performed. Part of the input electrical energy is stored in the electric field sustained between the electrodes in the piezoelectric or ferroelectric material due to its capacitive nature, the other part has been transformed into mechanical energy and is stored in the bimorph. The electrical input energy is calculated by:

$$U_{el} = \frac{1}{2}QV \tag{6}$$

substituting the direct equation for Q,

$$U_{el} = \frac{1}{2}(bF + cV)V \tag{7}$$

where the force is equal to zero, therefore,

$$U_{el} = \frac{1}{2}cV_0^2 = \frac{1}{2}\frac{\varepsilon_{33}^X Lw(1-k_{31}^2/4)}{t}V_0^2. \tag{8}$$

With reference to Fig. 2, which defines the free-tip deflection and maximum generative force (equal to blocking force but opposite in sign), the mechanical energy stored in the bimorph is:

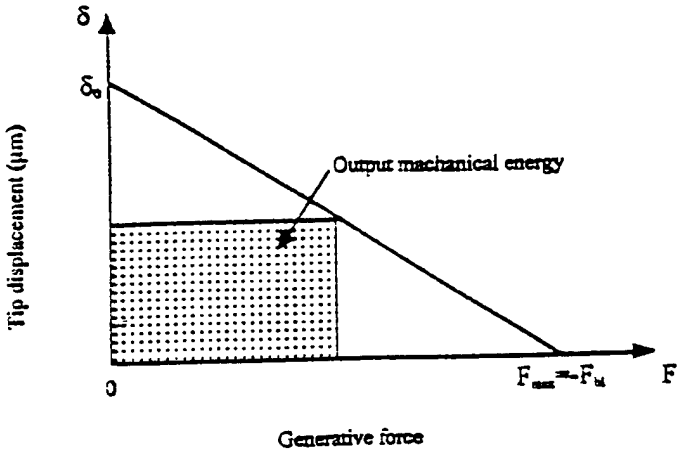

Fig. 2. Tip deflection vs. generative force for cantilever piezoelectric bending actuator.

$$U_{\text{mech}} = \frac{1}{2}\delta_0(-F_{\text{bl}}) \tag{9}$$

substituting (4) and (5),

$$U_{\text{mech}} = \frac{1}{2}\frac{b^2}{a}V_0^2 = \frac{9}{32}\frac{d_{31}^2}{s_{11}^{\bar{E}}}\frac{Lw}{t}V_0^2. \tag{10}$$

Usually the electromechanical coupling factor of piezoelectric material is defined as [1]:

$$k^2 = \frac{\text{Stored mechanical energy}}{\text{Input electrical energy.}} \tag{11}$$

Therefore, the electromechanical coupling factor of the bimorph can be represented as:

$$k_b^2 = \frac{U_{\text{mech}}}{U_{\text{el}}}. \tag{12}$$

Substituting (8) and (10), and using $k_{31}^2 = d_{31}^2/\varepsilon_{33}^X s_{11}^E$,

$$k_b^2 = \frac{b^2}{ac} = \frac{9}{16}\frac{k_{31}^2}{1 - k_{31}^2/4}. \tag{13}$$

Obviousiy, a bimorph actuator made from a high k_{31} material will have a high k_b value. The k_{31} values of some commercial soft-type PZT ceramics are listed in Table I, among which Motorola 3203HD ceramic has the highest $k_{31} = 0.44$. Using (13), the electromechanical coupling factor of a bimorph actuator made from this material is $k_b = 0.34$. Therefore, a bimorph actuator will have a lower electromechanical coupling factor than the material from which it is made.

B. Energy Transmission Coefficient of Bimorph

Not all the stored mechanical energy actually can be used for driving an external load, and the actual work done by the bimorph tip vibration depends on the mechanical load. Without a mechanical load or under a completely clamped condition, there is zero output work. Energy transmission coefficient, λ, usually is defined to evaluate the actual work done by piezoelectric devices [1]:

$$\lambda = \frac{\text{Output mechanical energy}}{\text{Input electrical energy}}. \tag{14}$$

First, consider the case that the bimorph tip is subjected to a constant external force (load) F, in the direction perpendicular to bimorph length direction. When an electric voltage V is applied on the bimorph, the input electric energy is expressed by (7). The output mechanical energy can be calculated as (Fig. 2):

$$U_{\text{out}} = -\int F\,d\delta = -F\delta = -(aF + bV)F. \tag{15}$$

Therefore, the energy transmission coefficient is:

$$\lambda = \frac{U_{\text{out}}}{U_{\text{el}}} = -\frac{2(aF + bV)F}{(bF + cV)V}. \tag{16}$$

Under a proper external force (load), a maximum energy transmission coefficient can be achieved. To determine an appropriate external force F under a certain applied electric voltage to maximize the λ value, we substitute F/V with y to obtain:

$$\lambda = \frac{2ay^2 + 2by}{by - c}. \tag{17}$$

By $\frac{d\lambda}{dy} = 0$, we can obtain the following equation:

$$y_0^2 - 2\frac{c}{b}y_0 - \frac{c}{a} = 0 \tag{18}$$

thus

$$y_0 = -\frac{c}{b} + \sqrt{\left(\frac{c}{b}\right)^2 - \frac{c}{a}}. \tag{19}$$

By substituting (19) into (17), the maximum energy transmission coefficient can be obtained as:

$$\begin{aligned}\lambda_{\max} &= -2\frac{ay_0^2 + by_0}{by_0 + c} \\ &= -2\left[a\left(-c/b + \sqrt{(c/b)^2 - c/a}\right)^2\right. \\ &\quad \left. + b\left(-c/b + \sqrt{(c/b)^2 - c/a}\right)\right] \\ &\quad \div \left[b\left(-c/b + \sqrt{(c/b)^2 - c/a}\right) + c\right] \\ &= 2\left(2\frac{ac}{b^2} - 2\frac{ac}{b^2}\sqrt{1 - \frac{b^2}{ac}} - 1\right) \\ &= 2\left(\sqrt{\frac{ac}{b^2}} - \sqrt{\frac{ac}{b^2} - 1}\right)^2.\end{aligned} \tag{20}$$

If we realize that (13) gives a value for ac/b^2, we get:

$$\frac{ac}{b^2} = \frac{16}{9}\frac{1 - k_{31}^2/4}{k_{31}^2} = \frac{1}{k_b^2}. \tag{21}$$

$$\begin{pmatrix}\delta\\ Q\end{pmatrix}=\begin{pmatrix}\dfrac{4s_{11}^{p}s_{11}^{m}(s_{11}^{p}t_m+s_{11}^{m}t_p)L^3}{Kw} & \dfrac{3d_{31}s_{11}^{p}s_{11}^{m}t_m(t_m+t_p)L^2}{K}\\ \dfrac{3d_{31}s_{11}^{p}s_{11}^{m}t_m(t_m+t_p)L^2}{K} & \dfrac{Lw}{t_p}\left(\varepsilon_{33}^{X}-\dfrac{d_{31}^2t_m(s_{11}^{m}t_p^3+s_{11}^{p}t_m^3)}{K}\right)\end{pmatrix}\begin{pmatrix}F\\ V\end{pmatrix} \tag{28}$$

The maximum energy transmission coefficient of bimorph under constant external force loading condition can be expressed in terms of transverse electromechanical coupling factor k_{31}^2 of piezoelectric ceramic:

$$\lambda_{\max}=2\left(\sqrt{1/k_b^2}-\sqrt{1/k_b^2-1}\right)^2=\frac{32}{9k_{31}^2}\left(\sqrt{1-k_{31}^2/4}-\sqrt{1-13k_{31}^2/16}\right)^2. \tag{22}$$

Therefore, for a cantilever bimorph made from soft PZT ceramic (Motorola 3203HD), under the condition of constant external force, using $k_{31}=0.44$, its maximum energy transmission coefficient can be calculated. $\lambda_{\max}=0.06075$, indicating that by choosing a proper external loading, a maximum 6.1% of input electrical energy can be transferred into mechanical output energy. The other portion of electrical energy remains in the bimorph if dielectric loss is zero. Using (19), the condition that satisfies the maximum energy transmission is:

$$y_0=\frac{F_0}{V_0}=-\frac{c}{b}\left(1-\sqrt{1-\frac{b^2}{ac}}\right) \tag{23}$$

substituting (3) and (21), we have:

$$\frac{F_0}{V_0}=-\frac{1}{6}\frac{wt}{L}\frac{d_{31}}{s_{11}^{E}}(4/k_{31}^2-1)\left(1-\sqrt{\frac{1-13k_{31}^2/16}{1-k_{31}^2/4}}\right). \tag{24}$$

For given tip load (F_0) and driving voltage, bimorph dimension can be designed to achieve maximum energy transmission using (24); or, for a given bimorph actuator and a given driving voltage, the external load can be specified.

C. Maximum Mechanical Output Energy of Bimorph

The above condition for maximum energy transmission does not coincide with the condition that produces the maximum output mechanical energy. Assuming linear piezoelectricity, the maximum output mechanical energy can be obtained when the external load is half of the maximum generative force, i.e.,

$$U_{\text{m-max}}=-\delta F=-\left(a\frac{F_{bl}}{2}+bV_0\right)\frac{F_{bl}}{2}=\frac{9}{64}\frac{Lw}{t}\frac{d_{31}^2}{s_{11}^{E}}V_0^2. \tag{25}$$

In this case, the input electrical energy is given by

$$U_{el}=\frac{1}{2}QV_0=\frac{1}{2}\left(b\frac{F_{bl}}{2}+cV_0\right)V_0=\frac{\varepsilon_{33}^{X}}{64}\frac{Lw}{t}(32-17k_{31}^2)V_0^2. \tag{26}$$

Using (25) and (26), we can calculate the energy transmission coefficient of bimorph when maximum output mechanical energy is achieved,

$$\lambda=\frac{U_{\text{m-max}}}{U_{el}}=\frac{9k_{31}^2}{32-17k_{31}^2} \tag{27}$$

if $k_{31}=0.44$, $\lambda=0.060692$, which is very close to $\lambda_{\max}$, but a theoretically different value.

III. Analysis of Unimorph Actuator

In unimorph actuator, a piezoelectric layer and an elastic layer are bonded together. The application of electric field across the piezoelectric layer will induce bending motion because of the constrain of the elastic layer. Similar to the case of bimorph, the electromechanical coupling factor of a unimorph actuator also can be derived by using the constitutive equation of the unimorph. The constitutive relations of cantilever mounted unimorphs also have been derived by Smits *et al.* [5], which describes the behavior of the unimorph under static conditions. If a unimorph is subjected to an applied electric voltage and an external force acts on the tip of the unimorph perpendicular to the length direction, then the generated tip deflection and electrical charge can be expressed by (28) (top of this page)

where

$$K=(s_{11}^{m})^2(t_p)^4+4s_{11}^{m}s_{11}^{p}t_m(t_p)^3+6s_{11}^{m}s_{11}^{p}(t_m)^2(t_p)^2+4s_{11}^{m}s_{11}^{p}t_p(t_m)^3+(s_{11}^{p})^2(t_m)^4 \tag{29}$$

s_{11}^{m} and s_{11}^{p} are the elastic compliance of the elastic layer and the piezoelectric layer; t_m and t_p are the thickness of the elastic layer and the piezoelectric layer. The bonding layer thickness is usually very thin and its effect can be neglected.

Equation (28) also can be written as (2),

$$\delta=aF+bV$$
$$Q=bF+cV$$

where

$$a = \frac{4s_{11}^p s_{11}^m (s_{11}^p t_m + s_{11}^m t_p) L^3}{Kw},$$
$$b = \frac{3d_{31} s_{11}^p s_{11}^m t_m (t_m + t_p) L^2}{K}, \quad (30)$$
$$c = \frac{Lw}{t_p}\left(\varepsilon_{33}^X - \frac{d_{31}^2 t_m (s_{11}^m t_p^3 + s_{11}^p t_m^3)}{K}\right).$$

For analyzing the effect of the elastic layer on the unimorph actuator performance, we define:

$$A = \frac{s_{11}^p}{s_{11}^m} = \frac{E_m}{E_p}, \quad B = \frac{t_m}{t_p}$$

where E_m and E_p are Young's modulus of elastic (metal) layer and piezoelectric ceramic layer. Then (30) can be simplified as:

$$a = \frac{4s_{11}^p L^3}{wt_p^3} \frac{AB + 1}{1 + 4AB + 6AB^2 + 4AB^3 + A^2B^4}$$
$$b = \frac{3d_{31} L^2}{t_p^2} \frac{AB(B + 1)}{1 + 4AB + 6AB^2 + 4AB^3 + A^2B^4} \quad (31)$$
$$c = \frac{Lw\varepsilon_{33}^X}{t_p}\left[1 - k_{31}^2 \frac{AB(1 + AB^3)}{1 + 4AB + 6AB^2 + 4AB^3 + A^2B^4}\right]$$

$k_{31}^2 = d_{31}^2/\varepsilon_{33}^X s_{11}^p$ is used above. Following a similar procedure, as for the bimorph actuator, the electromechanical coupling coefficient, maximum energy transmission coefficient, and maximum mechanical output coefficient can be derived for the unimorph.

A. Electromechanical Coupling Factor of Unimorph Actuator

The free-tip deflection and blocking force of unimorph actuator can be obtained by (29):

$$\delta_0 = bV_0 = \frac{3L^2}{t_p^2} \frac{AB(1 + B)}{A^2B^4 + 2A(2B + 3B^2 + 2B^3) + 1} d_{31} V_o \quad (32)$$

$$F_{bl} = \frac{b}{a} V_0 = -\frac{3wt_p}{4s_{11}^p L} \frac{AB(B + 1)}{(AB + 1)} d_{31} V_0. \quad (33)$$

For a free cantilever unimorph actuator, if no external mechanical load is present at the vibrating end, with an applied voltage V_o, electrical energy is input into the unimorph, unimorph will be bent to a maximum tip deflection δ_0 but no work will be performed. Part of the input electrical energy is stored in the electric field sustained between the electrodes in the piezoelectric or ferroelectric material due to its capacitive nature, the other part has been transformed into mechanical energy and stored in the unimorph. The electrical input energy is calculated by:

$$U_{el} = \frac{1}{2} QV \quad (34)$$

substituting the direct equation for Q,

$$U_{el} = \frac{1}{2}(bF + cV)V \quad (35)$$

TABLE I
MATERIALS PROPERTIES USED IN CALCULATION.

Materials	k_{31}	Young's modulus (N/m^2)	A ($= E_m/E_p$)
PZT 3203HD	−0.44	6.2×10^{10}	/
PZT 5H	−0.39	6.2×10^{10}	/
PZT 5A	−0.34	6.1×10^{10}	/
PZT 4	−0.33	8.2×10^{10}	/
Aluminum	/	6.5×10^{10}	1.05
Steel	/	19.5×10^{10}	3.14
Brass	/	11×10^{10}	1.77
Acrylic	/	0.31×10^{10}	0.05

where the force is equal to zero, therefore we get:

$$U_{ei} = \frac{1}{2} cV_0^2$$
$$= \frac{1}{2} \frac{\varepsilon_{33}^X Lw}{t_p} \times \left[1 - k_{31}^2 \frac{AB(1 + AB^3)}{A^2B^4 + 2A(2B + 3B^2 + 2B^3) + 1}\right] V_0^2. \quad (36)$$

The mechanical energy stored in the unimorph is:

$$U_{mech} = \frac{1}{2} \delta_0 (-F_{bl}) \quad (37)$$

substituting (32) and (33) into (37), we obtain:

$$U_{mech} = \frac{1}{2} \frac{b^2}{a} V_0$$
$$= \frac{9d_{31}^2 Lw}{8s_{11}^p t_p} \times \frac{A^2B^2(1 - B)^2}{[A^2B^4 + 2A(2B - 3B^2 - 2B^3) + 1](AB + 1)} V_0^2. \quad (38)$$

Therefore, the electromechanical coupling factor of bimorph can be represented as:

$$k_u^2 = \frac{U_{mech}}{U_{ei}}$$

i.e., the expanded form in (39) (top of next page). Therefore, the electromechanical coupling coefficient of the unimorph actuator is a function of Young's modulus ratio and thickness ratio of the elastic layer and the piezoelectric layer. Obviously, the use of high k_{31} material for unimorph fabrication will lead to high electromechanical coupling coefficient for the actuator. For a given piezoelectric material used for actuator fabrication, k_{31} is a constant. Using $k_{31} = 0.44$ for soft PZT ceramics, we can plot k_u^2 against thickness ratio B for a series of unimorph actuators fabricated using stainless steel, brass, aluminum, or acrylic as the elastic layers bonded with soft PZT ceramic layer. The results are shown in Fig. 3. The related physical properties of PZT ceramics and elastic materials are listed in Table I. A maximum electromechanical coupling coefficient can be obtained by adjusting the thickness ratio of

$$k_u^2 = \frac{b^2}{ac} = \frac{9k_{31}^2}{4}\frac{A^2B^2(1-B)^2}{[A^2B^4 + 2A(2B+3B^2+2B^3)+1-k_{31}^2AB(1+AB^3)](AB-1)}. \quad (39)$$

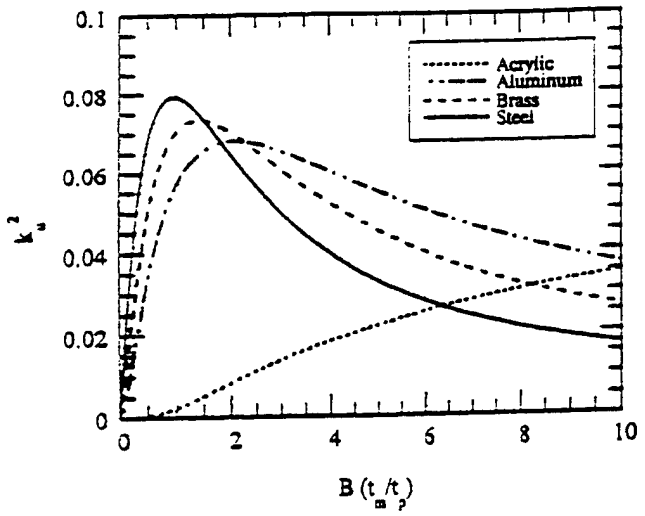

Fig. 3. The electromechanical coupling coefficients are plotted against thickness ratio of elastic layer and piezoelectric layer for different unimorph actuators.

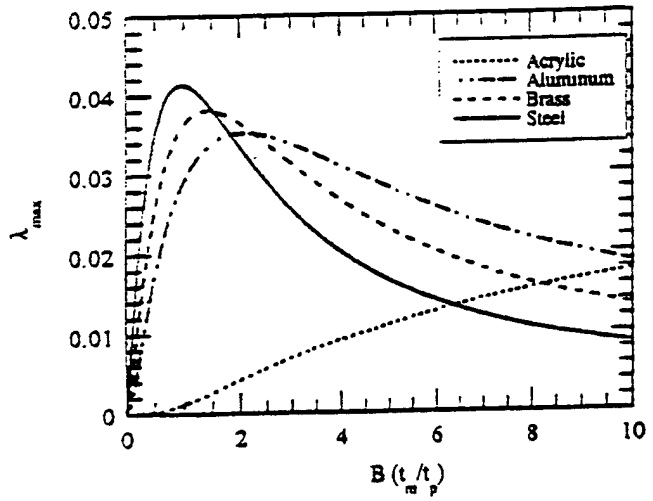

Fig. 4. The maximum energy transmission coefficients are plotted against thickness ratio of elastic layer and piezoelectric layer for different unimorph actuators.

the elastic layer and the ceramic layer. This is clear if we consider two limiting cases:

- When the piezoelectric layer thickness approaches zero (i.e., $B \to \infty$), there is an infinitely small applied moment for bending deformation. Thus, tip deflection and generative force approach zero, and the stored mechanical energy will be infinitely small, so the electromechanical coupling coefficient approaches zero.
- When the elastic layer thickness approaches zero (i.e., $B \to 0$), the transverse strain of the piezoelectric layer is subjected to an infinitely small constrain force from the thin elastic layer; thus the generative bending motion will be small, and electromechanical coupling coefficient will again approach to zero in this case. Therefore, a maximum electromechanical coupling coefficient can be observed between these two limiting cases.

In addition, as the A value increases, the maximum electromechanical coupling coefficient point shifts to lower B values (thinner elastic layer). And the maximum electromechanical coupling coefficient also increases with A value. Therefore, to obtain higher electromechanical coupling coefficient, a stiffer elastic layer (such as stainless steel layer) is preferred in unimorph actuator fabrication. Compared with the bimorph actuator, the unimorph actuator always has lower electromechanical coupling coefficient. It has been demonstrated that, for cantilever unimorph actuator with a fixed actuator total thickness, maximum tip deflection and generative force can be obtained under condition [15]:

$$B_{max} = \sqrt{\frac{1}{A}} \quad (40)$$

i.e., the thickness ratio for maximum tip deflection and generative force is equal to the reciprocal square root of Young's modulus ratio. It can be verified that under this condition, the interface of the elastic layer and the piezoelectric layer coincides with the neutral plane (axis) of the actuator. However, B values for maximum electromechanical coupling coefficient is not the same as that for maximum tip deflection and generative force. For example, for a unimorph actuator consisting of a stainless steel layer and a soft PZT layer, the Young's modulus ratio is about 3.14. The maximum electromechanical coupling coefficient $k_u^2 = 0.08$ is achieved at thickness ratio $B \cong 0.96$ instead of 0.564. The electromechanical coupling coefficient $k_u^2 = 0.071$ at $B = 0.564$ where maximum tip deflection and generative force is achieved.

B. Energy Transmission Coefficient of Unimorph Actuator

An energy transmission coefficient can be defined for the unimorph actuator (14). Considering that the unimorph tip is subjected to a constant external force (load), in the direction perpendicular to unimorph length direction. The maximum energy transmission coefficient is:

$$\lambda_{max} = 2\left(\sqrt{\frac{1}{k_u^2}} - \sqrt{\frac{1}{k_u^2}-1}\right)^2. \quad (41)$$

In Fig. 4. λ_{max} is plotted against thickness ratio B for a series of actuators made up from stainless steel, brass, aluminum, and acrylic layers with a soft PZT layer. The same

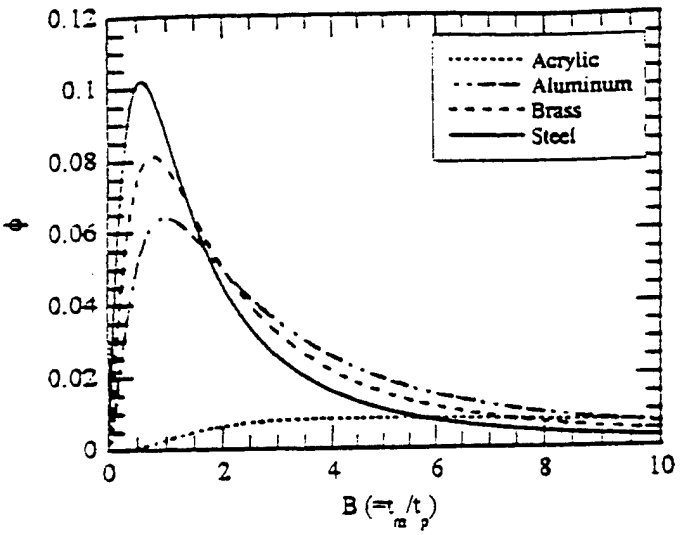

Fig. 5. o is plotted against thickness ratio for a series of unimorph actuators.

variation trend is observed as for the electromechanical coupling coefficient. Again, stiffer elastic layer is preferred to achieve higher maximum energy transmission coefficient for unimorph actuators. For three typical unimorph actuators using stainless steel, brass, and aluminum as the elastic layers bonded with soft PZT layer, the highest λ_{max} values are 4.14%, 3.81%, and 3.52% when $B = 0.96$, 1.4, and 2.1, respectively. These results demonstrate that quite a small portion of the input electrical energy can be transferred into output mechanical energy in cantilever unimorph actuators. The other portion of electrical energy remains in the piezoelectric ceramic layer to sustain the applied electrical field because of its capacitive property (high dielectric constant), neglecting losses. This remaining energy will flow back to power source and reused in the next driving cycle. The external force (load) that satisfies the condition for maximum energy transmission can be calculated using (23) and (31) if the driving voltage is given, or for a known external load and a specified driving voltage, an actuator can be designed to achieve the highest maximum energy transmission coefficient.

C. Maximum Mechanical Output Energy

In practical applications, it is often of concern how much mechanical output energy can be provided by piezoelectric actuators. As in the case of unimorph actuator, the maximum output mechanical energy of unimorph can be obtained when the external load is half of the maximum generative force, i.e.:

$$U_{m\text{-}max} = -\delta F = -\left(a\frac{F_{bl}}{2} + bV_0\right)\frac{F_{bl}}{2} = \frac{9d_{31}^2 Lw}{16s_{11}^2 t_p} \times \frac{A^2B^2(1+B)^2}{[A^2B^4 + 2A(2B+3B^2+2B^3)+1](AB+1)} \cdot V_0^2. \quad (42)$$

Therefore, the maximum output mechanical energy of unimorph actuator varies with A and B values. Through choosing appropriate A and B values, output mechanical energy can be maximized. If the thickness of the actuator is fixed, i.e., $t_m + t_p = t$, because of $t_m/t_p = B$, we have $t_p = t/(B+1)$. Note that $E_3 = V_0/t_p$, here E_3 is electric field strength. E_3 is assumed constant while varying B values. Substituting E_3 and t_p into (42):

$$U_{m\text{-}max} = \frac{9d_{31}^2 Lwt}{16s_{11}^2} \times \frac{A^2B^2(1+B)}{[A^2B^4 + 2A(2B+3B^2+2B^3)+1](AB+1)} E_3^2. \quad (43)$$

To visualize the variation of mechanical output energy with Young's modulus ratio and thickness ratio in unimorph actuators, a nondimensional parameter ϕ can be defined:

$$\phi = \frac{A^2B^2(1-B)}{[A^2B^4 + 2A(2B-3B^2-2B^3)+1](AB+1)}. \quad (44)$$

In Fig. 5, ϕ is plotted as a function of B values for a series of unimorph actuators (different A values). A maximum ϕ can obtained at an appropriate thickness ratio for a unimorph actuator. The condition for maximum mechanical output energy can be verified as $B = \sqrt{1/A}$. This is clear because at this thickness ratio both maximum tip deflection and maximum blocking force are obtained [15]. The maximum ϕ value for unimorph actuator with a given total thickness and under a given electric field can be simplified as.

$$\phi = \frac{A}{4(1+\sqrt{A})^2}. \quad (45)$$

We can calculate the energy transmission coefficient under this circumstance. The input electrical energy is given by (46) (top of next page). Therefore, the energy transmission coefficient can be calculated as shown in (47) (top of next page). Obviously, the mechanical output coefficient of unimorph actuator also depends on the Young's modulus ratio and the thickness ratio of the elastic layer and the piezoelectric layer. Substituting $B = \sqrt{1/A}$ into (47), we can have:

$$\lambda = \frac{9k_{31}^2(A-\sqrt{A})}{32A + 64\sqrt{A} + 32 - k_{31}^2(9A + 17\sqrt{A} + 8)}. \quad (48)$$

Using $k_{31} = 0.44$, and $A = 3.14$, 1.77, 1.05 for unimorphs consisting of stainless steel, brass, and aluminum as the elastic layers bonded with a soft PZT layer, when maximum output mechanical energy is achieved, the energy transmission coefficients are 3.673%, 3.28%, and 2.91%.

From Figs. 3, 4, and 5, it can be found that the use of a polymeric elastic layer for unimorph actuator fabrication will lead to very low electromechanical coupling, low energy transmission, and low output mechanical energy

$$U_{el} = \frac{1}{2}QV_0 = \frac{1}{2}\left(b\frac{F_{bl}}{2} + cV_0\right)V_0$$
$$= \frac{Lw}{16t_p}\left[-9\frac{d_{31}^2}{s_{11}^2}\frac{A^2B^2(1+B)^2}{[A^2B^4+2A(2B+3B^2+2B^3)+1](AB+1)} + 8\varepsilon_{33}^X\left(1-k_{31}^2\frac{AB(1+AB^3)}{A^2B^4+2A(2B+3B^2+2B^3)+1}\right)\right]\cdot V_0^2. \quad (46)$$

$$\lambda = \frac{U_{m\text{-}max}}{U_{el}} = \left[-1+\frac{8}{9k_{31}^2}\frac{[A^2B^4+2A(2B+3B^2+2B^3)+1-k_{31}^2(1+AB^3)](AB-1)}{A^2B^2(1+B)^2}\right]^{-1}. \quad (47)$$

because of their low elastic stiffness. In order to achieve as high as possible output mechanical energy in unimorph actuator, a stiff elastic layer is preferred.

IV. Conclusions

Electromechanical coupling mechanism in piezoelectric cantilever bimorph and unimorph actuators have been quantitatively analyzed based on their constitutive equations. Three actuator characteristic parameters, namely electromechanical coupling coefficient, maximum energy transmission coefficient, and maximum mechanical output energy, are discussed for cantilever bimorph and unimorph actuators. In the case of bimorph actuator, if the effect of the bonding layer is neglected, these coefficients are directly related to the transverse coupling factor k_{31}. In the case of unimorph actuator, these parameters also depend on the Young's modulus and thickness of the elastic layer. Maximum values for these parameters can be obtained by choosing an appropriate thickness ratio and Young's modulus ratio of elastic and piezoelectric layers. Calculation results for four unimorph actuators indicate that the use of stiffer elastic material is preferred to an increase electromechanical coupling in unimorph actuator. Comparing with the longitudinal, transverse, or shear mode actuators, bending mode actuators have lower electromechanical coupling compared with longitudinal or transverse mode actuators, because internal stresses are built up when converting transverse motion into bending motion.

References

[1] K. Uchino. *Piezoelectric Actuator and Ultrasonic Motors.* Boston, MA: Kluwer Academic, 1996.

[2] K. Uchino. "Recent topics of ceramic actuators: How to develop new ceramic devices." *Ferroelectrics*, vol. 91, pp. 281–292, 1989.

[3] ——. "Ceramic actuators: Principles and applications," *MRS Bulletin*, p. 42, April, 1993.

[4] J. G. Smits, S. I. Dalke and T. K. Cooney. "The constituent equations of piezoelectric bimorphs." *Sens. Actuators, A*, vol. 28, pp. 41–61, 1991.

[5] J. G. Smits and W.-S. Choi. "The constituent equations of piezoelectric heterogeneous bimorphs." *IEEE Trans. Ultrason., Ferroelect., Freq. Contr.*, vol. 38, no. 3, pp. 256–270, 1991.

[6] S. Burke and J. Hubbard. "Active vibration control of a simple supported beam using a spatially distributed actuator," *IEEE Contr. Syst. Mag.*, pp. 25–30, 1987.

[7] T. Bailey and J. Hubbard. "Distributed piezoelectric-polymer active vibration control of a cantilever beam," *AIAA J. Guidance Contr.*, vol. 6, pp. 605–611, 1985.

[8] E. Crawley and J. de Luis. "Use of piezoelectric actuators as elements of intelligent structures," *AIAA J.*, vol. 25, pp. 1373–1385, 1985.

[9] J. Jones and C. Fuller. "Experiments on reduction of propeller induced interior noise by active control of cylinder vibration," *J. Sound Vib.*, vol. 112, pp. 389–396, 1987.

[10] C. Lee. "Theory of laminated piezoelectric plates for the design of distributed sensors/actuators, Part I: Governing equations and reciprocal relationships," *J. Acoust. Soc. Amer.*, vol. 87, pp. 1144–1158, 1990.

[11] S. Kim and J. Jones. "A study of actuators for the active control of distributed elastic systems," in *Proc. NOISE-CON*, pp. 283–290, 1991.

[12] ——. "Optimal design of piezo-actuators for active noise and vibration control," *AIAA J.*, vol. 29, pp. 2047–2053, 1991.

[13] Q.-M. Wang and L. E. Cross. "Construction and evaluation of a new type of air acoustic actuator." Presented at the 98th Annual Meeting of the America Ceramic Society, Indianapolis, IN, 1996.

[14] B. Xu, Q. Zhang, V. D. Kugel, Q.-M. Wang, and L. E. Cross, "Optimization of bimorph based double amplifier actuator under quasistatic situation." *Proc. 10th IEEE Int. Symp. Applications Ferroelect.*, vol. II, pp. 217–220, East Brunswick, NJ, 1996.

[15] Q.-M. Wang and L. E. Cross. "Performance analysis of piezoelectric cantilever bending actuators." *Ferroelectrics*, vol. 215, pp. 187–213, 1998.

[16] J. G. Smits and T. K. Cooney. "The effectiveness of piezoelectric bimorph actuator to perform mechanical work under various constant loading conditions." *Ferroelectrics*, vol. 119, pp. 89–105, 1991.

Qing-Ming Wang was born on August 20, 1964 in Sichuan Province, China. He received the B.S. and M.S. degrees in Ceramic Science and Engineering from Tsinghua University, Beijing, China in 1987 and 1989, respectively, and the Ph.D. degree in Materials from The Pennsylvania State University in 1998.

From 1990 to 1992, he worked as a product development engineer in a technology development company in Beijing where he participated in the research and development of electronic ceramics and devices. From 1992 to 1994, he was a research assistant at New Mexico Institute of Mining and Technology, working on Ni-Zn ferrite and composites for EMI and RFI filter application. From 1994 to 1998, he was a graduate research assistant in the Materials Research Laboratory of The Pennsylvania State University, working in the area of piezoelectric actuators and sensors for active noise cancellation and vibration damping. He is currently a staff engineer and materials scientist in Lexmark International, Inc., Lexington, Kentucky. His primary research interests are piezoelectric and electrostrictive

ceramics, thin/thick films, actuators and sensors, piezoelectric materials for microelectromechanical systems (MEMS) applications, device design, and microfabrication.

Dr. Wang is a member of the American Ceramic Society, the Materials Research Society, and the International Microelectronics and Packaging Society (IMAPS).

Xiao-Hong Du (M'98) received the B.S.E.E. degree from Huazhong University of Science and Technology, Wuhan, in 1983, and the M.S. degree in Mathematics from New Mexico Institute of Mining and Technology in 1994. Currently, he is working toward the Ph.D. degree in the Electrical Engineering Department at The Pennsylvania State University, University Park, in the area of piezoelectric transducers and actuators.

Baomin Xu received his Ph.D. degree in Ceramic Science from Shanghai Institute of Ceramics, Chinese Academy of Sciences, in 1994. He is currently Research Associate at the Materials Research Laboratory of The Pennsylvania State University. His research interests include preparation and application of ferroelectric thin and thick films; piezoelectric materials and devices for sensor, actuator, and transducer applications; and dielectric materials.

Dr. Xu is a member of the American Ceramic Society and the Materials Research Society.

L. Eric Cross received his B.Sc. (Hons) degree in Physics from Leeds University in 1948 and the Ph.D. degree in Physics in 1953. He was a University Scholar, an Assistant Professor, and an ICI Fellow at the University of Leeds. After a short period at the Electrical Research Association in Leatherhead Surrey, he moved to the United States to take up a position at the developing Materials Research Laboratory (MRL) at The Pennsylvania State University, University Park. He was, for many years, Associate Director of MRL and was the Laboratory Director from 1985 to 1989. He is now an Evan Pugh Professor of Electrical Engineering at The Pennsylvania State University.

His interests are in dielectric and ferroelectric crystals; piezoelectric and electrostrictive ceramics; and composites for sensor, actuator, and transducer applications and as components in "smart" materials and structures. He has co-authored more than 500 technical papers and sections of six books.

Dr. Cross is a member of the National Academy of Engineering and the Japanese Physical Society and is a Fellow of the American Institute of Physics, the American Ceramic Society, and the American Optical Society. He is a United States representative for ferroelectrics on IUPAP and a member of the Defense Sciences Research Council of ARPA.

APPENDIX 53

ELSEVIER

Materials Chemistry and Physics 58 (1999) 20–25

MATERIALS CHEMISTRY AND PHYSICS

Analysis of high temperature reduction processing of RAINBOW actuator

Qing-Ming Wang*,1, L. Eric Cross

Intercollege Materials Research Laboratory, The Pennsylvania State university, University Park, PA 16802-4800, USA

Received 10 November 1997; received in revised form 23 September 1998; accepted 28 September 1998

Abstract

Reduced and internally biased oxide wafer (RAINBOW) actuator, a new type of monolithic bending device, is composed of a chemically reduced non-piezoelectric layer and a piezoelectric ceramic layer. The formation of the reduced layer is achieved through high temperature chemical reduction of one side of piezoelectric ceramic disc or plate by contact with a reduction agent (i.e., solid graphite). Samples with different reduction thickness are prepared under different conditions and the fabrication processing is discussed from thermodynamic and kinetic considerations. It is proposed that the reduction reaction of PZT ceramic is proceeded by the formation and diffusion of oxygen vacancies. This process simply follows parabolic law. The diffusion rate constant and activation energy of this reduction process are also determined in this study, which can be used to predict the reduction layer thickness at a given temperature. © 1999 Elsevier Science S.A. All rights reserved.

Keywords: RAINBOW actuator; Piezoelectric PZT ceramics; Diffusion; Activation energy

1. Introduction

Recently, a new type of monolithic piezoelectric bending actuator called reduced and internally biased oxide wafer (RAINBOW) device was developed through a special processing technique by Haertling [1,2] in Clemson University. Comparing with conventional bimorph and unimorph type ceramic benders, RAINBOW actuator demonstrated some unique features: (1) a dome-shaped monolithic composite structure, by which delamination problems usually found in conventional benders can be avoided; (2) larger axial displacement level due to its dome or saddle-like configuration; and (3) higher mechanical strength due to the existence of internal pre-stresses. RAINBOW actuator is fabricated by selectively reducing one surface of high lead-containing piezoelectric materials such as PLZT on flat carbon block at elevated temperature. The reduction process of oxide ceramics produces a reduced composite layer with complex composition and phases. It was reported [3,4] that this reduced layer is composed of metallic lead, TiO_2, ZrO_2, $ZrTiO_4$ oxides and reduced PZT or PLZT ceramics. Some metallic lead phase is located intergranularly around other oxide phases, making the reduced layer to show metallic conduction behavior. Since the reduced layer and the remaining PZT or PLZT layer have different thermal expansion coefficients, internal thermal stresses will be generated when materials are cooled down to room temperature after reduction. RAINBOWs can be made into wafer or cantilever type actuators depending on the application requirements. When an electric field is applied across such a composite disc wafer or cantilever, large axial displacement or tip deflection can be obtained.

To optimize RAINBOW actuator performance, a suitable thickness ratio of reduction layer and piezoelectric layer has to be designed [5,6]. The reduction layer thickness is determined by the thermodynamics and kinetics of the reduction process. Therefore, a study on the chemical reaction and diffusion process in the fabrication processing of RAINBOWs is important from the view point of fabrication of these devices. Previous studies [2,4] on RAINBOW devices have reported that in the high temperature reduction process, an approximate linear relationship exists between the reduced layer thickness and reduction time. However, our study on the fabrication processing of soft PZT-5H based RAINBOW actuators indicates that the oxygen diffusion across the reduced layer is the rate-limiting process and a simple parabolic law is followed in this kinetic process. Experimental results and discussions on the difference between our results and previous conclusions are presented.

*Corresponding author.

[1]Currently affiliated with Lexmark International, Inc., Lexington, Kentucky 40550.

0254-0584/99/$ – see front matter

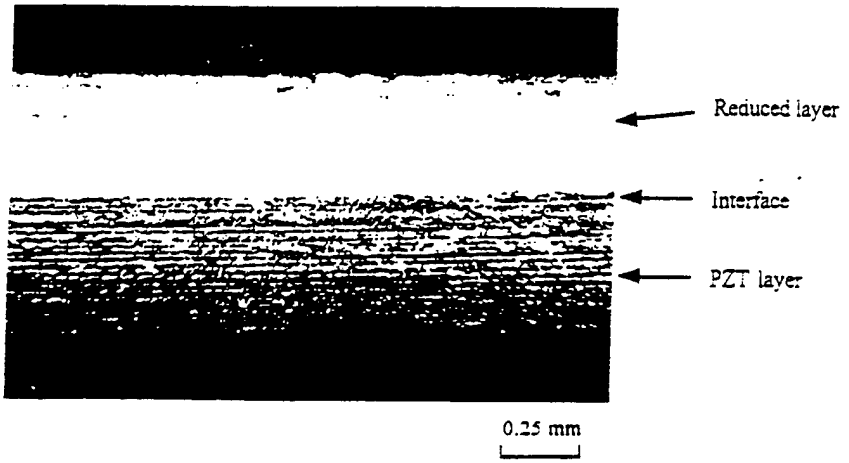

Fig. 1. Optical Photograph of RAINBOW actuator cross-section.

2. Experimental procedures

RAINBOWs with different reduction layer thickness are prepared by using a commercial PZT-5H type ceramic. Ceramic plates with dimension of 50.0 mm × 12.5 mm × 1.02 mm were cut from bulk PZT ceramics which were purchased from the manufacturer (PZT 3203HD, Motorola Ceramic Division, Albuquerque, NM). As described by Haertling [2], a high density graphite block was used as a high temperature reduction agent. After cutting and polishing, ceramic plates are then placed on a polished graphite block. This assembly is introduced into furnace with air atmosphere and heated to a temperature from 975°C to 1085°C for a period of time from 5 min to 12 h. As a consequence of the high temperature chemical reaction between oxide ceramics and carbon, a reduced layer was formed on the bottom side of ceramic plate. It should be noted here that it is found a much longer reduction time has to be used to achieve a comparable reduction thickness as compared with previous studies where PLZT ceramics were reduced at 975°C for a certain period of time (usually less than 1 h) [2,4]. Different reduction layer thickness is obtained by changing reduction temperature and time. After reduction, this assembly is rapidly cooled down to room temperature to avoid possible re-oxidation of the reduced layer. Cooling rate was found to be very critical in RAINBOW fabrication processing. If material is slowly cooled down in furnace, re-oxidation occurs and this will introduce an insulating oxide layer with white or yellow color on the bottom of ceramic plate, which will degrade the conducting property of the already-reduced-layer. But too fast cooling rate may result in sample breakage because of very large temperature gradient inside the sample, which is caused by a non-uniform contraction between surface and interior of sample. Usually, the reaction near sample edges is not uniform because both side and top surfaces are exposed to air atmosphere thus edges are cut after reduction. An optical microscope (UNIMET-Unitron 8630, McBain Instruments) was used to measure the reduced layer thickness. As an example, Fig. 1 shows a typical photograph of a cross-section of RAINBOW prepared by heating to 1035°C for 5 h indicating a very sharp reduced/PZT interface is obtained in this heat treating processing. A reduced layer thickness $t_r = 0.48$ mm was obtained at this condition.

3. Results and discussion

In Fig. 2 the reduction thickness of RAINBOW actuators is plotted against the square root of reduction time for several reaction temperatures from 975°C to 1085°C. Different from the previously reported results for PLZT-based RAINBOWs [2], where reduction thickness is approximately proportional to time, we find that in the present case the parabolic law is followed between reduction thickness and time in high temperature reduction reaction. This

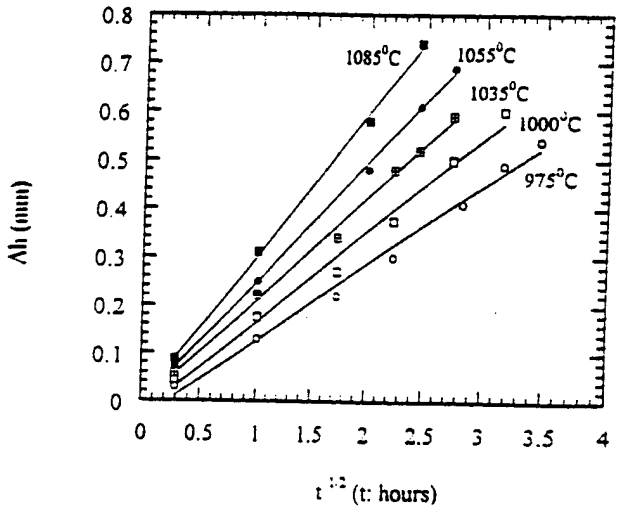

Fig. 2. Reduction layer thickness as a function of reduction time at several temperature.

difference can be explained by tracing the rate-controlling process in the high temperature reduction reaction. It is usually found that, in the case of oxidation of metals or reduction of oxide solids, the reaction kinetics is controlled by surface or interface reaction at initial stage of reaction processes when reduced layer is less than 5 μm thick [7]. The reaction rate is then independent of reduction layer thickness. However, as the reaction proceeds, if the formed product layer has a dense structure, diffusion of reaction species through product layer may become the rate-controlling process, and in this case a parabolic law is followed [8]. However, if the reaction product is porous or with channel structure through which gaseous species can easily pass, the interface reaction will always be rate-controlling process thus no matter how thick the product layer is, a linear relationship between thickness and time could be obtained. This observation is applicable to the case of PLZT-based RAINBOW actuators [4] in which, micro-channel and porous structure was formed in the reduction layer. This micro-structure could account for the observed non-parabolic thickness-time relationship in the reduction processes of PLZT-based RAINBOWs. It should be noted that micro-structure of reduction layer depends on both chemical nature and physical properties of oxide ceramic and reduction layer. If a very dense piezoelectric ceramic is used, as in our present case where soft PZT 3203HD ceramic (fabricated through hot-pressing sintering) has a density of 7.89 g cm^{-3}, a quite dense reduction layer can be formed during the reduction processes. The density of the reduced layer has been measured to be 8.013 g mm^{-3} [5], and SEM and optical micro-structure observations of the cross-section of the fractured RAINBOW actuator indicate that the reduced layer is free of micro-cracks or micro-channels. Although the PLZT ceramics used for RAINBOW actuator fabrication in the previous studies [2,4] are also sintered through hot-pressing and had a high density of 7.93 g mm^{-3}, the reduced layer of the PLZT-based RAINBOW actuator is less dense than those fabricated by soft PZT 3203HD ceramics in our studies. The density of the reduced layer of PLZT-based RAINBOW is 8.00 g mm^{-3} which is given in [9]. Some pores, micro-cracks and micro-channels have been observed in previous studies [4]. It is also found in our experiments, the reduction rate in the PZT-based RAINBOW fabrication processing is lower than that in fabricating PLZT-based RAINBOW actuators, since a much longer reduction time has to be used to achieve a comparable reduction thickness at the same reduction temperature as compared with previous studies where PLZT ceramics were reduced at 975°C for a certain period of time (usually less than 1 h) [2,4]. Therefore, in the reduction processing of soft PZT-based RAINBOWs, diffusion of reaction species through the reduction layer could be the rate-controlling process. This argument is supported by the observation in Fig. 2. While in fabricating PLZT-based RAINBOW actuators, interface or boundary diffusion could be the rate-controlling process and an approximate linear relationship exists between reduction thickness and time, as observed in previous studies [2,4]. The different results obtained in the present and previous studies may be attributed to the composition difference in PZT and PLZT ceramics. The Lanthanum dopant in PLZT ceramics may result in higher chemical reactivity of PLZT ceramics, faster reduction processing, and as a result, different reduction layer micro-structure as compared with soft PZT ceramics.

Fig. 3 schematically shows the possible chemical reactions occurring in the high temperature fabrication processing of soft PZT-based RAINBOW actuators. The chemical reactions which may occur inside the reduced layer and at

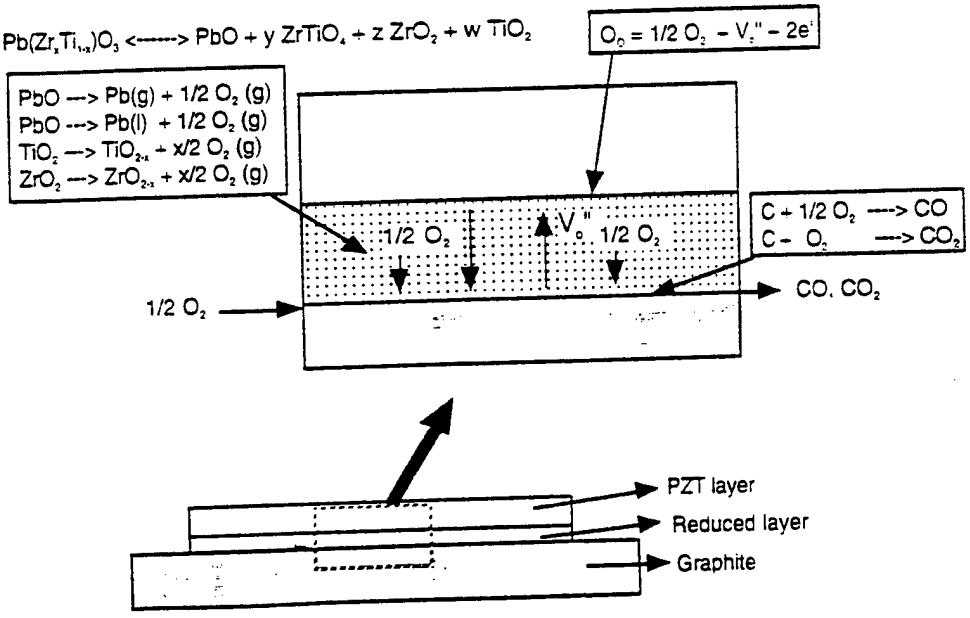

Fig. 3. Chemical reactions occurring in the fabrication processing of PZT-based RAINBOW actuators.

interfaces of both graphite/reduced layer and reduced layer/PZT layer during high temperature treatment are listed as follows:

Case 1: At graphite/reduced layer interface:

$$C(s) + \tfrac{1}{2}O_2(g) \longrightarrow CO(g) \quad (1)$$

$$C(s) + O_2(g) \longrightarrow CO_2(g) \quad (2)$$

$$CO(g) + \tfrac{1}{2}O_2(g) \longrightarrow CO_2(g) \quad (3)$$

Two possible sources provide oxygen for the above reactions. one is oxygen coming from air through interface diffusion. the other is oxygen taken from PZT ceramics by which PZT ceramic is reduced.

Case 2: Inside the reduced layer.

$$Pb(Zr_yTi_{1-y})O_3 \longrightarrow PbO + yZrTiO_2 + zZrO_2 + wTiO_2$$

$$PbO(s) \longrightarrow Pb(l) + \tfrac{1}{2}O_2(g)$$

$$PbO(s) \longrightarrow Pb(g) + \tfrac{1}{2}O_2(g)$$

$$ZrO_2(s) \longrightarrow ZrO_{2-x} + \tfrac{x}{2}O_2(g)$$

$$TiO_2(s) \longrightarrow TiO_{2-x} + \frac{x}{2}O_2(g) \quad (4)$$

Case 3: At reduced layer/PZT layer interface. the B-site ions. i.e.. Ti. Zr and Nb (Nb is the major dopant in soft PZT ceramics) are transition metal ions which have various valency states. At reducing atmosphere. as in the cases of formation of semi-conductor ceramics TiO_{2-x}, ZrO_{2-x} and Nb_2O_{5-x} under reduced atmosphere [10,11]. the following defect chemical reaction exists for PZT ceramics:

$$O_O^{\times} = \tfrac{1}{2}O_2(g) + V_O^{\cdot\cdot} + 2e' \quad (5)$$

Obviously. the liberation of oxygen results in the formation and diffusion of oxygen vacancies in opposite direction. which could be the rate-controlling process for this reduction processing of RAINBOW actuator. As reduction reaction proceeds at elevated temperatures. more and more oxygen will be consumed. Some PZT ceramic will become semi-conducting due to the loss of oxygen and the formation of weakly trapped electrons. Some PZT ceramics will be decomposed to mixture of oxides such as PbO. ZrO_2 and TiO_2. Some metal Pb will also be formed and located intergranularly in reduced layer. This leads to the metallic conduction behavior of reduced layer.

The equilibrium partial pressure of oxygen at graphite/ceramic interface under high temperature condition is an important parameter to evaluate the reduction processing. For Eq. (1) and Eq. (2). we can write the following equations:

$$k_1 = \frac{P_{CO}}{a_c\sqrt{(P_{O_2})}} \quad (6)$$

$$k_2 = \frac{P_{CO_2}}{a_c P_{O_2}} \quad (7)$$

where k_1 and k_2 are chemical reaction constants for Eq. (1) and Eq. (2). a_c is the activity of solid graphite. and P_{O_2}. P_{CO} and P_{CO_2} are partial pressures of oxygen. carbon monoxide and carbon dioxide gases. respectively.

Gibbs free energy for any chemical reaction can be expressed as

$$\Delta G = \Delta G^{\circ} + RT\ln k \quad (8)$$

At equilibrium. $\Delta G = 0$. for Eq. (1) and Eq. (2). we can have

$$\frac{P_{CO}}{a_c\sqrt{(P_{O_2})}} = \exp\left(\frac{-\Delta G_1^{\circ}}{RT}\right) \quad (9)$$

$$\frac{P_{CO_2}}{a_c P_{O_2}} = \exp\left(-\frac{\Delta G_2^{\circ}}{RT}\right) \quad (10)$$

Because the reaction proceeds at atmospheric condition. the following condition is satisfied

$$P_{O_2} + P_{CO} + P_{CO_2} = 0.21 \quad (11)$$

the activity of solid graphite a_c can be assumed to be 1. The values of ΔG_1° and ΔG_2° are

$$\Delta G_1^{\circ}[CO, g] = -111710 - 87.65T \quad (J/mole)$$

$$\Delta G_2^{\circ}[CO_2, g] = -394130 - 0.84T \quad (J/mole)$$

which is obtained from [8]. Therefore. the equilibrium partial pressure of O_2. CO and CO_2 can be calculated by Eqs. (9)–(11). If we assume the reaction temperature is 1000°C. then ΔG_1° and ΔG_2° are approximately −223.29 kJ and −393.06 kJ. respectively. The equilibrium partial pressure of oxygen at the graphite/ceramic interface is about 2.1×10^{-20}. which is very small. indicating that the oxygen concentration gradient is established between the two interfaces of graphite/reduced layer. and reduced layer/PZT layer. This concentration gradient is the driving force for oxygen transport and oxygen vacancy diffusion in the reduced layer. The equilibrium partial pressures of carbon monoxide and carbon dioxide are about 0.2097 and 0.0003. respectively at the interface. Therefore. most graphite is oxidized to CO rather than CO_2 at the interface. It should be noted that the chemical reactions at the interfaces are far from equilibrium and the above calculations and results based on equilibrium condition are only used to demonstrate that the existence of an oxygen concentration gradient provides the driving force of the reduction processing. With sufficient time PZT sample will be completely reduced.

For diffusion controlled process. the increase rate of product layer is proportional to chemical potential difference between the two interfaces but inversely proportional to the diffusion distance. i.e..

$$\frac{dh}{dt} = k_r\frac{\Delta\mu}{h} \quad (12)$$

where k_r is diffusion rate constant. $\Delta\mu$ the difference of chemical potential between the two interfaces. k_r is directly proportional to diffusion coefficient for diffusion controlled process and $\Delta\mu$ can be treated as a constant for a given

process at a given temperature. Integrating Eq. (12).

$$\int_0^{h} h\,\mathrm{d}h = K_r' \int_{t_0}^{t} \Delta\mu\,\mathrm{d}t$$

Thus

$$h^2 = 2k_r' t + A \tag{13}$$

where A is a constant and k_r' the parabolic rate constant. When $A = 0$, Eq. (12) is the ideal parabolic law. Parabolic rate constant at different reaction temperature can be calculated using the above equation and data shown in Fig. 2. In Fig. 4, diffusion rate constant k_r' is plotted against $1/T$ in logarithmic scale, which is fitted into a straight line. The temperature dependence of reduction shown in Fig. 4 indicates that a thermally activated process with constant activation energy is present which supports that the same reduction mechanism exits over the temperature range from 975°C to 1085°C. By using Arrhenius equation

$$k_r' = k_0 \exp\left(-\frac{Q}{kT}\right) \tag{14}$$

activation energy Q for this diffusion process can be obtained, which is approximately 113 kJ mole^{-1} and $k_0 = 9.8 \times 10^{-7}$ m^2 s^{-1}. k_0 is weakly related to temperature and usually can be treated as a constant in certain temperature range. These parameters can be used to predict the reduction thickness in RAINBOW fabrication processing. It should be noted that the above results and discussion are obtained using PZT-5H type high density ceramics, i.e., Motorola soft PZT 3203HD. For RAINBOW actuator fabrication using other piezoelectric materials, parameters could be different because the kinetic process is strongly dependent on materials properties such as micro-structure, grain size and grain size uniformity, density, dopants, chemical reactivity, etc. In our experiments, we also prepared RAINBOW actuators using a similar ceramic material, i.e., PKI550 (Piezo Kinetics, Bellefonte, PA) which has a similar chemical composition with PZT-5H or PZT 3203HD. However, the reduction process for PKI550 is observed to be much faster than that for PZT 3203HD. In addition, metallic lead spheres are observed after reduction of PKI550 ceramic wafers at 975°C for 30 min, indicating that liquid metallic lead formed in the high temperature reduction processing is not stable in the intergranular locations. These observation can be understood by considering ceramic density and micro-structure. Therefore, the reduction process and processing parameters are varied with the piezoelectric ceramics used for RAINBOW actuator fabrication. Usually, piezoelectric ceramics with high density and good micro-structural uniformity are desired for RAINBOW actuator fabrication.

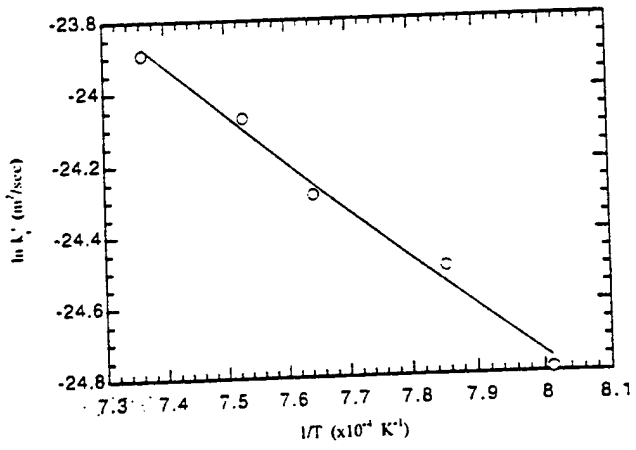

Fig. 4. Diffusion rate constant k_r' is plotted as a function of $1/T$ in logarithmic scale.

4. Conclusions

In summary, high temperature reduction processing for RAINBOW actuator fabrication is discussed from both thermodynamic and kinetic considerations. It was found that the reduction reaction of high density soft PZT ceramic is a diffusion-controlled process. Equilibrium oxygen partial pressure at graphite/ceramic interface is about 2.1×10^{-20}. The concentration gradients between the two interfaces, i.e., graphite/reduced layer interface and reduced layer/PZT layer interface, are the driving force for oxygen transport and oxygen vacancy diffusion in the reduction layer. At interface, most graphite is oxidized to carbon monoxide rather than carbon dioxide gas phases. The kinetic process fits well with parabolic law. Diffusion rate constant and activation energy are calculated based on the experimental data in the temperature range from 975°C to 1085°C. These parameters can be used to predict the reduction layer thickness at a given temperature.

Acknowledgements

This work was supported by the Office of Naval research under contract N00014-94-1-1140, which is gratefully acknowledged.

References

[1] G.H. Haertling, RAINBOW ceramics - A new type of ultra-high-displacement actuator, Am. Ceram. Soc. Bull. 73(1) (1994) 93–96.
[2] G.H. Haertling, Chemically reduced PLZT ceramics for ultra-high displacement actuators, Ferroelectrics 154 (1994) 101–106.
[3] G. Li, E. Furman, G.H. Haertling, Compositional and microstructure of chemically reduced PLZT ceramics, Ferroelectrics 182 (1996) 69–76.
[4] E. Catherine, L. Eric Cross, Clive A. Randall, Structure-property relations in a reduced and internally biased oxide wafer (RAINBOW) actuator materials, J. Am. Ceram. Soc. 79(8) (1996) 2041–2048.

[5] Q.-M. Wang, L. Eric Cross, Determination of Young's modulus of reduced layer of piezoelectric rainbow actuator, J. Appl. Phys. 83(15) (1998) 5358.

[6] Q.-M. Wang, L. Eric Cross, Tip deflection and blocking force of soft-PZT-based cantilever RAINBOW actuators, J. Am. Ceram. Soc. 1998, in press.

[7] P. Haasen, Physical metallurgy, translated by Janet Mordike, 3rd ed. (enlarged and revised), Cambridge University Press, New York, USA, 1996.

[8] R.T. DeHoff, Thermodynamics in Materials Science, McGraw-Hill, New York, 1993.

[9] E. Furman, G. Li, G.H. Haertling, An investigation of the resonance properties of RAINBOW devices, Ferroelectrics 160 (1994) 357–369.

[10] W.D. Kingery, H.K. Bowen, D.R. Uhlmann, Introduction to Ceramics, 2nd ed., Wiley, New York, 1976.

[11] J.H. Moon, H.M. Jang, Effects of sintering atmosphere on densification behavior and piezoelectric properties of $Pb(Ni_{1/3}Nb_{2/3})O_3$-$PbTiO_3$-$PbZrO_3$ ceramics, J. Am. Ceram. Soc. 76(2) (1993) 549–552.

APPENDIX 54

ELSEVIER

Sensors and Actuators 79 (2000) 22–30

SENSORS AND ACTUATORS A PHYSICAL

www.elsevier.nl/locate/sna

Torsional actuator based on mechanically amplified shear piezoelectric response

A.E. Glazounov [a], Q.M. Zhang [a,*], C. Kim [b]

[a] *Materials Research Laboratory, The Pennsylvania State University, University Park, PA 16802, USA*
[b] *Naval Research Laboratory, Washington, DC 20375, USA*

Received 7 October 1998; received in revised form 15 June 1999; accepted 1 July 1999

Abstract

A torsional actuator, based on the concept of mechanical amplification of piezoelectric shear strain and capable of generating large angular displacement, was proposed and studied experimentally. The actuator is a tube consisting of an even number of the segments poled along the length, which are adhesively bonded together, and the joints act as electrodes to apply the driving voltage. The experimental data measured on the prototype actuators (i) prove the proposed concept of mechanical amplification of small piezoelectric shear strain to generate large torsional motion, (ii) show that the actuator functions well both without load and under the torque load and (iii) demonstrate that the actuator can operate continuously for a long period of time without drop in its performance. Also, the results demonstrated that the proposed torsional actuator is capable of producing both large torque and large angular displacement in a compact package, sufficient to meet many smart structures requirements, and can be tailored for a variety of application requirements. Finally, one of the obvious advantages of the present design of the actuator is its simplicity: the piezoelectric shear strain is transformed directly into the angular displacement, whereas in the previously reported actuators, the conversion mechanism into the torsional motion was rather complicated which thus required a sophisticated design of the whole system.

Keywords: Torsional actuator; Shear strain; Piezoelectric ceramics; Nonlinearity; Reliability

1. Introduction

Piezoelectric ceramic materials, such as lead zirconate titanate (PZT) are now widely used in solid-state actuators and sensors which were designed for numerous applications, such as precision positioning, noise and vibration sensing and cancellation, linear motors, and many others [1,2]. In many of those applications, a large torsional displacement is required, for example, in robotics to achieve the micropositioning [3,4], in CD drivers [5], in helicopters to control the trailing edge flaps (TEF) of rotor blades [6–8], etc. To meet this demands, many works have recently been devoted to the development of actuators capable of generating a large angular displacement with a large torque output [3–9] from the piezoelectric strain.

Recently, a novel type of torsional actuator has been proposed [10]. Its concept is to use shear piezoelectric effect and tubular geometry in order to generate the angular displacement. The advantages of this design include (i) the possibility to obtain large angular displacement by using the geometrical amplification, L/R (where L and R are the length and the radius of the tube, respectively). Also, (ii) in most piezoelectric ceramic materials, the shear piezoelectric coefficient, d_{15}, has the highest value among piezoelectric coefficients, which also contributes to developing large values of torsional angle and torque output. Finally, (iii) the design is simple, because the piezoelectric shear strain is transformed directly into the angular displacement (whereas in the previously reported actuators, the conversion mechanism into the torsional motion was rather complicated, including the use of hinges, which thus required a sophisticated design of the whole system [4–9]).

It is the purpose of this paper to continue the study of the proposed torsional actuator and report the results of the

* Corresponding author. Tel.: +1-814-863-7846; fax: +1-814-863-7846; E-mail: qxz1@psu.edu

0924-4247/00/$ - see front matter
PII: S0924-4247(99)00250-2

detailed tests of its performance, which addresses both the device and material issues. The former include operation of the actuator in different conditions, such as without load, under the torque load, and at electromechanical resonance. Material issues are related with the utilization in this actuator of piezoelectric shear response of PZT ceramics, which has not yet received a broad use in the actuator applications. They include fatigue behavior, mechanical strength and nonlinear shear piezoelectric response of PZT ceramics.

2. Actuator design

An idea of the torsional actuator proposed recently [10] and studied in this work is to use the shear piezoelectric effect, where the external electric field is applied perpendicular to the direction of the remanent polarization, P_r (Fig. 1(a)), in order to produce the angular displacement. A schematic view of the actuator is shown in Fig. 1(b). The actuator is a tube consisting of an even number of piezoelectric ceramic segments which are adhesively bonded together using a conductive epoxy, which acts as electrodes to apply the driving field, E. The segments are poled along the length, where the polarization direction alternates between adjacent segments. Since the segments are electrically connected in parallel, they will exhibit a coherent shear deformation under the applied electric field. The cylindrical symmetry of the actuator will directly transform the shear strain, $S_5 = d_{15}E$, induced in each segment into the angular displacement, β, of the top of the tube with respect to its bottom (Fig. 1(b)) which is equal to:

$$\beta = \frac{L}{R_{out}} d_{15} E, \qquad (1)$$

where L is the length of the tube and R_{out} is its outer radius. This equation shows that even though the shear strain is usually quite small in the piezoelectric materials, a large torsional displacement β can be achieved by using a tubular structure with a large ratio of L/R_{out}. Using elastic properties of tube-shaped samples [11], the torque, T_{dev}, developed by the actuator can be found as:

$$T_{dev} = \frac{\pi\left(R_{out}^4 - R_{in}^4\right)}{2 s_{44} R_{out}} d_{15} E, \qquad (2)$$

where s_{44} is the shear elastic compliance of the material and R_{in} is the inner radius of the tube. According to Eq. (2), the torque T_{dev} is independent of the length of the tube, even though the angular displacement β increases linearly with L, Eq. (1).

3. Experimental

Prototype torsional actuators were fabricated from the commercial piezoelectric ceramic tubes of composition PZT-5A ("EDO", USA). Each tube was first cut into eight segments, which then were poled along the length using a continuous poling technique [12]. Finally, the segments were bonded together using a silver-filled epoxy adhesive MB-10HT/S ("Master Bond", USA), which was selected because it has both high shear strength, and is easy to process. This adhesive compound was coated on both surfaces of the segments, which were then assembled into the tubular actuator according to the design shown in Fig. 1(b), and cured at 125°C for 1 h using a vacuum bagging process. Consolidation of the joints by vacuum bagging lead to joints typically 25 μm in thickness and very uniform along their length [12]. The assembled single-tube prototype actuator had the following dimensions: $R_{in} = 0.96$ cm, $R_{out} = 1.27$ cm, and $L = 6.35$ cm, so that the aspect ratio in Eq. (1) was equal to $L/R_{out} = 5$.

According to Eq. (1), in the proposed design of torsional actuator, the angle β increases linearly with the

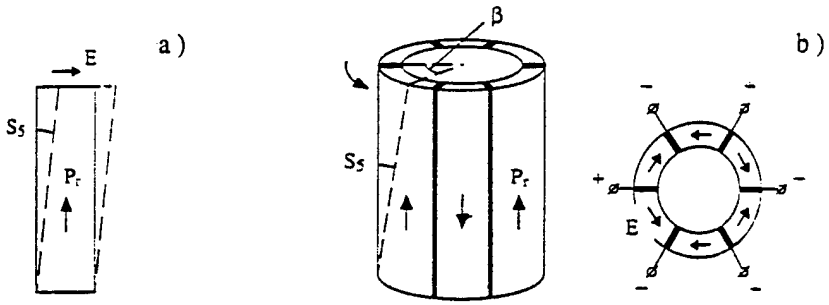

Fig. 1. (a) In piezoelectric shear effect, electric field, E, is applied perpendicular to the direction of the remanent polarization, P_r, thus, producing the shear strain, $S_5 = d_{15}E$, in the sample. Solid and dashed lines show the sample before and after deformation, respectively. (b) The proposed torsional actuator is a tube consisting of an even number of the segments of piezoelectric ceramics which are poled along the length and bonded together using a conductive epoxy. The polarization direction alternates between adjacent segments, as shown with arrows on the left. The electric field, E, is applied perpendicular to P_r, and also has opposite directions in neighboring segments (as shown with arrows on the right). Therefore, depending upon the polarity of applied voltage, the top of the tube will twist by angle β either clockwise or counterclockwise with respect to its bottom.

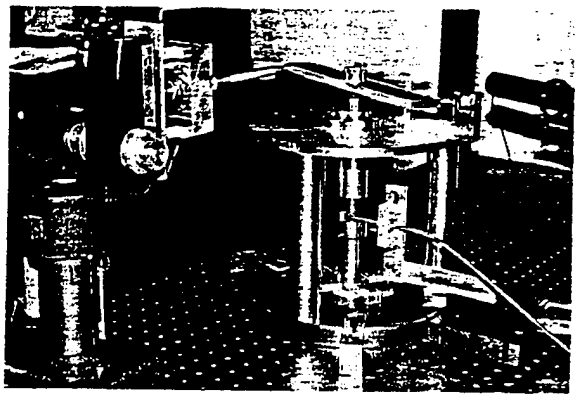

Fig. 2. A photograph of the set-up used for the study of the effect of external static torque on the response of the torsional actuator.

length L of the actuator. To test this hypothesis, two identical tubes with the dimensions described above were joint together lengthwise. The test included the characterization of the tubes before and after the joining them together.

To characterize the actuator, the torsional angle produced by the applied electric field was measured in the following experiments. In the load-free conditions, β was measured as a function of the amplitude and frequency of the ac driving field. Also, electrical fatigue test was performed, where the ac field with a fixed amplitude and frequency was applied to the actuator, and β was monitored as a function of time. Under the torque load, T, the torsional angle was measured as a function of dc and ac electric driving field at different values of T.

In all experiments, the actuator was tightly clamped with its bottom to the optical table, and its top was free to twist due to the applied electric field. In order to measure β, a small mirror was attached on the top of the tube and the distance change between the mirror and the optical fiber probe of a MTI-2000 fotonic sensor was measured. The electrical output signal from the MTI-2000 was monitored using an oscilloscope or SR-830 lock-in amplifier.

The effect of the torque load on the actuator performance was studied using a special set-up (Fig. 2) which was developed in Materials Research Laboratory [13]. Although, there are commercial torque load test machines available, they are not suitable for the torque load test of torsional actuators. The main reason is that these machines were mainly designed to test the properties of the metals, and therefore deal with the magnitudes of torque and twisting angle which are much larger than those expected for the piezoelectric actuators. Additionally, the commercial machines are very expensive, which does not justify their purchase and the following modification to meet the requirements of experiments with actuators. In the developed set-up (Fig. 2), the external torque was produced by applying a force to the lever using springs with different elastic constants.

4. Characteristics of prototype actuator

4.1. Proof of the concept of the torsional actuator

Fig. 3 summarizes the data which verify the concep the proposed torsional actuator. In Fig. 3(a), the torsic angle measured at 10 Hz is plotted as a function of amplitude of the ac driving voltage for two separate t (open circles), and for the same tubes joint lengthw (closed circles). For separate tubes, the actuation behav is almost identical and angular displacement is doub when the length of the actuator is increased by join these two tubes. This behavior agrees with predictions Eq. (1).

The further proof of the concept of the proposed t sional actuator is illustrated in Fig. 3(b). The plot co pares the data for the piezoelectric coefficient d_{15}

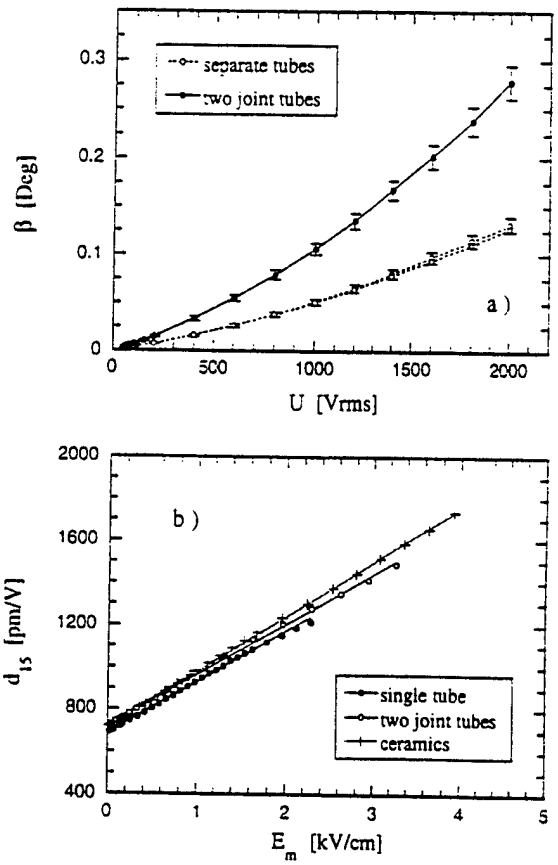

Fig. 3. (a) Angular displacement of torsional actuator as a function of th ac driving voltage for two separate tubes and two tubes joint as or assembly. (b) Piezoelectric shear coefficient d_{15} as a function of th amplitude of the ac driving field, E_m. Circles correspond to the da calculated from the torsional angle of the actuator, consisting of a sing tube (closed circles) and two joint tubes (open circles), using Eq. (1). Plu signs show the data measured directly from the cubic ceramic sample the same composition, PZT-5A. Symbols show the experimental data an the lines correspond to the fit of the data to the linear function, Eq. (7). I (a) and (b), the frequency of the ac voltage is 10 Hz.

PZT-5A ceramics derived from the experimentally measured data for $\beta(E_m)$ of a single tube (closed circles) and two tubes joint lengthwise (open circles) using Eq. (1), where the amplitude E_m of the driving field was substituted for E, with d_{15} values measured directly from the cubic ceramic samples of the same composition, PZT-5A ("EDO", USA). As one can see, the values of the d_{15} derived from the actuators are nearly the same as those measured on the cubic sample. The small, less than 5%, difference could be attributed to the difference in the aging states of ceramics in segments and cubic samples. To summarize, the results presented in Fig. 3(a) and (b) prove the concept of the proposed torsional actuator, Eq. (1), that is, to use the shear piezoelectric effect, d_{15}, and the geometrical amplification, L/R_{out}, to generate a large angular displacement, β.

4.2. Evaluation of torsional angle and torque output

The results reported in Section 4.1 demonstrate that knowing the material properties, d_{15}, the magnitude of driving electric field, E, and the tube dimensions, L and R_{out}, the torsional angle produced by the actuator (Fig. 1(b)) can be calculated using Eq. (1).

In order to evaluate the torque output, T_{dev}, developed by the actuator, we studied the effect of the torque load on static response of the prototypes. In these experiments, a static torque, T, was first applied to the actuator, thus, producing its initial twisting, β_0. Afterwards, a dc field was turned on, with the polarity to induce a twisting of the actuator in the direction opposite to β_0. In Fig. 4, the torsional angle β measured on the two joint tubes is plotted as a function of the driving field at different torque loads. The blocking torque of the actuator can be evaluated from the intersection of the curve $\beta(E)$ measured at a fixed torque load, with the dashed line corresponding to $\beta = 0$. The zero torsional angle means that at that value of the electric driving field the absolute value of the torque, T_{dev}, developed by the actuator is equal to the external static torque, T. For example, at $E = 2.5$ kV/cm, the torque output is approximately equal to $T_{dev} \approx 6$ N m, as can be concluded from the curve measured under external torque of 6 N m, Fig. 4.

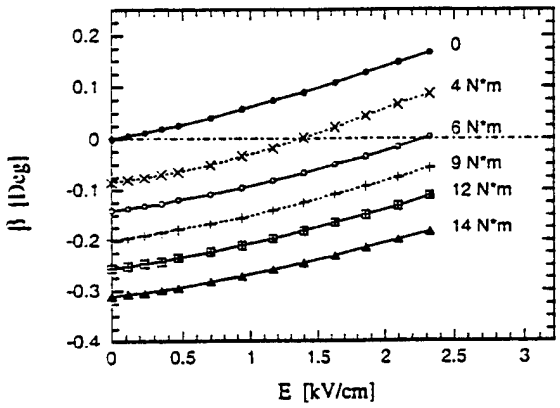

Fig. 4. Torsional angle of the two-tube actuator is plotted as a function of applied dc field at different external static torque.

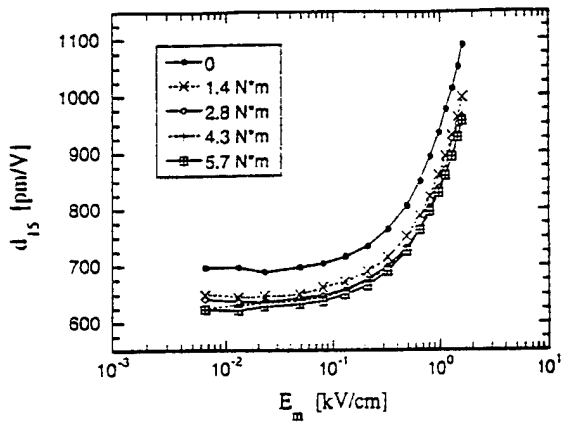

Fig. 5. The effect of the static torque on the dynamic response of the torsional actuator. The values of the piezoelectric coefficient d_{15} calculated from the data on the torsional angle are plotted as a function of the amplitude of the ac driving field. The frequency of the field is 10 Hz. The values of applied torque are given in the legend.

4.3. Effect of the torque load on actuator performance

The effect of the torque load on the static response of the prototype actuator is illustrated in Fig. 4 for the two-tube assembly. This data clearly demonstrates that the torque load almost does not change the response of the actuator to the dc field, because the initial twisting, β_0, can be completely nullified by the appropriate choice of the magnitude of the electric field, and because the slope of $\beta(E)$ curve, which according to Eq. (1) gives the shear piezoelectric coefficient, $d_{15}(E)$, does not show marked change with increasing T (cf. Fig. 4). Similar result was obtained for the single tube actuator.

In the experiment of investigating the effect of external torque on the dynamic response of the prototype actuator, an ac driving field of 10 Hz was applied to the actuator and the torsional angle was measured as a function of the ac field amplitude and the torque load. Fig. 5 shows the plot of the ac field dependence of piezoelectric coefficient d_{15} derived from the data on $\beta(E_m)$ using Eq. (1). Similar to the static response, the external torque does not affect significantly the actuator response to the ac field. Application of the torque results only in a small, less that 10%, change in d_{15} from its value measured under load-free condition, $T = 0$ N m. With the further increase in T, the d_{15} remains nearly constant (Fig. 5).

4.4. Frequency dependence of torsional angle

The frequency dependence of the torsional angle was measured within the frequency range 3–600 Hz under a

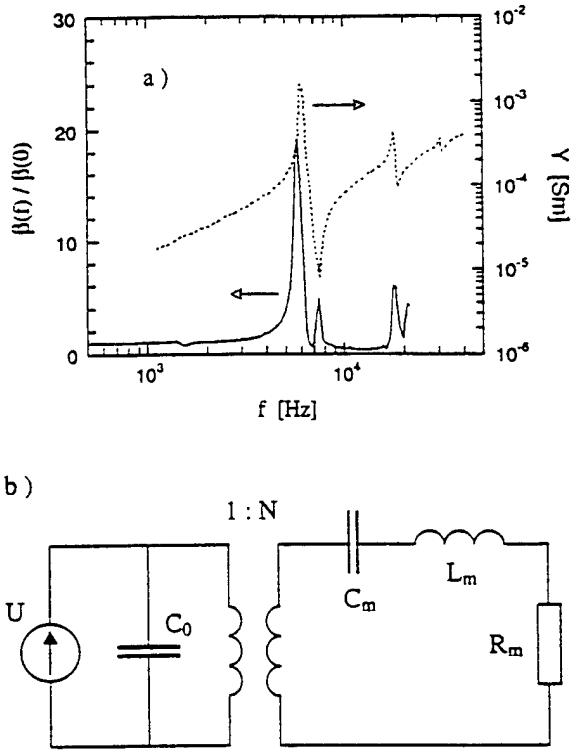

Fig. 6. (a) Frequency dependence of the torsional angle normalized over its static value (solid line) and of the electrical admittance of the torsional actuator (dashed line). (b) Equivalent circuit corresponding to the torsional actuator around its resonance frequency, $f_r = 6$ kHz.

relatively large electric fields. $E_m \approx 2$ kV/cm. Only a minor decrease in β, equal to 3% per decade, with increasing frequency was observed.

For small electric fields. $E_m = 50$ V/cm, the frequency dependence of β was measured over a broad frequency range from 100 Hz to 20 kHz. In Fig. 6(a), the solid line shows the frequency dependence of the ratio $\beta(f)/\beta(0)$, where $\beta(0)$ corresponds to the low-frequency value of the torsional angle, given by Eq. (1). A series of the peaks are seen in this curve. A comparison of $\beta(f)$ with the frequency dependence of the electrical admittance of the actuator (dashed line in Fig. 6(a)) shows that the peaks occur at resonance and antiresonance frequencies of the tube, which correspond to the maximum and minimum admittance, respectively.

In order to understand the origin of these peaks, we performed a theoretical analysis of the acoustic modes propagating in the tube. The analysis showed that the resonance peaks are related with the shear mode propagating along the axis z of the tube, i.e., along its length. When the bottom, $z = 0$, of the tube is mechanically clamped, and the top, $z = L$, is free, the angular displacement at the top of the tube can be written as:

$$\beta = d_{15} E \frac{L}{R_{out}} \frac{\tan \alpha L}{\alpha L}, \tag{3}$$

and the electrical admittance of the actuator is given by:

$$Y = j2\pi f C_0^T \left(1 - k_{15}^2 + k_{15}^2 \frac{\tan \alpha L}{\alpha L}\right), \tag{4}$$

where $\alpha = 2\pi f \sqrt{\rho s_{44}}$ (ρ is the density of PZT), k_{15} is shear electromechanical coupling coefficient, and C_0^T is the electrical capacitance of the tube in stress-free condition. The resonances occur when $\alpha L = n\pi/2$ (n is the odd value), which gives the resonance frequency equal to: $f_r = n/4L\sqrt{\rho s_{44}}$. Using Eq. (4), around the first resonance frequency f_r with $n = 1$, we can substitute the tube with the equivalent circuit which is shown in Fig. 6(b). In this circuit, $C_0 = C_0^T(1 - k_{15}^2)$, $N = d_{15}(R_{out} - R_{in})/s_{44}$, $C_m = 8Ls_{44}/\pi^3(R_{out}^2 - R_{in}^2)$, $L_m = 1/(2\pi f_r)^2 C_M$, and we took into account mechanical losses in the actuator by introducing $R_m^{-1} = 2\pi f C_m Q_m$, where Q_m is the mechanical quality factor. Using the equivalent circuit, one can show that at resonance frequency, f_r, the time dependence of the torsional angle is given by:

$$\beta = \frac{8Q_m}{\pi^2} \frac{d_{15} E_m L}{R_{out}} \sin(2\pi f_r t - 90°), \tag{5}$$

when the electric driving field changes with time as: $E(t) = E_m \sin(2\pi f_r t)$. Eq. (5) shows that at resonance there is a phase shift of $-90°$ between the torsional angle and the driving field, and that the amplitude of the torsional angle should be amplified by the factor of $8Q_m/\pi^2$ compared to the low-frequency value given by Eq. (1).

Inspection of the experimental data showed that the model can fit the data nicely. Using actuator dimensions and material datasheet from "EDO", the resonance frequencies corresponding to $n = 1$, 3, 5 were estimated as: 6.2, 18.6, and 31 kHz, respectively, and were in a good agreement with the positions of the maxima in electrical admittance in Fig. 6(a). Also, from the peak in $\beta(f)/\beta(0)$ corresponding to the first resonance in Fig. 6(a), the mechanical quality factor of the actuator can be determined as $Q_m = 22$. This values closely compares with that determined from the half-width of the electrical conductance of the tube, which gave $Q_m \approx 20$. Finally, in direct measurements of the torsional angle, at resonance, $f_r = 6$ kHz, we observed the phase shift between $\beta(t)$ and driving field $E(t)$ very close to $-90°$. All these data indicate that the torsional actuator performed well also in resonance conditions.

The additional angular amplification of the torsional angle by a factor of $8Q_m/\pi^2$ at resonance frequency is very important for possible application of the torsional actuator in the piezoelectric motors, where the actuators usually operate in a resonance mode. To make the stator of the motor, the tube shown in Fig. 1(b) may be combined with another piezoelectric actuator generating longitudinal displacement. The combination of torsional and longitudinal displacements will produce an elliptical motion of the contact surface between the stator and rotor, which may be necessary to spin the rotor [14].

4.5. Reliability test of prototype actuator

At present, most commercially available solid state actuators are fabricated of the ferroelectric ceramics PZT. A common feature of ferroelectric materials is a fatigue, or a degradation of their properties caused by cycling them with the electrical field of large magnitude. In addition, in the tubular assembly of the actuator (Fig. 1(b)), there is also a possibility of the fatigue caused by bonding layer between segments. Therefore, the reliability test of the actuator should include the study of time variation of actuator performance related with its fatigue under required operation conditions.

In present work, the actuator was driven by an ac field of amplitude $E_m = 1.5$ kV/cm and frequency 20 Hz. The change in the torsional angle with time was monitored using a MTI-2000 fotonic sensor and lock-in amplifier. Fig. 7 shows β as a function of the number of the fatigue cycles, N. As one can see, the torsional angle remains nearly constant with N up to $3 \cdot 10^6$ cycles (which corresponds to 2 days of continuous operation). This result indicates that there is no degradation of torsional actuator caused by large ac driving field.

The absence of the fatigue shown in Fig. 7 agrees with the results of other studies of the fatigue in ferroelectric ceramics. For example, it was shown [15] that the fatigue in PZT ceramics was observed only when the amplitude of the ac driving field exceeded the coercive field, and, thus, caused the switching of the spontaneous polarization. The fatigue occurred already after 10^5 cycles. At the same time, when the driving field was smaller than the coercive field (even being very close to it), no fatigue was observed, up to 10^6 cycles [15]. Based on this result, one should not expect electrical fatigue in the case of the torsional actuator studied in this work. This is because in this actuator one uses the shear piezoelectric effect, where the electric field is applied in the direction perpendicular to the spontaneous polarization, and drives the material with field lower than the coercive field, in order not to switch the polarization in the direction along the field.

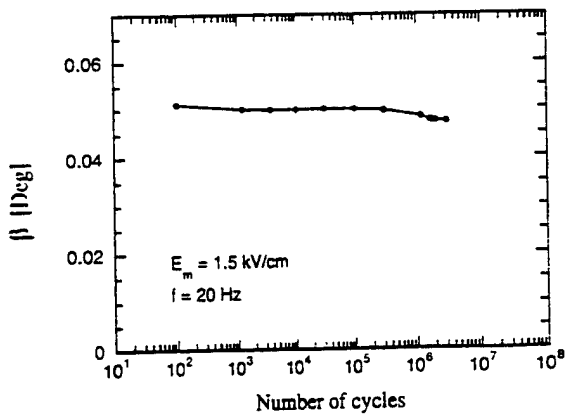

Fig. 7. Torsional angle is plotted as a function of the number of fatigue cycles.

For torsional actuators studied in this work, the experiments were limited to the use of the driving field of $E_m = 2$–3 kV/cm. This limit was mostly determined by the desire to avoid a possible damage to the actuator due to the electrical short circuit related with the discharge over the surface of the segments, which was observed above approximately 3–3.5 kV/cm. If special precautions, related with an electrical insulation of the contacts are made, the electric driving field can be significantly higher. Special test was performed on a cubic sample of PZT-5A immersed into silicone oil, where electric field was applied in the direction perpendicular to the spontaneous polarization, and the shear strain, $S_5(E)$, was measured using MTI-2000 fotonic sensor. With electric fields as high as $E_m = 9$ kV/cm, no evidence for the polarization switching into direction along the electric field was observed: the field dependence of induced strain, $S_5(E)$, had a cigar-like shape and remained fully reversible upon increase and decrease of the field amplitude, E_m. If the polarization switching occurred, the strain would change from shear to longitudinal one and its field dependence would have a shape of the "butterfly loop", which characterizes the strain related with the polarization reversal in ferroelectric materials [16].

Another reliability test included the measurements of the mechanical strength of the torsional actuator. The results of this study will be published separately. Here, we mention only that the mechanical fracture strength of the actuator was determined by the mechanical strength of PZT ceramics, and not by the joints between ceramic segments. This conclusion was suggested by the inspection of the fragments of the broken prototype actuator, and was supported by the fact that the fracture shear stress of the tube, $\sigma_{fr} = 13$ MPa, almost coincided with that of PZT ceramics of the same composition, $\sigma_{fr} \approx 14$ MPa, which was measured for the cubic ceramic sample [17].

5. Tailoring of the characteristics of the torsional actuator for different applications

The specific values of torsional angle and torque output can be different for each particular application. Using the results obtained in this work, we can evaluate the proposed torsional actuator to its application in helicopter rotor blades in TEF, where the actuation should reduce the vibration and improve the lifting power [6–8]. The eight seat commercial helicopter [12] requires the following values: $\beta = \pm 4°$ and $T_{dev} = 5 \pm 3$ N m. The prototype torsional actuators made of PZT-5A ceramics has $d_{15} = 1800$ pm/V at $E = 4$ kV/cm (Fig. 3(b)), which yields the angular displacement $\beta = \pm 0.4°$ (for $L/R_{out} = 10$), and the torque output $T_{dev} = 40$ N m. Even though the angular displacement is smaller than the required values, it can be

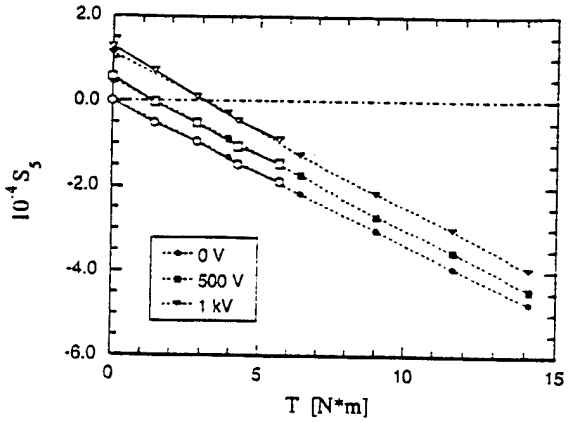

Fig. 8. Shear strain calculated from the experimentally measured values of the torsional angle is plotted as a function of the external static torque at different values of the dc driving voltage. Closed symbols correspond to the actuator consisting of two joint tubes and open circles show the data for the single tube.

increased by using an additional amplification mechanisms. Possible solutions include either hinges (in this case, some excess torque output can be traded off, since T_{dev} is much larger than the value required for TEF application) or an accumulation of displacement over many periods of the ac driving voltage. The latter approach is employed in linear "inchworm" actuators or ultrasonic motors. Based on tubular actuator described in this work, a torsional "inchworm" motor was developed. As will be shown in a separate publication [18], the motor produces a smooth stepwise motion within 360° interval with a precise control over angular positioning. These features make the motor useful for various applications, not only the active control of TEF.

Each particular application will set the requirements not only for the absolute values of the torsional angle and/or torque developed, but also will limit the actuator dimensions. Based on the result of this study, we can suggest the following ways to improve the characteristics of the proposed torsional actuator. The increase in the magnitude of induced shear strain, $S_5 = d_{15}E$, will result in the increase of both β and T_{dev}, as predicted by Eqs. (1) and (2). This implies the use of larger values of driving electric field and the development the new piezoelectric materials with higher values of shear piezoelectric coefficient, d_{15} (see Section 6). From the engineering point of view, the increase in the torque output of the actuator, Eq. (2), can be achieved by using the tube with a larger outer radius, R_{out} (which gives an increase proportional to R_{out}^3), and with a smaller ratio R_{in}/R_{out}.

At this point, we would like to stress one important advantage of the present tubular design of the torsional actuator. As predicted by Eq. (1), the tube with a larger length L will produce larger torsional angle, whereas the torque output will remain the same, Eq. (2). We can prove this statement using the experimental results for the single tube and for the two tubes joint lengthwise. Fig. 3(a) already showed that the joining two identical tubes double the torsional angle. To demonstrate that the torque output remains the same, for the same tubes we compare the data for the torsional angle, β, measured as a function of static torque load, T, at different magnitudes of the dc driving voltage. Using Eq. (1), we calculate the shear strain as $S_5 = \beta R_{out}/L$, and plot the data for $S_5(T)$ in Fig. 8. As one can see, for the same value of the driving field, the data for single tube and two joint tubes agree well. Since according to Eq. (2), the shear strain produces the torque T_{dev}, this result indicates that for tubular actuator, the torque output is independent of the length of the tube.

The last feature represents an important advantage of the present design of torsional actuator over another design based on piezoelectric bimorphs where the displacement of the tip of the bimorph due to its bending under the driving electric field is converted into the torsional motion using the system of levers [6]. In the bimorph system, the produced torsional angle depends upon the displacement of the tip of the bimorph, η. Since η changes with the length, L_b, of the bimorph, as [19] $\eta \propto L_b^2$, the longer the bimorph, the larger should be the torsional angle β. However, the increase in L_b will result simultaneously in the decrease of the force, F, developed by the bimorph, since the force is inversely proportional to the length of the bimorph: [19] $F \propto L_b^{-1}$. In contrast, the tubular actuator (Fig. 1(b)) is free of this drawback, because, as we showed before, its torque output is independent of the length, L, of the tube. Therefore, by increasing L, one can achieve larger torsional angle, Eq. (1): $\beta \propto L/R_{out}$, without drop in the produced torque.

Finally, we suggest that instead of increasing the length of the tube, larger values of the torsional angle can be achieved by a slight modification of the actuator geometry. One alternative to the tubular assembly (Fig. 1(b)) is a conical actuator which is schematically drawn in Fig. 9. The advantage of this configuration is that the radius of the end 1 can be made much larger than that of the end 2. If end 1 is fixed at a support and end 2 generates the twisting, this design is quite desirable. For conical geometry, the length, L, of the ceramic segments becomes longer

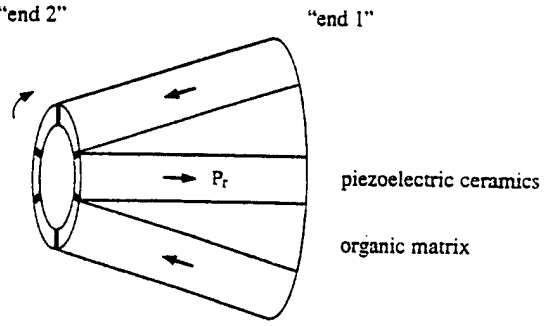

Fig. 9. Schematic drawing of the torsional actuator fabricated in the form of the cone. It is expected, that in the real application, the end 1 is fixed at a support, while the torsional displacement is produced at the end 2.

than that in the tubular structure (Fig. 1(b)), and the effective outer radius of the actuator, R_{out}, becomes smaller, since now it is the radius of the actuator at the end 2. The combined effect will be the increase in the amplification factor, L/R_{out}, in Eq. (1) and, therefore, in the produced torsional angle.

6. Nonlinear piezoelectric effect

In actuator and transducer applications, the piezoelectric ceramics is often subjected to high electric fields where the electric field dependence of induced strain is strongly nonlinear [2]. It is believed that the nonlinearity of the piezoelectric response of PZT ceramics is controlled by the irreversible displacement of domain walls [20–22] which separate regions of the material with different orientation of spontaneous polarization. The domain wall motion may be affected by many factors, including the crystal structure and microstructure of ceramics, the presence of impurities, dopants, defects, and a local variation in the composition of ceramics [2,21]. Possible mechanisms of domain wall motions have recently been discussed in detail in Refs. [21,22].

Shear piezoelectric response of PZT-5A strongly depends upon the magnitude of the driving electric field. This is evident from Fig. 3(b), where one can see that at $E = 3$ kV/cm, the magnitude of piezoelectric shear coefficient, d_{15}, of PZT-5A is doubled compared to the low field value, which is usually reported in manufacturer datasheets. Also, one can see that within the studied range of the ac field amplitude, the data corresponding to both ceramic sample and tubular actuators can be fit to the linear function:

$$d_{15} = d_{15}(0) + aE_m, \tag{6}$$

where $d_{15}(0)$ is the low-field limit of piezoelectric shear coefficient and a is the parameter. The fit of the data to Eq. (6) is shown in Fig. 3(b) with the lines.

This result suggests two conclusions which are important for practical application of PZT. First, the knowledge of how the material response changes with the amplitude of the driving field and its proper mathematical description are important for the modeling of the device performance. The data shown in Fig. 3(b) contradicts to a conventional description of strain response of ferroelectrics, where the field induced strain is expressed in terms of the Taylor series expansion in terms of electric field. Using symmetry arguments, one would expect to have the following expression for $d_{15}(E)$ [22]:

$$d_{15} = d_{15}(0) + b_1 E_m^2 + b_2 E_m^4 + \ldots \tag{7}$$

Thus, for the device modeling, Eqs. (1) and (2), one should use the experimentally derived linear dependence of $d_{15}(E)$, Eq. (6), rather than the polynomial expansion, Eq. (7). The second conclusion is important for the materials development for their application in torsional actuator. The strong change in the piezoelectric shear coefficient with electric driving field indicates that one should optimize the entire characteristic $d_{15}(E)$ in order to achieve the highest value of the piezoelectric coefficient, $d_{15}(E)$, as a function of the driving field. The higher the d_{15}, the larger will be the values of the torsional angle and the torque output, according to Eqs. (1) and (2).

7. Summary

In this work, we performed a detailed experimental study of a novel type of the piezoelectric torsional actuator. The data obtained prove the proposed concept of the torsional actuator, show that the actuator functions well both without load and under the torque load, and demonstrate that the actuator can operate continuously for a long period of time without drop in its performance. Comparison of the experimental data obtained on the tube and ceramic samples, such as piezoelectric shear coefficient, d_{15}, and mechanical fracture stress, σ_m, indicates that the material properties determine the performance of the torsional actuator. Also, the experimental results demonstrated that the proposed torsional actuator is capable of producing both large torque and large angular displacement in a compact package, sufficient to meet many smart structures requirements, and can be tailored for a variety of application requirements. Finally, one of the obvious advantages of the present design of the actuator is its simplicity: the piezoelectric shear strain is transformed directly into the angular displacement.

Acknowledgements

The authors wish to thank Dr. W. Chen (PSU) for his help in designing the torque load set-up, and DARPA for the financial support of this work.

References

[1] K. Uchino, Electrostrictive actuators: materials and application, Bull. Am. Ceram. Soc. 65 (1986) 647.

[2] L.E. Cross, Ferroelectric ceramics: materials and application issues, Ceram. Trans. 68 (1996) 15.

[3] Y. Fuda, T. Yoshida, Piezoelectric torsional actuator, Ferroelectrics 160 (1994) 323.

[4] J. Satonobu, N. Torii, K. Nakamura, S. Ueha, Construction of megatorque hybrid transducer type ultrasonic motor, Jpn. J. Appl. Phys. 35 (1996) 5038.

[5] A. Yabuki, M. Aoyagi, Y. Tomikawa, T. Takano, Piezoelectric linear motors for driving head element of CD-ROM, Jpn. J. Appl. Phys. 33 (1994) 5365.

[6] D.K. Samak, I. Chopra, A feasibility to build a smart rotor: trailing edge flap actuation, Proc. of the 1993 SPIE's North American Symposium on Smart Structures and Materials, Albuquerque, NM, 1993.

[7] I. Chopra, Status of application of smart structures technology to rotocraft systems, Presented at the Innovation in rotocraft technology, Royal Aeronautical Society, London, June 1997.
[8] E.F. Prechtl, S.R. Hall, Design of a high efficiency discrete servo-flap actuator for helicopter rotor control, SPIE Conference on Smart Structures and Materials, SPIE 3041 (1997) 158.
[9] M. Aoyagi, S. Tsuchiya, Y. Tomikawa, Trial production of an ultrasonic motor using longitudinal and torsional vibrations of a rod vibrator driven by piezoceramic plates inserted in its axial direction, Jpn. J. Appl. Phys. 36 (1997) 6106.
[10] A.E. Glazounov, Q.M. Zhang, C. Kim, Piezoelectric actuator generating torsional displacement from piezoelectric d_{15} shear response, Appl. Phys. Lett. 72 (1998) 2526.
[11] P.Ch. Chou, N.J. Pagano, Elasticity: tensor, dyadic, and engineering approaches, Dover Publications, New York, 1992, pp. 115–144.
[12] C. Kim, D. Lewis III, C.Cm. Wu, A.E. Glazounov, Q.M. Zhang, High authority piezoelectric torsional actuators, Presented at ISAF-98, Montreux, Switzerland, August 1998.
[13] A.E. Glazounov, Q.M. Zhang, C. Kim, A new torsional actuator based on shear piezoelectric response, SPIE Conference on Smart Structures and Materials, SPIE 3324 (1998) 82.
[14] S. Ueha, Y. Tomikawa, Ultrasonic Motors, Clarendon Press, Oxford, 1993.
[15] D. Wang, E. Fotinich, G. Carman, Influence of temperature on the electromechanical and fatigue behavior of piezoelectric ceramics, J. Appl. Phys. 83 (1998) 5342.
[16] B. Jaffe, W. Cook, H. Jaffe, Piezoelectric Ceramics, Academic Press, London, 1971.
[17] A.E. Glazounov, Q.M. Zhang, C.Cm. Wu, C. Kim, to be published.
[18] A.E. Glazounov, S. Wang, Q.M. Zhang, C. Kim, High efficiency piezoelectric motor combining continuous rotation with precise control over angular positioning, submitted to Appl. Phys. Lett.
[19] V.D. Kugel, S. Chadran, L.E. Cross, Caterpillar-type piezoelectric d_{33} bimorph transducer, Appl. Phys. Lett. 69 (1996) 2021.
[20] Q.M. Zhang, W.Y. Pan, S.J. Jang, L.E. Cross, Domain wall excitations and their contributions to the weak-signal response of doped lead zirconate titanate ceramics, J. Appl. Phys. 64 (1988) 6445.
[21] D. Damjanovic, Stress and frequency dependence of the direct piezoelectric effect in ferroelectric ceramics, J. Appl. Phys. 82 (1997) 1788.
[22] V. Mueller, Q.M. Zhang, Shear response of lead zirconate titanate piezoceramics, J. Appl. Phys. 83 (1998) 3754.

APPENDIX 55

ELSEVIER

Sensors and Actuators 79 (2000) 8–12

SENSORS AND ACTUATORS A PHYSICAL

www.elsevier.nl/locate/sna

Piezoelectric ceramic bimorph coupled to thin metal plate as cooling fan for electronic devices

Ju Hyun Yoo [a], Jae Il Hong [b], Wenwn Cao [c,*]

[a] *Department of Electrical Engineering, Semyung Univ., 21-1, Sinwol-dong, Jechon, Choong-Buk, South Korea*
[b] *Department of Electricity, Daeyeu Tech. Jr. College, 255 BokJung-dong, SooJung-ku, SungNam, South Korea*
[c] *Material Research Laboratory, The Pennsylvania State University, PA 16802, USA*

Received 13 February 1998; received in revised form 4 December 1998; accepted 10 May 1999

Abstract

Several types of piezoelectric fans for cooling electronic devices were constructed and tested at 60 Hz, 110 V and 220 V, respectively. The aim of the work is to investigate the possibility of replacing the rotary type of fan in some noise-sensitive electronic devices. Different vibrating metal plates were tested and analyzed theoretically. It is found that the resonant frequency of the vibrating plate decreases with the increase of its length (l) if the length of the piezoelectric ceramic bimorph (L) is kept constant. The series-type fan with $l = 31.8$ mm, made of phosphor bronze vibrating plate (S6), shows the highest value of fan tip displacement of 35.5 mm and produced wind velocity of 3.1 m/s driven by a 220 V, 60 Hz power source.

Keywords: Piezoelectric fan; Vibrating plate; PZT-5; Displacement; Wind velocity

1. Introduction

Most of the cooling fans in computers and other high power electronic devices are of the rotary type. Although satisfactory in many applications, the electromagnetic noise produced by the motor is often not desirable. An alternative is to use piezoelectric bimorph-type fans, which can generate airflow and efficiently control wind velocity with relatively simple structures. The advantages of these bimorph-type fans include: no electromagnetic noise, long lifetime ~25,000 (h) and low power consumption (less than 100 mW) in comparison with the electromagnetic rotary type counterpart [1–4]. Therefore, theoretically speaking, piezoelectric bimorph-type fans could replace rotary fans in many electronic devices.

This study is focused on the design, fabrication and testing of piezoelectric fans that can be operated at 60 Hz, 220 V. PZT-5 ceramics used for the ceramic bimorphs were manufactured by conventional sintering process for 90 min at 1300°C. The piezoelectric coefficient $d_{31} = -173$ (10^{-12} m/V) for this ceramic material. Different kinds of metals were used to make the vibrating plate and the results were compared to theoretical analysis. The resonant frequency, displacement and wind velocity for each of the fans were measured. Possibility of using these piezoelectric fans for cooling an electronic component was evaluated.

2. Experimental procedure

There are several steps for making these bimorph fans. First, PZT-5 powder (Edo, EC-65) was pressed into a plate shape by using a steel molder and an oil press at a pressure of 1 ton/cm^2. Then, the green ceramic plates were sintered at 1300°C for 90 min. Afterwards, these fired ceramic plates were lapped down to a thickness of 0.3–0.35 mm. Finally, silver paste was fired onto the surface of these plates at 600°C as electrodes. The piezoelectric ceramic plates were poled in silicone oil at 80°C by applying a DC field of 3.3 kV/mm for 30 min. Table 1 listed the physical properties of these PZT-5 ceramic plates.

The piezoelectric fans were fabricated by sandwiching a long metal shim between two layers of piezoelectric ceramic, which form either a series bimorph or a parallel bimorph as shown in Fig. 1. There are three basic parts in the fan structure: the base support, the bimorph embedded

* Corresponding author. Tel.: +1-814-865-4101; fax: +1-814-865-2326; E-mail: cao@math.psu.edu

0924-4247/00/$ - see front matter
PII: S0924-4247(99)00249-6

Table 1
Physical and electrical properties of PZT-5

Density (10^3 kg/m^3)	7.5
Young's modulus (10^{10} N/m)	6.6
Curie point (°C)	350
Mechanical Q	100
Dielectric constant	1725
Dielectric loss (1 kHz)	2.0
k_{31}	0.36
k_p	0.62
d_{31} (10^{-12} m/V)	−173

in the support and the metal vibrating plate. Fig. 1(a–c) are three different types of designs. In Fig. 1(a), the metal shim is much wider than the width of the bimorph; in Fig. 1(b), the width of the metal shim and the bimorph are the same while in Fig. 1(c), two bimorphs were attached to the metal shim. Fig. 1(d) illustrates the side view of the structure. The symbols are defined as the following: T — total thickness, L — the length of ceramic substrate, W — the width of ceramic substrate, w — the width of the vibrating plate, l — the length of the vibrating plate. The two ceramic plates in the bimorph are either connected in series which we call S-type, or in parallel which we call P-type.

The resonance properties of a typical piezoelectric ceramic bimorph with dimensions of 0.30 mm × 12.4 mm × 39 mm were measured by using a Network Analyzer (HPE

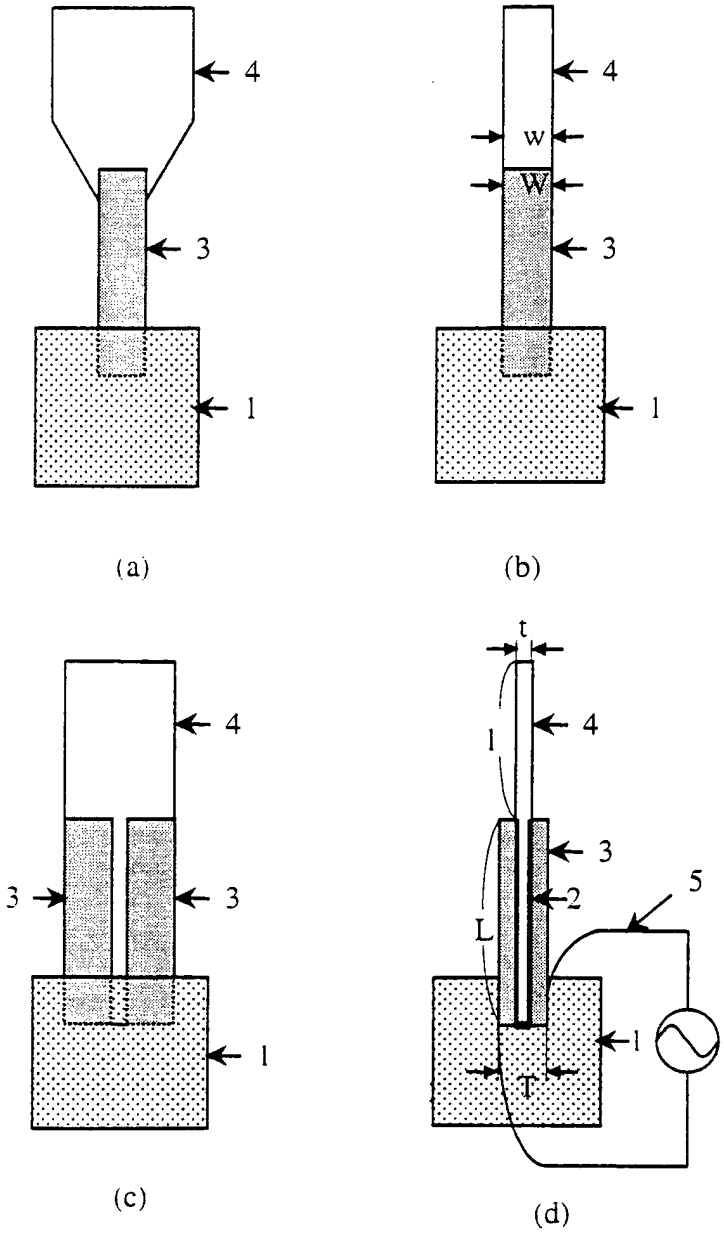

Fig. 1. Designs of the piezoelectric fans. Different parts are labeled as the following: 1, base support; 2, elastic adhesive; 3, ceramic bimorph; 4, metal vibrating plate; 5, AC voltage circuit.

Table 2
Classification and properties of the manufactured 60 Hz piezoelectric fan

Sample no.	d (mm)	L (mm)	w (mm)	l (mm)	W (mm)	t (mm)	Material of vibrating plate	Shape	Current (mA)	Displacement (mm)	Wind velocity (m/s)
P1	0.78	32	12.0	28.6	12.0	0.08	Phosphor bronze	Fig. 1(b)	2.83	34.7	3.0
S1	0.89	34	13.3	28.4	13.7	0.10	Brass	Fig. 1(b)	1.88	11.1	1.0
S2	0.97	35	13.3	46.1	13.1	0.15	Aluminum	Fig. 1(b)	1.90	23.3	1.9
S3	0.88	34	13.5	31.0	12.8	0.10	Phosphor bronze	Fig. 1(b)	2.02	29.4	2.2
S4	0.81	32	26.3	29.1	22.0	0.10	Brass	Fig. 1(c)	2.52	12.3	1.4
S5	0.87	34	25.2	47.0	22.0	0.15	Aluminum	Fig. 1(c)	2.86	13.4	1.4
S6	0.80	33	25.8	31.8	22.0	0.10	Phosphor bronze	Fig. 1(c)	3.59	35.5	3.1
S7	0.84	34	12.5	27.4	22.0	0.08	Phosphor bronze	Fig. 1(a)	1.92	26.3	2.2
S8	0.79	35	13.3	28.2	13.2	0.08	Phosphor bronze	Fig. 1(b)	2.21	33.3	2.3

5100). It was found that the resonant frequency, f_r, which defines the minimum impedance and the anti-resonant frequency, f_a, which defines the maximum impedance are 37.12 kHz and 39.068 kHz, respectively, with a resonant resistance of 2 Ω. Therefore, the thickness resonance is much higher than the designed operating frequency of 60 Hz for the fan.

Several designs using different metal vibrating plates were investigated and all the results are given in Table 2. The wind velocity of the piezoelectric fan was measured by using a wind velocity meter (Testovent 4000). The distance between the fan and the wind velocity meter was maintained at 1 mm for all the measurements. The displacements of parallel-type piezoelectric fans were measured at 110 V, 60 Hz, while those series-type piezoelectric fans were measured at 220 V, 60 Hz, by using a ruler and a high-speed camera.

3. Results and discussion

In order to investigate the resonant frequency of P1-type piezoelectric fans, an electrical current meter was put in series with the fan and connected to the constant voltage source. The output power of the fan is reflected in terms of the electric current (proportional to the power consumption at a constant voltage). At resonance, there will be a maximum output of wind so that the current will also be a maximum.

It was found that the resonance frequency of the fan is mainly determined by the length l of the vibrating plate while the width of the vibrating plate w has little influence. The 60 Hz resonance was achieved by gradually reducing the length l while monitoring the electric current. As shown in Table 2, there is a direct relationship between the maximum tip displacement of the metal plate and the wind velocity produced. On the other hand, there is a strong non-linear relationship between the vibrating plate length and the maximum tip displacement.

In order to better understand this complex relationship, we have performed a simple dynamical plate bending analysis assuming the bimorph is fixed. In the first-order approximation, the resonance frequency of a vibrating plate with one end fixed can be derived from the plate bending theory [5]:

$$f_r \propto \frac{t}{l^2}\sqrt{\frac{Y}{12\rho(1-\sigma^2)}} \tag{1}$$

Where ρ, σ, Y, l and t are density, Poisson's ratio, Young's modulus, vibrating plate length and thickness, respectively. An ideal plate with a perfectly fixed end would have a proportional coefficient of $\pi/8$, but in general, we must find this factor from experiment for different geometry, i.e., write the relationship as:

$$f_r = G\frac{t}{l^2}\sqrt{\frac{Y}{12\rho(1-\sigma^2)}} \tag{2}$$

where the factor G will also differ for different vibrating materials.

One can see from Eq. (2) that the resonance frequency increases with the decrease of the length of the vibrating plate l. Shown in Table 3 are the experimentally measured resonance frequencies for a fan made of phosphor bronze metal plate of different length, and the corresponding calculated values by using Eq. (2) with the factor $G = 0.558$. The agreement is very good. According to Table 3, the optimum design length for the bronze vibrating plate is 28.6 mm for which the measured resonant frequency is 60 Hz.

Table 3
Resonant frequency of P1-type fan with different lengths of the vibrating plate

l (mm)	Measured value (Hz)	Calculated value (Hz)
69	10	10.31
60	13	13.63
50	19	19.63
40	30	30.67
30	53	54.52
28.6	60	59.99

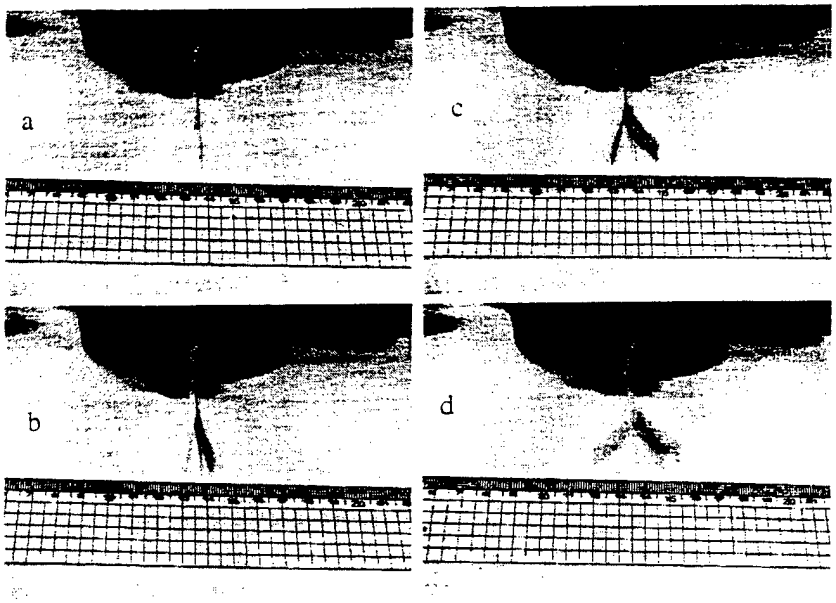

Fig. 2. Photos of the vibrating shape of a P1-type piezoelectric fan at different driving voltages at 60 Hz: (a) $V = 0$ V, (b) $V = 30$ V, (c) $V = 70$ V and (d) $V = 110$ V.

The width and thickness of the fan are increased when two sets of bimorphs are used in a fan design to increase the bending force of the plates as shown in Fig. 1(c). To understand this, let us look at the driving bending force by the ceramic bimorph for the vibration when an electric potential is applied. According to Ref. [3], the bending force is given by:

$$F = \frac{3WTd_{31}VY_c}{2L} \tag{3}$$

where V is the applied voltage, T is the thickness of the bimorph, d_{31} is the transverse piezoelectric constant, and Y_c is the Young's modulus of the ceramic, L and W are the length and the width of the bimorph, respectively, as shown in Fig. 1(d). We therefore expect to gain a larger bending force for a wider vibrating plate. However, it is found that although a higher level of force could be achieved by increasing W, it also produces unwanted audible noises. Therefore, in this study, the maximum number of bimorphs used was limited to two and the width of the vibrating plate was limited to 22 mm.

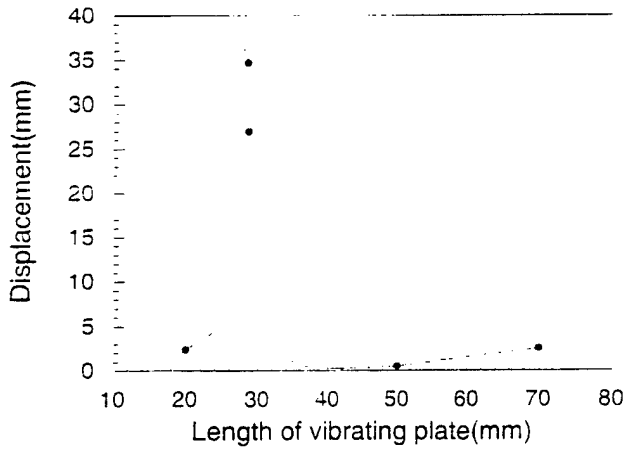

Fig. 3. Maximum fan tip displacement vs. vibrating plate length for a P1-type piezoelectric fan.

The vibrating plate is operated at its fundamental resonance as shown in Fig. 2, which is for P1-type fan with $l = 28.6$ mm driven by three different voltage levels of 30 V, 70 V and 110 V at 60 Hz. We can measure the maximum tip displacement from these photos. Results are given in Table 2 for one parallel connected bimorph fan (P1) and eight series connected bimorph fans (S1–S8). Fig. 3 shows the tip displacement of the P1-type fan driven by a 110 V, 60 Hz power source as a function of the vibrating plate length. The fan has a fairly sharp resonance as shown in Fig. 3. The maximum tip displacement for a P1-type fan increases with l at the beginning, reaches a maximum value of 34.7 mm at $l = 28.6$ mm, then starts to decrease with a further increase of the vibrating plate length. It is therefore important to find the optimum plate length for maximum efficiency at any given operating frequency.

High efficiency also depends on many other factors besides the length of the vibrating plate, such as the density and Young's modulus of the vibrating plate. In our

Table 4
Material properties of vibrating plates used for the piezoelectric fans

Vibrating plate	Density (10^3 kg/m^3)	Poisson's ratio	Young's modulus (10^{11} N/m^2)
Brass	8.5	0.35	1.006
Aluminum	2.7	0.345	0.703
Phosphor bronze	8.8	0.33	1.078

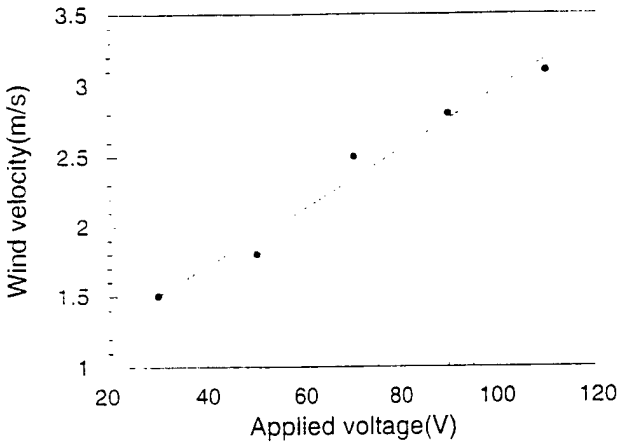

Fig. 4. Wind velocity for different applied voltages for a P1-type piezoelectric fan.

experiments, three kinds of vibrating plates were used and their material properties are given in Table 4.

There is a strong material dependence of the maximum tip displacement for a given fan design. Experimentally, we found that the fan design S6, consisting of two ceramic bimorphs and phosphor bronze vibrating plate, has the highest maximum value of 35.5 mm tip displacement under a 220 V, 60 Hz electrical drive. The second best is the S3 fan, which has one bimorph and a phosphor bronze vibrating plate. There is a nearly linear relationship between the applied voltage and the achieved wind velocity for any given design as shown in Fig. 4. This can be understood from Eq. (3) where the driving force is linearly proportional to the applied voltage, V. The wind velocity obtained from a P1 parallel-type fan reaches the maximum values of 3 m/s and from the S6 series-type fan reaches 3.1 m/s, respectively, under the driving of 110 V, 60 Hz and 220 V, 60 Hz power sources.

4. Summary and conclusions

We have investigated several designs of piezoelectric cooling fans for use in the ventilation of electronic devices. The design is aiming at using conventional electric power source of 60 Hz, 110 V and 220 V without the use of any electromagnetic transformers. The designs are very simple and easy to fabricate, the advantage of these type of fans is the elimination of unwanted electromagnetic noises from the rotary type fans. It is found that the most effective design is to use a phosphor bronze vibrating plate with either parallel or series connection of the piezoceramic plates in the bimorph structure. The estimated length of the vibrating plate can be calculated by using Eq. (2) with the factor $G = 0.558$. For other vibrating plate materials, one needs to figure out the G-factor experimentally before predicting the design length of the vibrating metal plate. The relationship of Eq. (2) holds very well from our experimental verifications.

We found a direct relationship between the tip displacement and the wind velocity when the fan is operated in the fundamental resonance of the metal plate. Therefore, one could use either as the optimization criterion.

Besides phosphor bronze, aluminum is also a good choice as the vibrating plate based on our investigation. Although one sacrifices a little on the performance by using aluminum plate, the material cost will be substantially reduced for mass production.

References

[1] S. Kamihara et al., Piezoelectric Bimorph Type Actuator and Piezoelectric Fan, Application of Piezoelectric Ceramics, Gakken-sha, 1989, pp. 68–74, in Japanese.
[2] K. Kawaguchi et al., Piezoelectric Fan, Application of Piezoelectric Ceramics, Gakken-sha, 1989, pp. 75–80, in Japanese.
[3] R. Sato, T. Taniguchi, M. Ohba, Characteristics of a Piezoelectric Bimorph in Use of an Actuator and the Application to a Piezoelectric Relay, OMRON Technics, No. 70, 1983, p. 52.
[4] S. Asakura et al., Small Type Fan, JP. Patent H5-29799, 1993.
[5] L.D. Landau, E.M. Lifshitz, Theory of Elasticity, Pergamon, Oxford, 1986.

Biographies

Ju Hyun Yoo received his PhD degree in Electrical Engineering from the Yonsei University, Korea in 1990. He is currently working in Semyung University as an associate professor of Electrical Engineering. His research interests are in the area of piezoelectric devices, including piezoelectric transformers, actuators, and ultrasonic sensors.

Jae Il Hong received his PhD degree in Electrical Materials from the Yonsei University, Korea in 1991. He is an Assistant Professor in the Department of Electricity of Dong Seoul College. His current research interest include finite element analysis of the piezoelectric ceramic devices, such as piezoelectric fans, actuators and transformers, and the characterization of acoustic emission sensors for partial discharge and particle detection in G.I.S. and transformers.

Wenwu Cao received his PhD degree in Condensed Matter Physics from the Pennsylvania State University, USA in 1987. He is currently an Associate Professor of Mathematics and Materials Science, a joint appointment between the Materials Research Laboratory and the Department of Mathematics of the Pennsylvania State University. His current research interests are: the formation of domain structures and their contribution to the dielectric, elastic and piezoelectric properties in ferroelectric materials, design of ultrasonic transducer and piezoelectric actuators using finite element methods.

ACTUATOR STUDIES

Photostriction

APPENDIX 56

Photostrictive Actuators

Patcharin Poosanaas, Kazuhiko Tonooka *, and Kenji Uchino

International Center for Actuators and Transducers, Mcterials Research Laboratory,

The Pennsylvania State University, University Park, PA 16802

* *Materials Division, Hokkaido National Industrial Research Institute, Sapporo, Japan*

ABSTRACT

Photostrictive materials, exhibiting light induced strain, are of interest for future generation wireless remote control photo-actuators, micro-actuators, and micro-sensors applications. (Pb, La)(Zr, Ti) O_3 (PLZT) ceramics doped with WO_3 exhibit large photostriction under uniform illumination of near-ultraviolet light. Using a bimorph configuration, a photo-driven relay and a micro walking device have been demonstrated. However, for the fabrication of these devices, materials exhibiting higher photovoltaic effect and higher response speed must be developed. The present paper reviews a new theoretical model for photovoltaic effect first, then enhanced performance photostrictive materials through sample surface characteristics, finally its potential future applications.

Keywords: Photovoltaic effect, Photostriction, Photostrictive actuators, Surface characteristics, PLZT ceramics

1. Introduction

The continuing thrust towards greater miniaturization and integration of microrobotics and microelectronics has resulted in significant work towards development of ceramic actuators, utilizing their wavelength-dependent optical actuation mechanisms. In the recent times, *Photostrictive actuators* - which directly converts the photonic energy to mechanical motion - have drawn significant attention for their potential usage in microactuation and microsensing applications.

Photostrictive materials have the ability to convert light directly to physical motion. The mechanism of photostriction can be described as the superposition of the photovoltaic and converse piezoelectric effects. When noncentrosymmetric materials, such as ferroelectric single crystals or polarized ferroelectric ceramics, are uniformly illuminated, a high voltage considerably exceeding the band gap energy is generated. In certain ferroelectric materials this photovoltage is of the order of kV/cm (10^5V/m). Along with this photovoltage, mechanical strain is also induced due to the converse piezoelectric effect. The fortuitous combination of these two effects makes these ferroelectrics suitable for wireless actuator applications, activated and driven by incident light. These optical actuators have received considerable attention for applications in areas related to micromechanics, ultrahigh vacuum and space technologies. Optical actuators are also anticipated to be used as the driving component in optically controlled "electromagnetic-noise free" systems. The photostrictive effect has also recently been used in fabricating a photophonic device, where light was transformed directly into sound from the mechanical vibration induced by intermittent illumination.

The photostrictive effect has been studied mainly in ferroelectric polycrystalline materials for potential commercial applications. Lanthanum-modified lead zirconate titanate (PLZT) ceramic is one of the most promising photostrictive materials due to its relatively high piezoelectric coefficient and ease of fabrication. However, previous studies have shown that for commercial applications, improvements in photovoltaic efficiency and response speed of the PLZT ceramics are essential. The improvement in photostrictive properties require consideration of several parameters, such as:

- material parameters (e.g. composition and stoichiometry, dopant type and concentration)
- processing condition (e.g. processing route and parameters) and microstructure, and
- sample configuration and performance testing conditions (e.g. surface characteristics and illumination).

The photostrictive response of a material can be considerably increased and controlled by understanding the influence of these parameters and by optimizing these parameters. This paper reviews a new model for explaining the photovoltaic effect first, then the fundamentals of photostrictive effect in PLZT ceramics, and finally describes some of the potential applications. The influence of sample geometry has also been illustrated.

2. Photostrictive Effect

Photostriction is a phenomenon in which strain is induced in the sample by incident light. In principle, this effect arises from a superposition of the photovoltaic effect, i.e. generation of large voltage from the irradiation of light, and the converse-piezoelectric effect, i.e. expansion or

contraction under the voltage applied [1]. It must be noted that the photostrictive effect is different from the thermal dilatation and pyroelectricity, where strain is produced due to the temperature rise from the light illumination.

The photostrictive phenomenon has been observed in certain ferroelectric materials. The figure of merit of photostriction is generally expressed as the product of photovoltage, E_{ph}, and the piezoelectric constant, d_{33}. Therefore, for application purposes, enhancement and/or optimization of photostrictive properties requires consideration of both the terms in the figure of merit. Recently, PLZT ceramics have gained considerable attention due to their excellent photostrictive properties, high d_{33} and ease of fabrication.

2.1 Mechanism of photovoltaic effect

When a noncentrosymmetric ferroelectric material is illuminated with uniform light having a wavelength corresponding to the absorption edge of the material, a steady photovoltage/ photocurrent is generated [2]. In some materials, the photovoltage generated is greater than the band-gap energy, and can be of the order of several kV/cm. This phenomenon, referred to as the anomalous photovoltaic effect (APV), is different from the corresponding phenomenon in the p-n junction of semiconductors (e.g. solar battery) [3, 4]. The APV effect is observed only in the direction of the spontaneous polarization (P_s) in the ferroelectric material. The generated photovoltage is proportional to the sample length along the P_s direction. The APV effect has been observed to disappear in the paraelectric phases.

The origin of photovoltaic effect is not yet clear, even though several models have been proposed on the mechanism of photovoltaic effect. The key issue in understanding the APV mechanism is the importance of both, impurity doping as well as crystal asymmetry. Figure 1 illustrates one of the proposed models, the electron energy band model proposed for PLZT ceramics by one of the authors [5]. The energy band is basically generated by the hybridized orbit of p-orbital of oxygen and d-orbit of Ti/Zr. The donor impurity levels induced in accordance with La doping (or other dopants) are present slightly above the valence band. The transition from these levels with an asymmetric potential due to the crystallographic anisotropy may provide the "preferred" momentum to the electron. Electromotive force is generated when electrons excited by light move in a certain direction of the ferroelectric crystal, which may arise along the spontaneous polarization direction. The asymmetric crystal exhibiting a photovoltaic response is also piezoelectric in principle, and therefore, a photostriction effect is expected as a coupling of the bulk photovoltaic voltage with the piezoelectric constant.

Fig 1

Recently the mechanism of APV has also been proposed based on the voltage source model. The possibility of generating an effective dc field has been explained on the basis of nonlinear properties of a ferroelectric material having noncentric symmetry [6]. The details of the model are explained in the following section.

2.1.1 Voltage Source Model

The photovoltaic properties are attributed to the photocarriers and internal electric fields generated by short-wavelength illumination. The optical nonlinearity of the second order has been proposed as the origin of photo-induced dc field generation. The expression for the polarization of dielectrics, considering the non-linear effect up to the second order is given by [7]:

$$P = \varepsilon_o(\chi_1 E_{op} + \chi_2 E_{op}^2) \qquad [1]$$

where ε_0 is the permittivity of vacuum, χ_1 is the linear susceptibility, χ_2 is the nonlinear susceptibility of the second order, and E_{op} is the electric field at an optical frequency.

In ferroelectric ceramics, nonlinearity is expected to appear due to the poling. To the first approximation, the susceptibilities (χ_1) and (χ_2) can be assumed to be constant. The illuminating light - being an electromagnetic wave - will provide an electric field for charges in dielectrics. When an alternating electric field with amplitude E_{op}, and optical frequency ω_{op}, is applied to a dielectric material having a nonlinear response, the polarization as a function of time, t, can be written as

$$P = \varepsilon_o\{\chi_1 E_{op}\cos(\omega_{op}t) + \chi_2 E_{op}^2\cos^2(\omega_{op}t)\} \qquad [2]$$

In a linear material, χ_2 will be zero and the induced polarization will be proportional to the applied electric field at any moment. As a result, in the linear material, the polarization oscillates at an optical frequency of ω_{op}. However, in a nonlinear material, an asymmetric polarization wave is produced due to the nonlinear dielectric response which suggests that the induced polarization contains the higher order components as well as the fundamental wave. The Fourier

analysis of the second harmonic wave shows that it contains the second harmonic component and also has a nonzero average. This average term of the induced polarization can result in a dc electric field for carriers.

In dielectrics, the value of the local electric field is different from the value of the macroscopic electric field. An additional field due to the polarization charges appears in polarized dielectrics. For simplicity, the local field in dielectrics has been approximated using the Lorentz relation for a ferroelectric material as [8]:

$$E_{local} = E + \frac{\gamma P}{3\varepsilon_o} \qquad [3]$$

where E is the macroscopic electric field and γ is the Lorentz factor.

When an alternating electric field at an optical frequency is applied, the local field in a dielectric material having second-order nonlinearity can be given as:

$$E_{local} = E_{op}\cos(\omega_{op}t) + \frac{\gamma}{3}\{\chi_1 E_{op}\cos(\omega_{op}t) + \chi_2 E_{op}^2\cos^2(\omega_{op}t)\} \qquad [4]$$

The average of the local electric field E_{local} in Eq. (4) will be:

$$\overline{E_{local}} = \frac{1}{6}\gamma\chi_2 E_{op}^2 \qquad [5]$$

It must be noted that Eq. (5) has been derived for nonlinear dielectrics under a coherent propagation of the light wave at a single frequency. However, the condition of coherent illumination may not be satisfied in the experimental conditions described in this work, where a mercury lamp is used as a light source. The nonlinear effect will be affected by to the degree of coherence. Therefore, considering the depression of nonlinear effect due to the incoherence, the expression for the effective dc field induced by incoherent light source may be modified as:

$$\overline{E_{local}} = c_1 \gamma \chi_2 (E_{op}^2)^{\beta} \quad [6]$$

where c_1 is a constant and β is a parameter expressing the depression effect.

Replacing the variable E^2_{op} with the intensity (I_{op}) [7], the following expression for the average induced (dc) field due to the incoherent light can be obtained:

$$E_{dc} = \overline{E_{local}} = c_2 \gamma \chi_2 (I_{op})^{\beta} \quad [7]$$

where c_2 is a constant and E_{dc} is the effective dc field for photoinduced carriers. Note that the induced field, E_{dc}, is proportional to the nonlinear susceptibility as well as the Lorentz factor, γ.

The concentration of carriers excited by optical irradiation is governed by the following rate equation,

$$\frac{dn_c}{dt} = g - Rn_c^2 - \frac{n_c}{\tau_c} \quad [8]$$

where n_c is the carrier density, g is the generation rate of the carrier, R is the recombination rate of the carrier, and τ_c is the intrinsic lifetime of the carrier. When the excitation is adequately strong, the recombination process dominates, and the carrier density becomes:

$$n_c = \sqrt{\frac{g}{R}} \quad [9]$$

The generation rate (g) being proportional to the light intensity (I_{op}), the carrier density can be written as :

$$n_c = c_3 \sqrt{\frac{I_{op}}{R}} \quad [10]$$

where c_3 is a constant. Introducing the carrier mobility (μ), the electric conductivity due to the photoinduced carriers will then become [2]

$$\sigma_{op} = qn_c\mu \quad [11]$$

where, q is the charge of the photocarrier. Combining Eqs. 10 and 11, the photoconductivity can be obtained as a function of light intensity,

$$\sigma_{op} = c_3 q\mu\sqrt{\frac{I_{op}}{R}} \quad [12]$$

The photocurrent will be the product of the photoconductivity and the photoinduced dc field:

$$J_{ph} = \sigma_{op} E_{dc} \quad [13]$$

Substituting Eqs. (7) and (12) to (13), the expression for the photocurrent can finally be obtained:

$$J_{ph} = c_4 q\mu\gamma\chi_2\sqrt{\frac{1}{R}}(I_{op})^{\beta+\frac{1}{2}} \quad [14]$$

where, c_4 is a constant. The Eqs. (12) and (14) provide a correlation for the photovoltaic response of ferroelectrics on the basis of optical nonlinearity.

2.1.2 Model Validation and Analysis

The predictions for the proposed model were validated against experimental measurements of photoconductivity and photocurrent. PLZT (3/52/48) ceramics samples were cut into the standard sizes of 5x5 mm^2 and polished to 1 mm thickness. The samples were poled along the length (5 mm) under a field of 2 kV/mm at 120 °C for 10 min. The present model was validated by comparing the experimental results with the prediction based on Eq. (12) for photoconductivity and Eq. (14) for photocurrent.

Figure 2 shows the plot of photoconductivity (σ_{op}) as a function of light intensity (I_{op}). The exponent relating the photoconductivity and the light intensity was calculated to be 0.54.

This is in good agreement with the value of 0.5 derived for the recombination process of the carriers (Eq. 12).

Fig 2

Figure 3 shows the experimental results of short-circuit photocurrent (J_{ph}) as a function of light intensity. The parameter β based on Eq. (14) was calculated to be 0.46. The value of parameter β is expected to lie between 0 and 1. The depression in β value can be attributed to the incoherent illumination of the mercury lamp.

Fig 3

Figure 4 shows the experimental results of the open-circuit photovoltage (E_{ph}) as a function of light intensity. The photovoltage was found to be proportional to the square root of the light intensity.

Fig 4

The experimental data was further analyzed to investigate the effects of incoherent illumination. Since a partial coherence of illuminating light can be achieved in a very small area, an increase in β value is expected in thinner photovoltaic samples. In order to reconfirm this effect,

the photocurrent was measured as a function of light intensity (Figure 5) in a very thin (140 μm) PLZT sample. The parameter β based on Eq. (14) was recalculated and was found to be 0.80, which is higher than β value of 0.46 in the thicker sample (1 mm thickness). These results suggest that the parameter β increases with a decrease in the thickness of photovoltaic sample, due to higher coherency of illumination in thinner samples. This suggests that an enhancement in the photovoltaic properties may be achieved in a very thin sample or by using coherent illumination.

Fig 5

2.2 Experimental setup for photovoltaic and photostrictive measurements

Figure 6 shows the experimental setup. Photovoltaic measurements were done using a high-input-impedance electrometer (Keithley 617), while the photostriction was measured by a displacement sensor (LVDT, Millitron model 1301). The photovoltage and photocurrent were determined from the current-voltage relation by applying voltage between -100 and +100 V, while illuminating the samples as described below. The photovoltage was determined in an open circuit state from the intercept of the horizontal applied voltage axis, while the photocurrent was obtained for the short circuit state from the intercept of the vertical current axis.

Fig 6

A short arc mercury lamp (Ushio Electric USH-500D) was used as a light source. The original lamp radiation was passed through an Infrared (IR) blocking filter and Ultraviolet (UV) bandpass filter to obtain a monochromatic beam with a maximum strength around 366 nm wavelength. Light with this wavelength has been reported to yield the maximum photovoltaic properties in the PLZT samples [9, 10].

3. Sample Geometry Dependence

Since the photostrictive effect is excited by the absorption of illumination in the surface layer of ceramics, it is apparent that the surface geometry of the photostrictive material will have a strong bearing on the generation of photocurrent and photovoltage. This surface characteristics is further reinforced by the absorption occurring at the surface layer of the piezoelectric material facing the illumination. Using a sample thickness closer to the penetration depth will ensure that the entire film will be active and efficiently utilized. Therefore, investigation of photovoltaic response as a function of sample thickness is desired in determining the optimal thickness range with maximum photovoltaic effect. In addition, studying the effect of surface roughness on the photovoltaic effect will provide an insight on the absorption dependence of photostriction.

3.1 Thickness dependence

In order to determine the optimum sample thickness, dependence of photovoltaic effect on sample thickness of PLZT (3/52/48) ceramics doped with 0.5 at.% WO_3 was examined. Photovoltaic response was found to increase with a decrease in sample thickness in PLZT

ceramics. A model has been proposed to explain and quantify the observed influence of sample thickness on photovoltaic response [11] as shown in Fig. 7, where the absorption coefficient is assumed to be independent of light intensity and the photocurrent density is taken to be proportional to light intensity. The sample is assumed to comprise of thin slices along the thickness direction of the sample. A circuit diagram representing these layers is also shown in the same figure.

Fig 7

Figure 8 shows the plot between the normalized photocurrent (i_m) and sample thickness calculated for the external resistance (R_m = 200 TΩ). The computed results shows good agreement with the experimental data. With increasing in sample thickness, i_m increases, reaches a maxima, and subsequently it decreases with the sample thickness. The decrease in i_m can mainly be attributed to the dark conductivity (σ_d). The optimum thickness (for the present set of samples) which yields maximum photocurrent is found at 33 μm. The extremely low value of optimum thickness implies that the lower sample thickness will be expected to give better photovoltaic response.

Fig 8

3.2 Surface roughness dependence

The effect of surface roughness on photovoltaic and photostrictive properties was examined in the PLZT ceramics, the sample as used in section 3.1, with different surface roughness obtained by polishing to different surface finishes. The surface roughness was measured by a profilometer (Tencor, Alpha-Step 200) and the average surface roughness was determined using the graphical center line method.

The variation of photovoltaic (photovoltage and photocurrent) and photostrictive properties with surface roughness are plotted in Figs. 9 (a)-(c). The photovoltaic and photostrictive responses increase exponentially with decreasing surface roughness. This is due to the fact that, with increase in surface roughness the penetration depth of the illumination decreases, while contributions from multiple reflections increase.

Fig 9

A model has been proposed to explain and quantify the influence of surface roughness. The effect of multireflection has not been considered in the following formulation. Two different shapes, a sine profile and a "V" profile roughness (Fig. 10 (a)), were assumed for simplicity. In both these shapes, the amplitude was taken as a center line roughness (r) and the wavelength as (g). The detail will be make only for a "V" profile.

Fig 10

The corresponding equations for the unit cell of the "V" profile rough surface (Fig. 10 (b) and (c)) are:

$$y = r(\frac{4x}{g} + 1), \qquad where \ \frac{-g}{4} \le x \le \frac{g}{4}, \qquad [15]$$

$$\tan\theta_i = \frac{dy}{dx} = \frac{4r}{g} \qquad [16]$$

where θ_i is an angle with the vertical incident beam. By means of Snell's law [7],

$$n_i \sin\theta_i = n_t \sin\theta_t \qquad [17]$$

where θ_t is the transmitted angle, n_i and n_t are the refractive indexes of air and PLZT sample respectively, the transmittance (T) is given by:

$$T = \frac{I_t \cos\theta_t}{I_i \cos\theta_i} = [\frac{n_t \cos\theta_t}{n_i \cos\theta_i}]t^2 \qquad [18]$$

The transmitted light intensity (I_t) will then be:

$$I_t = I_i T = I_i n_i t^2 \qquad [19]$$

This intensity will further decrease due to absorption. If the sample thickness is greater than the penetration depth ($1/\alpha$), the average intensity (I_o) reaching the sample below the rough surface will be:

$$I_o = (\frac{2}{g}) x \int_{\frac{-g}{4}}^{\frac{g}{4}} \int_{0}^{\infty} I_t(x) \exp(-\alpha z) dz dx \qquad [20]$$

where, z is the sample thickness

This average intensity (I_o) can be substituted in sample thickness model which has been reported earlier [11] to examine the influence of surface roughness on photocurrent. The

normalized photocurrent (i_m) computed using above formula, is plotted in Fig. 11 as a function of surface roughness for the two chosen surface profiles. The experimental results are also plotted. A wavelength of roughness at 1 μm gave the best fit of the experimental results which is close to the size of the grain size of the sample.

Fig 11

4. Potential Applications Based on Photovoltaic and Photostrictive Effects

The direct conversion of photonic to mechanical motion by the photostrictive effect can lead to two broad classes of applications - microactuation and microsensing. Potential applications for microactuation include [12] :

- an alternative mechanism for converting solar energy directly into mechanical motion for planetary exploration.
- direct corrective control in adaptive optics/interferometer
- optical micropositioning
- solar tracking actuator/shutter for self alignment of the spacecraft to the sun for optimal power generation using solar sails
- optically controlled valves for space applications
- optically controlled microrobots
- photophones

The potential microsensing applications include:

- a variety of tunable sensors for incident radiation (UV, visible etc.) based on the deflection as a function of incident radiation intensity
- indirect microsensors based on the photodeflection when the device is loaded with condensing moisture (microhygrometer) or incident interstellar dust (microbalance)).

We have successfully demonstrated the application of photoactuation in PLZT ceramic wafers as photo-driven relay [9] and photo-driven micro walking machine [13]. These devices are designed to use incident light and have no lead wires or electric circuits.

Figure 12 illustrates a photodriven relay device using a PLZT bimorph as the driver which consists of two ceramic plates bonded together with their polarization directions opposing each other. A dummy PLZT plate was positioned adjacent to the bimorph to cancel the photovoltage generated in the bimorph. Utilizing the dual beam method, switching was controlled by alternately irradiating the bimorph and the dummy, which can avoid the time delay due to low dark conductivity. The amount of displacement observed at a tip of the bimorph was about 150 μm with the delay time of 1-2 seconds [9].

Fig 12

Figure 13 shows a micro-walking machine using photostrictive bimorphs with two ceramic legs fixed on a plastic board. The structure is simple having only two ceramic legs (5 mm x20 mm x 0.35 mm). When the two legs were irradiated alternately, the device moved like an

inchworm at a speed of several tens of microns per minute [13]. The photostrictive bimorph as a whole was caused to bend by ± 150 μm as if it averted the radiation of light. The walking speed can be increased to approximately 1 mm/ min by providing some contrivances such as the use of a foothold having microgroves fitted to the steps of the legs.

Fig 13

Photomechanical resonance in a PLZT bimorph has been successfully demonstrated using chopped UV irradiation having neither electrical lead wire or circuits. A thin cover glass was attached on the photostrictive bimorph structure to decrease the resonance frequency so as to easily observe the photo-induced resonance. The dual beam method was used to irradiate the two sides of the bimorph alternately, intermittently with a 180° phase difference. The mechanical resonance was determined by changing the chopper frequency. The resonance frequency was about 75 Hz, which is smaller than the audible frequency range [4]. However the achievement of photo-induced mechanical resonance in the audible frequency range suggests the possibility of photostrictive PLZT bimorph-type devices as photoacoustic components for the next communication age.

Recently, a new application of highly efficient, photostrictive PLZT films on flexible substrates has been conceived for usage in the new class of small vehicles for future space missions [14].

In addition some promising devices, which can be fabricated based on tailoring photostrictive films on the flexible substrate in a unimorph structure, are micro walking device and light chasing device.

Micro walking device can be designed into arch-shaped photoactuating composite films (Fig. 14 (a)) with a triangular top (Fig. 14 (b)). Photoactuating films may be fabricated from PLZT solutions and coated on one side of a suitable flexible substrate which will then be designed to have a curvature of 1 cm^{-1}. A slight difference in length between the right and left legs could be designed in order to provide a slight difference between their resonance frequencies. This would facilitate in controlling this device in both clockwise and counterclockwise rotations. A light chopper operating at a frequency close to resonance could be used to illuminate the device, in order to maximize the vibration of the bimorph which will then provide the capability to turn by applying different resonance frequencies of two legs.

In order to maximize the photostrictive properties of the sample, the sample geometry could be determined from the proposed model in section 3.1. After coating suitable UV transparent electrode, the film could then be poled along the thickness. Under uniform illumination on the upper side of the device, the PLZT film on that side would contract. Since the PLZT film is bonded onto the substrate, the whole device would then decrease the curvature and move.

Fig 14

A 'sunflower' device for chasing the light source may be designed using photoactuating film composites. By tailoring the absorption edge of PLZT ceramics through impurity doping, the device can be utilized for tracking solar radiation. Figure 15 shows the principle of this 'light source chasing' device. Two unimorphs are attached to both sides of a solar panel (Fig 15 (a)). When the light source positioned equidistantly between the two unimorphs, there is no difference in the strain due to photostrictive effect which results in the stable state of the solar panel (gray line in Fig. 15 (b)). When the light source moves to the right-hand side, for example, the intensity at B side will be stronger than A side. The photoactuating film on B side would deflect more than the A side which, leads to the panel canting and moving to track the light source.

Fig 15

5. Summary

Photostrictive actuators are driven only by the irradiation of light without requiring the electrical lead wire connection. Therefore they can be employed in ultra high vacuum or outer space. The direct conversion of photonic to mechanical motion by photostrictive effect can lead to two broad classes of applications, microactuator and microsensing which will open new vistas in the actuator technology. It is evident that the photovoltaic and photostrictive effects are strongly dependent on the surface characteristics of the sample. The surface characteristics are, therefore, of extreme importance during the fabrication of high efficiency photostrictive device. It is expected that the sample thickness and roughness which will be crucial in designing thick film

bimorphs for enhancements in the efficiency of a micromechanical device. We introduced two new devices, microwalking and light chasing device in this article.

REFERENCES

1. Uchino, K. and M. Aizawa, 1985, *"Photostrictive Actuators Using PLZT Ceramics"*, Jpn. J. Appl. Phys. Suppl., 24, 139-141.
2. Fridkin, V.M., in *Photoferroelectrics*, edited by M. Cardona, P. Fulde, and H.-J. Queisser, Solid-State Sciences 9, (Springer-Verlag, New York, 1979), pp. 85-113.
3. Uchino, K., 1996, *" New Applications of Photostriction"*, Innovations Mater. Res., 1(1), 11-22.
4. Chu, S.Y. and K. Uchino, 1994, *"Impurity Doping effect on Photostriction in PLZT Ceramics"* J. Adv. Performance Mater., 1, 129-143.
5. Tanimura, M. and K. Uchino, 1988, *"Effect of Impurity Doping on Photostrictive in Ferroelectrics"*, Sensors and Materials, 1, 47-56.
6. Tonooka, K., P. Poosanaas, and K. Uchino, " *Mechanism of Bulk Photovoltaic Effect in Ferroelectrics"*, In: Conference Proceedings on SPIE'98 Smart Structure of Materials, Sandiego, California, March 1998, (to be published).
7. Hecht, E., in *Optics,* with contributions by Alfred Zajac, 2nd ed., (Addison-Wesley Publishing, Massachusetts, 1987), pp. 44, 81-104, 610-616.
8. Kittel, C., in *Introduction to Solid States Physics*, 7th ed., (John Wiley & Sons, Inc., New York, 1996), p388.

9. Sada, T., M. Inoue, and K. Uchino, 1987, *"Photostriction in PLZT Ceramics"*, J. Ceram. Soc. Jpn. Inter. Ed., 95, 499-504.

10. Nonaka, K., M. Akiyama, A. Takase, T. Baba, K. Yamamoto, and H. Ito, 1995, *"Nonstoichiometry Effects and Their Additivity on Anomalous Photovoltaic Efficiency in Lead Lanthanum Zirconate Titanate Ceramics"*,Jpn. J. Appl. Phys., 34, 5380-5383.

11. Poosanaas, P., A. Dogan, S. Thakoor, and K. Uchino, 1998, *"Influence of Sample Thickness on the Performance of Photostrictive Ceramics"*, J. Appl. Phys., 84 (3), 1508-1512.

12. Thakoor, S., P. Poosanaas, J.M. Morookian, A. Yavrovian, L. Lowry, N. Marzwell, J. Nelson, R. Neurgaokar, and K. Uchino, " *Optical Microactuation in Piezoceramics"*, In: Conference Proceedings on SPIE'98 Smart Structure of Materials, San Diego, California, March 1998, (to be published).

13. Uchino, K., 1989, " *Micro Walking Machine Using Piezoelectric Actuators"*, J. Rob. Mech., 124, 44-47.

14. Thakoor, S., J.M. Morookian, and J.A. Cutts, " *The Role of Piezoceramics Microactuation for Advanced Mobility"*, In: Conference Proceedings 10th IEEE Int'l Symposium on Applications of Ferroelectrics Transactions, 1, 1996, 205-211,

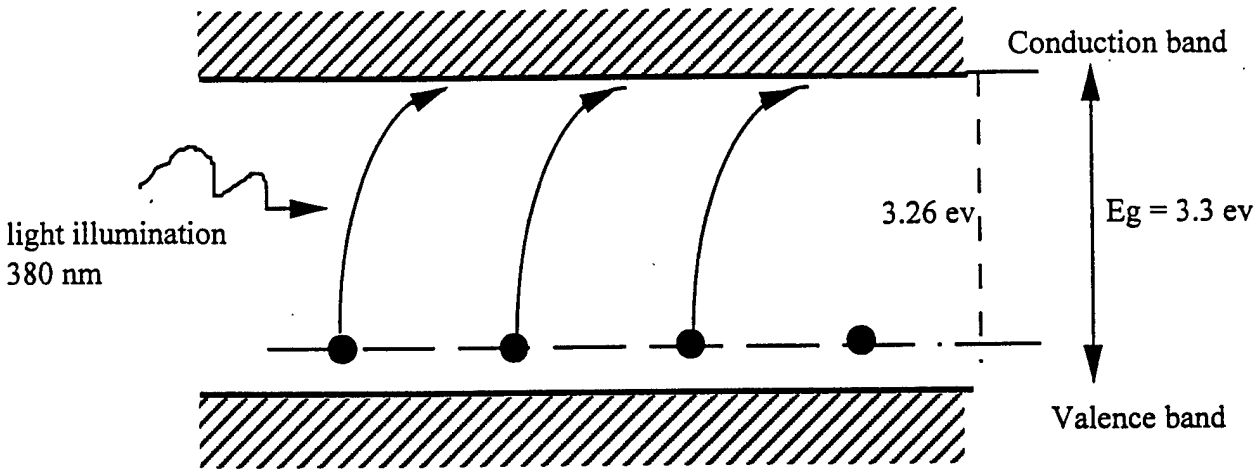

Clarks Work

Fig 1

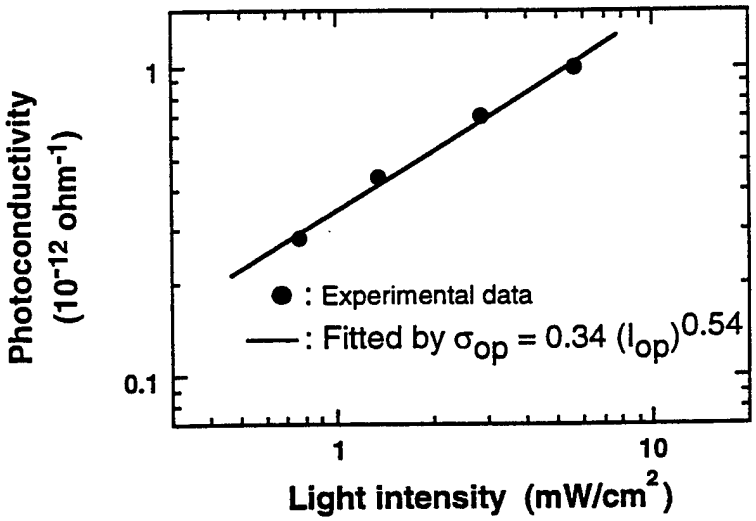

Kaleida Graph

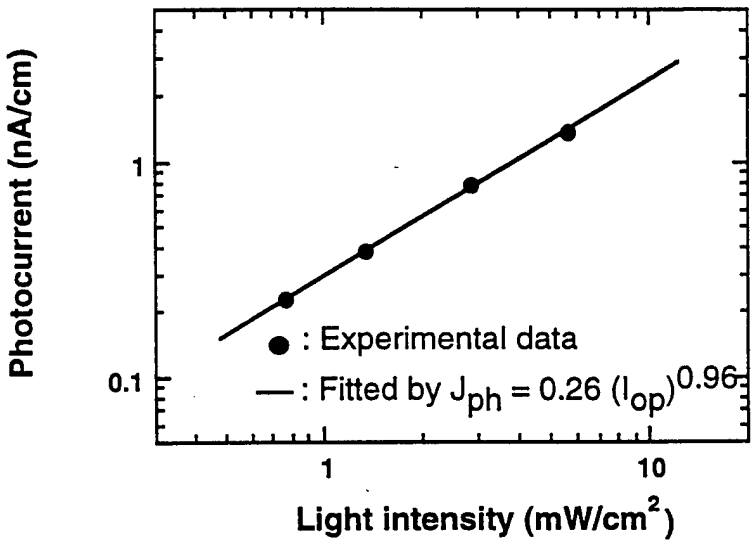
Photocurrent (nA/cm)
1
0.1
1
10
Light intensity (mW/cm^2)
● : Experimental data
— : Fitted by $J_{ph} = 0.26\ (I_{op})^{0.96}$

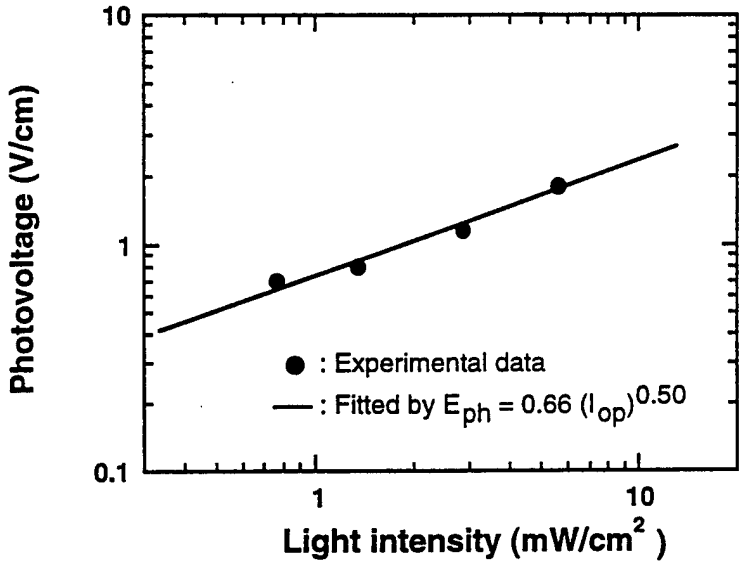
10
1
0.1
Photovoltage (V/cm)
1
10
Light intensity (mW/cm^2)
● : Experimental data
— : Fitted by $E_{ph} = 0.66\ (I_{op})^{0.50}$

Fig 4

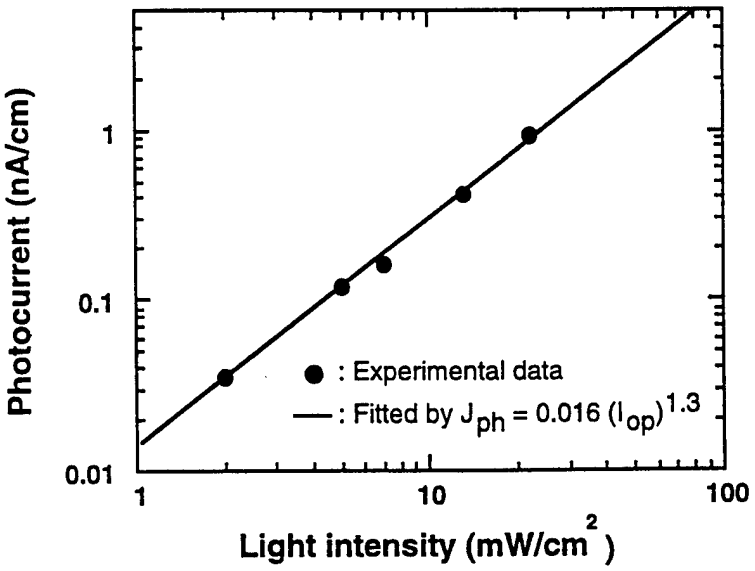
Photocurrent (nA/cm)
1
0.1
0.01
1
10
100
Light intensity (mW/cm^2)
● : Experimental data
—— : Fitted by $J_{ph} = 0.016\ (I_{op})^{1.3}$

Fig 5

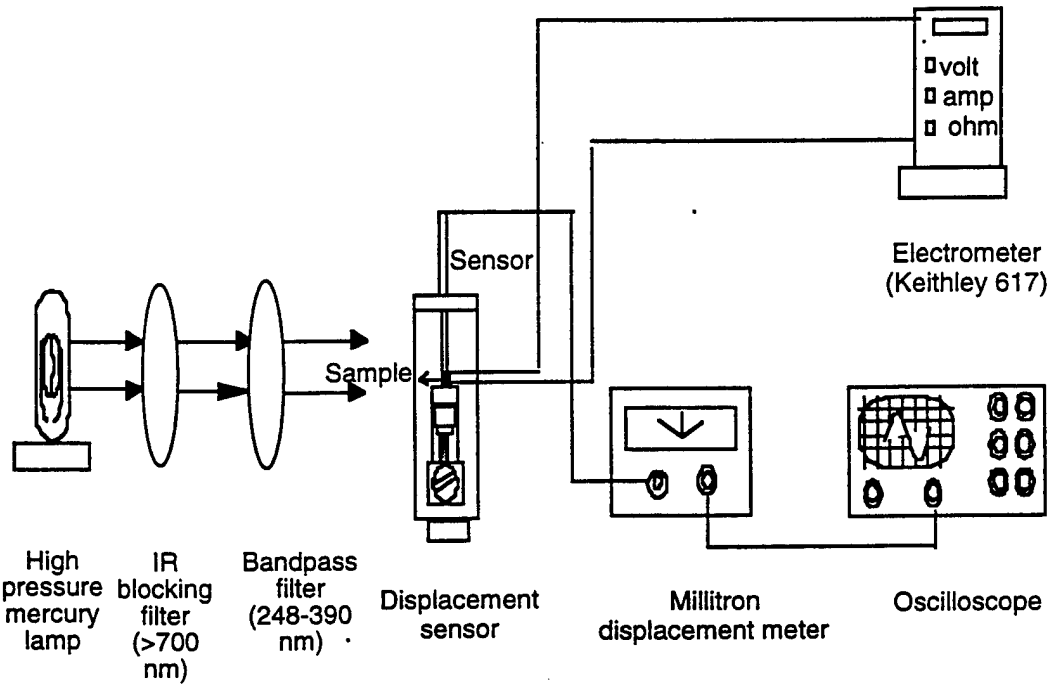
volt
amp
ohm
Electrometer
(Keithley 617)
Sensor
Sample
High pressure mercury lamp
IR blocking filter (>700 nm)
Bandpass filter (248-390 nm)
Displacement sensor
Millitron displacement meter
Oscilloscope

Fig 6

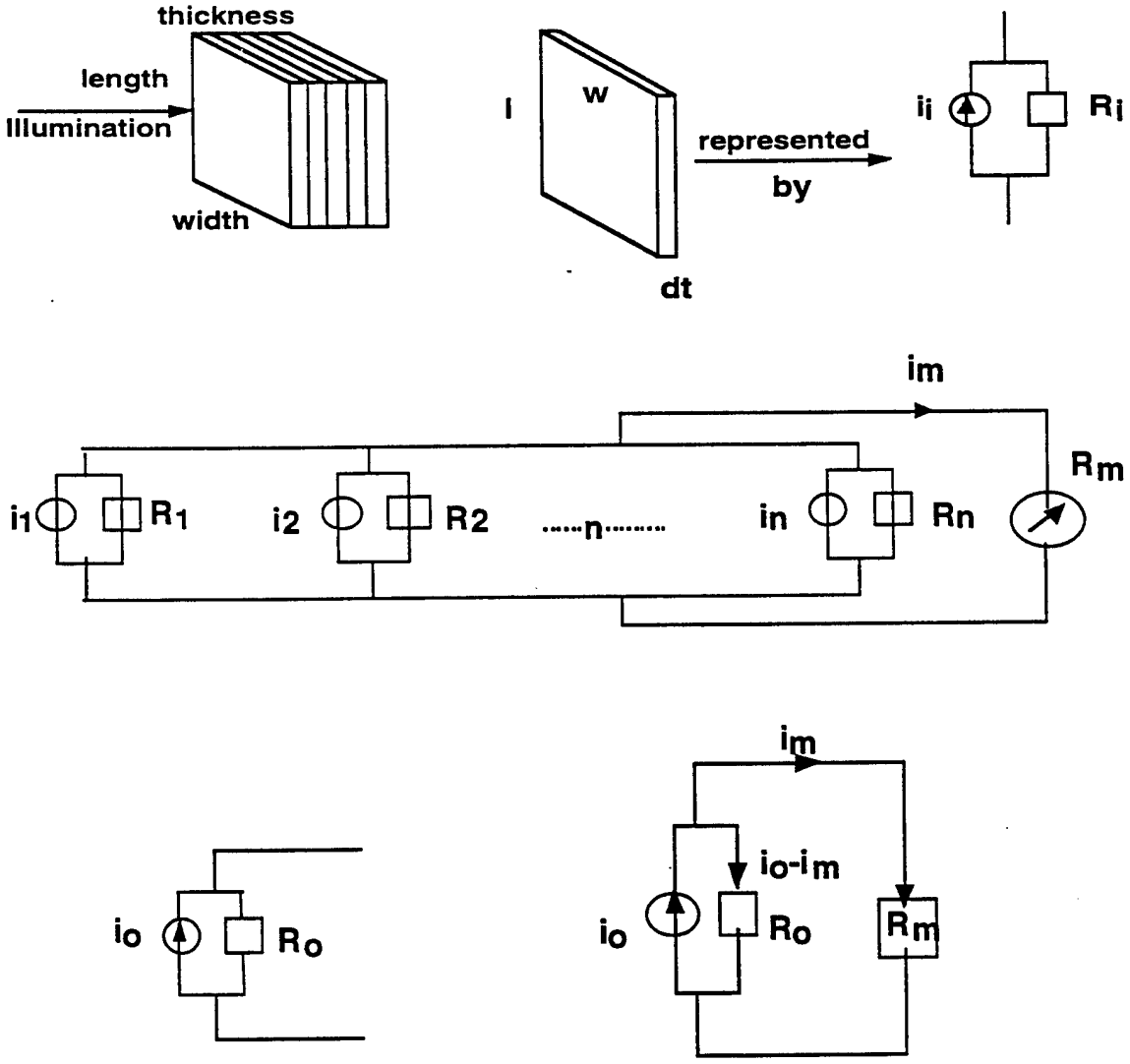
thickness
length
Illumination
width
l
w
dt
represented
by
ii
Ri
im
Rm
i1
R1
i2
R2
.....n.....
in
Rn
io
Ro
im
io-im
io
Ro
Rm

Fig 7

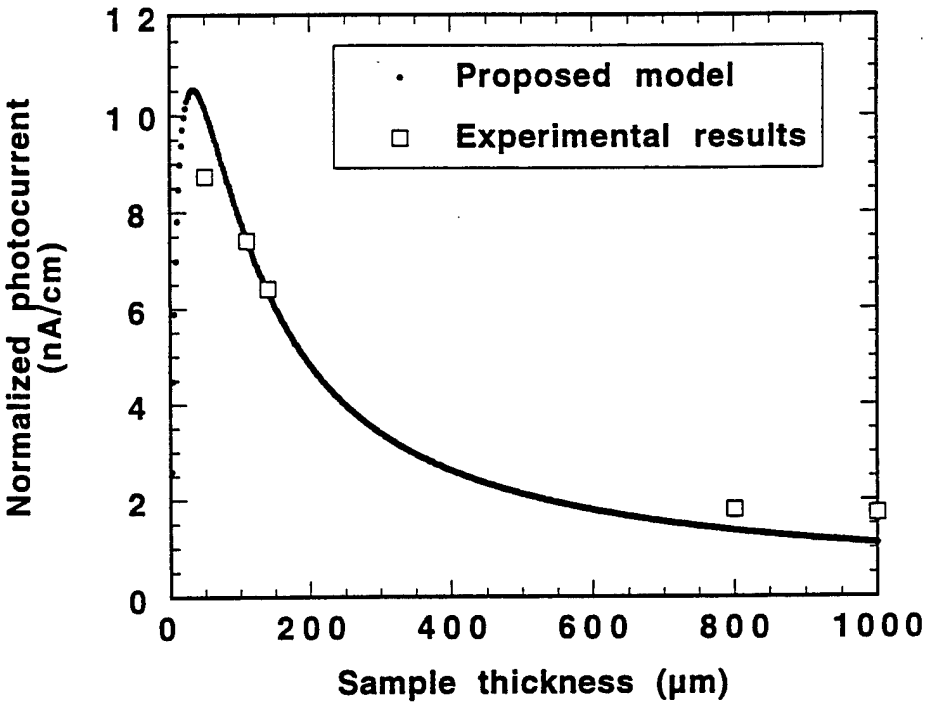
Normalized photocurrent (nA/cm)
1 2
1 0
8
6
4
2
0
0
200
400
600
800
1000
Sample thickness (μm)
Proposed model
Experimental results

Fig 8

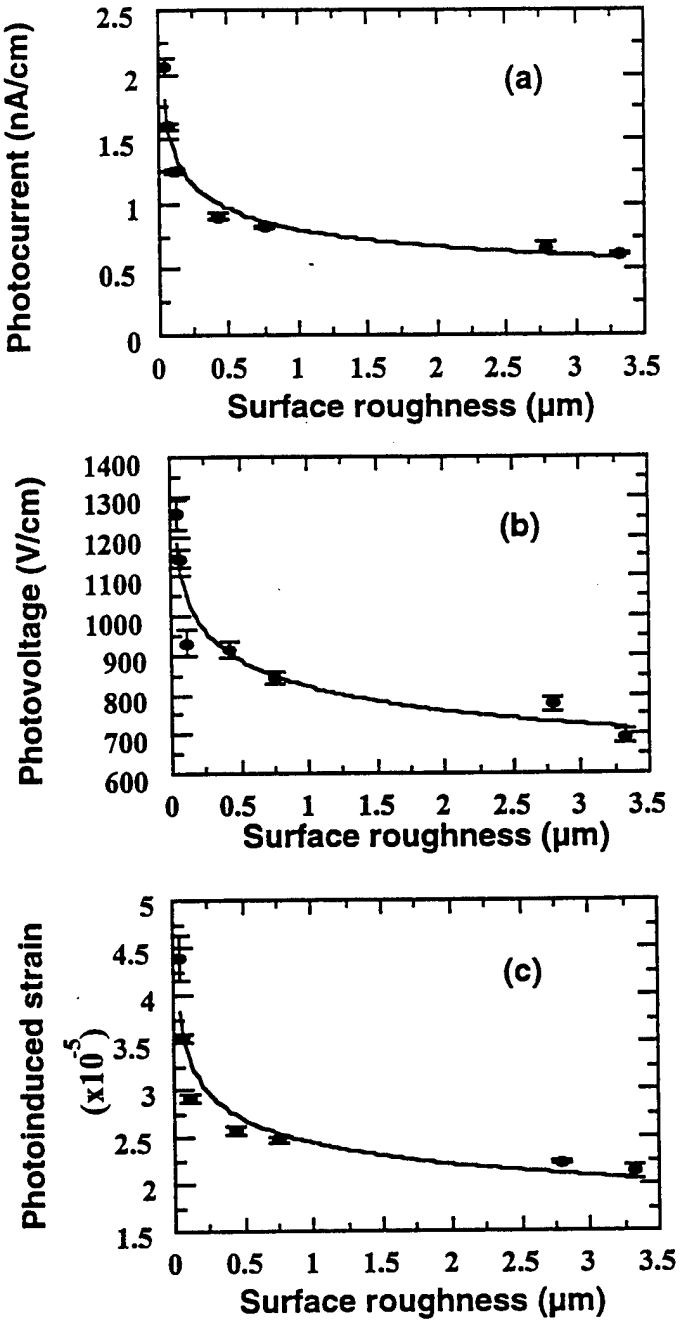
Photocurrent (nA/cm)
2.5
2
1.5
1
0.5
0
(a)
0 0.5 1 1.5 2 2.5 3 3.5
Surface roughness (μm)
Photovoltage (V/cm)
1400
1300
1200
1100
1000
900
800
700
600
(b)
0 0.5 1 1.5 2 2.5 3 3.5
Surface roughness (μm)
Photoinduced strain
(x10^-5)
5
4.5
4
3.5
3
2.5
2
1.5
(c)
0 0.5 1 1.5 2 2.5 3 3.5
Surface roughness (μm)

Fig 9

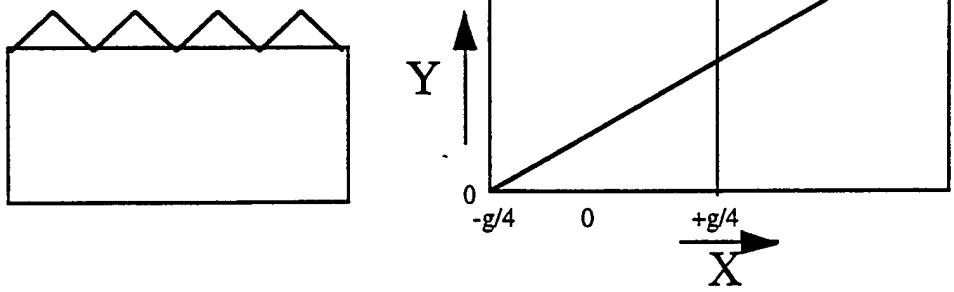

(a) Rough Sample (V-shaped)

(b) Unit cell of the rough surface

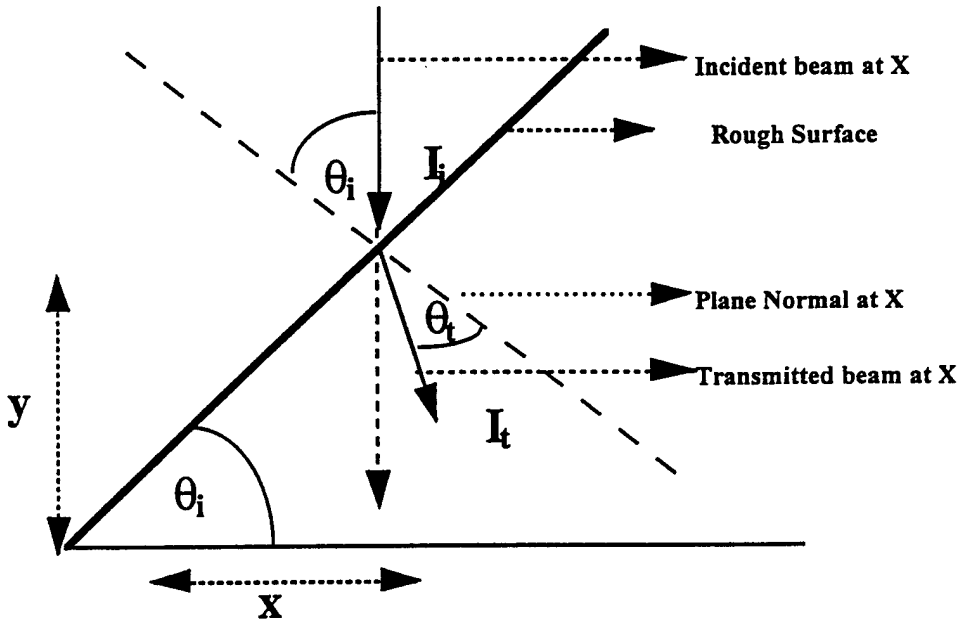

(c) Trajectory of light beam in the rough surface

Fig 10

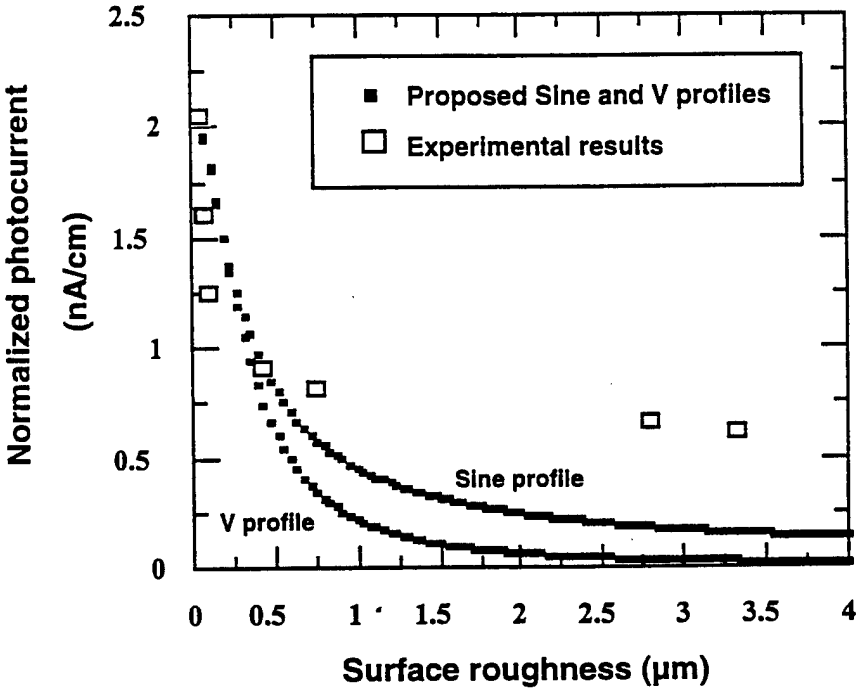
Normalized photocurrent
(nA/cm)
2.5
2
1.5
1
0.5
0
Proposed Sine and V profiles
Experimental results
Sine profile
V profile
0
0.5
1
1.5
2
2.5
3
3.5
4
Surface roughness (μm)

Fig 11

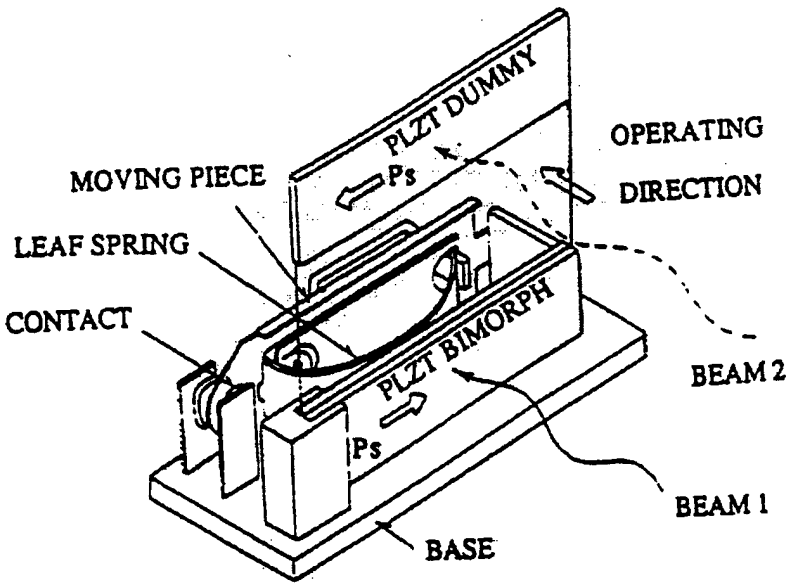
PLZT DUMMY
Ps
OPERATING
DIRECTION
MOVING PIECE
LEAF SPRING
CONTACT
PLZT BIMORPH
BEAM 2
Ps
BEAM 1
BASE

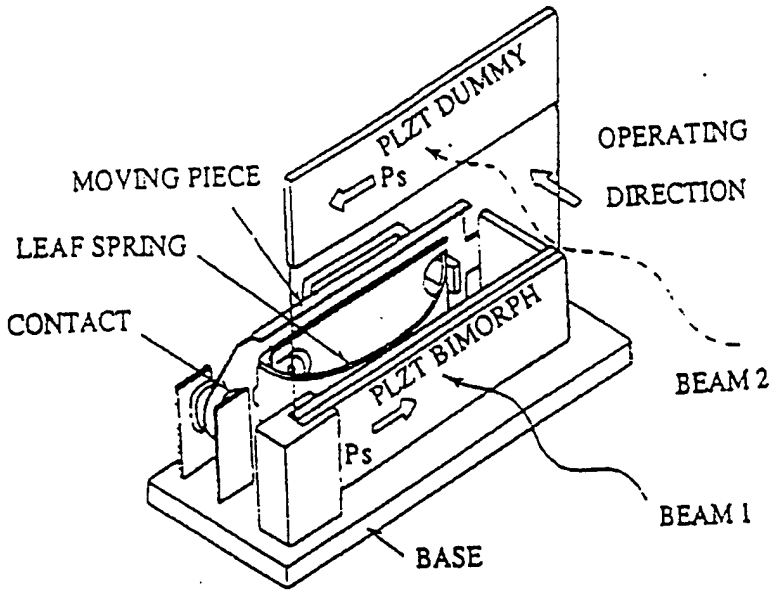
PLZT DUMMY
Ps
OPERATING
DIRECTION
MOVING PIECE
LEAF SPRING
CONTACT
PLZT BIMORPH
BEAM 2
Ps
BEAM 1
BASE

Fig 12

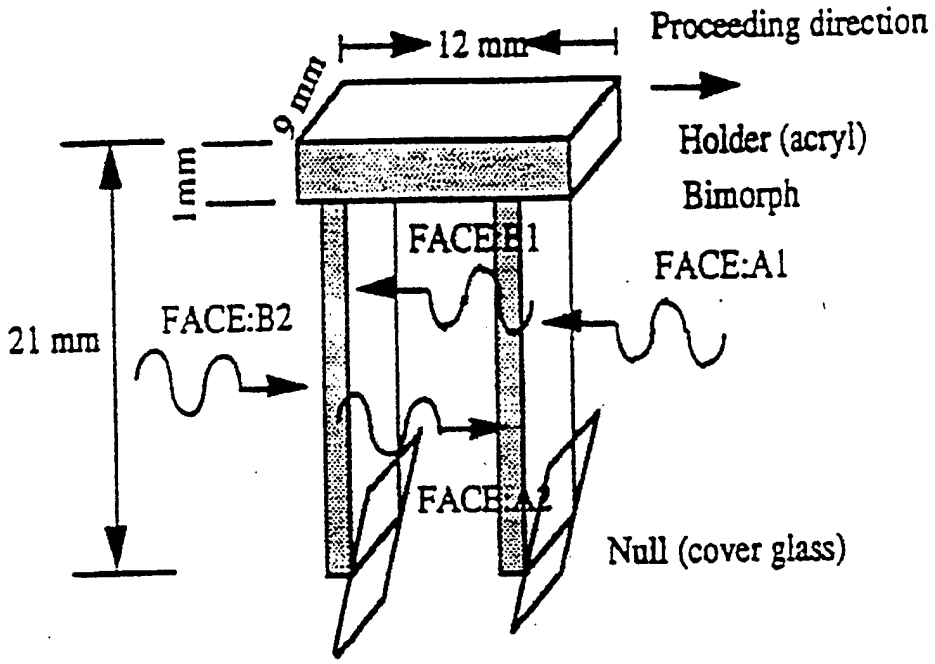
12 mm
Proceeding direction
9 mm
Holder (acryl)
1 mm
Bimorph
FACE:B1
FACE:A1
21 mm
FACE:B2
FACE:A2
Null (cover glass)

Fig 13

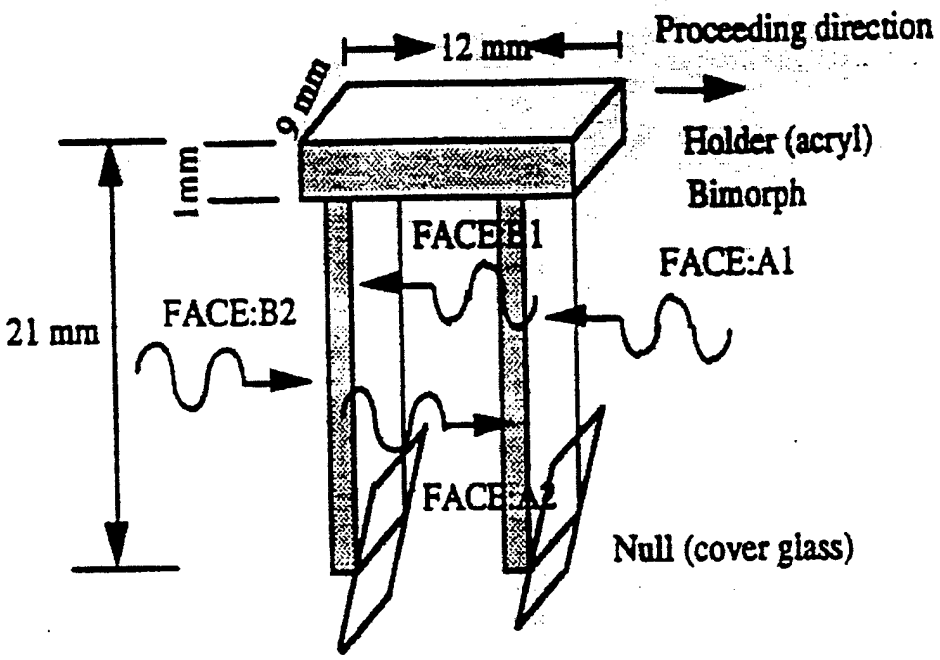
12 mm
Proceeding direction
9 mm
Holder (acryl)
Bimorph
1mm
FACE:B1
FACE:A1
21 mm
FACE:B2
FACE:A2
Null (cover glass)

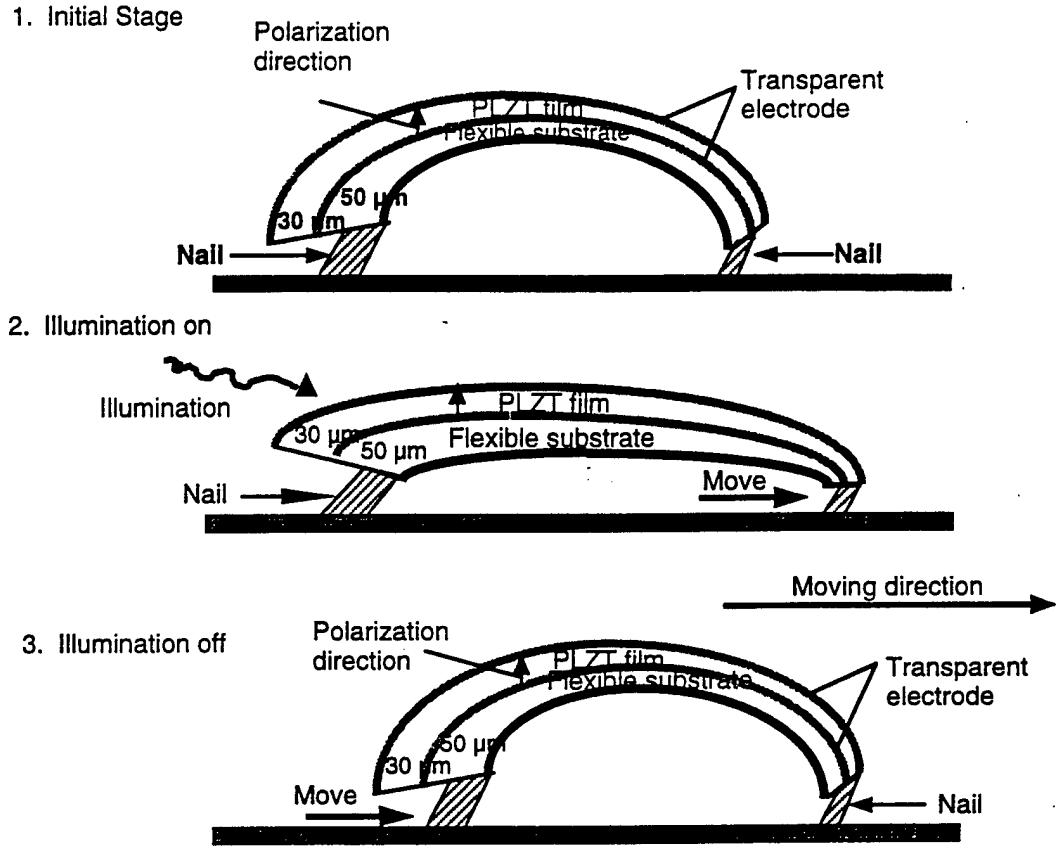
1. Initial Stage
Polarization direction
Transparent electrode
PLZT film
Flexible substrate
50 μm
30 μm
Nail
Nail
2. Illumination on
Illumination
PLZT film
30 μm
50 μm
Flexible substrate
Nail
Move
Moving direction
3. Illumination off
Polarization direction
PLZT film
Flexible substrate
Transparent electrode
50 μm
30 μm
Move
Nail
(a)
A
B
(b)

Fig 14

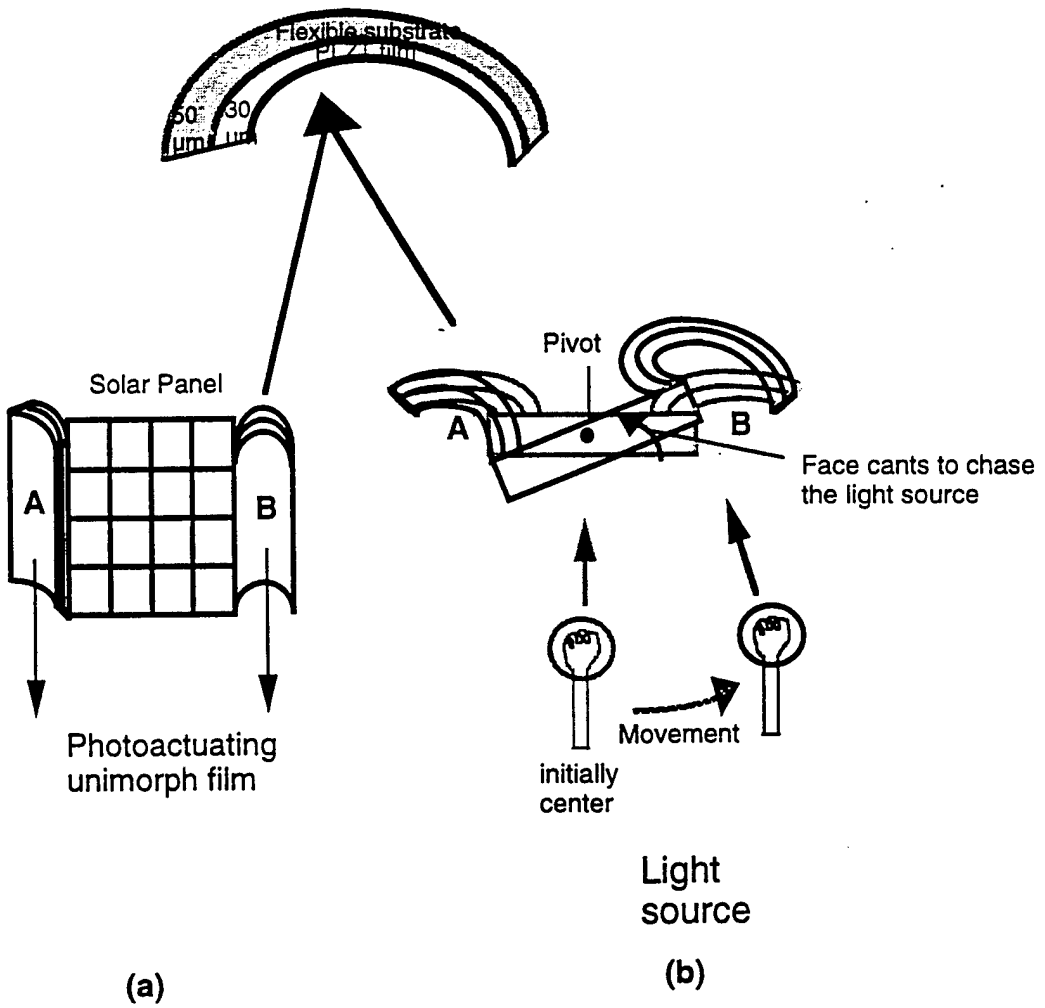
Flexible substrate
50 μm
30 μm
Solar Panel
A
B
Photoactuating unimorph film
(a)
Pivot
A
B
Face cants to chase the light source
Movement
initially center
Light source
(b)

Fig 1

Contact authors

1. **Kenji Uchino**

   134 Materials Research Laboratory

   The Pennsylvania State University, University park, State College, PA 16802

   Tel (814) 863-8035

   Fax (814) 865-2326

   e-mail address kenjiuchino@alpha.mrl.psu.edu

2. **Patcharin Poosanaas**

   A9, Materials Research Laboratory

   The Pennsylvania State University, University Park, State College, PA 16802

   Tel. (814) 865-2434

   Fax (814) 865-2326

   e-mail address: pxp138@psu.edu

Figure captions

Figure 1. Energy band gap model of excited transition from impurity level in PLZT [5].

Figure 2. Dependence of photoconductivity on illumination intensity in PLZT (3/52/48) ceramics. The exponent of the curve was found to be 0.54 which is closed to the model.

Figure 3. Dependence of photocurrent on illumination intensity for 1 mm thick sample of PLZT (3/52/48) ceramics. The parameter β was estimated to be 0.46.

Figure 4. Dependence of photovoltage on illumination intensity in PLZT (3/52/48) ceramics. Photovoltage was found to be proportional to the square root of the light intensity.

Figure 5. Dependence of photocurrent in thin sample (140 μm) of PLZT (3/52/48) ceramics on illumination intensity. The parameter β was estimated to be 0.80 by the curve fitting.

Figure 6. Experimental set up for photovoltaic and photostrictive measurements.

Figure 7. Schematic of the model to compute the dependence of photocurrent on sample thickness. The sample has been modeled as thin slices along the thickness direction and the corresponding circuit diagrams are also shown.

Figure 8. Comparison of measured and computed normalized photocurrent in 0.5 at% WO_3 doped PLZT (3/52/48) ceramics. The optimum thickness was found at 33 μm.

Figure 9. Variation of (a) photocurrent, (b) photovoltage, and (c) photo-induced strain with surface roughness in 0.5 at% WO_3 doped PLZT ceramics.

Figure 10. Schematic diagram of the V-shaped model (a) rough sample, (b) unit cell of the rough sample, and (c) trajectory of light beam in the rough surface.

ELSEVIER

Materials Chemistry and Physics 61 (1999) 36–41

MATERIALS CHEMISTRY AND PHYSICS

www.elsevier.com/locate/matchemphys

Photostrictive effect in lanthanum-modified lead zirconate titanate ceramics near the morphotropic phase boundary

Patcharin Poosanaas, Kenji Uchino*

International Center for Actuators and Transducers, Materials Research Laboratory, The Pennsylvania State University, University Park, PA 16802, USA

Abstract

Photostrictive effect in lanthanum-modified lead zirconate titanate (PLZT) ceramics, one of the promising candidates for photostrictive materials, has been investigated with different contents of La and the ratio of Zr/Ti near the morphotropic phase boundary compositions. The maximum photocurrent and photovoltage were obtained at different compositions of PLZT ceramics: maximum photocurrent at 4/48/52, maximum photovoltage at 5/54/46. New figures of merit for evaluating these materials, which includes both the magnitude of strain and response speed, were proposed. © 1999 Published by Elsevier Science S.A. All rights reserved.

Keywords: Photovoltaic effect; Photostriction; PLZT ceramics; Compositional variation; Morphotropic phase boundary; Photostrictive actuators

1. Introduction

Lanthanum-modified lead zirconate titanate (PLZT) ceramics are known to exhibit a range of interesting electro-optical properties [1,2]. Recently, the application of PLZT in photostrictive actuators has drawn considerable attention [3–7]. The idea of photo-driven actuator arises from the photostrictive effect, which is the combination of the photovoltaic and converse-piezoelectric effects in ferroelectric materials. Such a direct conversion of photonic to mechanical energy by the photostrictive effect can lead to a broad range of applications. One of the promising applications is the tailored films of photostrictive PLZT on a flexible substrate for bio-morphic explorers in future space missions [8]. Moreover, they can be used for photostrictive motors, transducers, advanced mobiles, shape controllers, and microvalves [8,9].

The photostrictive materials were evaluated on the basis of the product of photovoltage (E_{ph}) and the piezoelectric coefficient (d_{33}). Fig. 1 shows the room temperature phase diagram of the PLZT system by Haertling and Land [1]. The largest product of E_{ph} and d_{33} has been reported for the PLZT 3/52/48, which is around the morphotropic phase boundary (MPB) separating the rhombohedral and tetragonal ferroelectric phases in Fig. 1 [5,7]. However, a rigorous comprehensive investigation on the compositional dependence, varying both La concentration and Zr/Ti ratio especially close to the MPB, has not yet been carried out. Since the material characteristics, i.e. dielectric, piezoelectric, and photovoltaic properties of PLZT are sensitive to compositional variation, investigation of compositional dependence near MPB is very important for the material optimization.

In pursuit of an enhanced photostrictive material, this paper examines the optimum composition range for obtaining the maximum photovoltaic effect in the PLZT ceramics.

2. Experimental procedure

PLZT compositions are given in the form of $Pb_{1-x}La_x(Zr_yTi_{1-y})_{1-x/4}O_3$ (abbreviated as PLZT $X/Y/Z$, $X=100x$; $Y=100y$; and $Z=100(1-y)$). PLZT ceramics with concentration of La varying from 2 to 5 at. %, Zr/Ti ratio varying from 48/52 to 54/46 were prepared by the conventional oxide mixing process (see Fig. 1). These series of compositions are located in the area of morphotropic phase boundary, including the particular composition 3/52/48 which was reported to exhibit the maximum photovoltaic effect. Fig. 2 illustrates a flow chart for the sample preparation by the conventional oxide mixing process. The details of this technique was reported in an earlier publication [10].

Phase identification was performed using X-ray diffraction (Scintag diffractometer, Vax 3100 System). All samples exhibited perovskite structures. Microstructure and grain size of the samples were observed by scanning electron

*Corresponding author. Fax: +1-814-865-2326
E-mail address: pxp138@psu.edu (K. Uchino)

0254-0584/99/$ – see front matter
PII: S0254-0584(99)00110-8

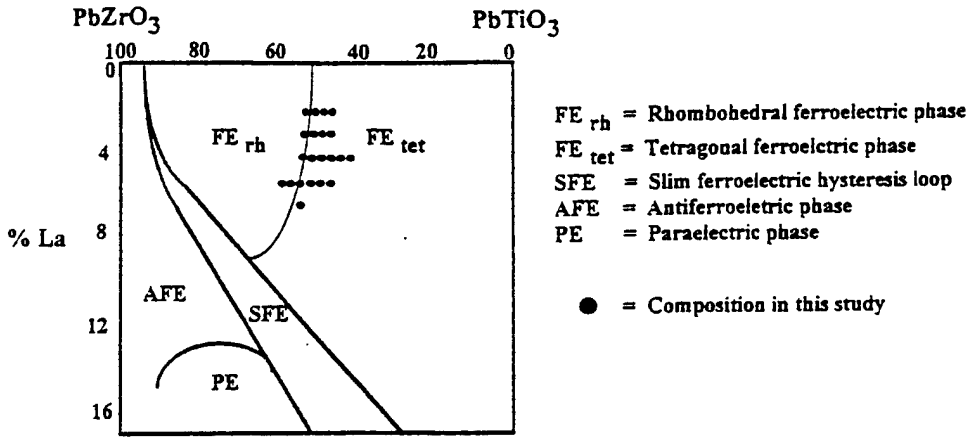

Fig. 1. Room temperature phase diagram of PLZT system showing the morphotropic phase boundary separating the rhombohedral and tetragonal ferroelectric phases [1] and the compositions that have been investigated in this study.

microscopy (ISI-DS 130). Dielectric properties of PLZT samples were measured with an impedance analyzer (HP-4284A). Samples for dielectric measurements were polished to about 10 mm in diameter, and 1 mm in thickness, then electroded with platinum (Pt) by sputtering. Piezoelectric properties of all the samples were measured by using a Berlincourt d_{33} meter (Channel Products) at 100 Hz. Samples for piezoelectric measurement were of the same configuration as for dielectric measurements, except that they were poled in silicone oil at 120°C under a 2 kV/mm electric field for 10 min.

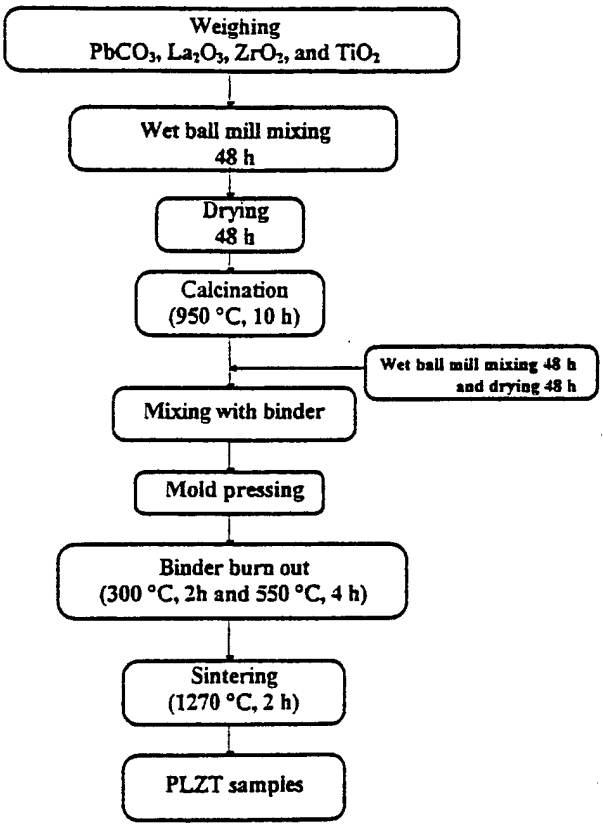

Fig. 2. Flow diagram of sample preparation by the conventional oxide mixing process.

The samples of $5\times5\times1$ mm^3 were cut and polished for photovoltaic measurements. The 5×1 mm^2 surfaces were Pt electroded. Photovoltaic measurements were done by using a high-input impedance electrometer (Keithley 617). The photovoltage and photocurrent were determined from the current–voltage relation by applying voltage in the range from -100 to $+100$ V along with the radiating light to the samples. The photovoltage was determined in an open circuit state from the intercept of the horizontal applied voltage axis, while the photocurrent was obtained from the short circuit state from the intercept of the vertical current axis. A high pressure mercury lamp (Ushio Electric USH-500D) was used as a light source. The white radiation was passed through an IR blocking filter and an UV bandpass filter to obtain a monochromatic beam with a maximum strength around 366 nm wavelength and an intensity of 3.25 mW/cm^2, before illuminating the samples (5×5 mm^2 polished surface). The light beam with this wavelength has been reported to yield the maximum photovoltaic properties for PLZT [7]. The details of this experimental set-up was reported in an earlier paper [10].

3. Results

3.1. Grain size

Since the photovoltaic and piezoelectric effects are strongly dependent on the grain size [5], the grain size data are shown firstly. Average grain sizes of the PLZT ceramics were obtained from the polished sample surface by SEM observations using the intercept method. Grain sizes of the samples ranged from 1 to 5 μm. Fig. 3 shows the average grain size as a function of Zr/Ti ratio and La content. The average grain size were observed to decrease with La

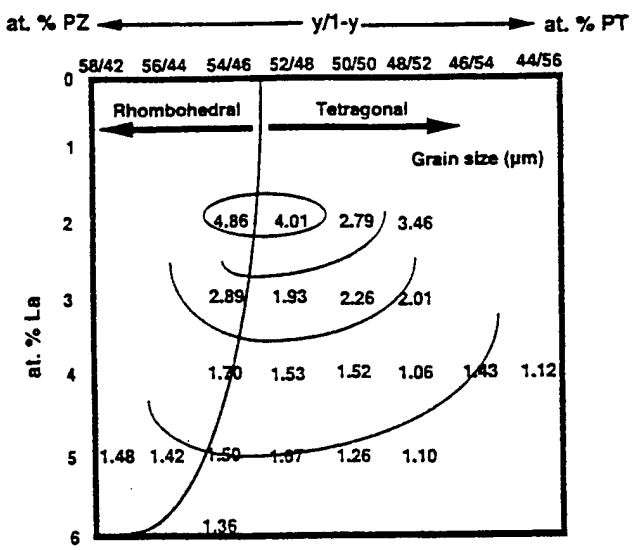

Fig. 3. The contour map of the average grain size in PLZT ceramics. Larger grain sizes were found along the MPB of PLZT system.

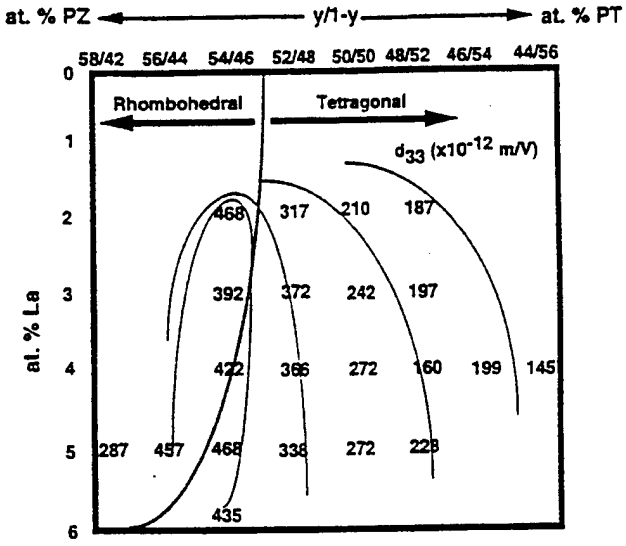

Fig. 5. Variation of piezoelectric constant (d_{33}) in the PLZT system. The maxima of d_{33} have been found along the MPB.

addition. As Zr/Ti ratio increased, the average grain size increased and approaches to the MPB region. This agrees with the previous report [11,12].

3.2. Dielectric and piezoelectric properties

Figs. 4 and 5 show the dielectric constant (ϵ) and piezoelectric constant (d_{33}) contour maps at room temperature for the PLZT system. The dielectric constant showed the maximum at the MPB for all the La content and decreased with increasing Ti content (decrease in Zr/Ti ratio). The d_{33} increased with increasing Zr/Ti ratio and the maximum d_{33} has been found at the MPB.

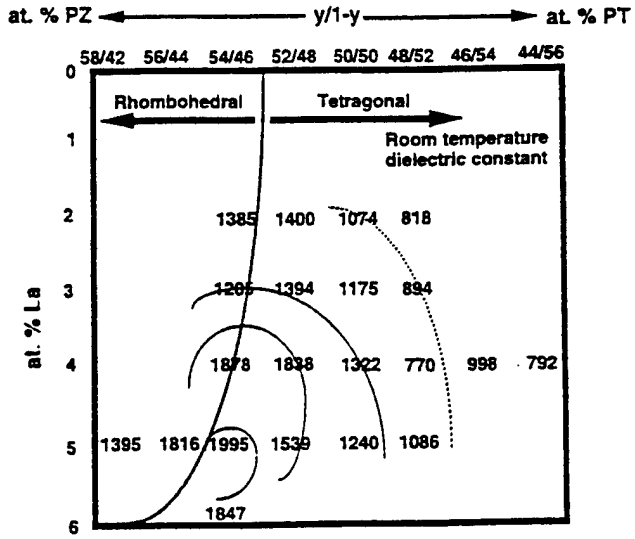

Fig. 4. Variation of room temperature dielectric constant as a function of compositional variation along the MPB of PLZT system. Dielectric constants show the maxima along the MPB.

3.3. Photovoltaic properties

The maximum photovoltaic properties has been reported earlier at PLZT 3/52/48 for a coarse composition change. The compositional variation especially around the MPB plays an important role. The contour map of the photocurrent at room temperature in the PLZT phase diagram is shown in Fig. 6, while Fig. 7 illustrates the photovoltage contour map. In these two figures, the solid circles indicate the location of PLZT 3/52/48 which has been reported earlier to exhibit the maximum photocurrent and photovoltage. In this new fine measurement, the maximum photocurrent and photovoltage have been found at different compositions of PLZT ceramics. The maximum photocurrent was found at PLZT 4/48/52 which corresponds to the tetragonal phase, while the maximum photovoltage was found at PLZT 5/54/46 which is along the MPB. The photocurrent and photovoltage were found to get enhanced by more than twice for these new compositions.

It is noteworthy that the maximum photocurrent and photovoltage are obtained at different compositions. In order to explain this, the current source model which has been proposed by one of the authors is used here [13]. The electron energy band of PLZT is basically generated by the hybridized orbit of p-orbital of oxygen and d-orbital of Ti/Zr. The donor impurity levels induced in accordance with La doping (or other dopants) are present slightly above the valence band. Transition from these levels with an asymmetric potential due to the crystallographic anisotropy may provide the preferred momentum to electron. Electromotive force is generated when electrons are excited by illumination and move in a certain direction of the ferroelectric materials, which may arise along the spontaneous polarization direction, resulting in photocurrent. PLZT 4/48/52 exhibits the maximum photocurrent, suggesting the product

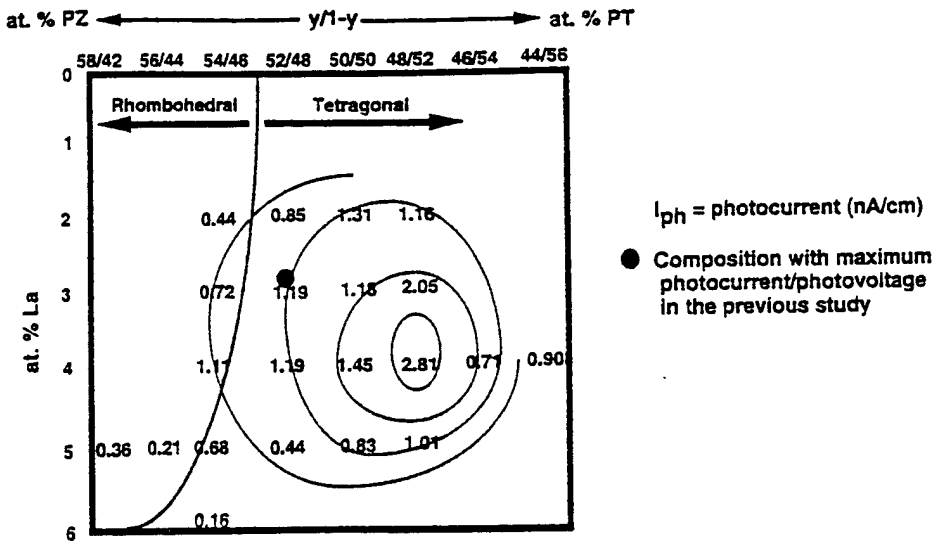

Fig. 6. The contour map of photocurrent in PLZT ceramics. The maximum photocurrent was found at PLZT 4/48/52 having tetragonal phase. (•) represented the maximum photocurrent composition reported earlier.

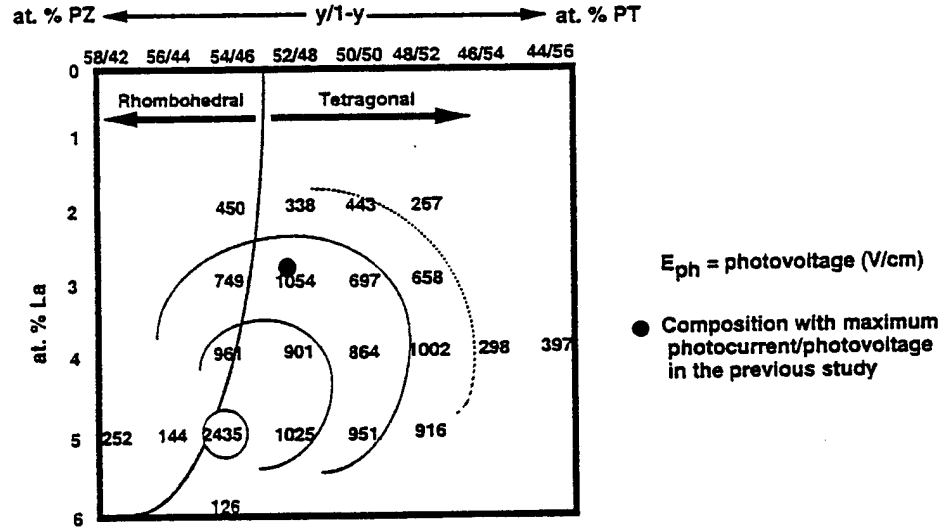

Fig. 7. The contour map of photovoltage in PLZT ceramics. Photovoltage was found to be maximum at PLZT 5/54/46 and along the MPB of PLZT system. (•) represented the composition with maximum photovoltage reported earlier.

of the number of impurity levels and the asymmetry of materials is maximized. As La content and Zr/Ti ratio increases, the system transforms to more symmetry form of cubic system resulting in decreasing photocurrent eventhough addition of La content will increase the impurity level. Photocurrent at rhombohedral phases lower than tetragonal phases can also be attributed to this reason as well.

Considering the contour map of photoconductance in the PLZT phase diagram in Fig. 8, which shows the minimum along the MPB especially for PLZT 5/54/46, photovoltage at this composition is observed as the maximum. The minimum of conductivity near the MPB of lead zirconate titanate (PZT) ceramics was also reported in the previous study [14].

4. Discussion

Since the maxima in photocurrent which governs the response speed and in photovoltage which governs the magnitude of strain are located at different compositions of PLZT ceramics, new figures of merit for photostriction should be proposed by considering both the terms for response speed and magnitude of strain. The new figures of merit for photostriction were derived as follows.

Since the strain is induced as a function of time, t, as

$$x_{ph} = d_{33}E_{ph}\left(1 - \exp\left(\frac{-t}{RC}\right)\right), \quad (1)$$

where x_{ph} is the photo-induced strain, d_{33}, the piezoelectric constant of the materials, E_{ph}, the photovoltage, I_{ph}, the

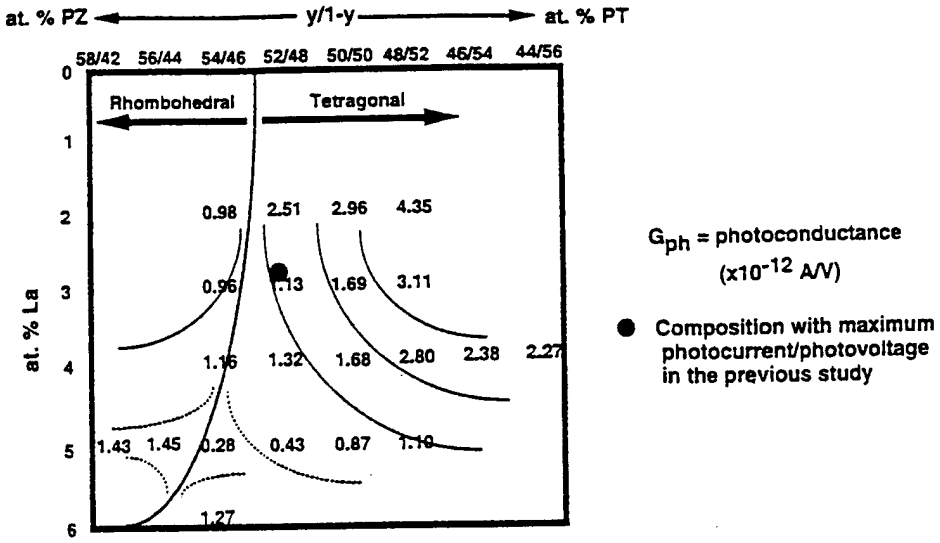

Fig. 8. The contour map of photoconductance in PLZT system. Photoconductance is minimum along the MPB. The minimum photoconductance was found at PLZT 5/54/46 where it also exhibits the maximum photovoltage.

photocurrent, t, the time, R and C are the resistance and the capacitance of the material, respectively.

For $t \ll 1$, we obtain

$$x_{ph} = d_{33}E_{ph}\left(\frac{t}{RC}\right). \quad (2)$$

Thus, the figure of merit for response speed should be provided by $d_{33}E_{ph}(1/RC)$.

Taking account of the relation $I_{ph} = E_{ph}/R$, this figure of merit is transformed to $d_{33}I_{ph}/C$.or, it can be given by $d_{33}I_{ph}/\epsilon$ (ϵ is the permittivity). On the other hand, for $t \gg 1$, the saturated strain is provided by:

For $t \gg 1$, we obtain

$$x_{ph} = d_{33}E_{ph}. \quad (3)$$

which is similar to the previous paper [6]. Thus, the figure of merit for the magnitude of strain is defined by $d_{33}E_{ph}$.

In order to obtain a high photo-induced strain, materials with high d_{33} and E_{ph} are needed. On the contrary, for high response speed, materials with high d_{33}, I_{ph}, and low dielectric constant are required. Figs. 9 and 10 show the contour maps of $d_{33}I_{ph}/C$ (s^{-1}) and $d_{33}E_{ph}$ (unitless) on the PLZT composition diagram, respectively.

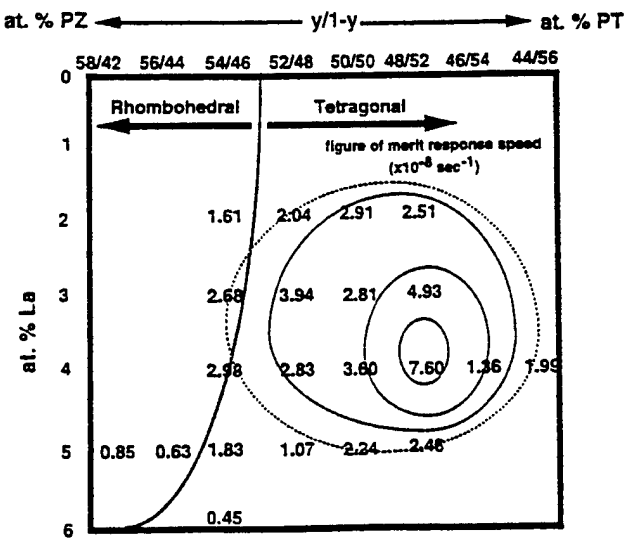

Fig. 9. The contour map of $d_{33}I_{ph}/C$, figure of merit for response speed. PLZT 4/48/52 is best suited for high response speed material in PLZT system.

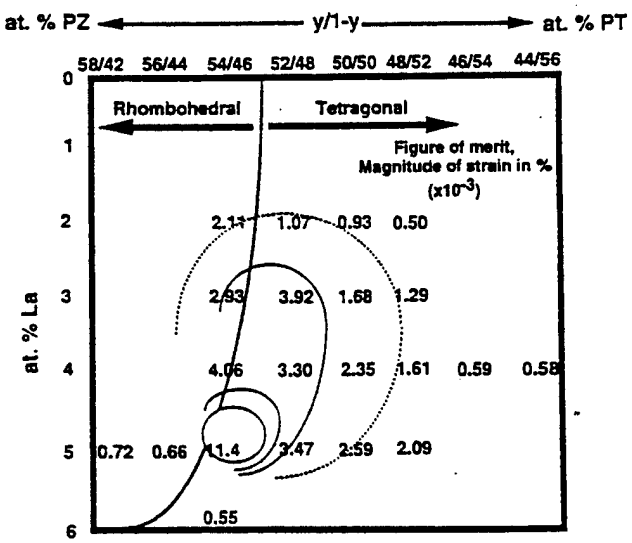

Fig. 10. The contour map of $d_{33}E_{ph}$, figure of merit for magnitude of strain. PLZT 5/54/46 is best suited for the maximum strain in PLZT system.

5. Conclusion

A rigorous investigation of the composition dependence, especially near the morphotropic boundary, on photovoltaic properties in PLZT ceramics was carried out in order to examine compositions for the maximum photovoltaic properties. It has been found that the maximum photocurrent and photovoltage exist at different compositions of PLZT ceramics. Maximum photocurrent was found at PLZT 4/48/52 which is in tetragonal phase, while maximum photovoltage was found at PLZT 5/54/46 which is around the MPB of the PLZT phase diagram. The photocurrent and photovoltage were improved more than twice higher for the new compositions of PLZT. The new figures of merit for photostriction for the magnitude of strain or the response speed term have been proposed. The high performance photostrictive materials can be tailored using these new compositions.

Acknowledgements

One of the authors (P. Poosanaas) would like to acknowledge the Royal Thai Government and Dr. Harit Sutabutr from the National Metal and Materials Technology Center (Thailand) for granting MOSTE fellowship.

References

[1] G. Haertling, C. Land, J. Am. Ceram. Soc. 54 (1971) 1.
[2] Y. Xu, Ferroelectric Materials and their Application, Elsevier, New York, 1991.
[3] S.Y. Chu, K. Uchino, Ferroelectrics 174 (1995) 185.
[4] S.Y. Chu, Z. Ye, K. Uchino, Smart Mater. Struct. Mater. 3 (1994) 114.
[5] T. Sada, M. Inoue, K. Uchino, J. Ceram. Soc. Jpn. Inter. Ed. 95 (1987) 499.
[6] K. Uchino, M. Aizawa, S. Nomura, Ferroelectrics 64 (1985) 199.
[7] K. Uchino, M. Aizawa, Jpn. J. Appl. Phys. Suppl. 24 (1985) 139.
[8] S. Thakoor, J.M. Morookian, J.A. Cutts, in: Proceedings of the 10th IEEE International Symposium on Applications of Ferroelectrics Transactions, vol. 1, 1996, p. 205.
[9] M. Sayer, M. Lukacs, T. Olding, Integrated Ferroelectrics 17 (1997) 1.
[10] P. Poosanaas, A. Dogan, A.V. Prasadarao, S. Komarneni, K. Uchino, J. Electroceramics 1 (1997) 111.
[11] G. Haertling, in: Proceedings of the Ninth IEEE International Symposium on Applications of Ferroelectrics Transactions, 1994, p. 313.
[12] M.A. Akbas, I.M. Reaney, W.E. Lee, J. Mater. Res. 11 (1996) 2293.
[13] K. Uchino, Innovations Mater. Res. 1 (1996) 11.
[14] K. Uchino, M. Yoshizaki, A. Nagao, Ferroelectrics 95 (1989) 161.